

# Pressure-Gain Combustion for Gas Turbines Based on Shock-Flame Interaction

A thesis accepted by the Faculty of Aerospace Engineering and Geodesy of the  
Universität Stuttgart in partial fulfilment of the requirements for the degree of  
Doctor of Engineering Sciences (Dr.-Ing.)

by

**Dipl.-Ing. Eugen Lutoschkin**

born in Rudnyj (Kazakhstan)

Main referee: PD Dr. Martin G. Rose MA. MSc. PhD. CEng., Universität Stuttgart

Co-referee: Prof. Dr. Lars-Erik Eriksson, Chalmers University of Technology

Co-referee: Prof. Dr. rer. nat. Uwe Riedel, Universität Stuttgart

Date of defence: 12.12.2013

Institute of Aircraft Propulsion Systems

University of Stuttgart

2014



## Acknowledgements

I express my gratitude to the Friedrich und Elisabeth Boysen Stiftung for the financial support of this work that was provided under the contract number Kz.BOY07-Nr.42.

I am especially indebted to my advisor PD Dr. Martin G. Rose for suggesting the topic and guiding me through this challenging project. I highly appreciated his time that he had always generously provided to me. Our discussions had always been a source of great inspiration and motivation.

Further, I would like to thank Professor Dr.-Ing. Stephan Staudacher for giving me the opportunity to write this thesis at the Institute of Aircraft Propulsion Systems of Stuttgart University. His advice and support helped me to stay focused and determined throughout this work.

I would also like to thank Professor Lars-Erik Eriksson and Professor Uwe Riedel for being my co-referees and reading through the thesis for me.

I am very grateful to Dr. Clemens Naumann and Dr. Juergen Herzler from DLR Stuttgart for their generous and highly valuable support during the experimental phase of this work.

My colleagues and friends have essentially contributed to make my stay at the Institute of Aircraft Propulsion Systems to become a pleasant and an unforgettable experience. My thanks belong to all of them.

My special thanks go to Dr.-Ing. Christian Kasper for his patience and his remarks during the proofreading of this thesis.

I am deeply grateful to my parents and my brothers for their absolute support in all of my endeavours. They have always been a source of great strength and confidence to me.

I don't think I could have accomplished this work without the motivation, support, and love of my beloved wife Viktoria.



# Contents

<b>Acknowledgements</b>	<b>I</b>
<b>Contents</b>	<b>III</b>
<b>Nomenclature</b>	<b>VII</b>
<b>List of Figures</b>	<b>XII</b>
<b>List of Tables</b>	<b>XVII</b>
<b>Abstract</b>	<b>XVIII</b>
<b>Zusammenfassung</b>	<b>XX</b>
<b>1 Introduction</b>	<b>1</b>
1.1 General Introduction and Motivation.....	1
1.2 Objectives of This Work.....	4
<b>2 Pressure-Gain Combustion – A Technical Review</b>	<b>6</b>
2.1 Modes of Combustion.....	6
2.2 Entropy Rise and Thermal Cycle Efficiency.....	11
2.3 Thermodynamic Benefit of Pressure-Gain Combustion in Gas Turbines.....	15
2.4 Review of the Existing PGC Concepts for Gas Turbine Applications.....	19
2.4.1 Elementary Constant Volume Combustors.....	20
2.4.2 Combustors Based on Reciprocating Internal Combustion Engines.....	21
2.4.3 Detonation Wave Combustors.....	22
2.4.4 Pulse Combustors.....	24
2.4.5 External and Internal Combustion Wave Rotors.....	26
<b>3 Pressure-Gain Combustion Based on Shock Wave-Flame Interaction</b>	<b>29</b>
3.1 The Rayleigh Criterion.....	29
3.2 Shock-Flame Interaction – Literature Review.....	31
3.2.1 Introduction.....	31
3.2.2 Shock Refractions at Reactive and Inert Gas Interfaces.....	32

3.2.3	Flame Front Deformation Induced by Shock-Flame Interaction .....	35
3.2.4	Generation of Pressure Waves at Disturbed Flame Fronts .....	37
3.2.5	Shock-Flame Interaction in Two-Phase Combustion Systems .....	40
3.3	Pressure-Gain Combustion Based on Shock-Flame Interaction – Concept Development .....	42
<b>4</b>	<b>Experimental Investigation of Shock Wave-Flame Interaction</b>	<b>45</b>
4.1	The Experimental Facility .....	45
4.1.1	Measurement Instrumentation .....	48
4.1.2	Experimental Configuration and Procedure .....	49
4.2	Preliminary Studies .....	50
4.2.1	Shock Experiments without Combustion .....	50
4.2.2	Combustion Experiments without Shock Wave Generation .....	53
4.3	Shock-Flame Interaction – Experimental Results .....	58
4.3.1	Pressure and Chemiluminescence Profiles s/f-Interaction .....	58
4.3.2	Pressure and Chemiluminescence Profiles f/s-Interaction .....	62
4.3.3	The Rayleigh Index .....	65
4.4	Discussion and Conclusions .....	69
<b>5</b>	<b>Analytical Modelling of Shock Wave-Flame Interaction</b>	<b>73</b>
5.1	Description of the Analytical Model .....	73
5.1.1	Incident Shock Wave .....	75
5.1.2	Combustion Modelling .....	76
5.1.3	Shock Refraction at the Flame Front .....	78
5.1.4	Deformation of the Flame Front due to Shock Wave Transition .....	79
5.1.5	Generation of Pressure Waves at the Distorted Flame Front .....	83
5.2	Model Verification on the Basis of Experimental Results .....	85
5.3	Results and Discussion .....	90
<b>6</b>	<b>Engine Performance Studies</b>	<b>97</b>
6.1	Simplified Engine Performance Model .....	97
6.1.1	Baseline Gas Turbine Engine Models .....	97
6.2	Integration of a Shock Combustor into a Gas Turbine Engine .....	99
6.3	Performance Results of Shock-Combustor Enhanced Engines .....	102
6.3.1	Performance of a Shock-Combustor Topped Industrial Gas Turbine .....	103
6.3.2	Performance of a Shock-Combustor Topped Turbofan Engine .....	111
<b>7</b>	<b>Conclusions and Future Work</b>	<b>118</b>

7.1 Summary and Conclusions.....	118
7.2 Future Work.....	121
<b>Appendix A</b>	<b>122</b>
<b>Bibliography</b>	<b>127</b>
<b>Curriculum Vitae</b>	<b>145</b>





## Nomenclature

### Latin Symbols

$a$	[m/s]	Speed of sound
$A_F$	[m <sup>2</sup> ]	Flame surface area (arbitrary shape)
$A_L$	[m <sup>2</sup> ]	Flame surface area of a laminar flame
$A_T$	[m <sup>2</sup> ]	Flame surface area of a turbulent (corrugated) flame
$At$	[-]	Atwood number
$C_p$	[J/kgK]	Specific heat capacity at constant pressure
$C_v$	[J/kgK]	Specific heat capacity at constant volume
$C_r, C_t$	[-]	Correction factors
$D_T$	[m]	Shock tube inner diameter
$d$	[m]	Droplet diameter
$\Delta E$	[J]	Increment of energy
FAR	[-]	Fuel to air ratio
$F_N$	[N]	Net thrust
$H_L$	[J/kg]	Lower heating value
$h$	[J/kg]	Specific enthalpy
$\vec{i}$	[-]	Unit vector in the x-direction
$\vec{j}$	[-]	Unit vector in the y-direction
$k$	[-]	Wave number
$\vec{k}$	[-]	Unit vector in the z-direction
$l_{int}$	[m]	Interface length
$\mathcal{M}$	[kg/mol]	Molar mass
$M$	[-]	Mach number (gas flow or propagating shock)
$\dot{m}$	[kg/s]	Mass flow rate
$P_s$	[W]	(Useful) Shaft power
$p$	[bar]	(static) Pressure
$p'$	[bar]	Fluctuating pressure
$\bar{p}$	[bar]	Mean pressure

## Nomenclature

---

$q$	[J/kg]	Effective energy release per unit mass of combustible mixture
$\bar{q}$	[J/kg]	Mean energy release
$q'$	[J/kg]	Fluctuating heat release per unit mass of mixture
$q_c$	[J/kg]	Heat of combustion per unit mass of mixture
$q_f$	[J/kg]	Heat of combustion per unit mass of mixture or LHV
$\mathcal{R}$	[J/molK]	Universal gas constant
$R$	[J/kgK]	Specific Gas Constant
$Re$	[-]	Reynolds number
$S$	[J/K]	Entropy
$s$	[J/kgK]	Specific entropy
$s_F$	[m/s]	Flame velocity relative to the unburned gas
$s_L$	[m/s]	Laminar Flame velocity
$s_T$	[m/s]	Turbulent Flame velocity
$T$	[K]	(static) Temperature
$T'$	[K]	Fluctuating temperature
$T_{max}$	[K]	Maximum cycle temperature
$t$	[s]	Time
$u$	[m/s]	Flow velocity in x-direction
$\Delta u$	[m/s]	Velocity increment
$U$	[m/s]	(Shock) Wave propagation velocity
$V$	[m <sup>3</sup> ]	Volume
$v_{int}$	[m/s]	Interface growth rate or velocity
$\vec{V}$	[m/s]	Flow velocity vector
$v$	[m/s]	Flow velocity in y-direction
$w$	[J/kg]	Useful specific cycle work
$We$	[-]	Weber number
$w$	[m/s]	Flow velocity in z-direction
$Y$	[-]	Mass fraction

## Greek Symbols

$\alpha$	[°]	Angle of incidence
$\alpha_{cr}$	[°]	Critical angle of incidence
$\Gamma$	[m <sup>2</sup> /s]	Circulation or deposited vorticity
$\gamma$	[m/s]	Strength of the vortex sheet

$\varepsilon$	[m]	Perturbation amplitude
$\varepsilon_0$	[m]	Initial perturbation amplitude
$\eta_{th}$	[-]	Thermal cycle efficiency
$\eta_{prop}$	[-]	Propulsive efficiency
$\Theta$	[-]	Chemiluminescence
$\kappa$	[-]	Ratio of specific heat capacities or adiabatic exponent
$\lambda$	[m]	Wave length
$\mu$	[-]	Engine bypass ratio
$\mu^2$	[-]	$= (\kappa_i - 1)(\kappa_i + 1)$
$\nu$	[m <sup>2</sup> /s]	Kinematic viscosity
$\xi$	[-]	Fraction of core mass flow rate used for shock generation
$\Pi$	[-]	Combustor pressure ratio
$\pi_c$	[-]	Compression Ratio
$\rho$	[kg/m <sup>3</sup> ]	(static) Density
$\sigma$	[kg/s <sup>2</sup> ]	Surface tension
$\tau$	[s]	Period of oscillation
$\tau_t$	[s]	Ignition delay time
$\Phi$	[-]	Equivalence ratio
$\varphi$	[-]	Cooling effectiveness
$\psi$	[Nkg/s <sup>2</sup> ]	Wave energy dissipation
$\omega$	[J/sm <sup>2</sup> ]	Heat release rate per unit flame surface area
$\Delta\omega$	[J/sm <sup>2</sup> ]	Finite increment of heat release rate per unit flame surface area
$\omega_v$	[1/s]	Vorticity
$\Omega$	[J/s]	Total heat release rate

### Symbols

$\frac{\partial}{\partial}$	Partial derivative
$\frac{D}{Dt}$	Substantial derivative, $= \frac{\partial}{\partial t} + u \frac{\partial}{\partial x} + v \frac{\partial}{\partial y} + w \frac{\partial}{\partial z}$
$\nabla$	Del, vector differential operator, $= \vec{i} \frac{\partial}{\partial x} + \vec{j} \frac{\partial}{\partial y} + \vec{k} \frac{\partial}{\partial z}$

### Subscripts

amb	Ambient
b	Burned
cool	Cooling
exp	Expansion wave
f	Fuel
i	Incident
r	Reflected
t	Total or stagnation value
tr	Transmitted
u	Unburned

### Abbreviations

ACARE	Advisory Council for Aeronautics Research in Europe
BBC	Brown, Boveri & Cie
CC	Cooling air Compressor
CCE	Compound Cycle Engine
CFD	Computational Fluid Dynamics
CJ <sub>L</sub>	Lower Chapman-Jouguet point
CJ <sub>U</sub>	Upper Chapman-Jouguet point
CP	Constant Pressure or Isobaric
CV	Constant Volume or Isochoric
DARPA	Defense Advanced Research Projects Agency
DDT	Deflagration to Detonation Transition
DLR	Deutsches Zentrum für Luft- u. Raumfahrt / German Aerospace Centre
DNS	Direct Numerical Simulation
eq.	Equation
FAR	Fuel to Air Ratio
FFT	Fast Fourier Transform
FJ	Fickett-Jacobs
HPC	High Pressure Compressor
HPT	High Pressure Turbine
HRR	Het Release Rate
X	

---

IC	Internal Combustion
ICWR	Internal Combustion Wave Rotor
IGTI	International Gas Turbine Institute
IPCC	Intergovernmental Panel on Climate Change
LES	Large Eddy Simulation
LHV	Lower heating Value of the fuel
LPC	Low Pressure Compressor
LPT	Low Pressure Turbine
NACA	National Advisory Committee for Aeronautics
OPR	Overall Pressure Ratio
PC	Pulse Combustor
PDC	Pulse Detonation Combustion
PDE	Pulse Detonation Engine
PG	Pressure-Gain
PGC	Pressure-Gain Combustion
R&D	Research & Development
RI	Rayleigh Index
RMI	Richtmyer-Meshkov Instability
RPK	Revenue Passenger Kilometres
PSFC	Power Specific Fuel Consumption
RTI	Rayleigh-Taylor Instability
s/f	Slow-fast Shock-Flame Interaction
f/s	Fast-slow Shock-Flame Interaction
SC	Shock Compressor
SFC	Specific Fuel Consumption
SFI	Shock-Flame Interaction
TDC	Top Dead Centre
TET	Turbine Entry Temperature or Turbine Inlet Temperature
TSFC	Thrust Specific Fuel Consumption
UHC	Unburned Hydrocarbons
URANS	Unsteady Reynolds Averaged Navier-Stokes Equations
WR	Wave Rotor
ZND	Zel'dovich, von Neumann, and Döring theory

## List of Figures

Figure 1.1: Price history of crude oil and natural gas 1990 – 2010 [25], 1 Btu = 1.055 kJ .....	2
Figure 2.1: Variation of physical properties through a ZND detonation wave [90].....	7
Figure 2.2: Schematics of a stationary, one-dimensional combustion wave .....	7
Figure 2.3: Schematics of Hugoniot curve with heat release and shock Hugoniot .....	9
Figure 2.4: Temperature-entropy-diagram of idealised Brayton, Humphrey and PDE cycles	12
Figure 2.5: a) Theoretical piston and cylinder arrangement of the FJ cycle, b) Pressure-specific volume diagram of the FJ cycle [174].....	14
Figure 2.6: Temperature-entropy diagram of real Brayton, Humphrey and PGC cycles .....	15
Figure 2.7: Thermal efficiency of ideal Brayton and Humphrey cycles for various TET versus compressor pressure ratio.....	16
Figure 2.8: Thermal efficiency versus compressor pressure ratio for real Brayton, Humphrey and PGC cycles.....	18
Figure 2.9: Temperature-entropy diagram of conventional Brayton and PGC gas turbine cycles for equal turbine work output.....	19
Figure 2.10: Schematics of the Holzwarth gas turbine engine [160] .....	20
Figure 2.11: Schematics of a CCE [17] .....	21
Figure 2.12: Qualitative cycle description of a single PDE tube [177].....	23
Figure 2.13: Schematics of an aero-valved pulse combustor [126] .....	24
Figure 2.14: Diagrammatic representation of the PC configuration for use with a small gas turbine [76], [77] .....	25
Figure 2.15: Scheme of wave rotor with a) external, and b) internal combustion .....	27
Figure 2.16: Schematics of an ICWR [106] .....	27
Figure 3.1: Schematics of a planar density interface at angle $\alpha$ to the incident shock.....	33
Figure 3.2: Wave-diagrams of a) slow-fast, and b) fast-slow shock-flame refraction [132] ....	34

Figure 3.3: Evolution of RMI at a single-mode interface perturbation [26] .....	36
Figure 3.4: Expansion of a volume of combustible mixture due to combustion. Frame of reference is fixed to the flame front .....	38
Figure 3.5: Breakup regimes of water droplets [49] .....	41
Figure 3.6: Schematic diagram of the pressure profile behind a shock wave and further increase in pressure following heat addition .....	43
Figure 4.1: Total dimensions of the shock tube test facility .....	45
Figure 4.2: Schematics of the shock tube test facility and instrumentation .....	46
Figure 4.3: Detailed design of the test section .....	47
Figure 4.4: Schematics of the “unfolded” test section and positioning of measurement instrumentation .....	48
Figure 4.5: Chemiluminescence spectrum of a stoichiometric premixed CH <sub>4</sub> -air flame [92] ..	49
Figure 4.6: Raw and conditioned pressure transducer data.....	51
Figure 4.7: Full pressure record of the incident and the reflected shock waves: conf1, M <sub>i</sub> = 1.41 .....	52
Figure 4.8: Static pressure and chemiluminescence emission profiles after ignition in conf1	54
Figure 4.10: Numerical simulation of flame propagation after ignition in conf1 .....	55
Figure 4.11: Static pressure and chemiluminescence emission profiles after ignition in conf2 .....	56
Figure 4.12: Numerical simulation of flame propagation after ignition in conf2 .....	57
Figure 4.13: Pressure and chemiluminescence profiles, incident shock only, s/f, M <sub>i</sub> = 1.38 ..	60
Figure 4.14: Pressure and chemiluminescence profiles of the incident and the reflected shock waves, s/f, M <sub>i</sub> = 1.38 .....	61
Figure 4.15: Pressure and chemiluminescence profiles of the incident and the reflected shock waves, f/s, M <sub>i</sub> = 1.11 .....	63
Figure 4.16: Instantaneous Rayleigh index RI of the incident shock on the t-x plane, s/f, M <sub>i</sub> = 1.38 .....	66
Figure 4.17: Instantaneous Rayleigh index RI of the incident and the reflected shocks on the t-x plane, s/f, M <sub>i</sub> = 1.38 .....	67
Figure 4.18: Instantaneous Rayleigh index RI on the t-x plane, f/s, M <sub>i</sub> = 1.11 .....	68

## List of Figures

---

Figure 4.19: Max. chemiluminescence intensities $\Theta_{\max}$ due to incident interaction normalised by the intensity of the undisturbed flame $\Theta_0=0.065$ , for different interaction modes and $M_i$ ...	70
Figure 4.20: Maximum measured pressure values $p_{\max}$ normalised by the filling pressure $p_{\text{fill}}=2.25$ bar, for different interaction modes and $M_i$ .....	71
Figure 5.1: Structure of the analytical model .....	74
Figure 5.2: Flame geometry at the moment of interaction and corresponding two-dimensional model.....	75
Figure 5.3: Initial configuration for calculation of a) s/f-interaction, b) f/s-interaction .....	76
Figure 5.4: Critical angle $\alpha_{\text{cr}}$ as a function of $M_i$ for s/f and f/s interactions, $\rho_2/\rho_1 = 0.114$ .....	80
Figure 5.5: Areas of regular and irregular interaction for a f/s-interaction, $\rho_2/\rho_1 = 0.114$ , $\varepsilon_0 = 1$ . $48\lambda$ , $\lambda = 2D_T$ .....	81
Figure 5.6: Maximum interface growth time as a function of incident shock Mach number ...	82
Figure 5.7: Wave diagrams of shock refractions and additional, combustion induced pressure waves generated at the flame front for a) s/f and b) f/s modes of interaction .....	84
Figure 5.8: Wave diagrams of the shock-flame interaction event including experimental and analytically calculated data for the Cases 1-4 .....	86
Figure 5.9: Comparison of experimentally measured and numerically predicted pressure levels for the experimental Cases 1-4 .....	88
Figure 5.10: Total deposited circulation as a function of incident shock Mach number and initial flame geometry .....	90
Figure 5.11: Length growth rate of the two-dimensional flame front as a function of incident shock Mach number and initial flame geometry .....	91
Figure 5.12: Maximum increase in the heat release rate of the flame relative to the undisturbed flame as a function of incident shock Mach number and initial flame geometry.	92
Figure 5.13: Change in entropy relative to isobaric combustion as a function of incident shock Mach number and initial flame geometry .....	93
Figure 5.14: Change in static and total pressure relative to isobaric combustion as a function of incident shock Mach number and initial flame geometry.....	94
Figure 5.15: Change in static and total temperature relative to isobaric combustion as a function of incident shock Mach number and initial flame geometry .....	95



Figure 6.1: Configurations of the baseline engines, GT1: twin-spool industrial gas turbine, GT2: twin-spool high-bypass turbofan engine .....	98
Figure 6.2: Schematics of the shock-combustor enhanced high-pressure engine core.....	100
Figure 6.3: Performance parameters of the shock-combustor enhanced industrial gas turbine GT1.1 relative to the baseline engine GT1 for the fixed turbine inlet temperature $T_{t4}$ .....	104
Figure 6.4: Influence of a variation in $\pi_{SC}$ on the thermal efficiency of the shock-combustor enhanced industrial gas turbine .....	105
Figure 6.5: Total temperatures at the inlet and outlet of the shock compressor.....	106
Figure 6.6: Influence of a reduced polytropic turbine efficiency on the thermal efficiency of the shock-combustor enhanced industrial gas turbine .....	107
Figure 6.7: Performance parameters of the shock-combustor enhanced industrial gas turbine GT1.2 relative to the baseline engine GT1 for the fixed shaft power $P_S$ .....	108
Figure 6.8: HPT cooling air temperature normalised by the coolant temperature of the baseline engine GT1 .....	110
Figure 6.9: LPT inlet temperature for the two topping configurations GT1.1 and GT1.2 relative to the baseline engine GT1 .....	111
Figure 6.10: Performance parameters of the shock-combustor enhanced turbofan engine relative to the baseline engine GT2 for the fixed turbine inlet temperature $T_{t4}$ .....	112
Figure 6.11: Nozzle pressure ratio of the shock-combustor enhanced turbofan engine relative to the baseline engine GT2 for the fixed turbine inlet temperature $T_{t4}$ .....	114
Figure 6.12: Nozzle exit flow velocity of the shock-combustor enhanced turbofan engine relative to the baseline engine GT2 for the fixed turbine inlet temperature $T_{t4}$ .....	114
Figure 6.13: Fuel mass flow rate of the shock-combustor enhanced turbofan engine relative to the baseline engine GT2 for the fixed turbine inlet temperature $T_{t4}$ .....	115
Figure 6.14: Influence of a variation in $\pi_{SC}$ on the thermal efficiency of the shock-combustor enhanced turbofan engine.....	115
Figure 6.15: Influence of a reduced polytropic turbine efficiency on the thermal efficiency of the shock-combustor enhanced turbofan engine .....	116
Figure A.1: Pressure and chemiluminescence profiles of the incident and the reflected shock waves, s/f, $M_i = 1.26$ .....	123
Figure A.2: Pressure and chemiluminescence profiles of the incident and the reflected shock waves, s/f, $M_i = 1.55$ .....	124

## List of Figures

---

Figure A.3: Instantaneous Rayleigh index $RI$ , $s/f$ , $M_i = 1.26$ .....	125
Figure A.4: Instantaneous Rayleigh index $RI$ , $s/f$ , $M_i = 1.55$ .....	126

## List of Tables

Table 2.1: Qualitative differences between detonations and deflagrations in gases [51] .....	11
Table 4.1: Maximum intensities of RI for different interaction modes and different incident shock Mach numbers .....	69
Table 5.1: Model input parameters for the four experimental cases .....	85
Table 6.1: Design ambient conditions and performance parameters of the baseline engines	99
Table A.1: Mass fractions, molar masses, and coefficients for the unburned mixture, eq. (5.3), $300\text{ K} < T < 1000\text{ K}$ , from [100], [124] .....	122
Table A.2: Mass fractions, molar masses, and coefficients for the combustion products, eq. (5.3), $1000\text{ K} < T < 5000\text{ K}$ , from [100], [124] .....	122
Table A.3: Empirical constants for the calculation of laminar burning velocity, eq. (5.8) .....	122

## Abstract

One method to significantly improve the performance of gas turbine engines is to use the thermodynamically more efficient unsteady, pressure-rise combustion. In this work it is proposed to exploit the interaction of shock waves with a pre-mixed flame to achieve a time-averaged, combustion-induced pressure rise. The physical phenomena occurring in the course of shock-flame interaction are very complex and yet not understood in detail. In order to shed additional light onto the underlying mechanism and to gain understanding of the changes in gas state achievable due to a single interaction event, passage of shock waves through a pre-mixed flame was studied both experimentally and analytically.

Pre-mixed combustion of a nearly-stoichiometric methane-oxygen-argon mixture was used in the experiments performed on a shock tube test rig. It was shown that both the heat release rate of the flame and the pressure are temporally amplified due to passage of a shock wave through the flame. Both the increase in pressure and the heat release of the flame were demonstrated to grow parabolically with the Mach number of the incident shock. Considerably higher increases in pressure and heat release were observed when the shock approached the flame from the burned gas side (called fast-slow mode of interaction) for the same incident shock strength. Further, the existence of regions with positive coupling between unsteady pressure and heat release oscillations was demonstrated after each transition of a shock wave through the flame front.

Subsequently, an analytical quasi-one-dimensional model of the interaction between a shock wave and a sinusoidal flame was developed. Given known initial flow field and flame geometries as well as the incident shock Mach number, the model allows the calculation of a fully defined one-dimensional flow field that is formed at the end of a single shock-flame interaction event. The analytical model was successfully verified using experimental data. It was found that a single shock-flame interaction event generates a dramatic increase in pressure compared to isobaric combustion with the same unburned gas conditions. In contrast, the according increase in temperature remains at a relatively moderate level. Further, the combustion entropy is significantly reduced through a single shock-flame interaction event compared to the reference isobaric combustion process. The resulting changes in pressure, temperature and entropy rise with increasing incident shock strength and growing curvature of the flame front. They are significantly stronger in the fast-slow mode of interaction. This is a

consequence of higher rates of gas compression and flame surface growth in this interaction type.

Finally, a theoretical configuration of a shock-combustor enhanced high-pressure engine core was proposed and applied to two types of baseline engines: a twin-spool industrial gas turbine and a twin-spool high-bypass turbofan engine. The performance of the topped engines was evaluated using two variables: the combustor pressure ratio  $\Pi$  and the fraction of the core mass flow used to generate shock waves  $\xi$ . Generally, the performance of the topped engines rises for growing  $\Pi$  and deteriorates with increasing  $\xi$ . Already for relatively moderate combustor pressure ratios ( $\Pi \leq 1.4$ ) and relatively high  $\xi$  ( $\xi \leq 0.1$ ) the specific fuel consumption and the thermal efficiency of the topped engines are forecast to improve by up to 13 % and 5 percentage points compared to the baseline engines, respectively.

## Zusammenfassung

Der Einsatz instationärer Verbrennung mit Druckaufbau stellt eine Methode zur maßgeblichen Steigerung der Leistungsfähigkeit von Gasturbinen dar. In der vorliegenden Arbeit wird der Vorschlag untersucht, die Verdichtungsstoß-Flammen-Interaktion dazu zu nutzen, einen mittleren, verbrennungsinduzierten Druckanstieg zu erzeugen. Die bei der Verdichtungsstoß-Flammen-Interaktion auftretenden physikalischen Phänomene sind sehr komplex und noch nicht hinreichend genau verstanden. Um die zugrundeliegenden Mechanismen näher zu beleuchten sowie neue Erkenntnisse über die thermodynamischen Zustandsänderungen infolge eines einzelnen Interaktionsvorgangs zu erlangen, wurde der Durchgang von Verdichtungsstößen durch eine vorgemischte Flamme experimentell und analytisch untersucht.

Bei den Experimenten, die an einem Stoßrohr-Prüfstand durchgeführt wurden, wurde die vorgemischte Verbrennung einer nahezu stöchiometrischen Methan-Sauerstoff-Argon-Mischung verwendet. Es konnte gezeigt werden, dass sowohl der Druck als auch die Wärmefreisetzungsrate der Flamme infolge des Stoßdurchganges durch die Flammenfront verstärkt werden. Die Anstiege des Druckes und der Wärmefreisetzungsrate der Flamme wachen parabolisch mit der Mach-Zahl des einfallenden Verdichtungsstoßes. In den Fällen, in denen der einfallende Verdichtungsstoß von der Seite der verbrannten Gase auf die Flamme traf („schnell-langsam“-Interaktionsrichtung), wurde ein deutlich stärkerer Anstieg der Wärmefreisetzung der Flamme beobachtet. Darüber hinaus konnten Gebiete positiver Überlagerung zwischen den Druck- und Wärmefreisetzungs-schwankungen unmittelbar nach jedem Durchgang eines Verdichtungsstoßes durch eine Flamme nachgewiesen werden. In diesen Gebieten findet eine Anfachung der Druckschwankungen statt, was zu einer Verstärkung der sich fortpflanzenden Druckwellen führen kann.

Zusätzlich wurde ein quasi-eindimensionales, analytisches Berechnungsmodell der Verdichtungsstoß-Flammen-Interaktion entwickelt. Das Berechnungsmodell erlaubt die Ermittlung eines vollständig definierten, eindimensionalen Strömungsfeldes, das sich ausgehend von gegebenen Ausgangsströmungsfeld und Flammengeometrie sowie der Mach-Zahl des einfallenden Stoßes nach einem Interaktionsvorgang einstellt. Das Berechnungsmodell wurde anhand von Versuchsdaten verifiziert. Mit Hilfe der Berechnungsergebnisse konnte gezeigt werden, dass eine einzelne Verdichtungsstoß-Flammen-Interaktion im Vergleich zur isobaren Verbrennung bei gleichen Ausgangsströmungsbedingungen zu einem hohen Druckan-

stieg führt. Der Temperaturanstieg des verbrannten Gases fällt hingegen relativ moderat aus. Des Weiteren sinkt die Verbrennungsentropie infolge eines Interaktionsvorgangs im Vergleich zum isobaren Vergleichsverbrennungsprozess deutlich ab. Die resultierenden Änderungen des Druckes, der Temperatur und der Entropie steigen mit der Stärke des einfallenden Verdichtungsstoßes und der Wölbung der Flammenfront. Diese Effekte sind deutlich stärker im Fall von „schnell-langsam“-Interaktionen. Dies ist auf stärkere Kompressionseffekte sowie auf schnelleres Anwachsen der Flammenoberfläche bei dieser Interaktionsart zurück zu führen.

Anschließend wurde eine mögliche Konfiguration für einen mit einer Verdichtungsstoß-Brennkammer modifizierten Gasgenerator für Gasturbinen vorgestellt und untersucht. Der modifizierte Gasgenerator wurde in einem Leistungsrechnungsprogramm analytisch umgesetzt und in zwei Typen von Gasturbinen implementiert – eine stationäre Gasturbine und ein Zweiwellen-Zweistrom-Turboluftstrahltriebwerk. Die Leistung der beiden modifizierten Gasturbinen wurde in Abhängigkeit von zwei Variablen beurteilt – das Brennkammerdruckverhältnis  $\Pi$  und der Anteil des Kernmassenstroms, der zur Stoßerzeugung verwendet wird  $\xi$ . Die Leistungsparameter der modifizierten Gasturbinen verbesserten sich mit wachsendem  $\Pi$  und verschlechterten sich mit steigendem  $\xi$ . Es wurde ermittelt, dass bereits für relativ moderate Brennkammerdruckverhältnisse ( $\Pi \leq 1.4$ ) und relative hohe Werte von  $\xi$  ( $\xi \leq 0.1$ ) eine Verbesserung des spezifischen Brennstoffverbrauchs um bis zu 13 % und des thermischen Wirkungsgrades von bis zu 5 Prozentpunkte im Vergleich zum jeweiligen Ausgleichstriebwerk erreicht werden kann.





# 1 Introduction

## 1.1 General Introduction and Motivation

The unprecedented success story of civil aviation began with the commissioning of the De Havilland Comet, the first gas turbine powered commercial aircraft, back in 1952. Driven by the continued technological progress in airframe and particularly in gas turbine technology the air traffic, measured in revenue passenger kilometres (RPK), has been growing at a rate of around 5 % over the last 50 years [15]. Today, consistent economic growth, a more global business environment and growth in tourism contribute to maintaining this trend. According to long-term forecasts by industry leaders the expected annual average growth rate of air traffic is between 3.1 % and 5.4 %, thus resulting in more than a doubling of the worldwide air traffic and the aircraft fleet in service during the next 20 years [4], [18], [61]. Another business sector increasingly influenced by gas turbines is the electric power generation. Progressively growing world population has an ever rising hunger for energy. In 2010 the global energy consumption grew by 5.6 %, the largest rate of increase since 1973 [25]. Future projections forecast this trend to continue at a similar rate over the next 20 years [24]. Continued technological improvement and particularly the exploitation of gas turbine exhaust heat for steam turbine operation have made the combined cycle power plants with efficiencies of above 60 % increasingly attractive for energy production applications [93], [148]. Today, more than 50 % of the worldwide new power plants are gas turbine and combined cycle power facilities. This number is expected to further rise due to the need to replace out-dated facilities over the next years [144].

These numbers illustrate the demand of the market for gas turbine power in the future. However, commercial operation of gas turbines still relies heavily on the availability of low-cost hydro-carbon fuels such as kerosene and natural gas that is usually burned in industrial gas turbines. The reserves of fossil fuels have been forecast for decades but are still not confidently predictable. Under the assumption of constant consumption rate current proven reserves of oil and natural gas are estimated to last for 46 or 58 years respectively [25]. In Figure 1.1 the price history of crude oil and natural gas for the last 20 years is presented. Provided that there is a finite amount of fossil fuel in the crust of the earth, which is consumed at an increasing rate, it is obvious that the price will further rise.

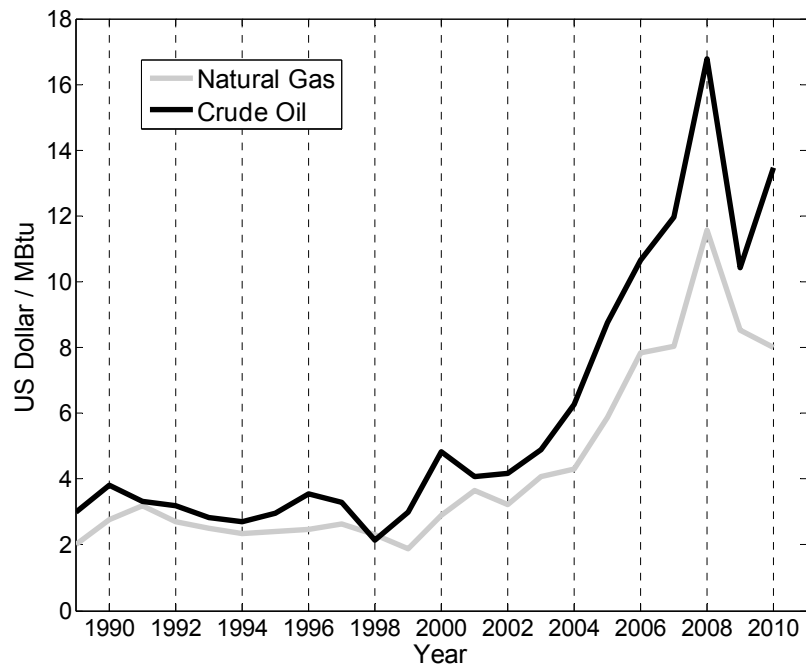


**Figure 1.1:** Price history of crude oil and natural gas 1990 – 2010 [25], 1 Btu = 1.055 kJ

Another important factor that has moved into the forefront during the last 40 years is the environmental impact of gas turbine operation. The emissions of ideal combustion of hydrocarbon fuels with air comprise water vapour ( $H_2O$ ) and carbon dioxide ( $CO_2$ ), which are the two most important contributors to the greenhouse effect [83], as well as further compounds of atmospheric air that do not participate in chemical reactions [95], [163]. In technical combustion systems the combustion process never occurs ideally. Hence, in real combustion additional pollutants are produced such as nitrogen oxides ( $NO_x$ ), highly toxic carbon monoxide (CO), and unburned hydrocarbons (UHC). Nitrogen oxides are harmful to human health in its own right, they also contribute to the formation of ozone-smog and are jointly responsible to cause acid rain in the atmosphere [95], [163], [144].

Further more, aircraft represent the only source of pollution that is emitted directly into the tropopause at 10-12 km altitude [163]. Although the overall aircraft engine emissions are currently relatively small, aviation's contribution to climate change is estimated to amount about 3.5 % of all anthropogenic sources, they will inevitably grow as air traffic increases [61]. These concerns have manifested themselves in form of international and local combustion emission regulations, which can be expected to become more stringent over the next years. So, the Strategic Research Agenda Targets of the Advisory Council for Aeronautics Research in Europe (ACARE) require an overall reduction of 50 % in the  $CO_2$  emissions per passenger kilometre and a  $NO_x$  reduction of 80 % from aviation by 2020 relative to 2000 [3]. Thus, despite an increasing market demand, the gas turbine manufacturers and operators are facing a set of socio-economic challenges in the future. Without reducing the use of gas

turbines such challenges can only be overcome by a further substantial increase in the fuel efficiency of gas turbines.

Gas turbine specific fuel consumption (SFC) is inversely proportional to the cycle thermal efficiency and, in the case of aircraft engines, additionally to the engine propulsive efficiency [149]. Following this definition there are two ways of reducing the engine SFC, first by improving the propulsive efficiency and secondly by increasing the thermal efficiency of the gas generator. An improvement in propulsive efficiency can be achieved by increasing the bypass ratio of the engine and reducing the velocity of the core exit flow [15], [102], [145]. This is presently the goal of a number of academic and industrial research and development (R&D) projects, e. g. DREAM, LeapX or the Open Rotor Concept by General Electric. The gas turbine thermal efficiency is largely determined by the overall pressure ratio (OPR), turbine entry temperature (TET) and the efficiencies of the turbo-components in the gas path (i. e. compressor and turbine) [15], [50], [59], [87]. Over the last five decades substantial effort has been spent by industry to increase gas turbine cycle efficiency by reducing the thermodynamic loss in turbo-components. This has led to compressor and turbine polytropic efficiencies in excess of 90 % giving very limited future potential for improvement of around 2 % increase in thermal efficiency over the next 10 years [15]. Continuous improvement in aerodynamics and cooling of turbo-machinery, mechanical design and materials have resulted in more than doubling of the thermal efficiency compared to the first gas turbine engines more than half a century ago [87], [102]. Today, further improvement in OPR and TET is possible, but only a modest improvement potential of 1-2 % in thermal efficiency seems to be technologically achievable [15], [50], [88], [102]. OPR is limited by compressor size and weight as well as temperature and maintenance issues. An increase in TET requires further progress in turbine materials and cooling technology, whereas an increased combustion temperature adversely affects the  $\text{NO}_x$  production during combustion [95], [163].

These arguments imply that over the next 10-15 years a reduction of SFC of merely 3-4 % relative to current gas turbine technology is attainable through improvements in thermal efficiency by conventional methods [15]. Although in aircraft engines the SFC improvement potential is augmented by the potential gains in propulsive efficiency, this number is still low and will not satisfy the demand of the market. Consequently, new and revolutionary ways to significantly increase the thermal cycle efficiency of gas turbines have to be addressed.

A look at the thermodynamic cycle used in a gas turbine reveals that it has not changed since its development by Sir Frank Whittle and Hans von Ohain in the 1930s. In all gas turbines fuel is combusted at nominally constant pressure conditions in a steady-flow combustion chamber in which burning occurs between compressor and turbine. Despite its mechanical simplicity this quasi-isobaric, steady-flow combustion has been identified to have major thermodynamic disadvantages. Françoise H. Reynst, a pioneer in the field of unsteady com-

bustion, described it as follows: "...it can be considered that combustion at constant pressure is a waste of energy, this transformation of chemical energy into heat being characterized by the greatest possible increase in entropy" [156]. Exergy<sup>1</sup> analyses of aircraft jet engines and simple cycle stationary gas turbines have revealed that the biggest share of the overall thermodynamic loss in the system, amounting up to 22-30 % respectively, is caused in the combustion chamber [58], [180]. The highly irreversible conversion of chemical energy into heat in conjunction with inevitable total pressure loss represents an obvious penalty to engine performance and limits the thermodynamic cycle efficiency of the engine. Consequently, it is the combustion chamber or rather the mechanism of combusting the fuel that offers the largest improvement potential in terms of gas turbine efficiency.

One method of improving this intrinsic drawback and achieving a step improvement in gas turbine performance is to replace the conventional isobaric combustor with a device achieving a pressure gain during the combustion process. Sir William Hawthorne, a British gas turbine combustion engineer and academic who worked on the development of the first gas turbine engines, made the following conclusion in his 1994 IGTI lecture: "...So far there has been no change in the thermodynamic cycle. The largest loss of thermodynamic availability occurs in the combustion chamber. What we need is a work producing combustion chamber." [53]. A rise in stagnation pressure across the combustion process results in a reduced combustion entropy rise and thus increased exergy of the combustor exit flow compared to conventional combustors. Consequently, increased turbine inlet availability translates into an increase in gas turbine thermal efficiency. In the last two decades, the PGC ideas have regained attention, mainly due to their theoretical high efficiency potential, and have been increasingly moving on the agenda of the engineering research community.

### 1.2 Objectives of This Work

The idea of pressure-gain combustion (PGC) is not new and can be traced back to the beginning of the last century and production of the Holzwarth engine (1906), the Marconnet engine (1908) and the Karavodine experimental gas turbine (1908) [10], [46], [165]. Both for power generation and for aerospace applications, specific hardware based on sophisticated cycles such as pulse detonation combustors (PDC), pulse combustors (PC) or wave rotors (WR) have been developed [10], [74]. Nevertheless, today there are still no viable pressure-rise combustion gas turbines. All such PGC concepts inherently contain a degree of unsteadiness resulting in a highly challenging technical realization of PGC in steady-flow ma-

---

<sup>1</sup> Exergy (also Availability) is the maximum useful work that can be extracted from a thermodynamic system on bringing it into equilibrium with its surroundings using an ideal process [11]

chines such as gas turbines [46], [54]. The main objective of this work is to investigate a new technique of achieving a combustion induced pressure rise. This concept is based on shock wave-flame interaction (SFI) – the interaction of moving shock waves with a flame front.

The passage of a shock wave through a flame zone causes a temporal increase in the heat release rate of the flame. Consequently, the rate of expansion of the burned gas is altered accordingly, thus, leading to pressure waves being emitted by the disturbed flame. Production of pressure waves and shock waves at the flame front following shock-flame interaction has been confirmed by a number of numerical and experimental studies [64], [67], [66], [82], [98], [132], [136], [140], [147], [153], [155]. The idea introduced in this work is to exploit this effect of pressure wave generation by shock-flame interaction for achieving a time-average total pressure rise across the combustion process in gas turbines

The physical phenomena occurring during shock-flame interaction are very complex and still not yet understood in detail. The primary motivation of this work is to improve understanding of the shock-flame interaction process. A series of shock-flame interaction experiments shall be conducted on a shock-tube facility. Further, an analytical, quasi-one-dimensional model of the shock-flame interaction process is to be developed comprising propagation of shock waves in gaseous media, chemical kinetics of combustion, refraction of shock waves at flame fronts, time-dependant evolution of flame surface area due to shock transition, and generation of pressure waves at the disturbed flame front. The validity of the analytical model shall be demonstrated on the basis of experimental data. This work will provide understanding of the main governing parameters of the interaction process, its behaviour with time, the achievable pressure-rise and resulting reduction in entropy generation. Such fundamental data is required for further concept development.

Other topics to be addressed in this work are the on-engine integration and the assessment of the performance improvement potential of a shock-augmented pressure-gain combustion system. This can be accomplished on the basis of a gas turbine engine performance model that is modified to account for such a pressure-gain combustor. A system for shock generation, and combustor and turbine cooling are performance relevant issues to be considered in this context. Governing input variables for performance analysis shall be identified based on these engine integration considerations. Finally, a parametric study is to be carried out in order to determine the theoretical performance improvement potential as well as the limitations of this concept.

## 2 Pressure-Gain Combustion – A Technical Review

### 2.1 Modes of Combustion

Zones of combustion are often referred to as “flame zones”, “flame fronts” or “combustion waves”. Within the flame front reactants are transformed into products through rapid chemical reactions, usually accompanied by emission of heat and light. In general, flames can be subdivided into two groups – premixed and diffusion flames [51], [90]. In premixed flames reactants and the oxidiser are gaseous and perfectly mixed before the chemical reaction occurs. Premixed flames will be the main focus of this work. Diffusion flames are controlled by mixing phenomena, where reactants diffuse into each other during the process of chemical reaction. This type of flames, which liquid fuel combustion also belongs to, will be addressed in a more detailed manner in Chapter 3.2.5.

In thermal engines three modes of combustion are usually used: constant pressure (CP), constant volume (CV) and detonative combustion. CP or isobaric combustion is widely used in gas turbines and diesel engines. CV combustion, also called isochoric, is also well known through the application in gasoline engines based on the Otto cycle. Both, the CP and CV combustion modes belong to the category of deflagrations, i.e. subsonic combustion waves sustained by chemical reactions as well as molecular and turbulent transport processes between the hot products and the fresh gas [63]. While in CP combustion the products are allowed to expand at nominally constant pressure, the products in CV combustion are spatially constrained, which leads to a pressure increase and an extremely fast heat release due to the compression [51], [90]. Contrary to deflagration, a detonation is a steady-state combustion wave propagating into combustible mixture at supersonic speed. According to the classical Zel’dovich, von Neumann, and Döring (ZND) detonation wave theory, assuming one-dimensional and steady flow, it can be described as a shock wave coupled to and sustained by a chemical reaction zone [51], [90]. The precursory shock wave sharply elevates the pressure and temperature of the fresh combustible mixture. Shock waves usually have a thickness in the order of a few mean free paths of the gas molecules (e.g. 68 nm in air at  $T = 25^{\circ}\text{C}$ ,  $p = 1 \text{ bar}$ ). After a short ignition delay time, called induction period, the fresh mixture ignites and reacts at a rate high enough for the deflagration to propagate at the velocity of the leading shock wave. The zone between the shock wave and the start of the chemical

reaction is called the induction zone. The chemical reaction is completed at the end of the reaction zone, when the thermodynamic equilibrium is reached. Gas expansion due to the energy released by the chemical reaction drives the preceding shock wave to form a self-sustained, steady detonation wave. In Figure 2.1 the variation of physical gas properties through a one-dimensional ZND detonation wave is qualitatively presented.

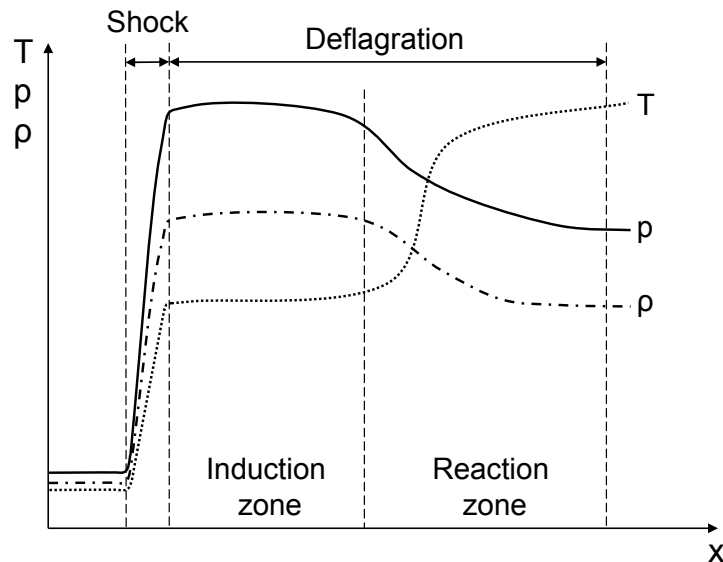


**Figure 2.1:** Variation of physical properties through a ZND detonation wave [90]

Besides the velocity of propagation there are further distinct differences between deflagrative and detonative combustion. The general characteristics of various combustion modes are best discussed using Hugoniot curve analysis. In Figure 2.2 a one-dimensional, stationary combustion wave is schematically presented in a frame of reference fixed to the wave. A transformation between the stationary and the propagating wave is achieved by means of changing the frame of reference to the absolute one. Subscripts 1 and 2 correspond to reactants upstream and products downstream of the flame front respectively. In the following analysis the combustion wave is assumed to be a planar, hydrodynamic discontinuity, with energy release occurring across it.

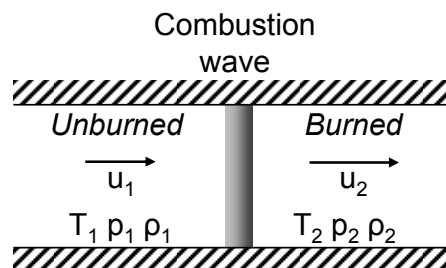


**Figure 2.2:** Schematics of a stationary, one-dimensional combustion wave

The conservation equations for steady, one-dimensional flow, with no body forces, no external heat addition or heat loss, and negligible diffusion effects applied to the combustion wave in a constant area duct as per Figure 2.2, are as follows [51]:

$$\rho_1 u_1 = \rho_2 u_2 \quad (2.1)$$

$$p_1 + \rho_1 u_1^2 = p_2 + \rho_2 u_2^2 \quad (2.2)$$

$$h_1 + \frac{1}{2} u_1^2 + q = h_2 + \frac{1}{2} u_2^2 \quad (2.3)$$

Further, perfect gas behaviour is assumed, implying that  $\kappa$ ,  $C_p$ ,  $C_v = \text{const}$ . The equation of state is then written

$$p = \rho RT . \quad (2.4)$$

From these equations, the (Rankine-)Hugoniot relation can be obtained by combining the conservation of mass (2.1) and energy (2.3) equations [90], [122], [169]

$$h_2 - h_1 = \frac{1}{2} (p_2 - p_1) \left( \frac{1}{\rho_1} - \frac{1}{\rho_2} \right) + q . \quad (2.5)$$

The Hugoniot determines all possible solutions for state 2 from a given set of properties of state 1 and a given energy release  $q$ . Typically, the Hugoniot curve is plotted on a pressure-specific volume  $p$ - $1/\rho$  diagram [35]. In Figure 2.3 a Hugoniot curve with heat release  $q$  and a shock Hugoniot (no heat release) are schematically shown. The point 1 in the diagram represents the initial state in the unburned gas. The straight lines, connecting points 1-CJ<sub>U</sub> and 1-CJ<sub>L</sub>, are called Rayleigh or Michelson lines. They are obtained by combining the equations (2.1) and (2.2) leading to the following relationship [51]

$$p_2 - p_1 = (\rho_1 u_1)^2 \left( \frac{1}{\rho_1} - \frac{1}{\rho_2} \right) \quad \text{or} \quad u_1^2 = \frac{1}{\rho_1} \left( \frac{p_2 - p_1}{\frac{1}{\rho_1} - \frac{1}{\rho_2}} \right) . \quad (2.6)$$

The slope of the Rayleigh line is proportional to the square of the magnitude of the flow velocity in the unburned gas, or alternatively, in case of a wave propagating into stagnant gas, to the combustion front propagation velocity. From imaginary values of  $u_1$  in eq. (2.6) it can be followed that solutions in the region between points CV and CP are physically impossible and can be omitted from further consideration. This region divides the Hugoniot curve into two regions. The region above point CV represents supersonic wave solutions and is called the detonation branch. The region below the CP point corresponds to subsonic waves and is referred to as the deflagration branch. Point CV denotes the final state for an adiabatic constant volume process. The Rayleigh line that connects the points 1 and CV has an infinite slope. This represents a limit of a combustion wave process with the wave speed approach-



ing infinity. In other words, an ideal CV combustion process is an instantaneous, explosive transformation of reactants into products. The point CP represents the final state for a constant pressure combustion process. This point does not represent a physically possible process either, because of the zero slope of the corresponding Rayleigh line. Hence it is a limiting case of an infinitely slow combustion wave.

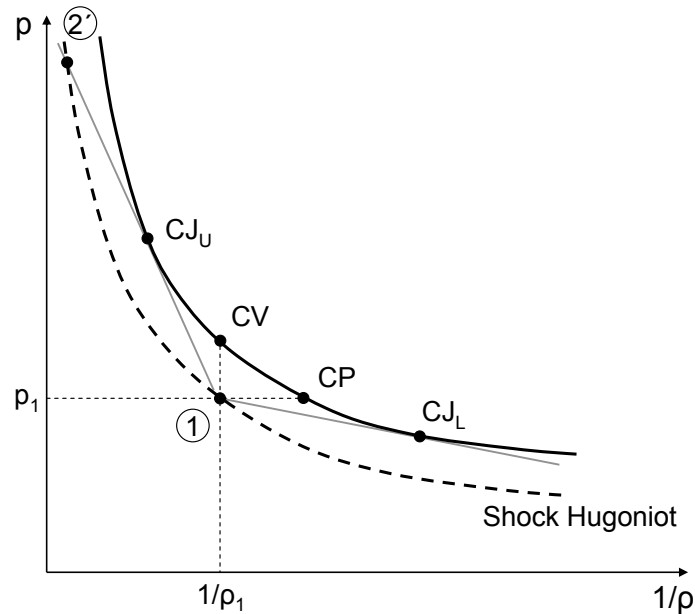


**Figure 2.3:** Schematics of Hugoniot curve with heat release and shock Hugoniot

The point where the Rayleigh line is tangent to the Hugoniot curve is called the Chapman-Jouguet (CJ) point in recognition of the fundamental work of Chapman (1905) and Jouguet (1899) in the field of detonation waves. The upper  $CJ_U$  point is located on the detonation branch of the Hugoniot and corresponds to the state of minimum possible detonation velocity and minimum entropy increase across a combustion wave [90], [174]. Further, at this point, the flow velocity at the end of the reaction zone equals the local speed of sound of the combustion products. The region of the Hugoniot curve between  $CJ_U$ - $CV$  corresponds to weak or under-driven detonations (supersonic flow to supersonic). In general, weak detonations can be ruled out due to the requirement of special gas mixtures with extremely high reaction rates [90]. Points above the  $CJ_U$  represent the strong or over-driven detonation solutions (supersonic flow to subsonic). Strong detonations are observed only under special experimental conditions, e.g. if there is some type of piston moving behind the detonation wave [35], [90], [174]. The lower  $CJ_L$  point, which lies on the Hugoniot deflagration branch, denotes the state of the fully developed deflagration with choked flow at the end of the reaction zone. This point corresponds to the maximum possible deflagration wave velocity and, contrary to the  $CJ_U$  point, to the maximum possible entropy increase across a combustion wave. Hugoniot region below point  $CJ_L$  represents strong deflagration solutions (subsonic flow to supersonic).

In constant area ducts it is, however, not possible to accelerate a subsonic flow beyond the sonic condition by heat addition [63], [146]. Therefore, this region can be considered as not physically attainable. The solutions between points CP-CJ<sub>L</sub> establish the region of weak deflagrations (subsonic flow to subsonic), which encompasses very slow laminar and faster moving turbulent flame fronts [35], [90], [174].

There exist two detonation initiation modes [51]. The fast mode initiation is brought about by an ignition blast or a strong shock wave and requires very high ignition energies for most fuels. The second, commonly used mode is based on deflagration to detonation transition (DDT). DDT involves flame acceleration to generate upstream conditions pertinent to the onset of detonation. An ignition in a combustible mixture at the closed end of a smooth tube usually generates a deflagration front, which propagates at subsonic speed into the fresh gas. Expanding combustion products generate pressure waves that propagate in the direction of flame movement, thus compressing and accelerating the fresh gas ahead of the flame. Increased pressure and temperature as well as (turbulent) movement of the unburned mixture increase the reaction rate of the flame. This leads to an enhanced expansion rate of the products. Hence, a feedback loop responsible for flame acceleration is established. For an accelerating flame, the preceding pressure waves finally coalesce to form a shock wave that propagates at a velocity higher than the velocity of the flame. This setup represents an unsteady double-discontinuity that cannot be treated by using the standard Hugoniot analysis [2], [116]. Further acceleration of the flame to catch up with the leading shock was described by Troshin [159] on the basis of the “generalized” Hugoniot curve. This curve represents the locus of flame speeds increasing from subsonic to the detonation velocity, and is discussed in detail in [35] and [159]. Such high burning velocities are possible due to the increase in flame surface area. The mechanisms responsible for the increase in flame surface area are turbulence, shock-flame interaction or intrinsic laminar flame instabilities [35]. When leading shock wave propagation velocity approaches the detonation velocity, a localised “explosion in explosion” [116] occurs between the shock and the following flame front to form a steady-state detonation wave [35].

Based on the considerations above, the only physically acceptable steady combustion waves are weak deflagrations and strong detonations including the CJ<sub>U</sub> point. However, from the practical point of view, there is only one solution for supersonic combustion waves, the CJ<sub>U</sub>, that turns out to be suitable for technical applications. In Table 2.1 typical values of thermodynamic property changes across deflagrations and detonations are presented in order to point out the qualitative differences between the two types of combustion waves. From the values in Table 2.1 and the discussion above, it can be concluded that weak deflagrations, commonly referred to as CP combustion, are always associated with a slight loss in pressure. On the contrary, during CV and detonative combustion there is always a significant

pressure rise. Therefore, only the CJ-detonation and the CV combustion modes can be considered expedient for PGC applications.

	Detonation	Deflagration
$u_1/a_1 = M_1$	5-10	0.0001-0.03
$u_1/u_2$	0.4-0.7	4-6
$p_1/p_2$	13-55	0.98-0.976
$T_1/T_2$	8-21	4-16
$\rho_1/\rho_2$	1.7-2.6	0.06-0.25

**Table 2.1:** Qualitative differences between detonations and deflagrations in gases [51]

## 2.2 Entropy Rise and Thermal Cycle Efficiency

In order to analyse the performance of steady-flow systems such as gas turbines, it is instructive to draw the various processes occurring inside the engine on a thermodynamic state diagram, e.g. T-s-diagram. The common sequence of processes encountered in air-breathing engines is compression, combustion, and expansion followed by a constant-pressure process to close the cycle. During the last process the exhaust gas is converted into inlet fluid by heat exchange with surroundings. In Figure 2.4 idealised Brayton (2-3-4-5-2), Humphrey (2-3-4'-5'-2) and Pulse Detonation Engine (PDE) (2-3-3a-4''-5''-2) cycles are qualitatively compared. For all cycles the inlet gas is compressed in an idealised, isentropic process from the compressor inlet temperature (state 2) to the combustor inlet temperature (state 3). In the Brayton cycle combustion occurs in a CP process 3-4, and in the Humphrey cycle heat is added in a CV process 3-4'. In the PDE cycle the process 3-4'' corresponds to the widely accepted model of a normal detonation (ZND) wave [41], [55], [79], [178]. Therein, the process 3-3a represents the thermodynamic change of state due to the leading shock wave, followed by a heat addition process in a constant area duct 3a-4''. Thermodynamic state at point 4'' corresponds to the conditions at  $CJ_U$  (see Figure 2.3), i. e. choked flow. The heat addition process is followed by a complex region of unsteady rarefaction waves, which isentropically expand the detonation products to a state between 4''-5''. Finally, the combustion products in all cycles are assumed to expand in an idealised, isentropic process to the initial pressure level.

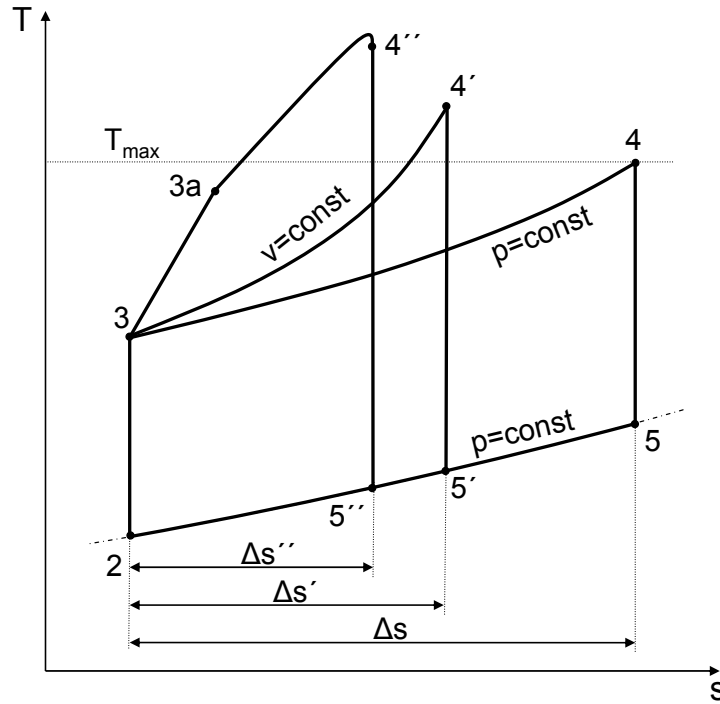


**Figure 2.4:** Temperature-entropy-diagram of idealised Brayton, Humphrey and PDE cycles

The thermal efficiency of any thermodynamic cycle can be defined as the ratio of the useful work of the cycle and the heat of combustion added to the cycle [47]

$$\eta_{th} = \frac{w}{q_C} \quad (2.7)$$

The useful work done by the cycle can be obtained as the difference between heat added and heat rejected during the isobaric process 5-2 [47], with  $q_C = FAR \cdot q_f / (1 + FAR)$ ,

$$w = q_{in} - q_{out} = q_C - q_{out} = q_{34} - q_{52} \quad (2.8)$$

Assuming the process 5-2 to be ideal, i.e. reversible, the heat removed can be expressed as

$$q_{out} = \int_2^5 T ds \quad (2.9)$$

Combining equations (2.7), (2.8), (2.9) and assuming perfect gas behaviour, the thermal cycle efficiency is written as [47], [174]

$$\eta_{th} = 1 - \frac{q_{out}}{q_C} = 1 - \frac{C_P(T_5 - T_2)}{q_C} = 1 - \frac{C_P T_2}{q_C} \left( \exp\left(\frac{s_5 - s_2}{C_P}\right) - 1 \right) \quad (2.10)$$

According to eq. (2.10), thermal efficiency decreases with increasing  $q_{out}$ , or in other words, it is maximised when the overall cycle entropy rise (between points 2-5 in Figure 2.5) is minimised. The overall entropy rise is a sum of entropy increments associated with every process the flow is subject to through the cycle. Neglecting the entropy generation due to thermal losses of the exhaust gas, the entropy rise associated with combustion is the dominant

source of thermodynamic loss in gas turbine systems [58], [174], [181]. Thus, the dependence of the thermal efficiency on the cycle total entropy rise renders the selection of the combustion mode a critical task with regard to engine performance.

The fact that detonation is associated with a minimum total entropy rise across a combustion wave has motivated a series of investigations into the application of detonation for steady-flow propulsion [39], [173], [174], [179]. In order to achieve a stationary detonation wave inside the combustor of such engines, the flow has to be accelerated to the supersonic CJ-detonation velocity at the entry to the combustion chamber. However, these studies demonstrated the performance of steady-detonation based engines to be substantially lower than those based on deflagrative combustion (turbojet and ramjet engines). The reason for such behaviour lies in the irreversible share of entropy generation in the combustor [174], [175]. The entropy rise of premixed combustion in a flowing gas can be subdivided in a minimum component  $\Delta s_{min}$  due to reversible addition of heat and an irreversible component  $\Delta s_{irr}$ , which is due to shock waves, friction, heat transfer, mixing processes, or heat addition at subsonic velocities (Rayleigh flow) [46]. It is written as

$$s_2 - s_1 = \Delta s_{min} - \Delta s_{irr} = C_P \ln \left( \frac{T_{t2}}{T_{t1}} \right) - R \ln \left( \frac{p_{t2}}{p_{t1}} \right) = C_P \ln \left( 1 + \frac{q_C}{C_P T_{t1}} \right) - R \left( \frac{p_{t2}}{p_{t1}} \right). \quad (2.11)$$

Equation (2.11) is given for an ideal stagnation or total state [174], the subscripts refer to those given in Figure 2.2. From eq. (2.11) it follows that a loss in stagnation pressure across a combustion wave directly refers to the irreversible entropy rise. Due to the leading shock wave of a detonation wave, the total pressure loss across a detonation is orders of magnitude larger than that across a deflagration. This directly translates into a much higher portion of irreversible entropy rise in detonations (more than 50 %) than in deflagrations (less than 5 %) [174]. Substituting eq. (2.11) into eq. (2.10), and using the notation of Figure 2.4, the thermal efficiency can be shown to be a function of the irreversible entropy rise.

$$\eta_{th} = 1 - \frac{C_P T_2}{q_C} \left( \left( 1 + \frac{q_C}{C_P T_{t3}} \right) \exp \left( \frac{\Delta s_{irr}}{C_P} \right) - 1 \right) \quad (2.12)$$

Equation (2.12) explains the poorer performance of steady-detonation compared to steady-deflagration engines. Zeldovich [179] and Wintenberger [174] conclude that the systematically lower performance in conjunction with practical problems such as stabilization of detonation, risk of pre-ignition and excessive temperatures, make detonation not practical for steady-flow combustion applications. Finally, Wintenberger suggests that unsteady detonation waves remain the only useful way of detonation application to propulsion (e.g. PDE). This findings agree well with the conclusions of Foa, who states that CP combustion always represents the optimum solution for steady-flow systems [45], and that the most efficient gas

turbine engine is characterised by a steady inflow, an unsteady combustion mode, and a steady or square wave type exhaust flow [46].

A framework for analysing unsteady detonations in a purely thermodynamic manner is provided by the Fickett-Jacobs (FJ) cycle [43]. The FJ cycle is a notional cycle that enables the treatment of unsteady detonations in a closed system avoiding the complexity of realistic unsteady gas dynamics (e.g. PDE). It is based on an idealised piston and cylinder arrangement, such as shown in Figure 2.5a. In Figure 2.5b the FJ cycle is qualitatively presented on the pressure-specific volume plane. The sequence of the cycle involves instantaneous initiation of detonation and acceleration of the pistons to the detonation wave velocity (see Figure 2.5b, path 1-2), extraction of mechanical work by bringing the detonation products to rest (2-3), adiabatic expansion (3-4) and isobaric cooling of the products (4-5), and, finally, conversion of products into reactants at constant pressure and temperature (5-6). A detailed description and analysis of the FJ cycle is provided by [174], [175] and [176].

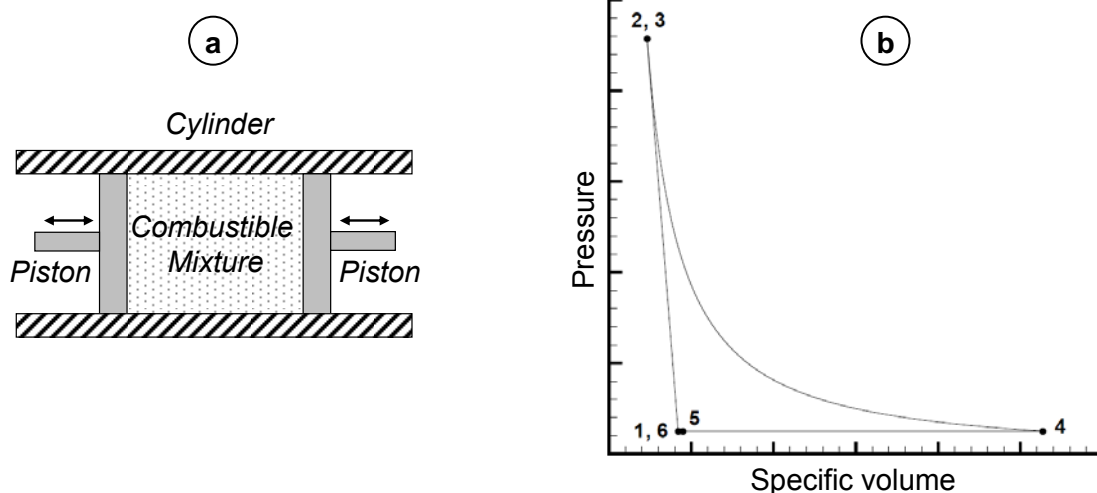


**Figure 2.5:** a) Theoretical piston and cylinder arrangement of the FJ cycle, b) Pressure-specific volume diagram of the FJ cycle [174]

Using the FJ cycle the upper limit of mechanical work extractable from detonating a given portion of a fuel can be determined. Calculations of Wintenberger [174] and Reynolds [130] for various fuels have shown that entropy rise of unsteady detonative combustion is by 14-24 % lower than that of CP combustion, but only 2-3 % below that generated by CV combustion. These results are reflected analogously in the results of thermal efficiencies of the respective thermodynamic cycles. Thus, for a given compression ratio, the FJ cycle has the highest thermal efficiency, followed by Humphrey cycle slightly below, and Brayton cycle with a considerably lower thermal efficiency [175], [178]. Similar values of entropy rise and thermal efficiency exhibited by the FJ and Humphrey cycles have motivated various researchers to use CV combustion as an alternative model to the CJ-theory in dealing with unsteady

detonation waves [42], [60], [79], [80]. The similarity between detonation and CV combustion was confirmed by Wintenberger [174] by considering the kinetic energy in a propagating detonation in contrast to CV combustion with no fluid motion. He demonstrated that the kinetic energy content of a propagating detonation wave constitutes less than 10 % of the chemical energy release of the fuel. This results in the two combustion processes under consideration to have essentially the same specific impulse if compared on the basis of a tube blow down model.

Based on the arguments presented above, in conjunction with technological difficulties associated with detonation wave combustion [179], it appears that detonative combustion is less attractive for PGC applications than CV combustion. Consequently, the main objective of pressure-gain combustion work is, to modify the CP mode of combustion in gas turbines so, that its performance moves closer to that of CV combustion [58]. It is also obvious that such a combustion mode will inevitably contain a degree of unsteadiness.

### 2.3 Thermodynamic Benefit of Pressure-Gain Combustion in Gas Turbines

In Figure 2.6 the real Brayton and Humphrey cycles, i.e. with lossy compression (2-3) and expansion (4-5) processes, are qualitatively presented in a T-s diagram. The third cycle schematically shown in the diagram, called the PGC cycle, is a real gas turbine cycle fitted with a pressure-gain combustion process.

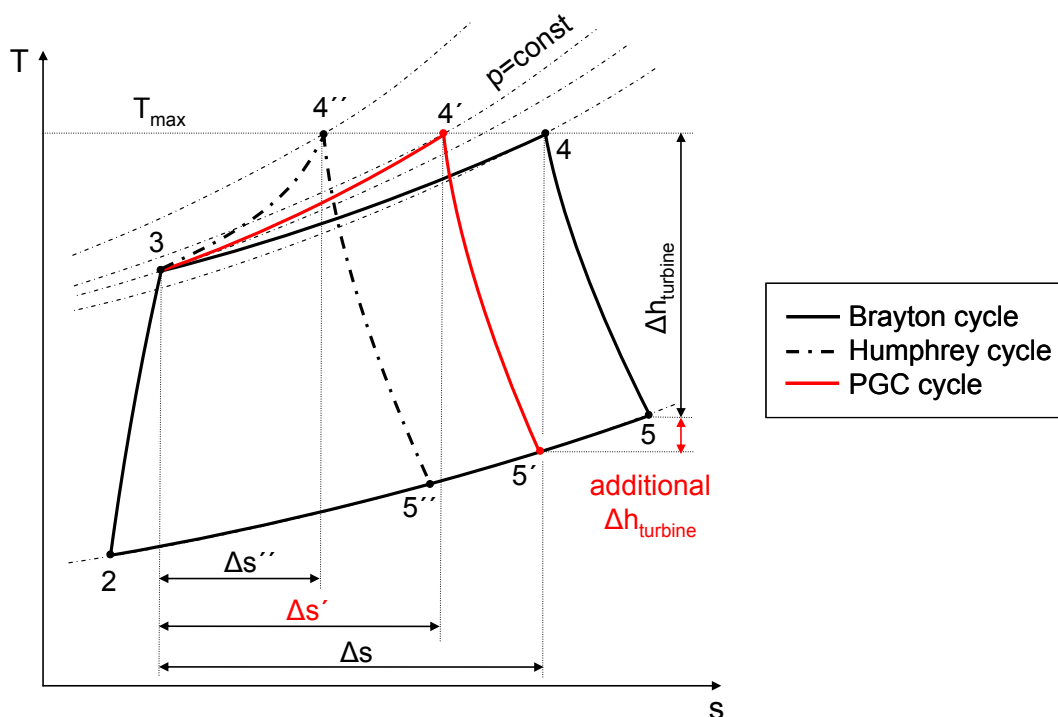


**Figure 2.6:** Temperature-entropy diagram of real Brayton, Humphrey and PGC cycles

The maximum cycle temperature  $T_{max}$ , which is consistent with TET, is assumed to be equivalent for the three cycles. TET and pressure at the end of the combustion process (states 4' and 4'') are assumed to be quasi-steady, time-averaged values when unsteady CV and PG combustion processes are considered.

Firstly, corresponding idealised, loss-free Brayton and Humphrey cycles are considered. Their thermal efficiencies are given by equations (2.13) and (2.14) respectively [89].

$$\eta_{th} = 1 - \frac{T_2}{T_1} = 1 - \frac{1}{\pi_C^{(\kappa-1/\kappa)}} \quad (2.13)$$

$$\eta_{th} = 1 - \kappa \frac{\left( (T_4/T_2)^{(1/\kappa)} \pi_C^{(1-\kappa/\kappa^2)} - 1 \right)}{\left( T_4/T_2 - \pi_C^{(\kappa-1/\kappa)} \right)} \quad (2.14)$$

The ideal Brayton cycle thermal efficiency depends only on the compressor pressure ratio. For the ideal Humphrey cycle, there is an additional dependence on the maximum cycle temperature  $T_4$  or TET. A plot of the thermal efficiency of ideal Brayton and Humphrey cycles as a function of compressor pressure ratio is presented in Figure 2.7. The initial cycle temperature used in the calculations was  $T_2 = 300$  K.

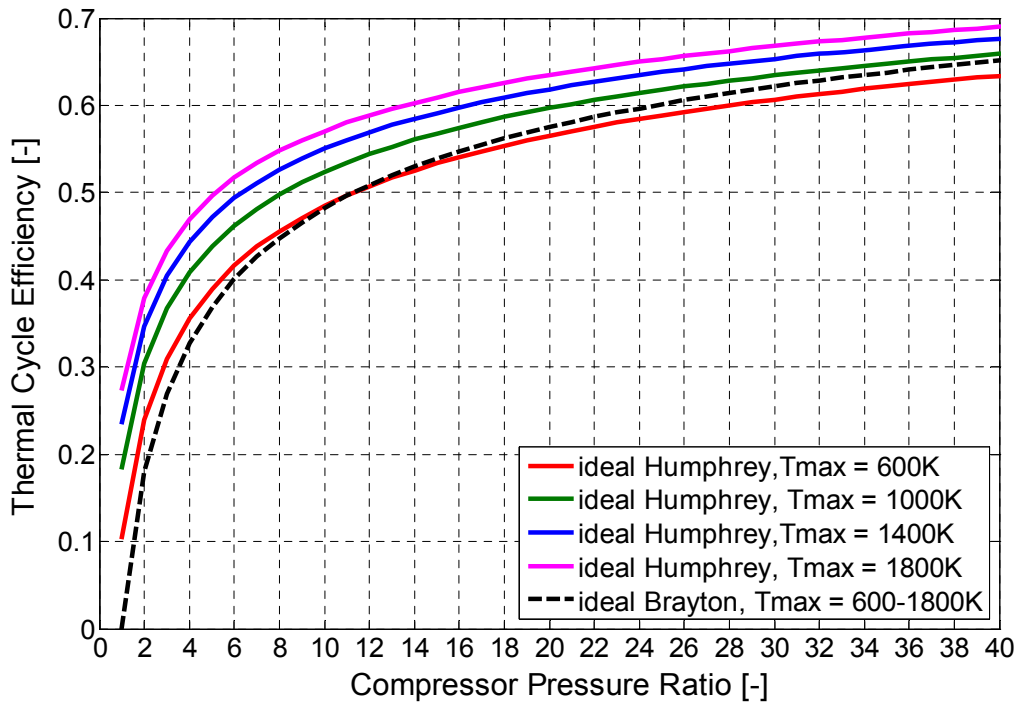


**Figure 2.7:** Thermal efficiency of ideal Brayton and Humphrey cycles for various TET versus compressor pressure ratio

The ideal Humphrey cycle is superior to the ideal Brayton cycle in terms of thermal efficiency due to a lower entropy rise during CV combustion. This is particularly true at low compres-



sion ratios and for high turbine entry temperatures [55], [89], [175], [178]. With increasing compressor pressure ratios the thermal efficiency of the Humphrey cycle approaches that of the Brayton cycle. The two values are equal at the point where the temperature  $T_3$  at the end of the compression process reaches the value of the fixed TET, rendering any further heat addition in the combustor impossible.

Now, thermal efficiency of real cycles is compared. The time-averaged pressure rise of the unsteady PGC process (3-4' in Figure 2.6) is assumed to be somewhere between those of CP and CV combustion. Under such arrangement, less entropy is generated during the PGC process than during CP combustion of the Brayton cycle, resulting in a higher possible temperature drop across the expansion process. If the compressor power demand is assumed to remain unchanged, this leads to an additional work output ( $\Delta h$ ) in the turbine. Further, due to compression during the combustion process, less fuel is required to heat the fluid from a fixed temperature  $T_3$  to  $T_{\max}$ . Thus, the thermal efficiency of the real PGC cycle can be given as a function of the averaged pressure rise in the combustor  $\Pi = p_4/p_3$  as follows [89], [126]

$$\eta_{th} = 1 - \frac{T_4/T_2 \left( 1 - \left( 1 - (1/\pi_C \Pi)^{(\kappa-1/\kappa)} \right) \eta_T \right) - 1}{\left( T_4/T_2 - \left( 1 + (\pi_C^{(\kappa-1/\kappa)} - 1)/\eta_C \right) \right)} \quad (2.15)$$

The equation for the thermal efficiency of the real Humphrey cycle is [89]

$$\eta_{th} = 1 - \kappa \frac{T_4/T_2 \left( 1 - \left( 1 - \left( T_2/T_4 \pi_C \left( 1 + (\pi_C^{(\kappa-1/\kappa)} - 1)/\eta_C \right) \right)^{(\kappa-1/\kappa)} \right) \eta_T \right) - 1}{\left( T_4/T_2 - \left( 1 + (\pi_C^{(\kappa-1/\kappa)} - 1)/\eta_C \right) \right)} \quad (2.16)$$

In eq. (2.15) and (2.16), the inefficiencies of the compression and expansion processes are reflected by introducing the compressor  $\eta_C$  and turbine  $\eta_T$  isentropic efficiencies. For  $\Pi = 0.97$  eq. (2.16) represents thermal efficiency of a conventional Brayton cycle.

In Figure 2.8 the thermal efficiencies of the real Brayton and the PGC cycle for various values of  $\Pi$  are plotted versus compressor pressure ratio. The thermal efficiency of the real Humphrey cycle is also shown for comparison. Following assumptions were used in this calculation  $T_2 = 300$  K,  $T_4 = 1700$  K,  $\kappa = 1.4$ ,  $\eta_C = 0.86$ ,  $\eta_T = 0.9$ . The PGC cycles show a better efficiency than the Brayton cycle for the whole range of pressure ratios studied. The benefit is the highest for small engines with a low compressor pressure ratio, and decreases for increasing compression and cycle temperature ratios. These findings agree well with other studies [5], [74], [91], [96], [166]. The real Humphrey cycle exhibits better performance than the PGC cycle at very low compressor pressure ratios ( $\pi$  less than 6) only. Its thermal efficiency quickly deteriorates with growing  $\pi$  and falls below that of the Brayton cycle at  $\pi = 14$ .

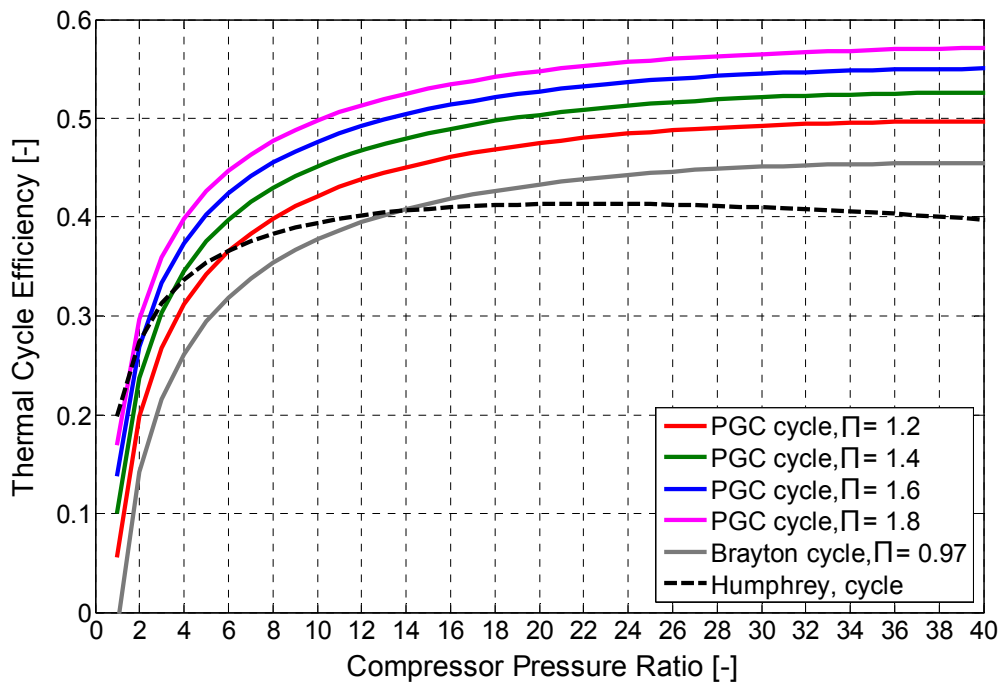


**Figure 2.8:** Thermal efficiency versus compressor pressure ratio for real Brayton, Humphrey and PGC cycles

In order to point out the theoretical potential of PGC, the effect of a 20 % combustor pressure-gain ( $\Pi = 1.2$ ) is evaluated for three representative types of engines. Thus, for a micro-jet engine operating at a compressor pressure ratio of 4 and TET of 1000 K, the expected theoretical rise in cycle efficiency is 30 %. A turboshaft-type engine with  $\pi_c = 20$  and TET = 1500 K is expected to achieve 11.4 % increase in cycle efficiency. And a turbojet with  $\pi_c$  of 38 and TET of 1800 K exhibits an improvement potential of 8.4 %. A resulting increase in specific power and specific fuel consumption is expected to be in the same order of magnitude [5], [77], [73]. The calculations shown above are performed irrespective of the detail how PGC is achieved. Hence, the results represent the upper bound of possible improvements.

An alternative implementation of PGC to a gas turbine cycle is schematically shown in Figure 2.9, where the turbine work output is the same as in the reference Brayton cycle. Besides the improvements in thermal efficiency and SFC described above, this cycle offers the advantage of a reduced TET. The pressure rise in the combustor can also be exploited by lowering the cycle pre-compression, i.e. reducing the number of compressor stages. Both modifications lead to a lighter, more reliable, more efficient and cheaper engine.

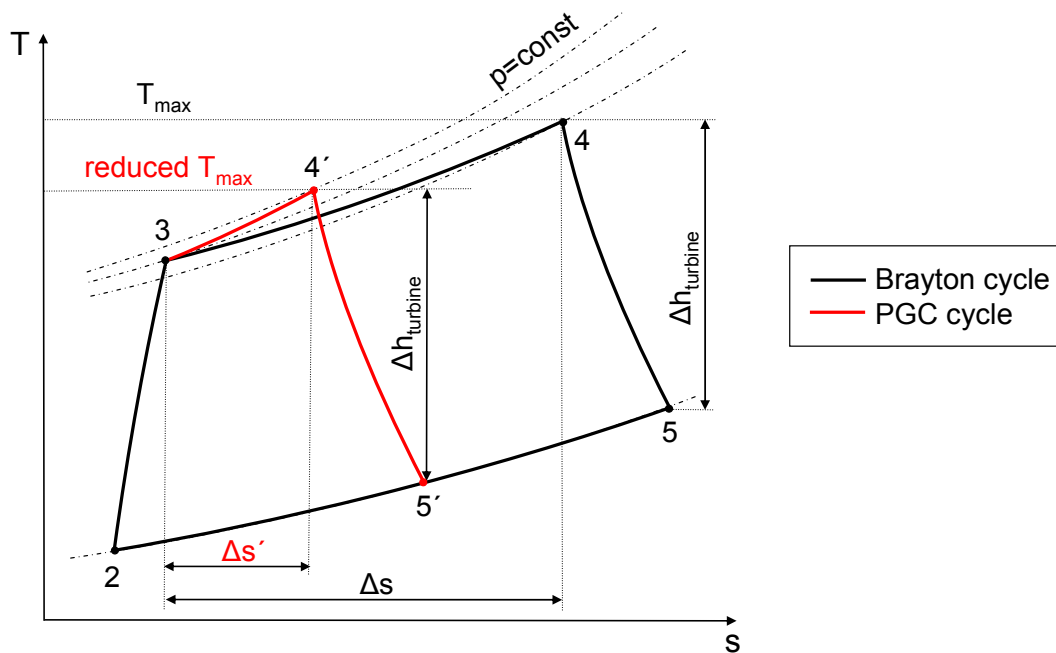


**Figure 2.9:** Temperature-entropy diagram of conventional Brayton and PGC gas turbine cycles for equal turbine work output

Despite the yet unsolved problems that would arise with the introduction of PGC, such as stability and dynamics of the unsteady combustion mode, combustor and turbine cooling, compressor and turbine interaction with unsteady combustor flow, mechanical and thermal stresses, this concept offers an immense, thermodynamically proven improvement potential for gas turbine efficiency.

The increased interest in PGC technology as well as its significance is best exemplified by the Vulcan project of the US government's Defense Advanced Research Projects Agency (DARPA). Vulcan is a multi-phase technology development programme to design, build and demonstrate a full-scale PGC turbine engine by the year 2014. Currently, Vulcan phase II with a total budget of \$62 million is underway, aiming at successful demonstration of a PGC gas turbine combustor [37].

## 2.4 Review of the Existing PGC Concepts for Gas Turbine Applications

Over the last century a plethora of various PGC concepts for application in gas turbines has been proposed, e.g. [12], [74], [105], [113], [134], [137], [167]. All of these concepts involve unsteady processes during combustion in order to generate a total pressure gain from inlet to outlet. Among all, detonation wave combustors, wave rotors, and valveless pulse combustors have been identified to be most promising and viable PGC concepts [74], [120]. They are

currently the subject of various industrial and academic research efforts; see [6], [54], [115], [131].

In this chapter, the proposed ideas are classified into five main categories depending on the mechanism how combustion pressure-gain is achieved, and a brief review of each is presented.

### 2.4.1 Elementary Constant Volume Combustors

The most famous example of idealised CV combustion application is the internal combustion engine operating on the Otto thermodynamic cycle. The first gas turbine engine utilising the explosive CV combustion was developed by the German engineer H. Holzwarth (1905) [10]. Its thermodynamic cycle was mainly derived from the Otto cycle, with the work being extracted by means of a rotating turbine instead of a piston. The operation of the engine is described by the Humphrey cycle (with or without pre-compression); see Figure 2.6. The separate cycle steps are – intake of air and fuel, (pre-compression), CV combustion of the charge accompanied by an increase in pressure, and exhaust of the combustion gases through nozzles directed against turbine blades. The first experimental version of the Holzwarth engine operated without pre-compression and raised the pressure during combustion by a factor of 4-5 above the ambient. The schematics of this engine are presented in Figure 2.10, including spring loaded inlet and outlet valves, ten CV combustors arranged in a circle around the turbine shaft, and water cooled combustor casing.

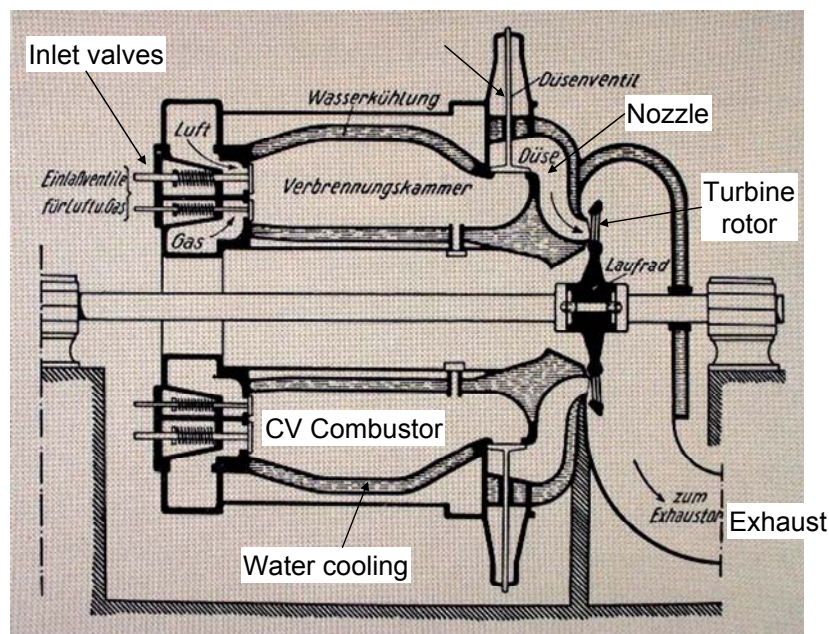


**Figure 2.10:** Schematics of the Holzwarth gas turbine engine [160]

This engine employed a scavenger fan to ensure subsequent induction of the fresh charge of air and exhibited a very low thermal efficiency (not further specified) [10], [8], [9]. Later models of the Holzwarth gas turbine, developed and built by the Swiss company Brown, Boveri & Cie. (BBC), incorporated a compressor for charge pre-compression with  $\pi_c = 3-4$ , and delivered a power of 5000 kW [8]. The development work on the Holzwarth gas turbine continued until around 1930. The Holzwarth type engines increasingly suffered from problems associated with high combustion gas temperatures of about 1950 K and mechanical valves control issues [9]. Finally, it became uncompetitive with the CP combustion based gas turbines with their relative mechanical simplicity and unprecedented power density. The improvements in the turbo-compressor technology contributed to this trend.

#### 2.4.2 Combustors Based on Reciprocating Internal Combustion Engines

Internal combustion engines achieve higher thermal efficiency than turbine engines, whereas the gas turbines are lighter and smaller than the IC engines for a given power output [167]. The compound cycle engines (CCE) represent a mechanism that combines the thermal efficiency of a rotary IC engine with the compact size and light weight of a gas turbine. In this concept a conventional gas turbine combustor is replaced by a highly supercharged, high-speed, two-stroke, direct-injected diesel engine [17], [28], [74], [170]. In Figure 2.11 schematics of a CCE are shown.

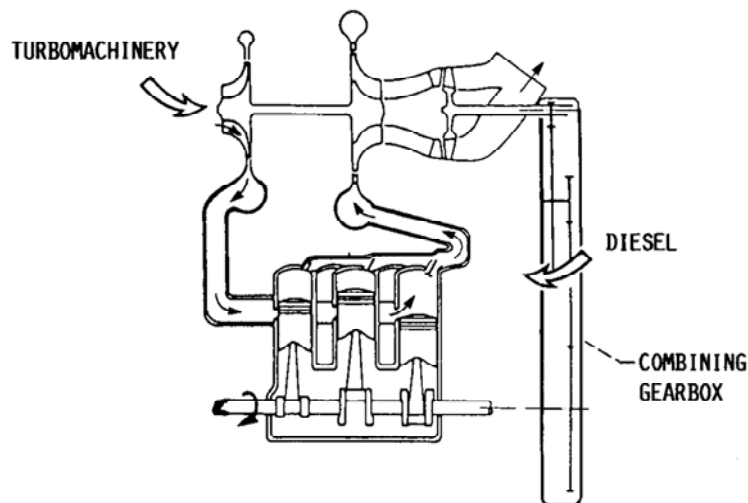


**Figure 2.11:** Schematics of a CCE [17]

The rotary compressor delivers highly pressurized air to the Diesel cylinders. Within the cylinders, the air is further compressed, mixed with fuel and combusted at high temperatures and pressures. Power is extracted from the combustion products during the expansion stroke

and the exhaust gases are directed to the rotary turbine module, where further work extraction takes place. The coupling between the IC engine and the turbo-machinery necessitates the use of a gear box. An alternative set up is presented in [167], where the conventional combustor is replaced by a series of rotary Wankel type IC engines.

During the 1940's and early 1950's, increased interest in compound cycle engines led to the development of the Nomad Napier engine by the Napier & Son Ltd in the UK. The engine was a turboprop topped with a turbocharged turbo-compound, two-stroke, twelve piston Diesel [53]. It demonstrated a SFC of less than 210 g/kWh and has since remained the most fuel efficient IC engine ever flown [17]. In the 1980's NASA conducted CCE research for military helicopter and turbofan engines [170]. For military helicopter engines a theoretical reduction in fuel consumption of 30-40 % was envisaged [17]. However, despite their high efficiency potential the CCE engines have always played a secondary role in aerospace propulsion. They are heavier and more complex than simple turbojet engines of the same power class due to mechanical interconnection of the IC engine with the turbo-machinery [17], [167]. Despite major advances achieved in diesel engine technology, the CCE engines remain inferior to gas turbines due to mechanical integration constraints, lower power density and reliability concerns. Today, the concept of turbo-charged IC engines is widely used in the automotive industry.

### 2.4.3 Detonation Wave Combustors

The details of detonation wave combustion have been discussed previously in Chapters 2.1 and 2.2. A combustor based on unsteady detonation waves can have two potential applications – as a pulse detonation engine (PDE) that uses detonation waves for thrust generation [99], or as a pulse detonation combustor (PDC) that is to replace a conventional combustion system in gas turbines [121], [161]. Both systems are very similar, they typically consist of an inlet with one or several inlet valves, a fuel injection system, one or multiple detonation tubes, and an exit nozzle [131], [174]. The cycle of a single PDE/PDC tube is graphically described in Figure 2.12. The air-fuel mixture is ignited and detonation is initiated at the closed end of the tube a). The propagating detonation b) reaches the open end and diffracts as a decaying shock, which generates an expansion wave propagating towards the closed end c). At the end of the exhaust process the tube contains quiescent combustion products d). The purging and filling process starts by opening the valve. The purging air, followed by the reactants, flows in and pushes the reactants out of the tube e)-g). Thereby, the purging air is used for controlling the mean exhaust temperature and avoiding pre-ignition of the fresh mixture. When the tube is entirely filled with reactants, the valve closes and the cycle is restarted h).

Multi-cycle experimental studies on a single detonation tube have been performed at frequencies between 5 Hz and 100 Hz [178]. The operational frequency of the PDE has a direct impact on the amount of time-averaged thrust that can be produced. Previous studies [141] have shown that there is a linear increase in thrust as the frequency of the PDE is enhanced. PDE/PDC work is motivated by the potential benefits in thermodynamic cycle efficiency through the use of detonation wave combustion, which represents a close approximation of the CV combustion process. Further advantages are relative simplicity and reliability of the hardware [74], [178]. The operating frequency of a PDE/PDC does not depend on the acoustics of the system because of supersonic wave propagation velocities. Therefore, it can be directly controlled by changing the detonation cycle [174]. This fact makes the system scalable and improves its adaptability to various types of application.

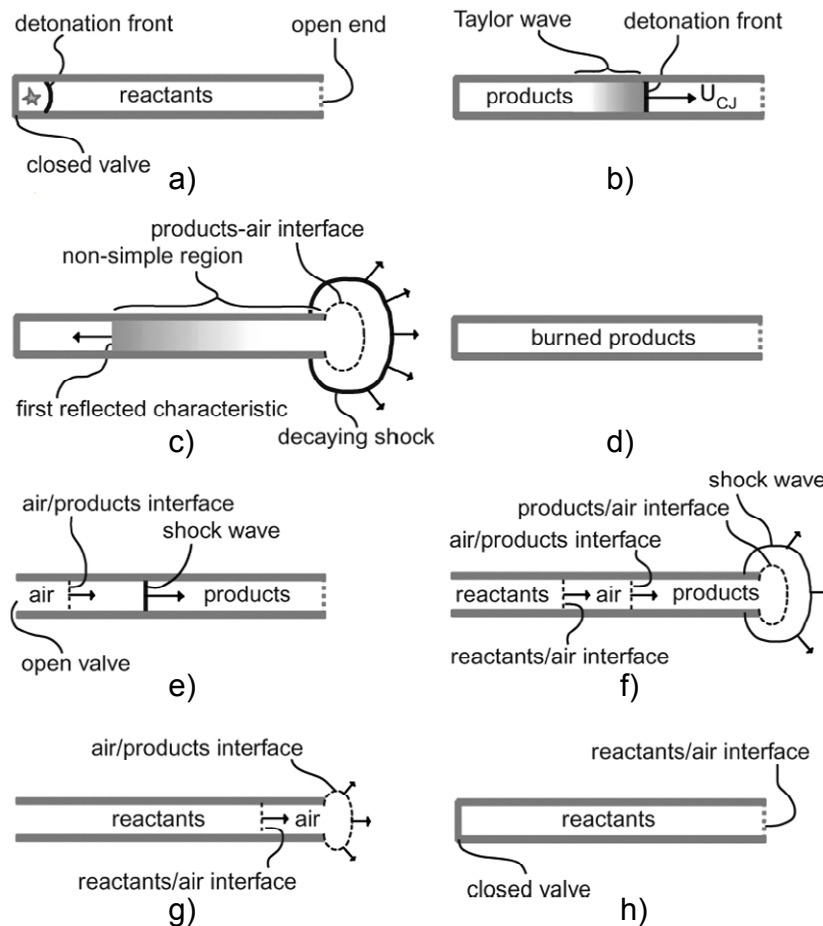


**Figure 2.12:** Qualitative cycle description of a single PDE tube [177]

First ideas of using detonative combustion in power generation, and air-breathing and rocket propulsion evolved in the 1940's and 50's. They were a result of considerable progress in understanding of detonation physics achieved during this period. After a pause, the PDE research was resumed in the 1980's involving extensive numerical and modelling efforts,

which are comprehensively reviewed in [65], [131] and [178]. These efforts led to the first sustained flight of a PDE-powered manned aircraft in 2008 [112].

Despite several thermodynamic cycle models that have been developed for PDEs, e.g. [55], [80], [121], [177], [178], there is still much uncertainty about the realistic system performance level [65], [174]. Further difficulties associated with application of PDC to gas turbines are prevention of inlet back flow, intrinsic system irreversibilities (see Chapter 2.2), and structural fatigue, due to highly unsteady exhaust flow as well as excessive pressures and temperatures of the combustion products [74]. Thus, the issues of PDC integration into a gas turbine and unsteady exhaust flow interaction with turbo-machinery have moved to the top of research agenda over the last years [27], [142], [152], [161]. The main question thereby, lies in the capability of a conventional design turbine to efficiently utilise the highly unsteady flow from the combustor.

#### 2.4.4 Pulse Combustors

Pulse combustors (PC) are self-excited, unsteady flow devices that are driven by intermittent combustion in a resonant mode. Hence, the operation of pulse combustors strongly depends on the geometrical parameters of the device. The PC generates a pulsating exhaust flow of elevated temperature and total pressure, resulting in a net pressure-gain from inlet to outlet [62], [78]. Pulse combustors can be subdivided into mechanically valved and valveless or aero-valved devices. Mechanically valved PCs use flapper or reed valves at the inlet to the combustion chamber that are subject to high temperature and pressure fluctuation, which represents a major drawback. Conversely, the aero-valved type of PCs incorporates no moving parts at all. Therein, unsteady wave motion is used to confine the periodic combustion. This PC type is preferred, because it combines the advantages of pressure-gain capability with relative mechanical simplicity [73]. The schematics of a generalised aero-valved PC are presented in Figure 2.13.

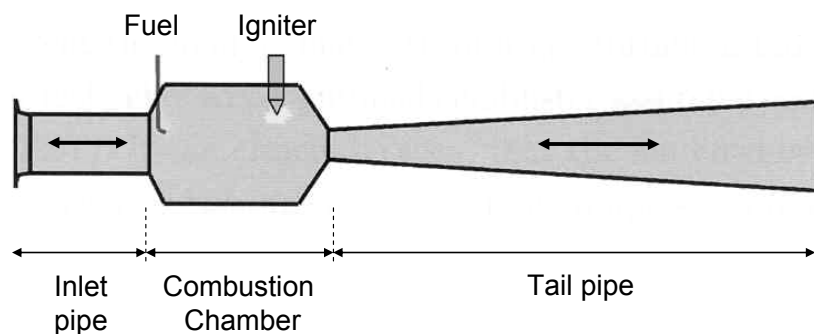


**Figure 2.13:** Schematics of an aero-valved pulse combustor [126]



The operation of a PC is often described by using a two-stroke engine analogy, with the common cycle steps – combustion, expansion of combustion products, scavenging, and compression of fresh charge [62], [108], [126]. The fresh air-fuel mixture is externally ignited, which initiates a rapid chemical reaction. The transient pressure rise and expansion of the hot gases cause an outflow of combustion products through both, the short inlet and the longer tail pipe. Inertia of the gas column in the tail pipe eventually causes a depression in the combustion chamber, which leads to flow reversal and fresh air inflow through the inlet pipe. Fresh charge of air is mixed with fuel and the remaining hot combustion products in the combustion chamber. The inertia of the reversed flow in the tailpipe compresses the gas mixture in the combustion zone. After some delay the fresh charge ignites due to the high-temperature of the residual combustion products. According to the Rayleigh criterion (see Chapter 3.1), this process is to be tuned so that ignition occurs exactly at the point of highest compression, thus resulting in the best pressure-gain performance.

The application of aero-valved PCs as a replacement for conventional gas turbine combustors was first proposed by Reynst in the 1930's [73], [156]. Subsequently, Kentfield et. al. have made a significant contribution to the development of the valve-less PC. They experimentally demonstrated a PC total pressure gain of 5-6 %, operating at a frequency of approximately 190 Hz under ambient laboratory conditions [72], [73]. A successful application of a PC to a small Cussons P.9000 gas turbine was demonstrated, which yielded a total pressure gain of 1.1-1.6 % over the full operating range of the gas turbine [77], [75]. In Figure 2.14 the mechanical arrangement of this prototype PC is shown.

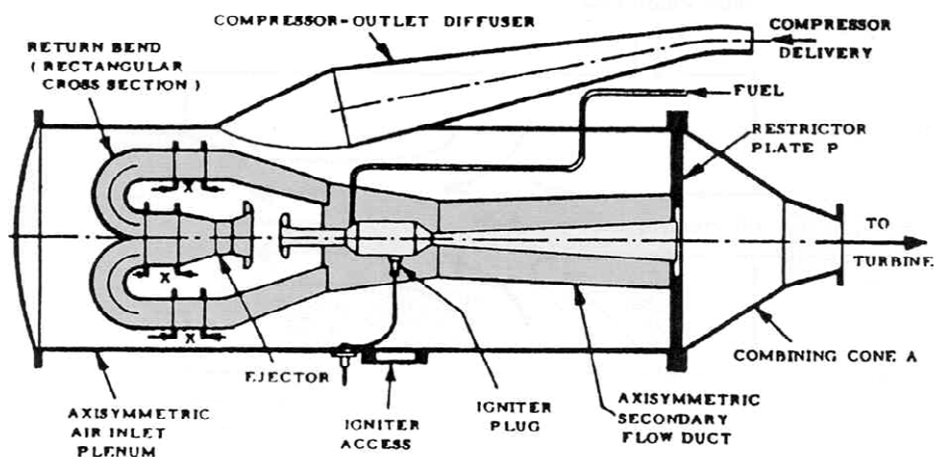


**Figure 2.14:** Diagrammatic representation of the PC configuration for use with a small gas turbine [76], [77]

The large plenum serves as a settling tank to protect the compressor from receiving cyclic pressure pulses from the combustor. The curved structure in Figure 2.14 is the thrust aug-

menter and flow rectifier that catches the outflow from the inlet pipe and redirects it towards the common exit nozzle. This flow is used to cool the combustor structure and contributes to the pressure-gain performance when tuned correctly [76]. Projections for larger gas turbines, e.g. higher mass flow rates, and optimised PC geometry predict a total pressure gain of up to 6-7 % [76]. Recently, it was experimentally shown that a significant improvement in fuel consumption of up to 65 % for a given pressure amplitude of a PC, is achieved by using a tuned unsteady fuel injection [115]. Pulse combustors have been demonstrated to operate on a variety of gaseous, liquid and solid (e.g. pulverised coal) fuels [78]. They exhibit the potential to reduce  $\text{NO}_x$  and CO emissions due to short residence time and lower average combustion temperature [71], [70]. The major drawback of PC lies, however, in their resonant mode of operation and resulting extreme sensitivity to geometrical and operational parameters [62].

#### 2.4.5 External and Internal Combustion Wave Rotors

The operation of dynamic pressure exchangers or wave rotors is based on the physical fact that equalisation of pressure between two fluids occurs faster than mixing [91]. A wave rotor is a machine that utilises unsteady wave motion (compression and expansion waves) to exchange energy between two fluids by direct action of mechanical work [6], [107], [172]. Typically, such devices consist of a number of parallel channels annularly arranged around an axis. While rotating at constant speed, the channels are periodically connected to ports of different pressure levels, which generates propagating pressure waves inside the channels. Various designs of wave rotors have been proposed. There are WR incorporating 2 to 5 connection ports to up- and downstream turbo-machinery, externally driven by a motor, or self-rotating through aerodynamically shaped channel walls [106], [166]. Generally, WR can be subdivided into two categories in terms of combustion. The first are WR where combustion occurs in an external combustor. The second are internal combustion wave rotors (ICWR). Schematics of these two configurations applied to a gas turbine are shown in Figure 2.15.

In Figure 2.15a, combustion is performed in a conventional CP burner, i.e. the WR is used as a topping cycle rather than a true pressure-gain combustor. Therein, the “cold” gases delivered by the compressor are further compressed through pressure exchange with the hot combustion gases exiting the combustor. The advantage of this cycle lies in the increase of the engine OPR and higher possible combustion temperatures leading to an improvement in engine thermal cycle efficiency and SFC [5], [172]. Experimental studies by General Electric and Rolls Royce have demonstrated achievable WR compression ratios of  $\pi_{WR} = 1.12-1.27$  depending on the wave rotor temperature ratio [74], [166], [171]. WR were developed in the 1940's as dynamic pressure exchangers for various applications [6], [10]. So far, their commercially most successful application was the Compresx<sup>®</sup> supercharger for diesel car engines

developed and built by BBC. Despite significant progress achieved, unsolved technological challenges have prevented an application of WRs to gas turbines. Such problems are engine integration, additional ducting and sealing with associated pressure losses, reliability and structural issues [166].

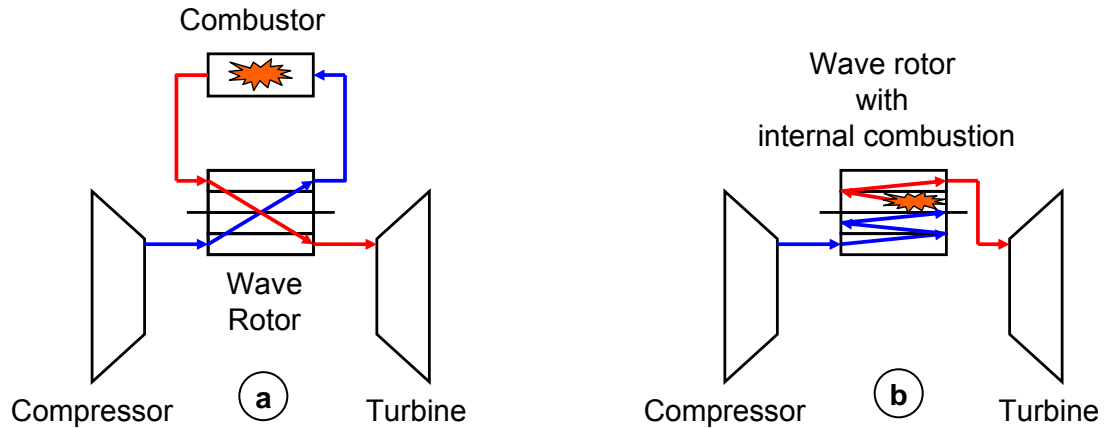


**Figure 2.15:** Scheme of wave rotor with a) external, and b) internal combustion

A further development of WR technology, the ICWR, incorporates “on-board” combustion, i.e. internal to the wave rotor passages. To the benefits of a simple WR, this configuration adds the advantage of reduced mechanical complexity by eliminating the need of an external combustor [107]. Schematics of such a device are shown in Figure 2.15b. In this system fuel is added to the inlet stream delivered by the compressor. Propagating pressure waves are generated in the channels by sequentially opening and closing inlet and outlet ports. After shock wave pre-compression, the mixture is ignited in the channels that are closed at both ends and combustion occurs at CV conditions. Finally, the combustion products are exhausted to the turbine and the channels are refilled. A sketch of an ICWR is presented in Figure 2.16 showing unsteady wave motion of hot and cold gases inside the channels.

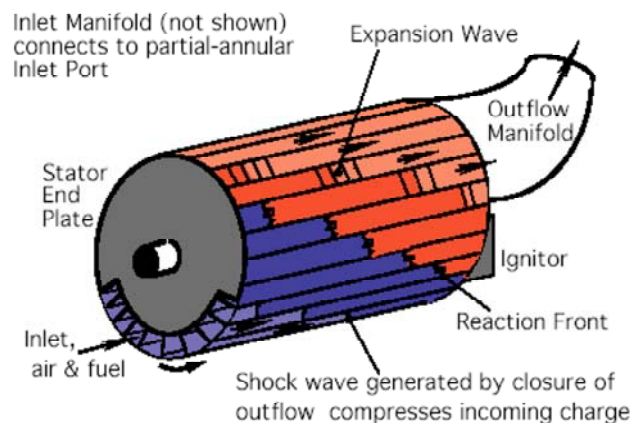


**Figure 2.16:** Schematics of an ICWR [106]

However, besides the thermodynamic benefits of idealised CV combustion, this setup introduces additional technological difficulties such as reliable ignition, dynamics of the CV combustion process, interaction between flame and pressure waves, sealing and thermal protection issues. A comprehensive review of this novel PGC technology is given in [6] and [106].

### 3 Pressure-Gain Combustion Based on Shock Wave-Flame Interaction

#### 3.1 The Rayleigh Criterion

The ideas of using unsteady combustion in gas turbines have preceded the development of steady-flow combustion as is used in most of today's gas turbines [10], [46], [143]. The advantages of intermittent combustion are related to the unsteady-flow phenomena such as inertia effects for emptying and filling of the combustion chamber, pre-compression of reactants through pressure exchange, and approximated CV combustion. In order to elucidate this point the stagnation enthalpy  $h_t$  of a fluid is defined as follows

$$h_t = h + e_{kin} = e + pv + e_{kin}. \quad (3.1)$$

Therein,  $h$  is the specific static enthalpy,  $e$  is the specific internal energy, and  $e_{kin}$  is the specific kinetic energy. If the flow domain is thought to be subdivided into a number of cells, the term  $pv$  is interpreted as the energy exchange process between adjacent cells as the fluid moves from cell to cell. It is referred to as flow work. Differentiating equation (3.1) and substituting the specific volume  $v$  by  $1/\rho$  yields

$$\frac{Dh_t}{Dt} = \frac{De}{Dt} + p \frac{Dv}{Dt} + \frac{1}{\rho} \frac{Dp}{Dt} + \frac{De_{kin}}{Dt}. \quad (3.2)$$

Using the second law expression  $Tds = de + pdv = dq$  and performing some manipulations one obtains the energy conservation equation for an adiabatic (no external heat transfer), reactive system, without transport and body forces

$$\frac{Dh_t}{Dt} = \frac{1}{\rho} \frac{\partial p}{\partial t} + T \frac{Ds}{Dt} = \frac{1}{\rho} \frac{\partial p}{\partial t} + \frac{\partial q}{\partial t} + \vec{V} \cdot \nabla q. \quad (3.3)$$

In the case of steady-flow, constant-pressure combustion equation (3.3) reduces to  $\vec{V} \cdot \nabla h_t = \vec{V} \cdot T \nabla s$ , where the irreversible heat release is the only type of energy output. If combustion is unsteady, and the heat release is not variable in space, i.e.  $\vec{V} \cdot \nabla q = 0$ , a portion of the heat release is directly converted into mechanical energy, e.g. in the form of propagating pressure waves that arise due to the inertia of the surrounding fluid. This is represented by the  $\partial p / \partial t$  term in eq. (3.3), which results from the flow work term in unsteady flow. Such pressure waves represent a mode of exergy and can be fully transformed into useful work,

e.g. through an idealised turbine [11]. This makes the unsteady heat addition process less irreversible and thus, more efficient, than the steady-flow one. For an ideal constant-volume combustion process the share of energy transformed into pressure fluctuations is found to be  $(\kappa-1)/\kappa$  [10]. Using the value of air  $\kappa = 1.4$ , this results in 29 % of the fuel chemical energy going into generation of pressure waves.

The heat release being accompanied by fluctuations of pressure in eq. (3.3), for  $\bar{V} \nabla q = 0$ , suggests a coupling mechanism between the two processes. This coupling between heat release and pressure was first described by Lord Rayleigh (1878). He formulated the Rayleigh criterion, which states that if a periodic heat release is in phase with a pressure oscillation, the amplitude of the pressure oscillation will be amplified [129]. A phenomenological formulation of the Rayleigh criterion is given by the inequality (3.4) [129].

$$\int_0^{\tau} \int_0^V p'(x,t) q'(x,t) dV dt > \int_0^{\tau} \int_0^V \Psi(x,t) dV dt \quad (3.4)$$

Therein,  $V$  is the control (combustor) volume,  $\tau$  is the period of oscillation,  $p'$  and  $q'$  are the fluctuating pressure and heat release respectively, and  $\Psi$  is the sum of damping (wave energy dissipation) terms. Energy can be dissipated from flow fluctuations by friction, heat and mass transfer, or acoustic radiation [10]. Thus, in order for the unsteady combustion process to be self-sustaining, the damping must be overcome by the total mechanical energy added to the oscillation per cycle. The energy added to the oscillating acoustic field is described by the left hand side of inequality (3.4) and represents the 'driving' for the oscillation. If the driving is stronger than the energy dissipation, the Rayleigh criterion is satisfied. This causes growing of the pressure oscillation amplitude in every cycle of oscillation and promotes instability of the system [117], [144]. The ultimate source of driving energy for such oscillations is the heat released by the combustion process [36].

An extended formulation of the Rayleigh criterion for linear, acoustic oscillations is given in [36], [127], [150] as follows

$$\Delta E(x,t) = \frac{\kappa - 1}{\kappa p} \int dV \int_t^{t+\tau} p'(x,t) q'(x,t) dt, \quad (3.5)$$

where  $\Delta E$  is the incremental energy added to the acoustic field over a period  $\tau$ . Driving of the oscillation occurs when  $\Delta E$  in eq. (3.5) is a positive value. This can be true only if  $p'$  and  $q'$  are exactly in phase or have a phase shift less than  $\pm 180^\circ$  [101]. A negative  $\Delta E$  will tend to damp out the oscillations.

Strictly speaking, the Rayleigh criterion as presented above is only valid for acoustic perturbations, i.e. isentropic flows. For the treatment of reacting, non-isentropic flows Chu [34] suggested to use a different stability criterion:

$$\Delta E(x, t) = \frac{1}{T_0} \int dV \int_t^{t+\tau} T'(x, t) q'(x, t) dt. \quad (3.6)$$

In equation (3.6), which is given for the case where viscous and thermal dissipation as well as boundary fluxes are neglected,  $\Delta E$  is the incremental energy added to the perturbation over a period  $\tau$ . It states that temperature  $T'$  and heat release  $q'$  fluctuations must be in phase for the instability to be excited. Chu derived this criterion explicitly accounting for entropy fluctuations in the perturbation. Nicoud and Poinso [110] further extended this formulation to the case where the entropy field is not constant over the flow domain and state that only this criterion should be used in analysing unstable flames. However, evaluation of this criterion represents a difficult task in experiments and necessitates detailed knowledge about various unsteady quantities that can only be provided by large eddy simulation (LES).

The coupling of heat release and pressure field has been identified to be a major cause of thermo-acoustic instabilities occurring in gas turbine and rocket combustors, ramjets and after-burners of jet engines, as well as in industrial furnaces [16], [94], [144]. Such instabilities produce pressure pulsations with quickly growing amplitudes, which can lead to structural damage or failure of the combustor [36], [38]. Methods of avoiding or controlling such instabilities, particularly in the new generation of gas turbine combustors operating in a lean premixed mode, have become an important field of research [38], [101], [117], [144]. In this sense, the “classic” Rayleigh criterion (eq. (3.5)) has become a common tool in identifying the operating conditions in which thermo-acoustic instabilities are promoted; see e.g. [16], [68], [127], [150].

## 3.2 Shock-Flame Interaction – Literature Review

### 3.2.1 Introduction

Interaction of pressure waves, both acoustic and shock waves, with a flame creates a system of transmitted and reflected waves as well as secondary pressure waves [98], [132]. These waves may reflect at the geometrical boundaries of the flow device and repeatedly interact with the flame. Under favourable conditions a feedback mechanism is established leading to the formation of a sustained pressure oscillation in the combustor. In steady, constant-flow combustion systems such oscillations must be eliminated as they may grow and detrimentally affect system performance or even cause mechanical damage [38]. On the contrary, the operation of unsteady-flow combustion systems, such as pulsejets, directly relies on the exploitation of this feedback mechanism [10].

Shock-flame interaction (SFI) has been given lots of attention with regard to its important role in the process of deflagration to detonation transition over the last decades. Numerical and experimental studies have demonstrated that multiple shock-flame interactions accelerate an initially laminar flame and create conditions under which DDT is promoted [82], [155], [154]. A comprehensive review of this topic is given in [118].

Recent developments in ICWR technology have also contributed to the increased interest in shock-flame interaction phenomena. As has been highlighted in Chapter 2.4.5, operation of these devices involves interaction between shock waves or strong pressure waves and combustion. Hence, a detailed understanding of the SFI physics is required for an optimum design of such devices [84].

Historically, Markstein [98] was the first to perform detailed experimental investigations into the phenomena of shock-flame interactions in the 1950's. Since, various analytical [30], [32], [132], numerical [64], [81], [82], [147], and experimental [66], [67], [98], [136], [140], [153], [155] studies have produced a significant contribution to the understanding of physical phenomena involved in SFI in both premixed, and two-phase, liquid-gas [29], [19], [20], [21], [22], [48] combustion systems.

The passage of a shock wave through a corrugated flame front causes a rise in gas temperature and pressure. Further, it temporarily increases the turbulence intensity, flame stretch, and flame surface area. The flame can be assumed to remain within the laminar flamelet regime throughout the whole SFI process [64], [81], [84], which allows for the turbulence effects to be neglected. Thus, shock-flame interaction has two main effects. It changes the thermodynamic mixture properties and modifies the flame surface area. The former is brought about by shock refraction at the flame front, which occurs instantaneously and generates a transmitted and a reflected wave. The latter is related to multidimensional, time-dependant effects of flame-vortex interaction and occurs with a certain time lag. The two effects, although interrelated and highly unsteady at various time and length scales, can be treated separately from each other [85], [132]. The combined result of the described phenomena is a temporal increase in the amount of energy released by a flame per unit time [32], [81], [84], [98], [132]. This, in turn, is responsible for a third SFI effect – the generation of secondary pressure waves at the distorted flame front [31], [32], [132].

### 3.2.2 Shock Refractions at Reactive and Inert Gas Interfaces

A flame front represents a reactive, hydrodynamic discontinuity that separates two gas volumes of different density, temperature and pressure. If an incident shock wave (index  $i$ ) propagating in a compressible medium encounters such an interface, it will refract at this interface and produce a transmitted (index  $tr$ ) and a reflected wave (index  $r$ ) [56], [132].



Shock refraction can be considered one-dimensional in nature and to occur instantaneously [85], [132]. Such a physical problem is schematically shown in Figure 3.1.

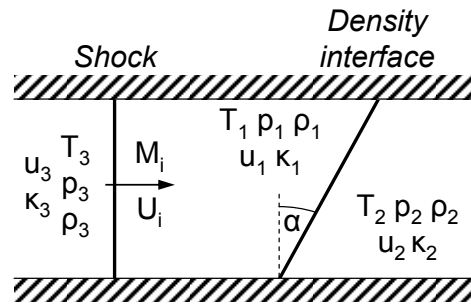


**Figure 3.1:** Schematics of a planar density interface at angle  $\alpha$  to the incident shock

Therein, the incident shock propagates through the incident gas with the state 1. The incident shock can be characterised by the Mach-number  $M_i$  or the propagation velocity  $U_i$ . When the shock traverses the gas interface, a transmitted wave will propagate further at the velocity  $U_t$  in the transmitted gas with the state 2. Additionally, a reflected wave will evolve and propagate at the velocity  $U_r$  in the opposite direction into the shocked incident gas with the state 3. For simplicity, the interface, between the incident and the reflected gases is assumed to be planar and parallel to the incident shock, i.e. the incidence angle  $\alpha = 0^\circ$ . Such head-on interactions do not cause any deformation of the gas interface.

Based on these assumptions Henderson [56] developed a rigorous definition of wave impedance, which determines the nature and intensity of shock refractions, as well as the fraction of shock energy and power that are reflected and transmitted. Generally there are two classes of shock refractions: “slow-fast” (s/f) and “fast-slow” (f/s). The terms “slow” and “fast” refer to the velocity of sound in the respective gas. The refraction is s/f if the incident shock wave travels in the low sound velocity medium, e.g. the cold, unburned gas. In such interactions the incident shock is transmitted as a shock, whereas the reflected wave is always an expansion fan. Conversely, in f/s refractions the incident shock propagates in the high sound velocity fluid, and both the reflected and transmitted waves are shocks. For shock refractions at non-reactive interfaces, an iterative calculation procedure of the post refraction flow field is presented in [14].

For reactive interfaces, the change in the thermodynamic state is governed by the chemical reactions occurring in the flame. Hence, when calculating such refractions, the dependence of the chemical kinetics (laminar flame speed) on mixture temperature and pressure must be taken into consideration [51]. Refraction systems consisting of incident, transmitted and reflected waves, which evolve following s/f and f/s shock-flame interaction, are schematically presented on a time-space plane in Figure 3.2.

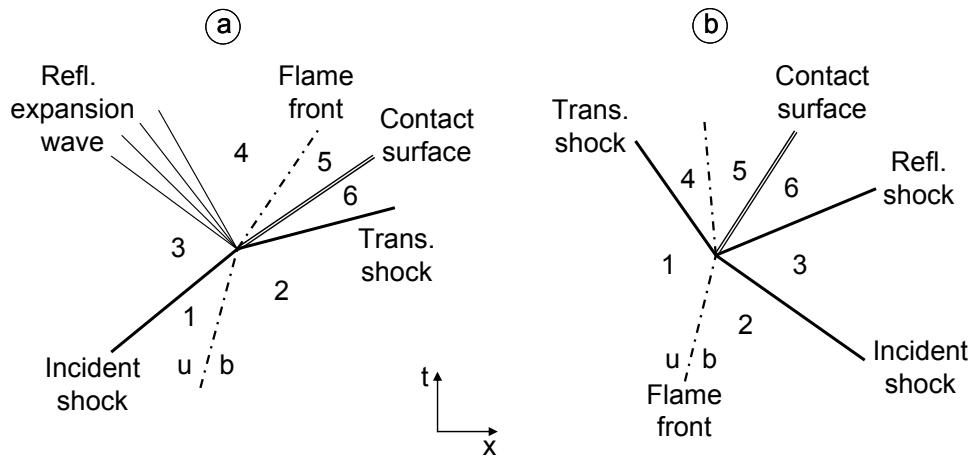


**Figure 3.2:** Wave-diagrams of a) slow-fast, and b) fast-slow shock-flame refraction [132]

The contact surface evolves at the instant of the interaction and separates the regions 5 and 6 in which the gas undergoes a different entropy rise. This is because the gas particles in region 5 are first subject to pressure wave action and then burn, whereas those in region 6 are burned before being affected by pressure waves. Following continuity conditions are valid across the contact surface:

$$\begin{aligned} \rho_5 &= \rho_6 \\ u_5 &= u_6 \end{aligned} \quad (3.7)$$

The continuity conditions of eq. (3.7) are applicable across all non-reactive media interfaces [56]. An iterative calculation procedure for determining the thermodynamic conditions in all six regions of the wave diagrams of Figure 3.2 is given by Rudinger in [132].

If the incident shock and the interface are not parallel to each other, then the calculations discussed above must be modified in order to account for the incidence angle  $\alpha$  [56]. For  $\alpha$  smaller than a critical angle  $\alpha_{cr}$  all waves are locally plane and meet at a single point on the interface. Such refractions are called regular and obey the theory discussed above. For  $\alpha \geq \alpha_{cr}$  the interface continuity conditions (3.7) do not hold any longer and refraction is irregular. This type of refractions involves Mach-reflections in the incident medium, and when the refraction is s/f, precursor shocks in the transmitted medium. The domain of irregular reflections is very complex and a detailed discussion is beyond the scope of this work. A more detailed description of this topic including the transition from regular to irregular refractions is given in [1] and [56]. For the  $\alpha_{cr}$  it can be said that, for a given stratification ( $\rho_1/\rho_0$ ) and a growing strength of the incident shock, it increases for s/f refractions, and decreases for f/s refractions [138], [139].

### 3.2.3 Flame Front Deformation Induced by Shock-Flame Interaction

Any perturbation on the interface between two fluids of different properties is amplified following interaction with a shock wave [26], [133]. Early shock-flame interaction experiments carried out by Markstein [98] showed that, besides the shock refraction, the passage of a shock wave through an initially curved laminar flame causes the flame area to increase and to become turbulent in some cases. Richtmyer (1960) was the first to theoretically describe the deformation of medium interfaces subject to shock induced, impulsive acceleration. His theory was then qualitatively confirmed by Meshkov's shock-tube experiments in 1969. Hence, this class of problems is since known as the Richtmyer-Meshkov instability (RMI) [26]. It is related to the Rayleigh-Taylor instability (RTI), however, differs notably from it through the impulsive interface acceleration induced by the shock passage.

The underlying mechanism for the amplification of interface perturbations is baroclinic vorticity generation resulting from the misalignment of the shock pressure gradient and the local density gradients across the interface [26], [125]. In Figure 3.3 schematics of a basic, non-reactive, two-dimensional configuration for the RMI are shown in the frame of reference fixed to the interface. The incident shock is flat and travelling in the direction normal to the interface. The interface separating two regions of different density is a discontinuity. For the sake of simplicity, the interface is assumed to be non-reactive and to have a simple single-mode sine function shape with known wavelength  $\lambda$  and initial amplitude  $\varepsilon_0$  (Figure 3.3a).

Following the refraction of the incident shock, a shock wave is transmitted, and a shock or an expansion wave, depending on the fluid properties, is reflected. As a result thereof, the interface is impulsively accelerated and travels at a constant velocity in the direction of the transmitted shock. An unstable vortex sheet of varying strength is created at the interface due to generation of baroclinic vorticity resulting from the local misalignment of pressure and density gradients; see Figure 3.3b. The overall result is that the initial perturbation amplitude grows continuously after the passage of the shock. During this early period the perturbation growth is linear in time. At later times, the perturbation amplitude evolution becomes non-linear. During this non-linear growth phase spikes or "funnels" of heavy fluid penetrate into the light fluid, and bubbles of light fluid spread into the heavy one (Figure 3.3c). Eventually the Kelvin-Helmholtz instability causes the roll-up of the funnels (Figure 3.3d) and a turbulent mixing zone develops between the fluids (Figure 3.3e) [26].

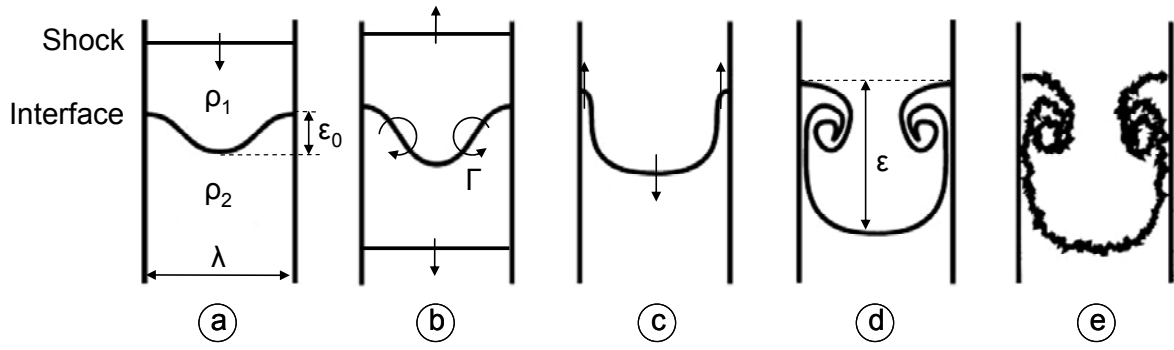


**Figure 3.3:** Evolution of RMI at a single-mode interface perturbation [26]

The growth rate of perturbation amplitude  $\varepsilon$  for the RMI (in the literature often designated by the symbol  $\eta$ ) was obtained by Richtmyer [26] as:

$$\frac{d\varepsilon(t)}{dt} = \dot{\varepsilon} = k \Delta u A t \varepsilon_0. \quad (3.8)$$

Therein,  $k = 2\pi/\lambda$  is the wave number of the perturbation,  $At = (\rho_2 - \rho_1)/(\rho_2 + \rho_1)$  is the post-shock Atwood number,  $\Delta u$  is the interface velocity change due to shock refraction, and  $\varepsilon_0$  is the initial perturbation amplitude. This equation describes the development of the interface while the amplitude is still small enough to remain in the linear regime. Nonlinear interface growth theories were developed by Sadot et. al. [135] or Li & Zhang [26], which are valid for all, the linear, early non-linear, and late asymptotic, growth regimes.

Kilchyk [84] performed numerical investigations into the interaction of shock and expansion waves with two-dimensional, single mode, sine-shape gas interfaces. He used both, inert and reactive interfaces, which were representative of stoichiometric propane combustion. In his work he demonstrated that the rate of perturbation amplitude change  $\dot{\varepsilon}$ , acquired using linear and non-linear theories, as well as assessed directly from numerical simulation, significantly differs from the rate of interface length change  $v_{int}$ . Furthermore, he concluded that the interface length increase remains near-linear with time for a considerably longer period than the perturbation amplitude growth. In the case of the reactive interface, the interface length reaches its maximum when the rate of interface increase is equal to the rate of interface “burn out” due to enhanced chemical kinetics of the flame. Kilchyk concludes that the interface perturbation amplitude growth rate is an inappropriate representative of the interface length growth in two dimensions or the interface surface growth in three dimensions respectively. Based on these results, he suggests a proportionality relationship between the interface length growth rate  $v_{int}$ , the deposited vorticity or circulation  $\Gamma$ , and the geometrical parameters of the initial interface  $\lambda$ ,  $\varepsilon_0$ :

$$v_{int} \sim \frac{\Gamma \varepsilon_0}{\lambda^2} \quad (3.9)$$

The relation (3.9) is valid for both, the s/f and f/s, classes of interactions [84]. However, the full expression may involve different sets of constants in the s/f and f/s interaction cases.

The evolution of vorticity  $\omega_v$  in an inviscid, two-dimensional flow can be expressed in terms of pressure and density gradients as follows [84], [139]:

$$\frac{D(\omega_v/\rho)}{Dt} = \frac{\nabla \rho \times \nabla p}{\rho^3} \quad (3.10)$$

Generation of vorticity is negligibly affected by the presence of chemical reactions at the interface [84], [158]. This allows the treatment of the fluid dynamic effects separately from the combustion processes. Oblique shock-interface interaction produces a shear layer at the interface. This leads to a difference in the tangential component of fluid velocity across the interface, which is responsible for circulation  $\Gamma$ . The circulation  $\Gamma$  is defined as a line integral around the density interface, and can be expressed in terms of the difference in tangential velocity  $u_{tan}$  across the interface with the total length  $l_{int}$  [84]:

$$\Gamma = \int_{l_{int}} \omega_v dx dy = l_{int} (u_{tan1} - u_{tan2}) \quad (3.11)$$

The strength of the generated vortex sheet  $\gamma$  is given by eq. (3.12) as the circulation per length of the interface, or as the jump of tangential velocity across the interface [84], [139].

$$\gamma = \frac{\Gamma}{l_{int}} = (u_{tan1} - u_{tan2}) \quad (3.12)$$

If the circulation generated at the interface is known, it is possible to determine the two-dimensional rate of interface length growth using relationship (3.9). Consequently, the total increase in the three-dimensional flame surface area resulting from a shock-flame interaction can be estimated for a given channel and initial flame geometries.

### 3.2.4 Generation of Pressure Waves at Disturbed Flame Fronts

Pressure waves are known to be generated by a flame in response to various kinds of perturbations such as changes in combustible mixture composition or variations in thermodynamic properties of the mixture. Well known examples of such phenomena are ignition processes, flame acceleration in ducts, or pressure wave and flame interactions [30], [31], [132].

The physical mechanism involved in the generation of pressure waves at flame fronts can be described as follows. The increased flame surface area, gas temperature and pressure result in a change in the rate of heat release (HRR) of the flame. The HRR is the amount of energy released by a flame per unit time. It is a function of the combustible mixture composition,

thermodynamic properties of the unburned gas, and flame surface area [32], [84]. The total rate of heat release is given by the equation (3.13) [132].

$$\Omega = q\rho_1 s_L A_F \quad (3.13)$$

In this equation  $q$  is the energy release per unit mass of the mixture;  $\rho_1$  is the density of the unburned gas;  $s_L$  is the laminar flame speed; and  $A_F$  is the flame surface area.

As a consequence of the elevated heat release rate, the rate of expansion of the burned gas is altered accordingly. This can be visualised by an idealised volume of unburned gas traversing a flame front; see Figure 3.4.

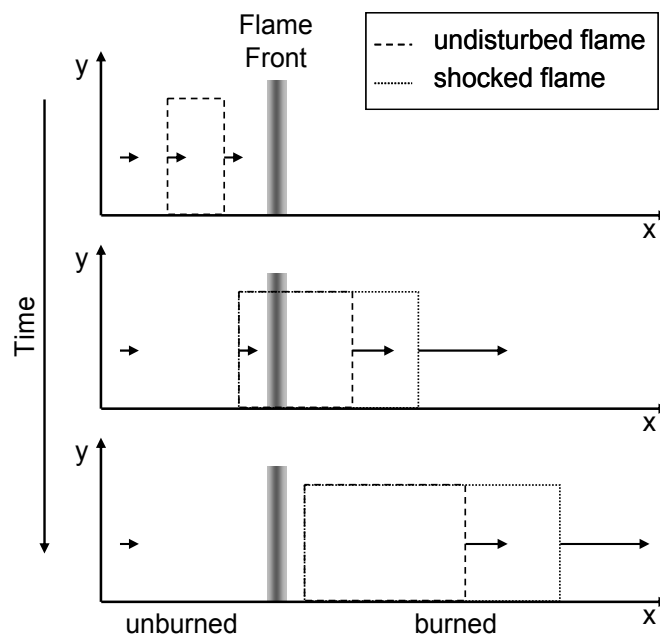


**Figure 3.4:** Expansion of a volume of combustible mixture due to combustion. Frame of reference is fixed to the flame front

In the case of the shocked flame the amount of heat added to the gas volume per unit time is higher compared to the undisturbed flame. This results in the gas expanding at a higher rate. Relative to the gas particles outside of the fictitious volume the boundaries of the expanding gas volume can be considered as solid walls. Thus, pressure waves are generated as a result of a change in the expansion rate of the burned gas [32].

The perturbation analysis theory proposed by Chu [30], [31], [32] provides the best basis for analytical treatment of such problems [132]. Chu considers a one-dimensional, compressible flow across a planar flame front; as shown in Figure 2.2. His analysis is valid for finite changes in thermodynamic variables and does not involve linear approximations. The rate of heat release per unit flame surface area  $\omega$  is defined as shown in eq. (3.14).

$$\omega = q\rho_1 s_F = q\rho_1 s_L \frac{A_F}{A_L} \quad (3.14)$$

This equation suggests that there will be a change in  $\omega$  whenever there are changes in the laminar flame speed  $s_L$ , unburned gas density  $\rho_1$ , or flame surface area  $A_F$ .  $A_L$  is the surface area of a planar, laminar flame that corresponds to the cross-sectional area of the combustion system.  $q$  is assumed to remain constant as long as the combustible mixture composition is not changed. Using the assumption of low Mach-number of the initial flame front ( $M_1 \ll 1$ , i.e.  $p_1 = p_2 = p$ ), and constant  $\kappa$  across the flame front ( $\kappa_1 = \kappa_2 = \kappa$ ), the following relation can be derived [32]:

$$\Delta\omega = \frac{1}{\kappa - 1} \frac{\rho(1 + \Delta\rho/\rho)(a_1 + a_2)(\Delta\rho/\rho)}{\sqrt{\left(\frac{\kappa + 1}{2\kappa} \left(\frac{\Delta\rho}{\rho}\right) + 1\right)}} \quad (3.15)$$

This equation allows the calculation of the finite pressure rise  $\Delta\rho$  generated in response to finite changes in the heat release rate of the flame  $\Delta\omega$ , regardless of how such changes are produced. The generated pressure waves are assumed to be of equal strength in both the burned and unburned gas  $\Delta\rho_1 = \Delta\rho_2 = \Delta\rho$  [32]. The relationship (3.15) was successfully applied by Scarinci et. al. to estimate the changes in flame heat release rate, resulting from experimental shock-flame interaction pressure records for different fuels [140].

For moderate changes in  $\omega$ , i.e.  $\delta\omega/\omega \ll 1$ , weak pressure waves with the pressure rise  $\delta\rho$ , where  $\delta\rho/p \ll 1$ , are generated at the flame. Following analytical relationship was derived by Chu for estimating such pressure waves under the assumption  $\kappa_1 = \kappa_2$  [32]:

$$\frac{\delta\rho}{\rho} = \frac{\kappa - 1}{a_1 + a_2} \frac{\delta\omega}{\rho} \quad (3.16)$$

The one-dimensional model discussed above allows the calculation of the pressure waves that are generated at the flame front as a result of changes in the heat release rate of the flame.

As per eq. (3.14), there exist two potential mechanisms that can lead to an increase in the rate of heat release of a flame: changes in the fuel burning rate per unit flame surface area  $\rho_1 s_L$  due to compression effects; and increase of the flame surface area due to RMI. Results of numerical and experimental investigations have demonstrated that the latter effect, i.e. the deformation of the flame surface, is the dominant mechanism in shock-flame interactions. This is particularly true for weak incident shocks, and low reactivity, i.e. low laminar flame speed, fuels [85], [140].

Khokhlov et. al. [81] performed numerical interaction studies of a shock wave and a sinusoidally perturbed, stoichiometric acetylene-air flame. He found that the combined effect of flame surface area growth and increase in the fuel consumption rate result in the heat re-

lease rate of the flame to rise by the factor 20-30 due to a single shock-flame interaction. His results also indicate that this increase is almost halved in two dimensions relative to three dimensional computations. The increase in heat release rate achieved in one dimensional computations is up to 20 times lower than in two dimensions because it is related to the compression effects only [82]. Considerably higher augmentation rates of flame energy release rate are achievable through multiple SFI [81], [82]. Scarinci et. al. [140] demonstrated increase factors of higher than 1000 in their multiple shock-flame interaction experiments using acetylene flames. In their numerical and experimental investigations Khokhlov, Thomas et. al. [82], [155] showed that multiple SFI create conditions under which DDT may occur. Shock velocities achieved prior to the onset of detonation in their studies were approximately half of the characteristic fuel  $CJ_0$ -detonation velocity. The pressure behind these waves corresponded to the CV combustion pressure of the initial mixture. Vorticity generated in these studies was shown to be insufficient to locally extinguish the flame [81].

### 3.2.5 Shock-Flame Interaction in Two-Phase Combustion Systems

The combustion of sprays of liquid fuels is of fundamental practical importance. A large portion of the world energy requirement, particularly in the transportation sector, is currently covered by burning of liquid fuels. Liquid fuel combustion is significantly different from gaseous fuel burning. It belongs to the group of diffusion flames, and involves droplets of liquid fuel reacting with the surrounding oxidising atmosphere, usually air. The fuel droplets evaporate and produce flammable vapour. The oxidant and the fuel vapour mix and burn in a diffusion flame surrounding the droplets [168]. Hence, the energy release is not instantaneous but occurs after some minimum time  $\tau_t$ . The total ignition delay time  $\tau_t$  is a simple sum of three characteristic times  $\tau_s$ ,  $\tau_m$ ,  $\tau_r$  [69].  $\tau_s$  is the characteristic time required for fuel-oxygen mixing including evaporation;  $\tau_m$  is the characteristic time required to mix hot products with the reactants, heating them up to the ignition temperature; and  $\tau_r$  is the chemical reaction induction time. The total ignition delay time can be reduced by shortening  $\tau_r$  through increased temperature and pressure of the reactants. Alternatively,  $\tau_s$  can be reduced by improving the quality of the spray, i.e. by generating smaller fuel droplets in order to accelerate evaporation and mixing.

Interaction of a propagating shock wave with a liquid droplet causes the droplet to break up, forming smaller droplets, and to partially evaporate. This is brought about by the shear stresses on the droplet surface in the high velocity flow associated with the shock. Various atomisation regimes have been identified in terms of the Weber number  $We = \rho u d / \sigma$  [20], [22]; see Figure 3.5. In this equation  $\rho$  is the post shock gas density,  $u$  is the post shock flow velocity relative to the droplet,  $d$  is the droplet diameter, and  $\sigma$  is the droplet surface tension.



For weak shock waves resulting in  $We \leq 10$ , no droplet breakup occurs. Values of  $We \geq Re^{1/2}$  result in an intensive droplet breakup (stripping mode and higher), leading to the formation of a cloud of very small, fast evaporating droplets with a diameter of  $d \approx 50 \mu\text{m}$  [22]. Therein,  $Re = du/\nu$  is the Reynolds number, where  $\nu$  is the kinematic viscosity of the post shock gas.

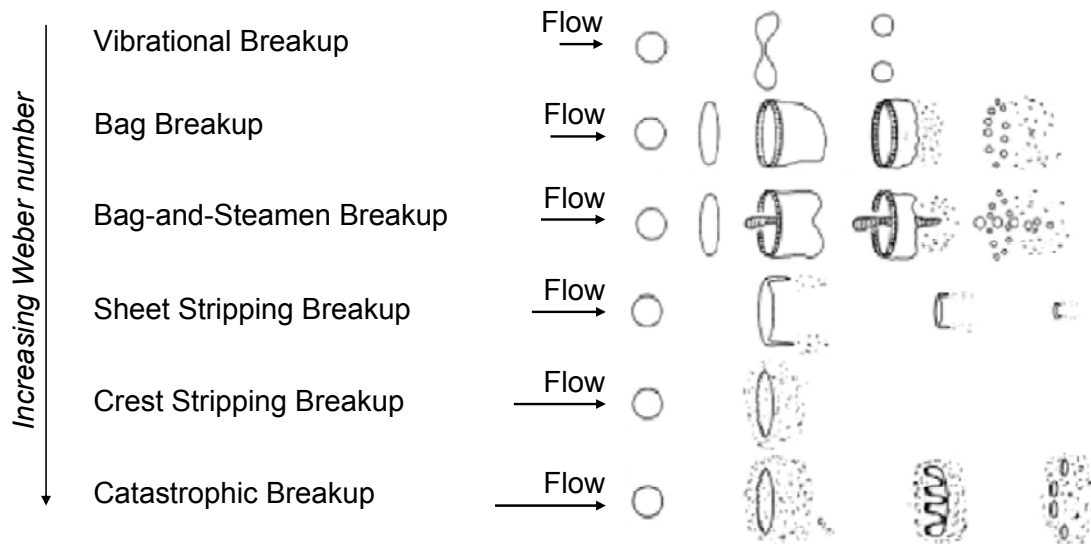


**Figure 3.5:** Breakup regimes of water droplets [49]

Consequently, the presence of a dispersed liquid phase has a substantial effect on the behaviour of the shock propagating through it. A portion of the energy and momentum of the post-shock fluid is consumed by the processes of droplet acceleration, breakup and evaporation. As a consequence, shock waves are attenuated when propagating through inert, two-phase liquid-gas flow systems. Higher attenuation rates are observed with smaller droplet size at constant mass loading of the liquid phase [22], [29].

In reactive two-phase mixtures, the energy of the chemical reaction overcomes the breakup losses and leads to the amplification of the incident shock. The condition for this to occur is that the energy is released as shortly as possible after the shock passage [29]. This is achieved either through the use of small droplets or by stronger incident shock waves. It leads to more intense droplet breakup and thus, shorter mixing times  $\tau_s$ , which in consequence accelerates the heat release process.

In their experimental studies Borisov et. al. successfully described the amplification of shock waves in burning two-phase mixtures on the basis of the Rayleigh criterion [19], [20], [21]. The explicit definition of the Rayleigh criterion is given in Chapter 3.1. Borisov et. al. demonstrated that the incident shock wave is amplified only if the total ignition delay time  $\tau_t$  is shorter than the post shock constant pressure interval  $\Delta t$  (see Figure 3.6), i.e. the combustion energy is released within the high pressure region behind the shock. In this case the

secondary pressure waves generated in response to the increased heat release contribute to the reinforcement of the incident shock wave. Their experimental results clearly show that droplet breakup is the main process responsible for the feedback mechanism between shock waves and combustion in two-phase mixtures. For strong shock waves and small droplets this feedback mechanism leads to the formation of a sustained detonation even within short axial distances [21], [29].

### **3.3 Pressure-Gain Combustion Based on Shock-Flame Interaction – Concept Development**

The Rayleigh criterion states that the mechanical energy in a pressure oscillation will grow in time when the fluctuating heat release rate is in phase with the underlying pressure field [33]. Hence, it provides a direct route to achieve an unsteady mode of pressure-gain combustion. However, although appearing obvious, the Rayleigh criterion has been barely used to identify and exploit the regimes of pressure-gain combustion rather than avoiding them [62].

Chu [33], [32] was the first to discuss the Rayleigh criterion on the basis of a piston engine analogy. Janus et. al. [62] developed that idea further into the “frequency matching” concept and applied it to analyse the operation of a pulse combustor; see Chapter 2.4.4 for detailed description. The “frequency matching” concept states that the frequency of the resonant acoustic pressure field and the frequency of combustion must be matched, i.e. be in phase, in order to achieve best pressure-gain performance. Janus et. al. confirmed the validity of this concept by demonstrating the best pressure-gain performance under frequency matching conditions in a numerical model of a pulse combustor. Hence, the Rayleigh criterion provides crucial guidance in the design and optimisation of unsteady PGC systems [115].

A major drawback of combustion concepts using interaction of a flame with resonant acoustic pressure waves, such as the PC, is their susceptibility to system geometry. The fact that the operating frequency of such devices is governed by resonance strongly limits the means of controlling them. This drawback can be overcome by using another type of flow field disturbance – the shock waves. Shock waves are characterised by supersonic propagation velocities and an abrupt, nearly discontinuous change in thermodynamic fluid properties [7]. A strongly idealised static pressure profile of a propagating shock wave is shown in Figure 3.6. It is characterised by a steep increase in pressure with the finite amplitude  $\Delta p$ , and a constant pressure interval  $\Delta t$ , which is followed by expansion wave induced pressure reduction. In previous chapters it was shown that SFI, in both premixed and two-phase combustion systems, is responsible for an increase in the flame energy release and generation of secondary pressure waves as implication thereof. Under certain conditions a feedback loop between the

flame and the shock induced pressure field may be established leading to a further, substantial increase in pressure. Detailed understanding of the underlying feedback mechanism enables controlled feedback and allows the exploitation of its thermodynamic pressure-gain potential. To the authors knowledge there exist no PGC concepts that exploit this feature of shock-flame interaction. The concept introduced in this work is based on the interaction of propagating shock waves with a fully developed flame. If the thermal energy of the shock disturbed flame front is released within the high pressure region behind the shock and is higher than the energy dissipated from the flow, the Rayleigh criterion will be satisfied. This leads to an increase in the pressure amplitude according to inequality (3.4); as schematically indicated in Figure 3.6. The essential condition for this to occur is that the constant high pressure time interval  $\Delta t$  behind the shock is sufficiently long to accommodate for the time dependent increase in flame heat release rate. Finally, a time-averaged pressure rise can be achieved by sequentially repeating at a certain frequency the phenomena described above and depicted in Figure 3.6.

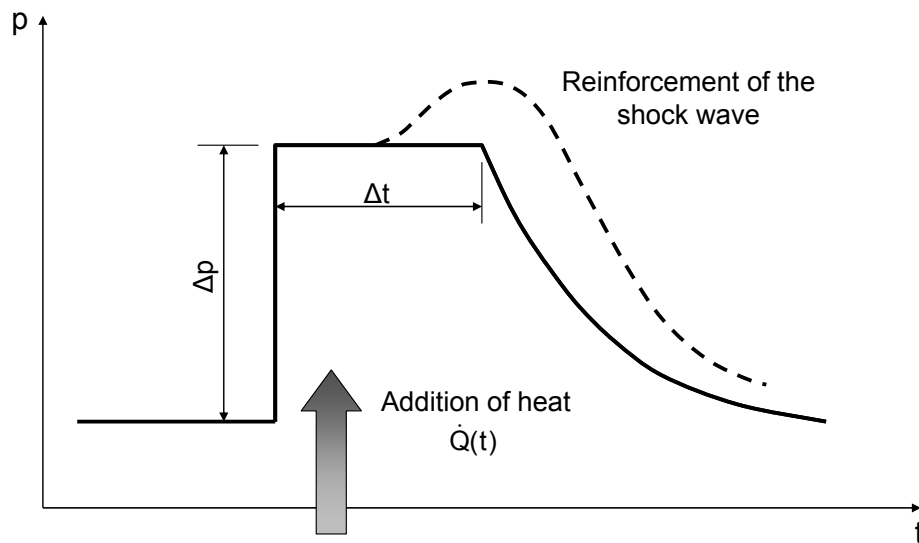


**Figure 3.6:** Schematic diagram of the pressure profile behind a shock wave and further increase in pressure following heat addition

Consequently, the PGC concept suggested and studied in this work is based on a controlled feedback loop between finite amplitude pressure waves and unsteady heat release. The feedback mechanism is reset with every successive shock wave hitting the flame. Use of shock waves eliminates the dependence of the operating frequency on the acoustics of the combustion system. Nevertheless, geometrical boundary conditions still play an important role. Shock waves reflect at walls and obstacles, which can cause multiple shock-flame interactions and affect the time-averaged pressure-gain performance. The theoretical concept

presented above possesses three degrees of freedom, which can be varied independently of each other. They are: the strength of the shock wave, expressed by the pressure amplitude  $\Delta p$  or the shock propagation velocity; the “length” of the shock wave  $\Delta t$ ; and the frequency at which shock-flame interaction is repeated. These independent control variables increase the flexibility of the concept and make it theoretically adaptable to various fuels, operational conditions, and system geometries.

The envisaged application of this concept to gas turbines aims at a steady inflow, unsteady outflow combustor that generates a time averaged rise in total pressure from inlet to outlet using shock-flame interaction. Theoretical considerations regarding mechanical realisation and integration of a potential shock-flame interaction combustor into a gas turbine cycle are presented and discussed in Chapter 6.2.

Despite significant achievements in theoretical and experimental modelling of shock-flame interaction in the last decades, there are still many uncertainties about this highly complex process [84]. A detailed understanding of shock-flame interaction physics, its pressure-rise potential, as well as the characteristic times, is required to enable further concept development. The main objective of this work is therefore, to provide a contribution to the understanding of shock-flame interactions, as well as to highlight the theoretical potential of the PGC concept based on shock-flame interaction.

## 4 Experimental Investigation of Shock Wave-Flame Interaction

For the experimental part of this work it was decided to conduct a series of shock-flame interaction experiments using a premixed flame. These studies should provide detailed information on pressure evolution and dynamic behaviour of the interaction process. Further, the experimental results will be used for verification and comparison with the analytical shock-flame interaction model developed in the course of this work, see Chapter 5.

### 4.1 The Experimental Facility

A shock tube is an ideal experimental tool for studying transient, high-temperature and high-pressure, gas-phase phenomena such as shock-flame interactions [98], [140], [153], [155]. It allows the creation of well-defined and uniform thermodynamic states in a controlled and highly-repeatable manner. Shock tubes are typically applied for super- and hypersonic flow studies, chemical kinetics investigations, studies on liquid-spray breakup and vaporisation, as well as combustion studies in both gaseous and heterogeneous mixtures [151].

A stainless steel, double-diaphragm shock tube located at the Shock Tube Laboratory of the German Aerospace Centre (DLR) Stuttgart was used for the experimental studies. In Figure 4.1 the schematics of the shock tube test facility are shown. Driver and driven section of the shock tube have a length of 2.015 m and 4.885 m, respectively. The internal tube diameter is 46 mm. The last downstream part of the driven section is equipped with eight piezoelectric pressure transducers mounted flush to the internal surface of the shock tube that can be used for the measurement of the incident shock velocity. For the experiments a special test section was designed, manufactured and mounted on the existing shock tube facility.

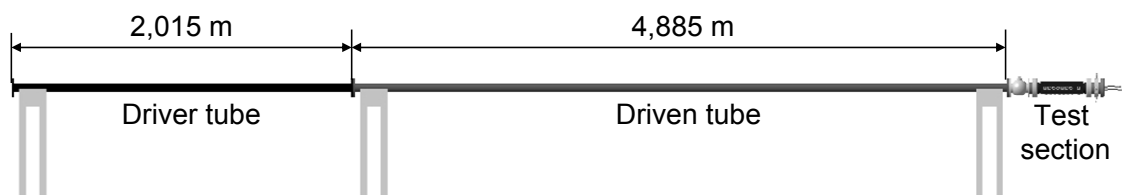
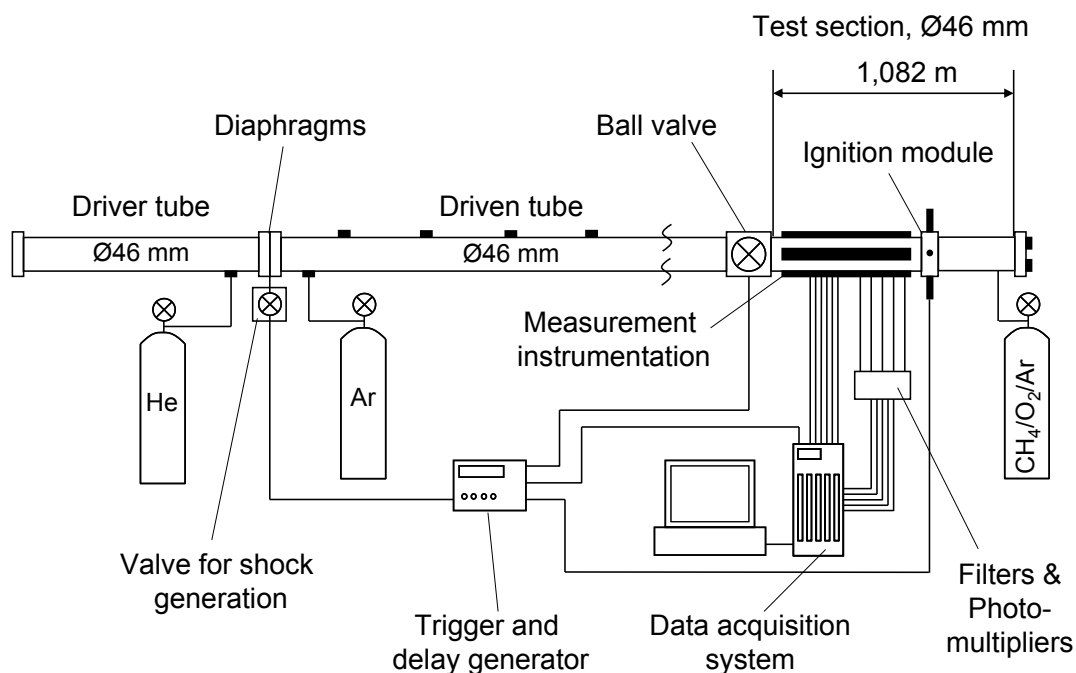


Figure 4.1: Total dimensions of the shock tube test facility

The schematic of the fully assembled experimental shock tube facility is presented in Figure 4.2. In all experiments helium (He) and argon (Ar) were used as driving and driven gas, respectively. The combustible mixture used was a nearly stoichiometric ( $\Phi = 0.989$ ) mixture of methane ( $\text{CH}_4$ ), oxygen ( $\text{O}_2$ ) and argon. In this mixture air nitrogen was proportionally substituted by argon in order to adjust the mixture impedance to that of the driven gas as closely as possible, hence reducing the shock refraction at the interface between the two gases. The specific heat of argon is lower than nitrogen, which results in higher reactivity, i.e. higher flame temperatures and burning velocities for argon mixtures [128]. A ball valve mounted between the driven tube and the test section was used to separate the driven gas from the combustible mixture at the beginning of each experiment.



**Figure 4.2:** Schematics of the shock tube test facility and instrumentation

The detailed design of the purpose-built test section including the ball valve is illustrated in Figure 4.3. The test section has a rectangular external shape and an inner diameter of 46 mm. It was designed to provide a source of ignition and to enable a detailed measurement of the shock-flame interaction process. The main component of the test section is the measurement section – a tube eroded from a block of stainless steel to provide high-precision surface. It is equipped with a total number of 32 axially and circumferentially distributed ports, which can accommodate different types of measurement instrumentation with a maximum diameter of 10 mm. The ignition module can be installed either in front of the measurement section or behind it. It includes four circumferentially distributed and simultaneously firing *BERU ZSE 012* pencil type ignition coils. A *YUASA 12 V, 38 Ah* battery was

used to power the ignition module. The test section is closed by the end flange, which also provides three ports for measurement instrumentation. The physical variables measured in the experiments were – static pressure, total pressure as well as flame chemiluminescence emissions. Detailed description of the measurement instrumentation is given in the next chapter.

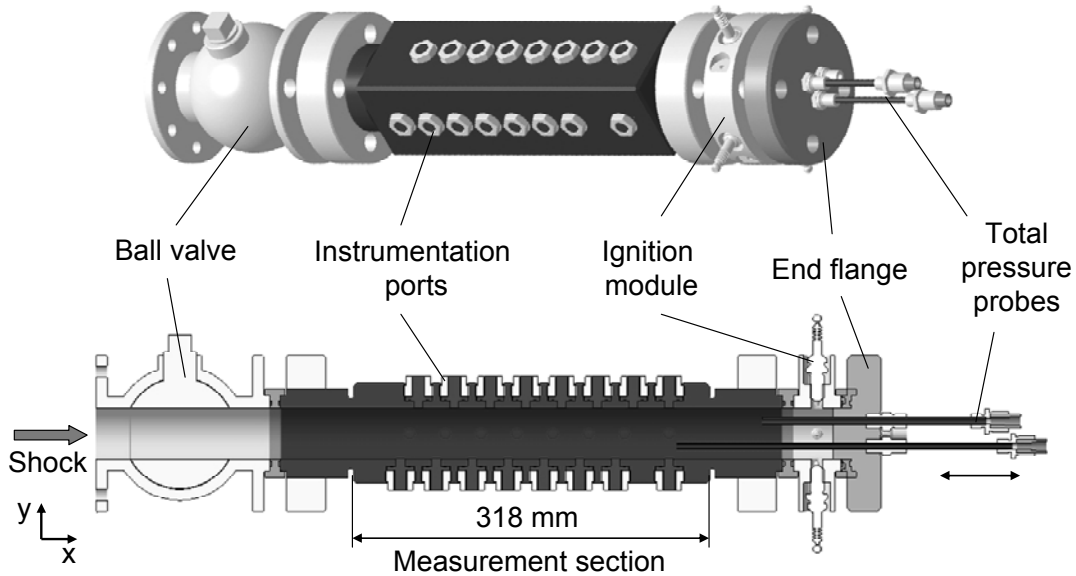


**Figure 4.3:** Detailed design of the test section

With regard to Figure 4.3 it is also mentioned that, in the experiments, an additional tube section with a length of 300 mm was installed between the ignition module and the end flange. The additional tube length allowed the extension of the available measurement time. It is the time interval between the interaction of the incident shock wave with the flame front and the arrival of the end wall reflected shock.

The instants of ignition and shock generation must be selected very carefully in order to make the shock and the flame interact within the confined measurement section. A trigger and delay generator with four independently programmable channels was used to precisely define the sequence of events in the experiments.

Operation of the shock tube facility requires further auxiliary equipment. Before each run, prior to the filling in of the test gases, the shock tube facility was evacuated to pressures below  $10^{-5}$  bar. A *Pfeiffer DUO 004A* vacuum pump was used to pump down the driver section. The driven section and the test section were evacuated with the *Pfeiffer DUO 012A* vacuum pump and subsequently by the *Balzerts TPU-170* turbo molecular high vacuum pump.

### 4.1.1 Measurement Instrumentation

In Figure 4.4 the schematic of the “unfolded” test section is shown in order to illustrate the exact positioning of the measurement instrumentation. There is a row of seven ports on each side of the test section, which are successively axially displaced by 8 mm relative to each other. The ports within each row have a distance of 32 mm from each other. Four additional ports are provided in the so called “monitoring plane”. Pressure and optical instrumentation, ten of each, was installed on opposing sides of the tube, providing an axial resolution of 16 mm respectively. Hence, the total highly resolved axial distance for the shock-flame interaction to occur in, referred to as the effective measurement section, was 152 mm in length.

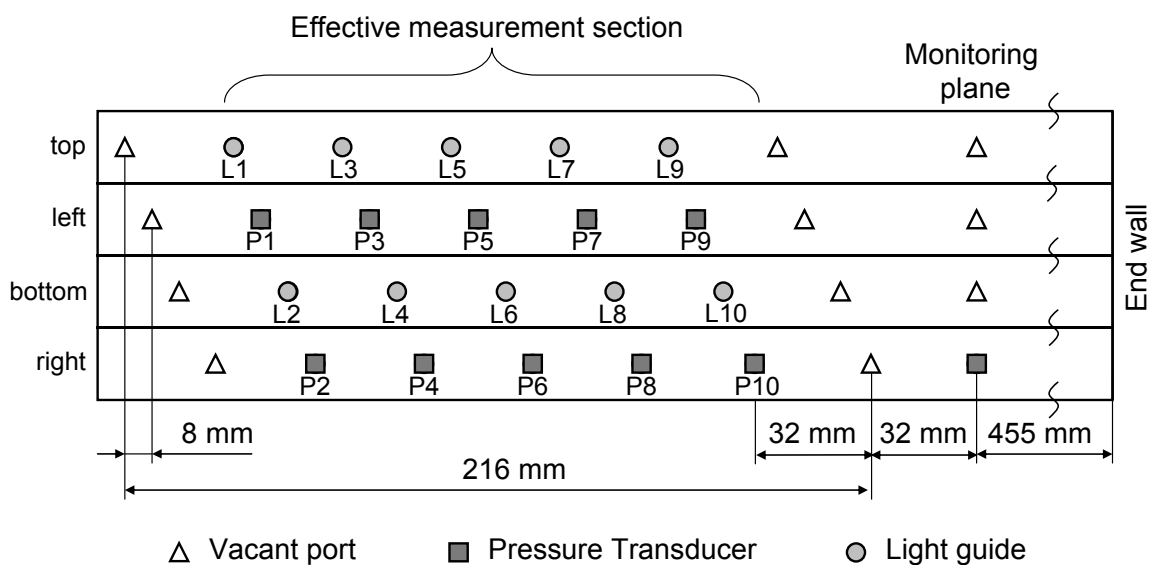


**Figure 4.4:** Schematics of the “unfolded” test section and positioning of measurement instrumentation

Transient static pressure traces were monitored using dynamic piezoelectric *OMEGA DPX101-1K* pressure transducers with a total pressure range 0-70 bar, a resonant frequency of 500 kHz, and a high frequency range of 170 kHz. The measurement uncertainty of these pressure transducers is given by the manufacturer at  $0.965 \cdot 10^{-3}$  bar. Ten pressure transducers of this type were mounted in the ports of the test section (see Figure 4.4) with the diaphragm flush to the internal surface of the test section. An additional absolute pressure transducer was installed in the monitoring plane to control the test section filling process.

Further, two piezoelectric *PCB 113A24* pressure transducers were used for measuring of the total pressure in flows with flow direction towards the end flange, i.e. in the direction of the incident shock wave. Therefore, the transducers were fitted into stainless steel tubes with the diaphragm flush with the end of the tubes and at  $90^\circ$  to the shock tube axis. The diaphragms of the transducers were shielded against undue heat transfer through a thin layer of rubber



silicone. The instrumented tubes were installed in the ports of the end flange (see Figure 4.3), so that they could be moved axially, allowing to take measurements in any plane of the test section.

Chemiluminescence is the electromagnetic radiation emitted during the de-excitation process of electronically excited species, such as  $\text{CH}^*$ ,  $\text{OH}^*$ ,  $\text{C}_2^*$ ,  $\text{CO}_2^*$ , that are formed via chemical reactions in the combustion zone [111]. Imaging of chemiluminescence is widely applied for flame position, shape, and structure detection, as well as a measure of flame heat release fluctuations [16], [52], [86], [94], [97], [150]. In the present study,  $\text{CH}^*$  radiation at wavelength  $\lambda = 431 \text{ nm}$  was employed as a qualitative measure of the heat released by the flame. The  $\text{CH}^*$  radicals emit light in a narrow spectral band, which is superimposed by the broadband emissions from  $\text{CO}_2^*$  [92], as shown in Figure 4.5. For an exact measurement the broadband  $\text{CO}_2^*$  emissions must be subtracted from the signal. However, for a qualitative and purely comparative heat release measurements performed in this study, it was deemed to be appropriate to use the uncorrected signal. *CeramOptec UV 600/660* fiber-optic light guides with a numerical aperture  $0.22 \pm 0.02$  and a stainless steel ferrule were mounted in the ports of the test section. They conducted the emission signal to the  $\lambda = 431 \pm 1 \text{ nm}$  interference filters. *Hamamatsu R928* photomultipliers operating at the voltage of 400 V were applied to amplify the filtered signal.

All pressure and optical experimental data was simultaneously recorded at the frequency of 1 MHz and the resolution of 16 Bit on a *LDS Nicolet* multi-channel transient recorder.

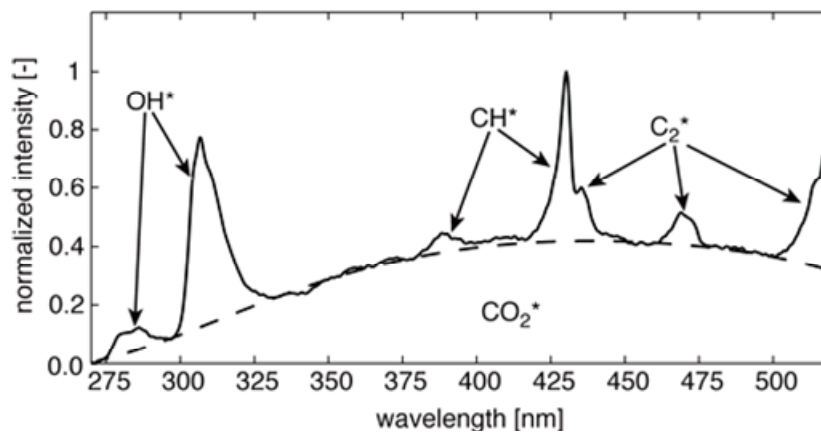


**Figure 4.5:** Chemiluminescence spectrum of a stoichiometric premixed  $\text{CH}_4$ -air flame [92]

#### 4.1.2 Experimental Configuration and Procedure

In order to study both classes of shock-flame interactions, the s/f and f/s, two different experimental configurations were used. The first configuration is the one shown in Figure 4.2 and will be referred to as “conf1” or “rear ignition configuration”. In this configuration the igni-

tion module is installed behind the measurement section. Following ignition a flame front propagates through the combustible mixture towards the incident shock. The interaction of this flame front and the incident shock wave, which is to occur within the instrumented section, is s/f. In this configuration, the interaction of the flame with incident shocks of different strength between  $M_i = 1.2$  and  $1.55$  was studied.

In the second experimental configuration the ignition module was mounted immediately behind the ball valve, i.e. in front of the measurement section. It will be referred to as “conf2” or “front ignition configuration”. Upon ignition, a flame front propagates towards the end flange, in the direction of the incident shock wave. The incident shock comes from the side of the hot burned gases and crosses the flame. This type of interaction is therefore f/s. In this configuration only shock waves with the mach number of  $M_i = 1.1$  were examined.

In all experiments aluminium foil diaphragms with thicknesses of 0.2-0.5 mm were used. Laboratory room temperature was between 21 and 24 °C. The initial filling pressure in the driven tube and the test section was kept at the same value, which varied between 2.15 and 2.25 bar. Upon filling of the shock tube facility to the desired pressures, the gases were allowed to rest for a short while in order for the temperatures to return back to the room temperature level. The experimental sequence was started by opening the ball valve. Exactly two seconds thereafter the diaphragms were burst and the shock wave was generated. The two seconds time interval between the events was chosen long enough to ensure full opening of the valve, but short enough to prevent excessive mixing of the driven and the test gases. The ignition and data acquisition were started simultaneously by the propagating incident shock wave, when it swept across the first pressure transducer located in the wall of the driven tube.

## 4.2 Preliminary Studies

Upon assembly and commissioning of the experimental facility a series of preliminary experiments was conducted. It included testing of the measurement instrumentation, shock only and combustion only experiments. For the subsequent analysis the direction towards the end flange, i.e. that of the incident shock wave, is defined as the positive x-direction.

### 4.2.1 Shock Experiments without Combustion

In the course of the preliminary studies an undue vibration was detected in the pressure records of the ten wall-mounted pressure transducers P1-P10. The pressure record of one representative pressure transducer, showing the incident and the reflected shock waves, is presented in Figure 4.6. The high frequency vibration occurs every time a shock wave

sweeps across the diaphragm of the transducer, and is damped out after a short period of time. A Fast Fourier Transform (FFT) of the transducer data exhibited a high intensity signal that occurred in the spectrum between 62 kHz and 150 kHz across different transducers. It was assumed that this systematic vibration was a result of the transducer diaphragm “ringing” when excited by a shock wave transition, rather than a physical phenomenon. This assumption was confirmed in an additional transducer test performed on a different shock tube. In this test, the response to shock excitation of two sample transducers was compared to equivalent transducers by other manufacturers under equal experimental conditions. Among all sensors tested, the *OMEGA* transducers were the only that exhibited that spurious, high-amplitude and high-frequency vibration response when being struck by a shock wave. In order to remove the transducer inherent vibration from the pressure record an order seven low pass digital elliptic filter with a cut-off frequency of 60 kHz was applied to the transducer data. Additionally, the original data was conditioned using a digital moving-average smoothing algorithm with an increment of 11 samples. The raw data as well as the conditioned signal are shown for comparison in Figure 4.6. Both signal conditioning methods eliminate the undue, transducer inherent vibration from the pressure record without essentially changing the residual, low frequency signal. Hence, the moving-average smoothing method is applied to all pressure data presented in the course of this work.

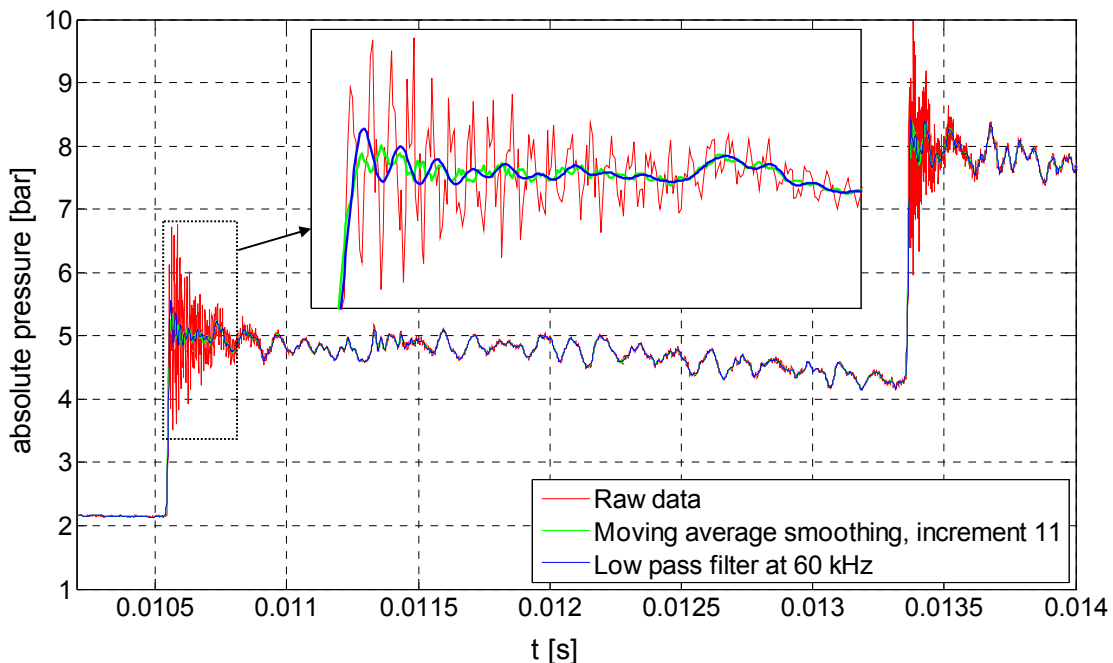


**Figure 4.6:** Raw and conditioned pressure transducer data

An exemplary full pressure record, including all static pressure sensors P1-P10 as well as both total pressure probes Pt1 and Pt2, is shown in Figure 4.7. Initial conditions in the test section were as follows: quiescent gas,  $\kappa_i = 1.54$ ,  $C_{p_i} = 654.75$  J/kgK,  $p_i = 2.25$  bar,

$T_i = 295$  K. At the time of around  $t \approx 0.0103$  s the incident shock wave arrives at the instrumented section and traverses it in the direction towards the end flange. Its axial movement is visualised by the sequential response of the pressure transducers P1-P10. In the experiment presented in Figure 4.7, the total pressure probes Pt1 and Pt2 were located between the effective measurement section and the end flange, at 430 mm and 230 mm from the end wall respectively. After a short overshoot these pressure sensors show a pressure level above that of the static transducers. This difference corresponds to the dynamic pressure head in the flow behind the incident shock. The pressure behind the incident shock remains at a constant level for some time and then begins to decline at  $t \approx 0.012$  s. This indicates the arrival of the expansion wave that is generated in the driver gas at the instant of diaphragm burst. It propagates through the driver tube, reflects from its end wall, and finally arrives in the test section causing the pressure to decrease gradually.

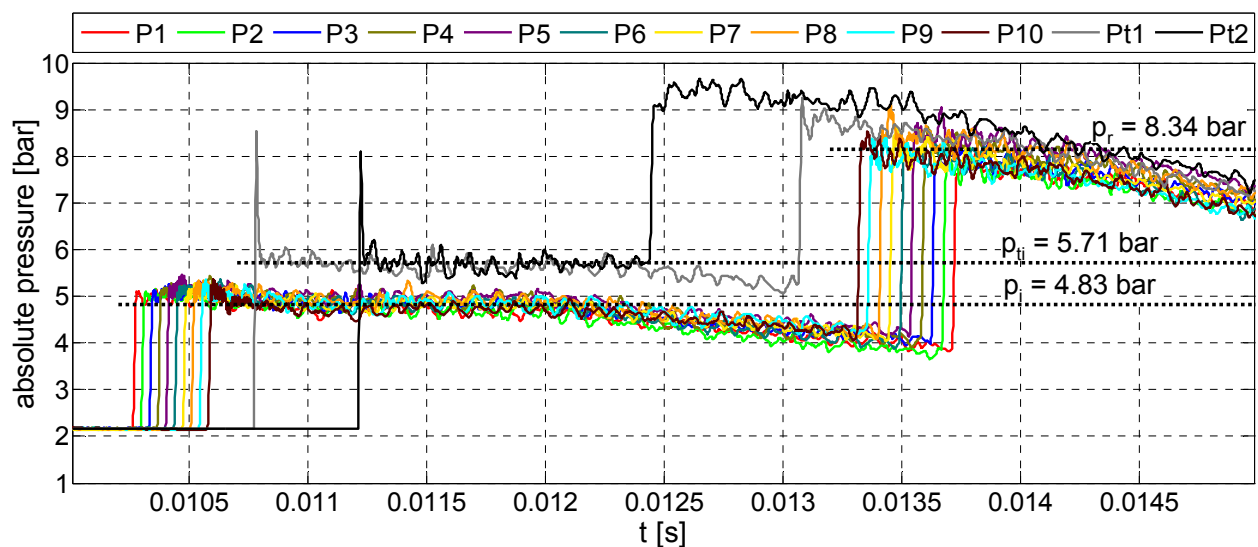


**Figure 4.7:** Full pressure record of the incident and the reflected shock waves: conf1,  
 $M_i = 1.41$

The incident shock wave arrives at the end wall of the test section and reflects from it. The reflected shock wave is formed propagating in the opposite direction into the pre-compressed gas. Hence, Pt2 ( $t \approx 0.0124$  s) is the first, and P1 ( $t \approx 0.0137$  s) is the last sensor to detect it. It is noted the total pressure probes display the same pressure as the static ones behind the reflected wave. This can have two reasons. Firstly, the flow velocity is directed away from the end wall and the total pressure probes are not capable of measuring the dynamic pressure. Secondly, the velocity behind the reflected shock wave is exactly zero under ideal, one-dimensional flow conditions [114].

Shock velocities can be calculated from the recorded pressure profiles in conjunction with the known spacing between the transducers. In the example discussed above the propagation

velocity of the incident shock was  $v_i = 455.3$  m/s, and that of the reflected shock was  $v_r = 356.3$  m/s. Using the known incident gas properties the corresponding incident shock Mach-number was derived to be  $M_i = 1.41$ . Further, pressures behind the incident and the reflected shock waves were analytically determined from the measured shock velocities and known incident gas properties. Therefore, standard shock equations were applied [114], [164]. For the sake of comparison the analytical values are highlighted by dotted lines in Figure 4.7. The compliance between analytical values and experimental data was found to be satisfactory.

A series of shock experiments with incident shock Mach-numbers ranging between  $M_i = 1.1 - 1.6$  was conducted for both experimental facility configurations conf1 and conf2. All recorded pressure profiles were equivalent to that presented in Figure 4.7.

#### 4.2.2 Combustion Experiments without Shock Wave Generation

Investigation of the ignition and flame propagation processes was carried out during the preliminary experimental phase. In these studies no shocks were generated. Thus, the shock tube diaphragm was replaced by a firm, 2 mm thick aluminium plate. The driven and the test section were filled with the driver gas and the test mixture respectively, to the equal initial pressure of 2.15-2.25 bar. In both configurations, ignition was initiated two seconds after the opening of the ball valve.

In Figure 4.8 representative records of static pressure and chemiluminescence emissions are shown. All signals were recorded simultaneously. The time  $t = 0$  corresponds to the instant of ignition. In the upper diagram of Figure 4.8 the static pressure records (solid lines) at two locations within the measurement section are presented. Ignition occurred in the vicinity of the end wall of the test section. Heat of combustion leads to an expansion of the burned gases. This expansion is constrained by the closed end of the tube, which results in a temporal increase in pressure from initial level of 2.2 bar to a peak pressure of around 3.1 bar. After reaching a peak value the pressure expands into the driver tube. The static pressure transducers were not protected from combustion induced heat transfer during the experiments in conf1. The steep drop in pressure records of the both pressure transducers at  $t \approx 0.0105$  s and  $t \approx 0.0136$  s respectively is, therefore, not related to any physical phenomenon in the fluid. It is an effect of the temperature gradient error occurring in piezoelectric transducers as a result of rapid temperature changes in the working fluid [157].

In the lower diagram the emission profiles from the installed light guides are shown. The sequential rise in the signals of the light guides from L10 to L1 allows tracing of the flame movement through the tube. The direction of flame propagation is in the negative x-direction. The measured velocity of flame propagation varied between 69.9 m/s and 73.6 m/s for differ-

ent experimental runs. The magenta line represents the total intensity of chemiluminescence, which is a simple sum of the single emission profiles. In this context it is important to mention that only a quarter of the total effective measurement section volume is captured by the light guides. The emission signal does not return to zero when the flame front moves out of the instrumented area. This remaining chemiluminescence signal for times larger than 0.013 s is attributed to the  $\text{CO}_2^*$  radiation in the hot combustion products.

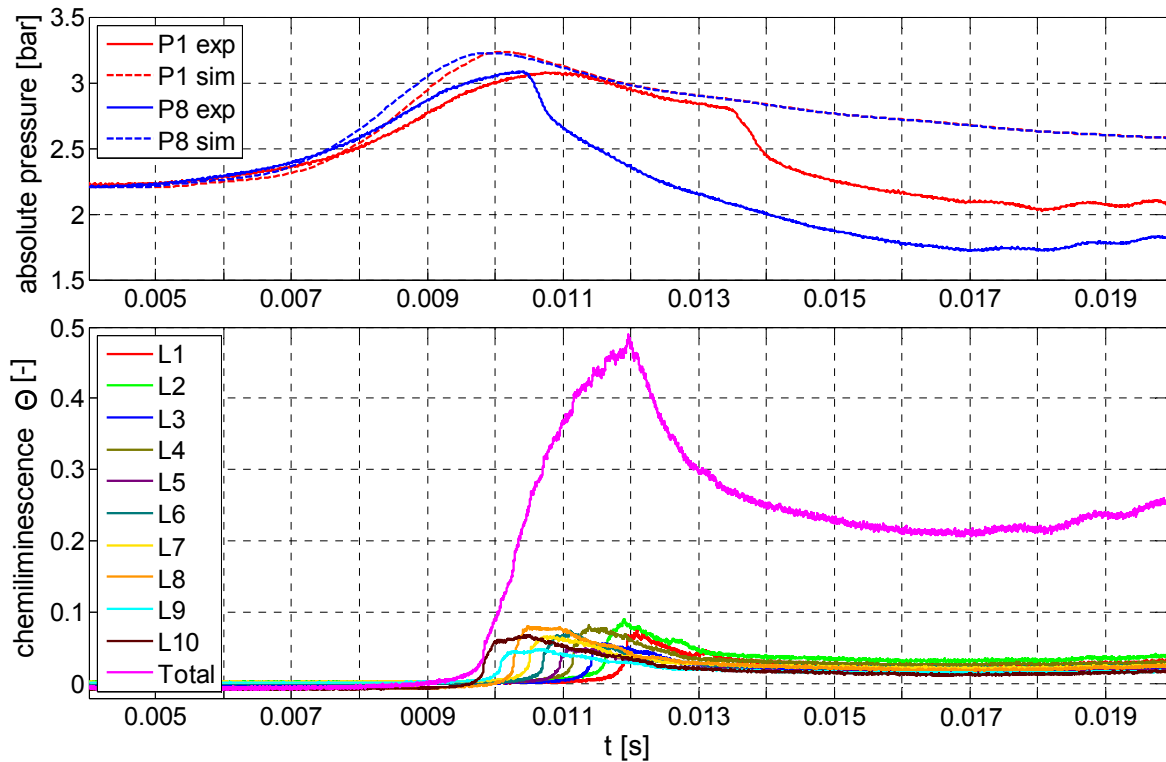


**Figure 4.8:** Static pressure and chemiluminescence emission profiles after ignition in conf1

The experimental facility did not provide visual access. However, information about the geometrical shape of the flame was of essential interest to the modelling of the shock-flame interaction process; see Chapter 5.1. In order to obtain such data, a basic numerical simulation of the ignition and flame propagation within the test section was performed using *ANSYS CFX*; see [13], [57]. *ANSYS CFX* is a CFD solver that provides a fully defined and highly resolved flow field solution based on URANS. A quasi two-dimensional numerical domain was used for combustion simulation; see Figure 4.9. Its length and height corresponded to the physical length and diameter of the shock tube facility, respectively. The spatial resolution in x and y directions was 0.5 mm for the test section part of the domain. The driver tube part of the domain had a much coarser resolution in order to reduce computational time. The thickness of the domain in z direction was one element. Rear and front walls of the domain, i.e. the surfaces in Figure 4.9 rectangular to the z-axis, were modelled as periodicities. All other domain boundaries were defined as solid walls with friction. The time step of the un-

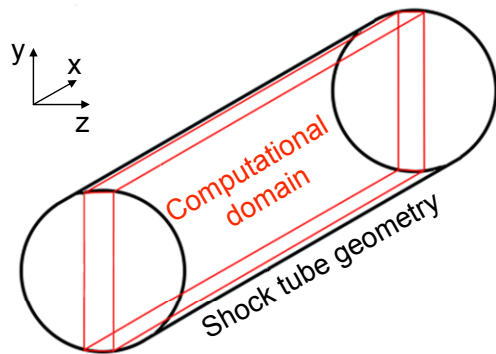


**Figure 4.9:** Schematics of the numerical domain for combustion simulation

steady calculation was  $5 \cdot 10^{-5}$  s. k-epsilon model was applied for turbulence. The CFX implemented Burning Velocity and Spark Ignition Models were used for combustion and ignition computations respectively. Detailed chemistry was provided by the pre-defined combustible mixture Laminar Flamelet Libraries. Axial locations of the ignition spot and the pressure monitor points were in accordance to the physical positions of the respective instrumentation in the test section of the experimental facil-

ity. Numerical combustion simulation was performed for both test facility configurations.

In Figure 4.10 numerically obtained flame propagation is shown for conf1. After ignition two flame fronts are formed. The left flame front propagates towards the measurement section and the driver tube, the right flame front propagates towards the end wall of the test section.

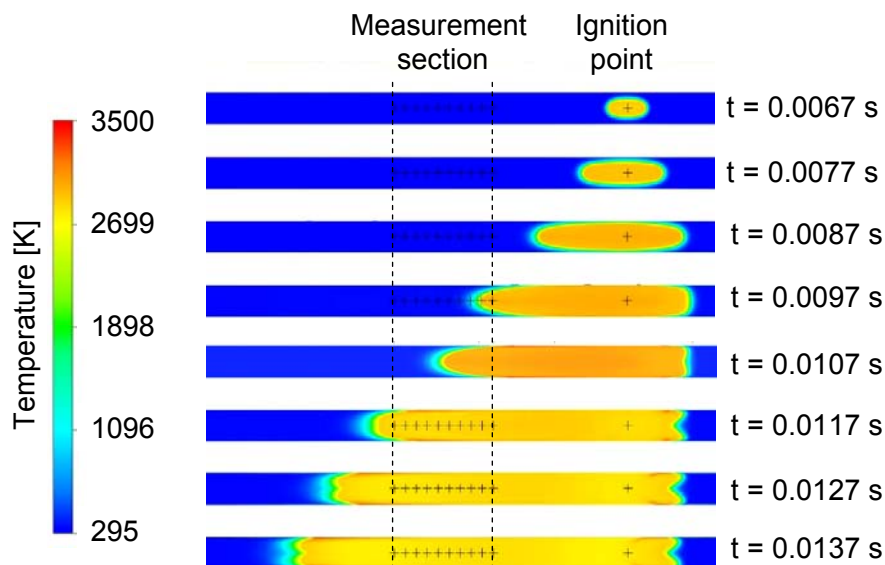


**Figure 4.10:** Numerical simulation of flame propagation after ignition in conf1

As has been mentioned previously, gas expansion causes a pressure rise in the region near the end wall. This elevated pressure then forms a pressure wave that propagates to the left towards the driver tube inducing a transient flow in the gas in the same direction. This flow has an effect on both flame fronts. Thus, the left flame is accelerated, while the right flame front is decelerated and transforms into the typical “tulip flame” [40] much quicker. The left flame front reaches the instrumented section at the time around 0.0095 s, which is in good

agreement with the experimental data; see Figure 4.8. The absolute flame velocity within the measurement section was 72-77 m/s. Pressure histories from the numerical combustion simulation are plotted as dotted lines into the upper diagram of Figure 4.8 for comparison with experimental data. Both, the flame velocity and the pressure were higher than the experimental values. Maximum deviation lay within ten percent limit.

Equivalent analysis was performed for conf2. In the upper diagram of Figure 4.11 static pressure records (solid lines) at two locations P1 and P8 in the test section are presented. Before experiments of conf2 the diaphragms of all pressure sensors were protected from heat transfer by a thin layer of rubber silicone. Hence, there is no evidence of spurious high temperature effects in the pressure profiles. As a result of gas expansion and its stagnation at the closed end the pressure in the test suction elevates from initially 2.5 bar to the peak value of 3.4 bar. However, the pressure does not rise monotonically. After an initial rise, there is a region of constant pressure between  $t \approx 0.011$  s and  $t \approx 0.015$  s followed by an additional increase. A similar behaviour is observed in the chemiluminescence emission records in the lower diagram of Figure 4.11. Therein, after the first three light sensors the flame front seems to stand still at  $t \approx 0.011$  s and continues to propagate at  $t \approx 0.014$  s. Such behaviour is best explained using the results of the according numerical simulation given in Figure 4.12.

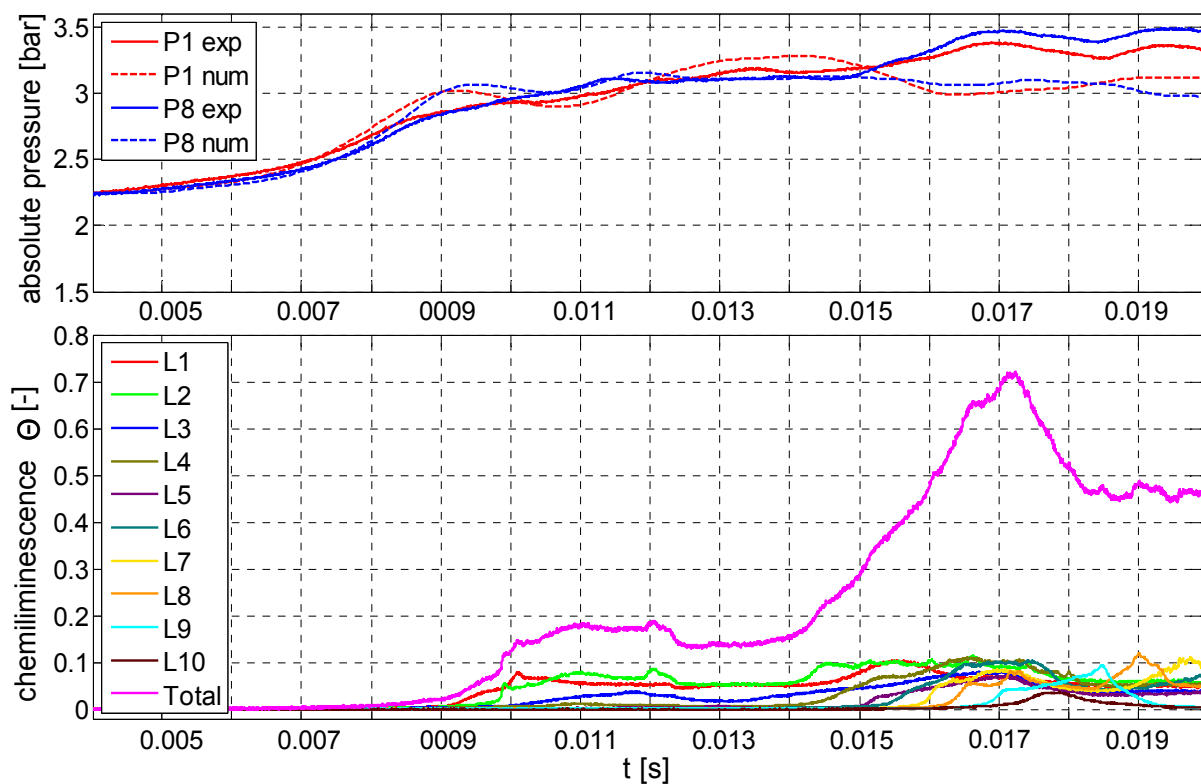


**Figure 4.11:** Static pressure and chemiluminescence emission profiles after ignition in conf2



In conf2 the ignition occurs upstream of the measurement section. After ignition, again, two flame fronts are formed, with the right flame propagating towards the closed end of the test section. Growing pressure between this flame front and the closed end produces a pressure wave that propagates to the left entraining a flow in the gas in the same direction. This fluid velocity decelerates the flame front at  $t \approx 0.01$  s and even reverses its propagation for a short period of time. Flame deceleration promotes the inversion of the flame shape and formation of the “tulip” flame, which begins to evolve at  $t \approx 0.011$  s. This effect is accompanied by a temporal decrease in flame surface area and hence, a reduction in the rate of pressure rise [40] (see Figure 4.11). In the following the flame burning velocity increases due to enhanced turbulence, which is illustrated by the broadening of the flame front. Hence, the flame is accelerated and restarts propagating in positive x-direction at  $t \approx 0.014$  s, as can be seen in both Figure 4.11 and Figure 4.12.

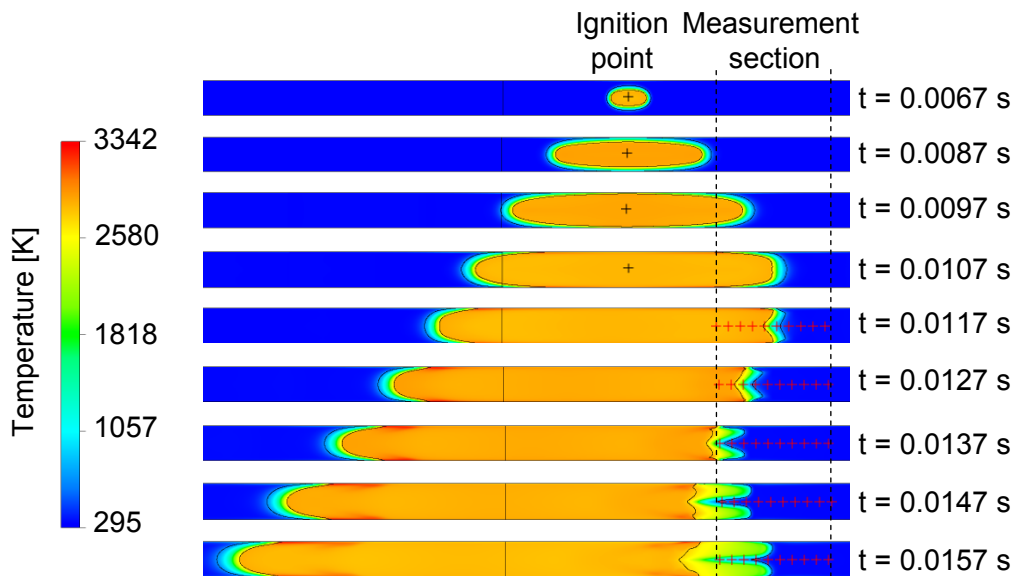


**Figure 4.12:** Numerical simulation of flame propagation after ignition in conf2

Pressure profiles obtained in the numerical simulation are compared with the experimental pressure records in the upper diagram of Figure 4.11 (dotted lines). Absolute flame propagation velocities were around 26 m/s for the early phase, and around 34 m/s for the later propagation phase. Deviation between numerical and experimental values was less than 10 % for flame velocities and below 15 % for pressures. Agreement between numerical and experimental results was deemed to be acceptable for both configurations.

Preliminary shock and combustion experiments discussed above provided crucial information for the following shock-flame interaction studies, particularly with regard to the timing of different events. Furthermore, detailed information on flow conditions and flame front geometry

obtained from numerical combustion simulation is essential for the analytical modelling of the shock-flame interaction, which is described in Chapter 5.1.

### 4.3 Shock-Flame Interaction – Experimental Results

#### 4.3.1 Pressure and Chemiluminescence Profiles s/f-Interaction

Shock wave and flame interaction experiments were conducted for three different incident shock Mach numbers:  $M_i \approx 1.25$ ,  $M_i \approx 1.4$ ,  $M_i \approx 1.55$  in the experimental set up conf1. The shock Mach number is defined in terms of the gas state into which the shock propagates [164]. In the experiments,  $M_i$  was determined from the absolute incident shock propagation velocity measured immediately before the interaction event, i.e. in the unburned mixture for conf1, or in the hot combustion products for conf2. Local gas properties required for Mach number calculation were extracted from the numerical combustion simulations, which are discussed in the previous chapter. In the analysis of the experimental data the recorded  $\text{CH}^*$  chemiluminescence is used as a qualitative measure of heat release of combustion.

In Figure 4.13 representative pressure and chemiluminescence profiles are shown for a s/f interaction experiment with an incident shock Mach number  $M_i = 1.38$ . Therein, each diagram contains pressure data recorded at different axial locations P1-P9 in the measurement section and chemiluminescence histories at the same locations. In the test rig the light guides had an axial displacement of 8 mm relative to the pressure sensors. In order to obtain light emissions at the locations of the pressure sensors, the recorded chemiluminescence data was interpolated by sequentially averaging the profiles of a pair of adjacent light guides.

In the presented experiment the initial undisturbed flame, denoted by  $f_i$ , enters the measurement section at the time  $t \approx 0.0092$  s at the rear end of the measurement section, i.e. light guide L9 is the first to detect it. The undisturbed flame has a chemiluminescence intensity of  $\Theta_0 \approx 0.065$ , and propagates in the negative x-direction at a velocity of 73 m/s. Conversely, the incident shock wave, denominated  $s_i$ , enters the front end of the measurement section and passes P1 at the time  $t \approx 0.0103$  s. Initially, it propagates through unburned combustible mixture at a velocity of 400 m/s in the positive x-direction, and has a pressure amplitude of 3.3 bar.

The interaction between the incident shock wave and the undisturbed flame occurs in the vicinity of pressure sensor P4. This interaction is s/f in nature. As a result of this, a reflected expansion wave and a transmitted shock wave are established. The propagation of the reflected expansion wave can be traced in space across the sensors P3-P1. It propagates at the sonic velocity of the shocked incident gas in the opposite direction to that of the incident

shock. A portion of the incident shock traverses the flame and continues to propagate in the hot combustion products in the same direction. This transmitted wave  $s_{tr}$  is shown in P5-P9. It is weaker in terms of pressure amplitude, which is around 1.4 bar, and moves faster than the incident shock. Its absolute propagation velocity is around 1100 m/s, which corresponds to  $M_{tr} = 1.2$  relative to the burned gas into which it propagates.

The effect of shock transition on the heat release of the flame is indicated by the chemiluminescence emission profiles. Interaction of the incident shock with the initial flame causes an increase in the heat release of the flame by 3-6 times relative to the undisturbed flame, which follows immediately upon shock transition; see L4-L9. In Figure 4.10 it was shown that, at the instant of incident shock arrival ( $t \approx 0.0104$  s), the flame has a convex shape regarding the incident shock with a substantial extent along the tube axis. Therefore, the event of shock-flame interaction does not occur at a single axial plane, but rather has a spatial extent equal to the axial length of the flame. Hence, the heat release histories shown in L4-L9 can be understood as a continued shock-flame interaction process when the incident shock traverses the spheroidal flame front. A visual presentation of such processes can be found in [98]. After reaching a peak value the chemiluminescence signal falls down to zero. This is not an indication of flame extinction. Fresh gas flow behind the incident shock wave entrains the flame front and conveys it out of the instrumented area.

The zone around the interaction of the incident shock and the crest of the convex flame front is characterised by relatively strong and highly unsteady pressure oscillations; see P3-P6. This behaviour can be attributed to the formation of an irregular shock refraction, when the local angle between the incident shock and the flame front exceeds a certain critical value. Thereby, a complex and unsteady system of transmitted and reflected pressure waves is locally established leading to temporal occurrence of relatively high amplitude pressure peaks [56], [98].

An additional weak shock wave  $s_{rf}$  enters the rear end of the instrumented section (P9) at the time  $t \approx 0.0114$  s. This pressure wave originates from the interaction of the transmitted incident shock  $s_{tr}$  with the second flame front, which is located between the measurement section and the end wall of the test section; see Figure 4.10. Because of the f/s nature of this interaction both the reflected and transmitted waves are shocks. Thereby, the reflected shock wave propagates back towards the measurement section. It interacts with the first distorted flame front, again producing a reflected and transmitted waves, before arriving at the measurement section at  $t \approx 0.0114$  s. There, it propagates in negative x-direction at the absolute velocity of 248.5 m/s. In terms of the shocked unburned gas into which it propagates it has a strength of  $M_{rf} = 1.24$ . The appearance of this secondary shock wave alters the gas state after the initial interaction. Hence, it represents the limiting factor in terms of the available observation time.

Figure 4.14 shows pressure and chemiluminescence profiles of Figure 4.13 for an extended period of time. Besides the waves  $s_i$ ,  $s_{tr}$ , and  $s_{rf}$ , that have already been discussed, there is evidence of additional pressure waves. At the time  $t \approx 0.0123$  s shock wave  $s_r$  enters the

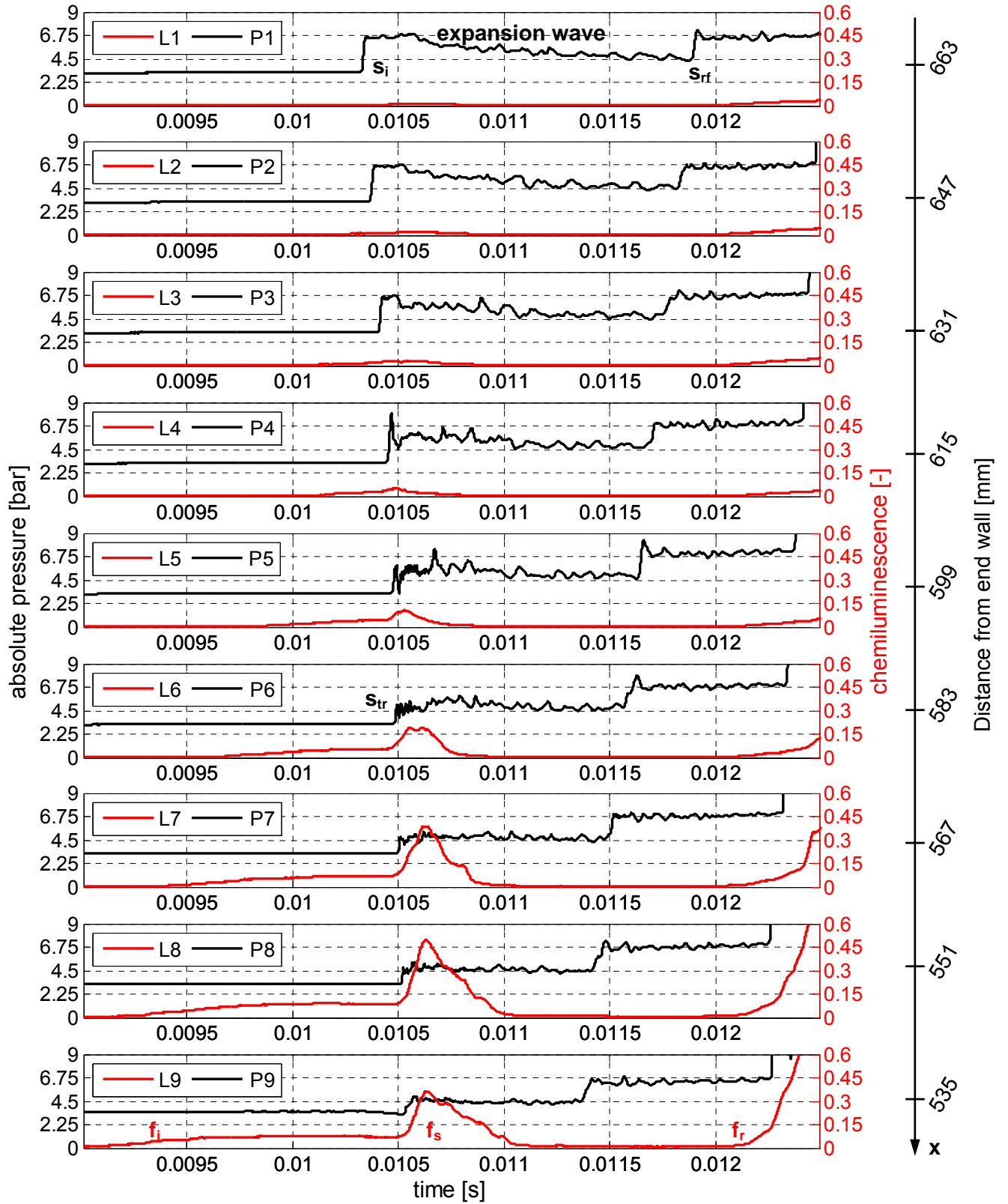
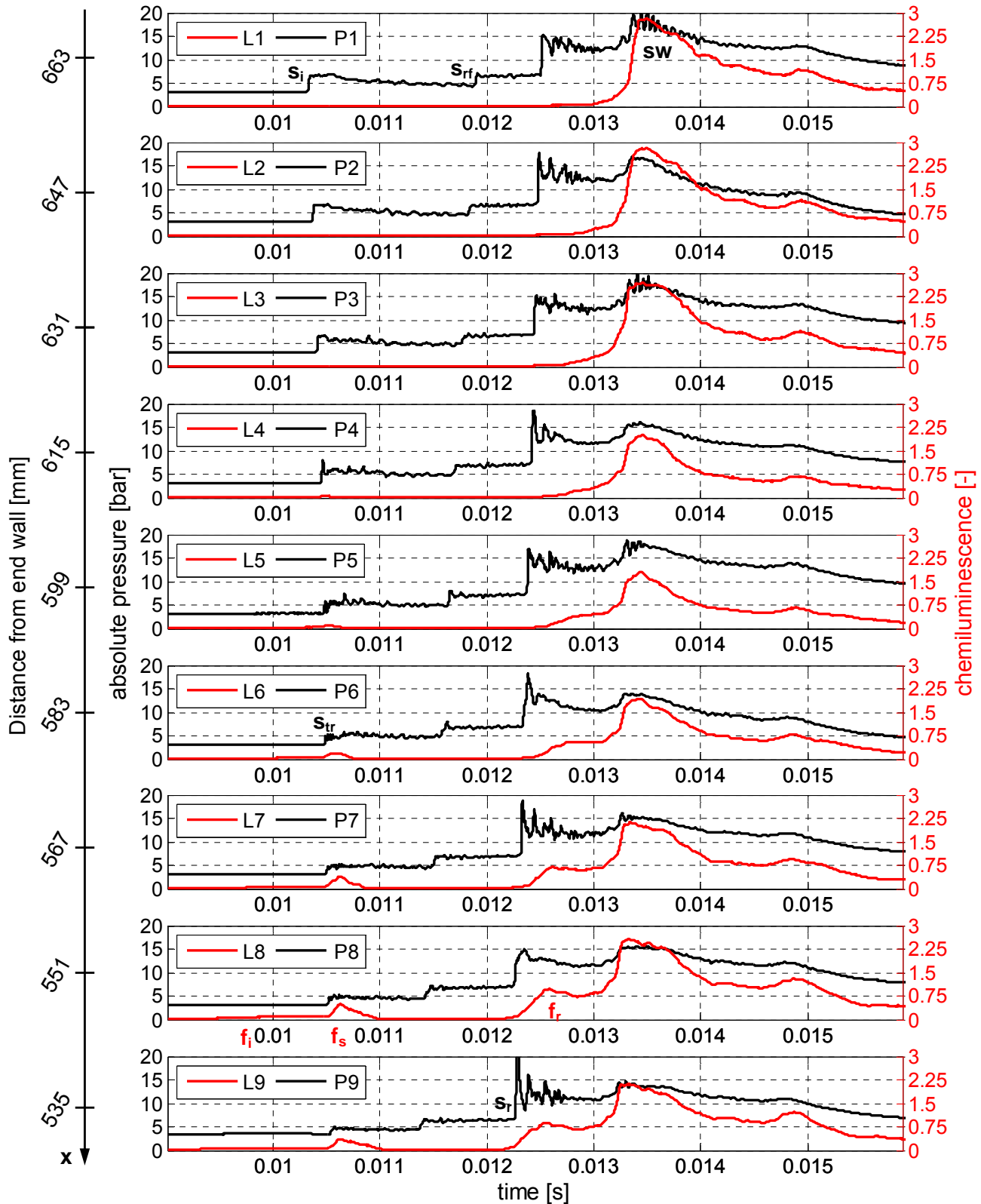


Figure 4.13: Pressure and chemiluminescence profiles, incident shock only,  $s/f$ ,  $M_i = 1.38$

instrumented section at P9. This shock wave represents the transmitted portion of the incident shock  $s_i$  that was reflected from the end wall of the test section. This shock wave trav-



**Figure 4.14:** Pressure and chemiluminescence profiles of the incident and the reflected shock waves,  $s/f$ ,  $M_i = 1.38$

ses both flame fronts before arriving at the measurement section. It propagates through the instrumented section in the negative  $x$ -direction at the average absolute velocity of 482.8 m/s, and has a pressure amplitude of 7-8 bar. In experiments without combustion and similar incident shock Mach numbers ( $M_i = 1.4$ ) corresponding values of 348 m/s and 4.2 bar were measured. From this comparison it follows that the reflected shock wave experiences a substantial amplification in the course of multiple interaction events. Interaction of the reflected shock wave  $s_r$  with the first flame front, that was distorted and shifted by the incident shock, is indicated by an increase in the heat release of the flame  $f_r$  in L9. This increase is stronger than that of the initial interaction by a factor 1.5-2.5. This increase initially occurs simultaneously with the passage of  $s_r$ . In the course of propagation the time lag between  $s_r$  and  $f_r$  grows (L7-L1) indicating that the shock wave propagates at a higher velocity than the flame. Intense gas-dynamic pressure perturbations are observed in the wake of the reflected shock  $s_r$  [82].

An additional phenomenon, denominated  $sw$ , is observed at the times between 0.013-0.014 s in Figure 4.14. It is a pressure wave that propagates in the negative  $x$ -direction at a velocity between 1000-1100 m/s in the absolute frame of reference. Interestingly, there is an increase in the heat release of the flame of a substantial magnitude that occurs simultaneously with the passage of this pressure wave. This coupling between pressure and heat release, i.e. a combustion front, remains stable for the entire length of the instrumented section. Furthermore, both pressure and heat release amplitudes of this phenomenon seem to grow in the course of its propagation. This suggests a positive feedback mechanism between the energy release at the combustion front and the pressure wave. Such behaviour agrees well with the characteristics of “strange waves” experimentally observed and reported by Thomas et. al. [155]. In their shock-flame interaction experiments they observed a sustained coupling between the reflected shock wave and the distorted, turbulent flame front to propagate at velocities of 800-900 m/s. They described this phenomenon as a form of propagating explosion where the local energy release at the flame drives a blast wave ahead of it. In a later numerical study on the same subject Oran and Gamezo demonstrated that the “strange wave” is a result of reactive shock bifurcation in the boundary layer of the test rig walls [118]. The pressure and chemiluminescence histories for  $s/f$  interaction experiments with  $M_i = 1.26$  and  $M_i = 1.55$  are given in the Appendix A; see Figure A.1 and Figure A.2. They are analogous to the case with  $M_i = 1.38$ , and will not be discussed in detail here.

### 4.3.2 Pressure and Chemiluminescence Profiles $f/s$ -Interaction

In conf2 only one Mach number range  $M_i \approx 1.1$  was studied. Pressure and chemiluminescence profiles of a representative  $f/s$ -interaction with incident shock wave Mach number

$M_i \approx 1.11$  are presented in Figure 4.15. Chemiluminescence intensity is used as a qualitative measure for the heat release of combustion.

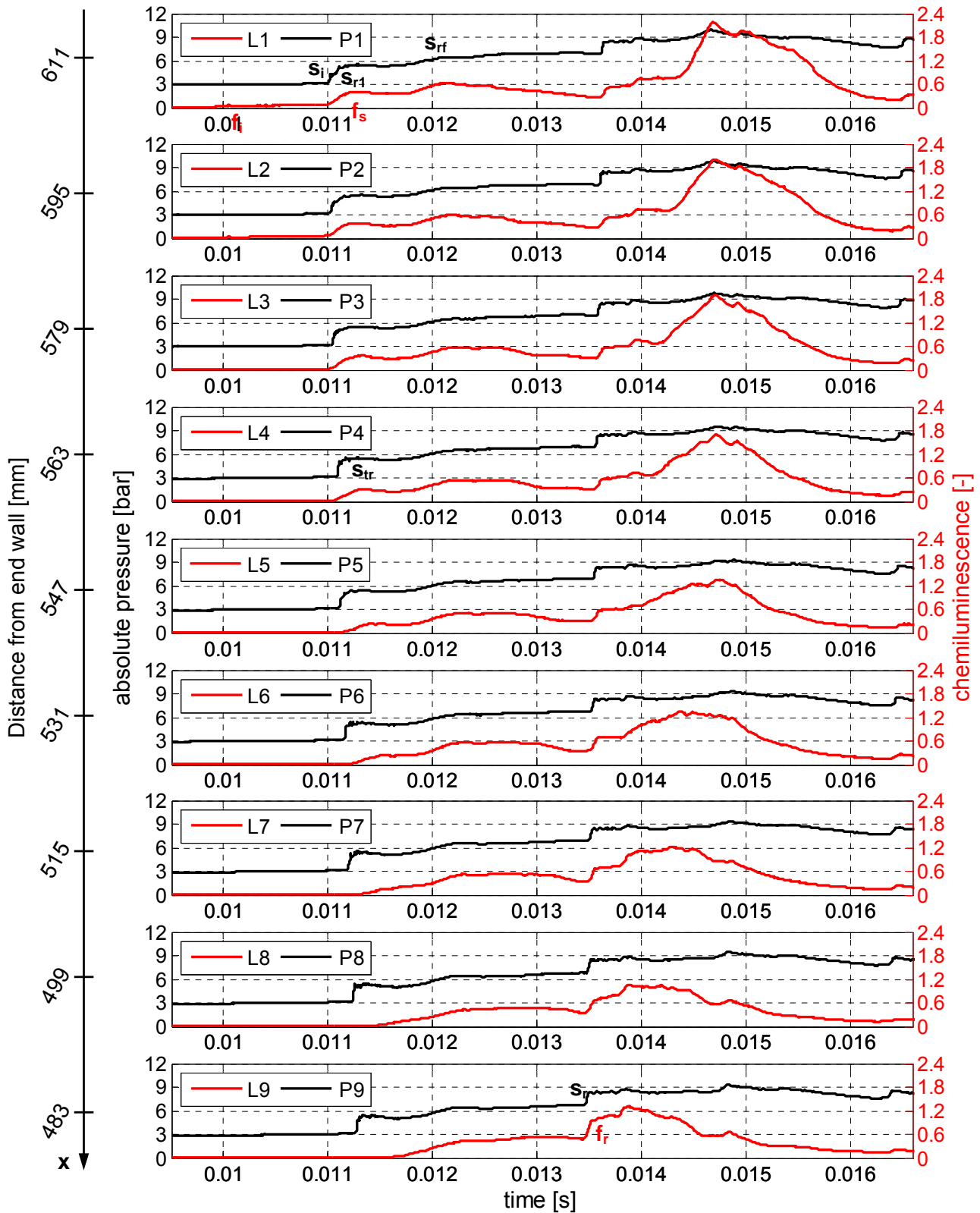


**Figure 4.15:** Pressure and chemiluminescence profiles of the incident and the reflected shock waves,  $f/s$ ,  $M_i = 1.11$

In this configuration, ignition is initiated at an axial location upstream of the measurement section, in terms of the incident shock direction of propagation. Following ignition, two flame fronts are formed; see Figure 4.12 for reference. The first flame propagates in the negative  $x$ -direction, i.e. towards the driver tube. The second one moves in the positive  $x$ -direction and reaches the instrumented section at the time  $t \approx 0.01$  s, as can be seen in L1 in Figure 4.15. The velocity of propagation of this undisturbed flame  $f_i$  in the laboratory frame of reference is 30.5 m/s. It has a chemiluminescence intensity of  $\Theta_0 \approx 0.065$ .

The incident shock traverses the first flame upstream of the instrumented section. Transmitted portion of this shock wave propagates through the hot combustion products and reaches P1 at  $t \approx 0.01$  s. This incident shock wave  $s_i$  propagates at the absolute velocity of 1082 m/s and has a pressure amplitude of 1 bar. Its strength corresponds to  $M_i \approx 1.1$  with respect to the gas into which it propagates. At the time when  $s_i$  enters the instrumented area, the undisturbed flame has a concave shape with regard to  $s_i$ , and an axial extent corresponding to approximately one half of the measurement section length; see Figure 4.12. Hence, the incident shock is already in contact with the rear, wall adjacent part of the flame when it passes P1. This continued shock-flame interaction is indicated by an increase in the heat release of the flame (6-8 times compared to the undisturbed flame) that occurs simultaneously with the passage of the incident shock in L1-L3. Because of the  $f/s$  nature of this shock-flame interaction both reflected and transmitted waves are shocks. Evidence of the reflected shock wave  $s_{r1}$  can be found in the pressure traces P2 and P1. After the pressure rise resulting from the incident shock there is another pressure rise of approximately 0.9 bar that propagates in the opposite direction to that of the incident shock.

In the proximity of P3 the incident shock crosses the crest of the flame front. The propagation path of this transmitted shock  $s_{tr}$  is extracted from the records of pressure sensors located downstream of P3.  $s_{tr}$  has a higher pressure amplitude (around 2 bar) than the incident shock  $s_i$ . It moves at the absolute velocity of 430 m/s ( $M_{tr} \approx 1.19$ ) through unburned combustible mixture towards the end wall of the test section. The disturbed flame front propagates in the same direction as  $s_{tr}$  however, at a lower velocity (approx. 143 m/s), as can be seen from growing time-lag between pressure and chemiluminescence increases in P4-P9 or L4-L9, respectively.

Between  $t \approx 0.012$  s and  $t \approx 0.013$  s there is evidence of an additional pressure wave that traverses the measurement section in the positive  $x$ -direction. This pressure wave  $s_{rf}$  is the reflection of  $s_{r1}$  from the first upstream flame, which returns to the measurement section as a sonic pressure wave characterised by a slow, gradual increase in pressure. A rise in the chemiluminescence intensity associated with  $s_{rf}$  indicates that the flame is still, at least partially, within the measurement section and responds to this pressure disturbance by an increase in heat release.



The transmitted shock wave  $s_{tr}$  reaches the end wall of the test section and returns to the measurement section at the time  $t \approx 0.0135$  s as the reflected shock  $s_r$ . It traverses the instrumented section in the negative  $x$ -direction from P9 to P1 at an absolute velocity ranging between 810-860 m/s for different runs. In the course of its propagation,  $s_r$  simultaneously induces a rise in flame heat release by further disrupting the distorted combustion zone that extends across the whole length of the measurement section. Subsequently, weak secondary pressure waves, which originate from repeated shock-flame interactions, continue to traverse the highly distorted flame zone further augmenting its deformation. This repeated disturbances lead to the formation of a turbulent flame [98], [155], which is indicated by a further significant increase in flame heat release from L9 to L1. Finally, the turbulent flame moves out of the instrumented area.

### 4.3.3 The Rayleigh Index

The Rayleigh criterion represents a major tool in pressure-gain combustion research. A detailed description of the Rayleigh criterion and its mathematical formulation are given in Chapter 3.1. In practice, an alternative formulation, the so called frequency Rayleigh index  $RI_f$ , is often used to identify regimes under which instability, or in other words reinforcement, of an unsteady pressure field is promoted. The  $RI_f$  is defined as follows [127]:

$$RI_f = \int_0^\tau \frac{p' q'}{\bar{p} \bar{q}} dt \quad (4.1)$$

In eq. (4.1)  $p'$ ,  $q'$  are pressure and heat release fluctuations, and  $\bar{p}$ ,  $\bar{q}$  are the mean values of pressure and heat release, respectively. Integration is performed over one cycle of oscillation to yield the frequency Rayleigh index, where  $\tau$  is the period of oscillation. A positive value for  $RI_f$  tends to amplify the unsteady pressure field, whereas a negative  $RI_f$  tends to damp out the oscillations.

In the current analysis the pressure field is characterised by discontinuous pressure changes due to shock wave action instead of periodic oscillations. For this reason eq. (4.1) is modified to obtain the instantaneous, dimensionless Rayleigh index  $RI$ :

$$RI = \frac{p' q'}{\bar{p} \bar{q}} \quad (4.2)$$

Equation (4.2) was applied to the experimentally recorded data in order to obtain a map of temporally and spatially resolved instantaneous Rayleigh index. In this calculations the heat release terms in eq. (4.2) were replaced by the measured  $CH^*$  chemiluminescence signal intensity. Mean pressure  $\bar{p}$  was defined at 3.1 bar, which corresponds to the averaged pressure value at the arrival of the incident shock wave. For the mean heat release  $\bar{q}$  the value of

$\Theta_0 = 0.065$  was selected, which is the average chemiluminescence intensity of the undisturbed flame. Pressure  $p'$  and heat release  $q'$  fluctuations were defined as the local, instantaneous deviations from the respective mean values  $\bar{p}$  and  $\bar{q}$ .

In Figure 4.16 and Figure 4.17 a contour plot of RI for a representative s/f-interaction with  $M_i = 1.38$  is given on a time-distance plane. Additionally, trajectories of various pressure waves and flame fronts indicating their propagation through the measurement section are plotted in the diagrams. The actual locations of the pressure and light sensors are indicated along the x-axis. The interaction of the incident shock with the initial undisturbed flame is shown in Figure 4.16. In Figure 4.17 both the incident and the reflected shocks are presented. These diagrams are best discussed in combination with Figure 4.14.

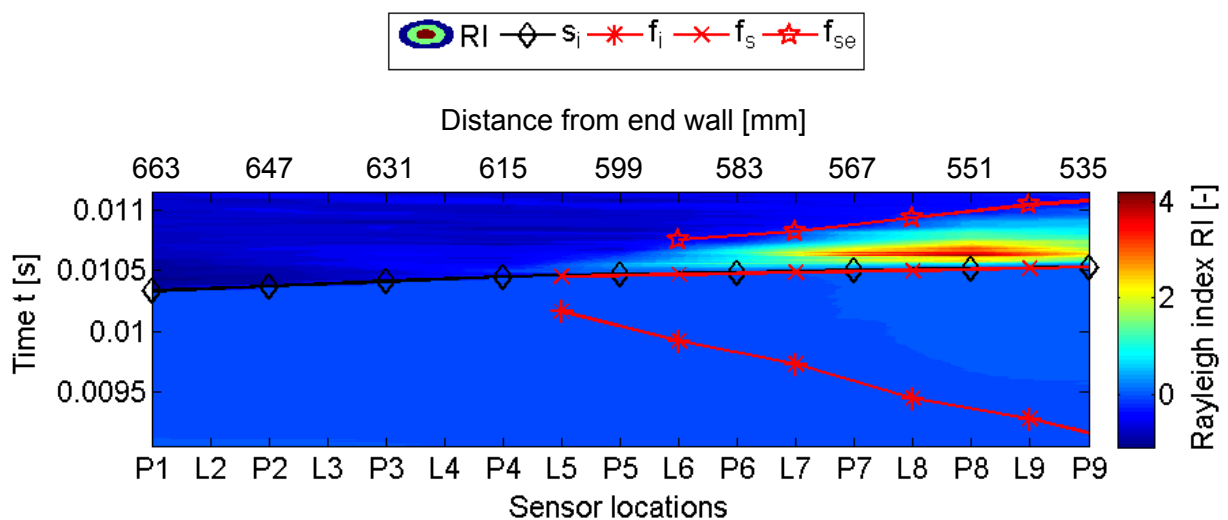


**Figure 4.16:** Instantaneous Rayleigh index RI of the incident shock on the t-x plane, s/f,  $M_i = 1.38$

There exist two regions of enhanced positive RI. The first peak in RI occurs when the incident shock interacts with the undisturbed flame front; see Figure 4.16. This interaction produces an increase in the HRR of the flame. This energy is released within the region of elevated pressure behind the incident shock wave  $s_i$ . Line  $f_{se}$  depicts the trajectory of the disturbed initial flame being moved out of the measurement section. As a consequence there is a region of positive RI between the lines  $s_i$  and  $f_{se}$  indicating a zone where combustion induced pressure growth is promoted.

The second region of high positive RI is found behind the reflected shock wave  $s_r$ ; see Figure 4.17. This shock wave further disturbs the already distorted flame front producing significantly higher pressure and heat release fluctuations  $p'$  and  $q'$  than the first interaction; see Figure 4.14. Consequently, the maximum values of RI achieved in this region are much higher than after the initial interaction – 180 compared to 4.5. These results confirm the find-

ings of Khokhlov et. al. [81] who report significantly higher rates of heat release and shock wave amplification to be produced by repeated shock-flame interactions compared to a single event. Analogous representation of RI for s/f-interactions with  $M_i = 1.25$  and  $M_i = 1.55$  are given in the Appendix A in Figure A.3 and Figure A.4 respectively. It is pointed out that in all s/f-interaction experiments the maximum values of RI were achieved immediately behind the “strange wave” sw; see Chapter 4.3.1. This fact confirms the existence of a strong positive feedback mechanism between the “strange wave” and the energy release at the combustion front.

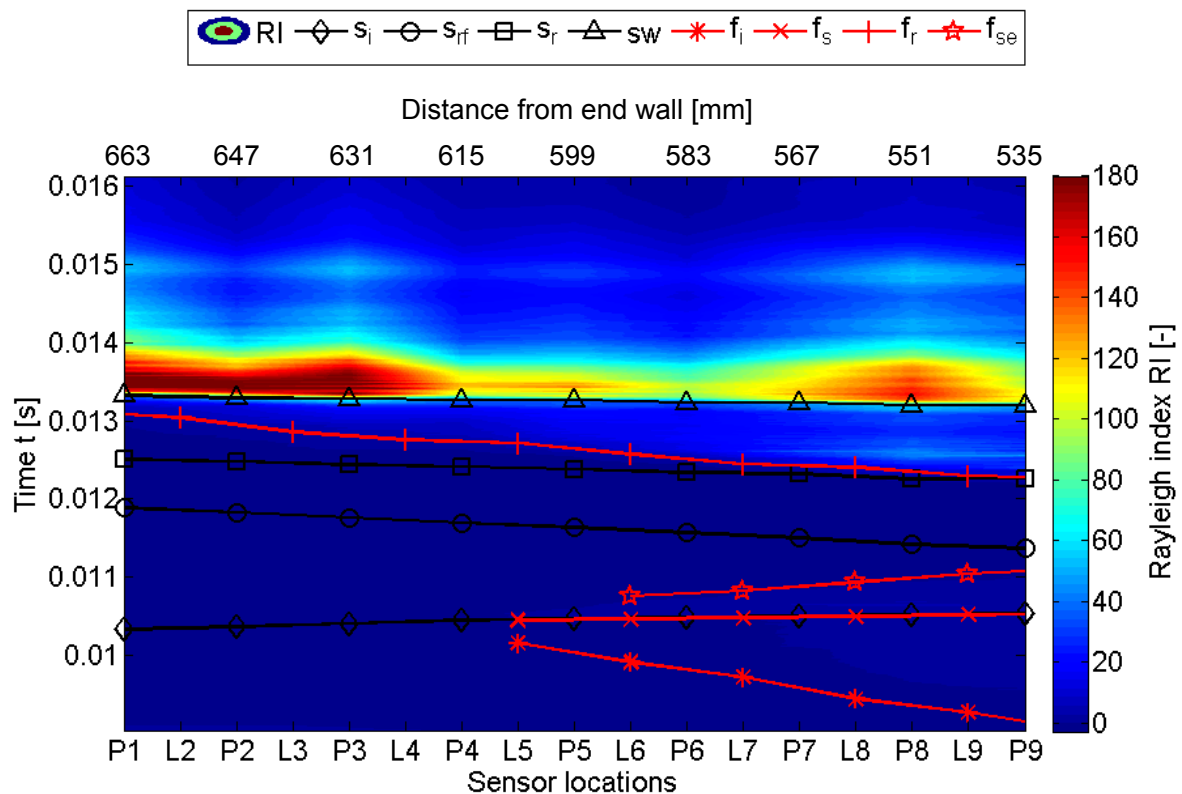


**Figure 4.17:** Instantaneous Rayleigh index RI of the incident and the reflected shocks on the  $t$ - $x$  plane, s/f,  $M_i = 1.38$

Contour plot of instantaneous Rayleigh index for a f/s-interaction with  $M_i = 1.11$  is shown in Figure 4.18. On the global map (upper diagram in Figure 4.18) the zone with the highest values of RI is located in the region behind the reflected shock  $s_r$ . This zone begins when  $s_r$  enters the instrumented section at P9, which induces a simultaneous increase in pressure and heat release of combustion; see Figure 4.15. The intensity of RI increases from around 30 up to a maximum value above 70 at  $t \approx 0.015$ , as the flame front evolves into a turbulent flame brush under the action of secondary pressure waves; see also Figure 4.15. The effect of the interaction of the incident shock  $s_i$  with the initial flame  $f_i$  is illustrated in the lower diagram of Figure 4.18. Therein an additional sharp increase in RI from 4 to a value above 8 is observed

at  $t \approx 0.012$ . This increase is related to the secondary reflection  $s_{rf}$ , which propagates through the measurement section inducing a simultaneous increase in the heat release of the deformed flame. The trajectory of propagation of  $s_{rf}$  is not shown in Figure 4.18.

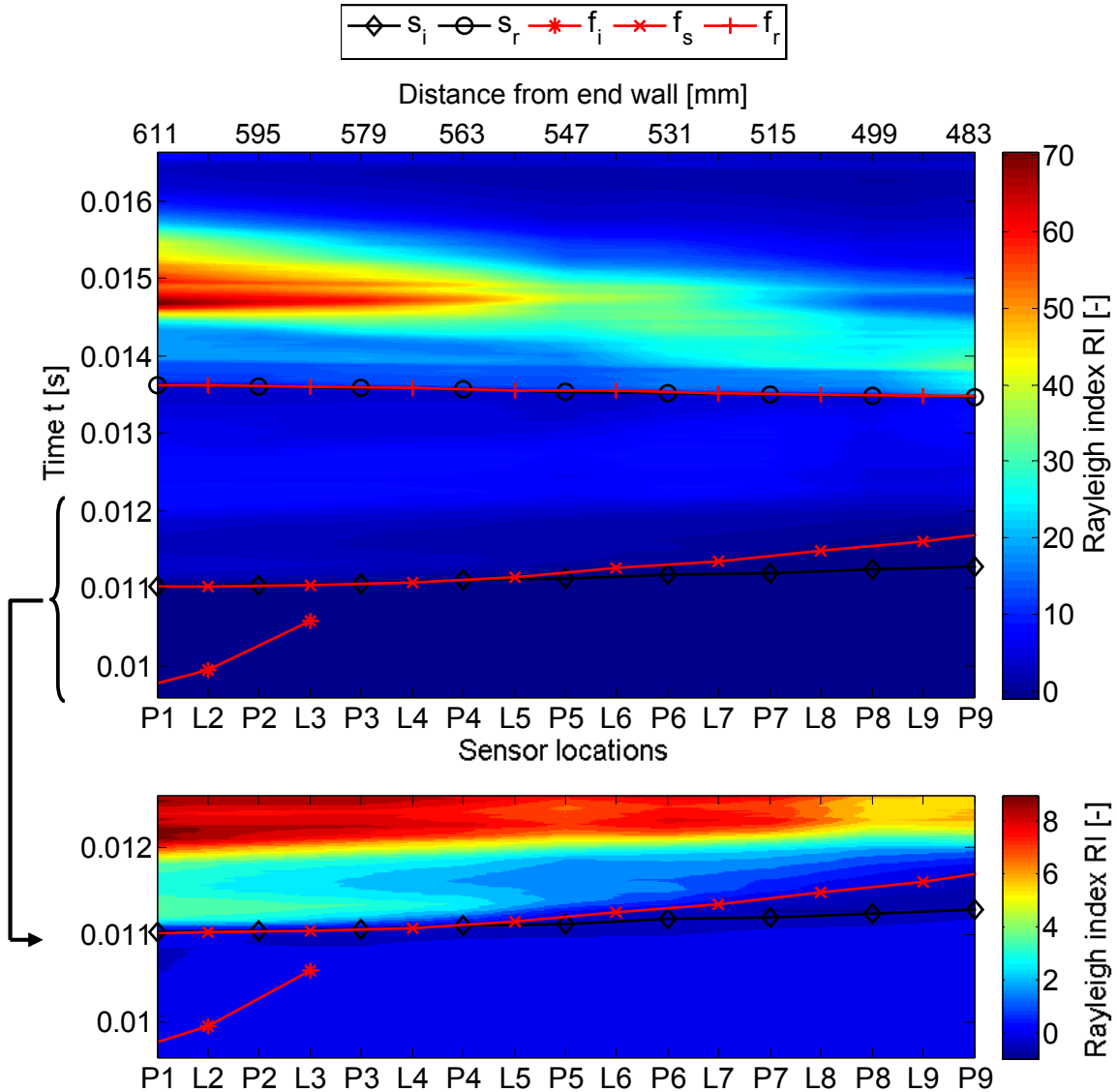


**Figure 4.18:** Instantaneous Rayleigh index RI on the t-x plane,  $f/s$ ,  $M_i = 1.11$

These results clearly demonstrate the characteristics of shock-flame interaction to establish conditions favourable for combustion induced amplification of pressure waves. Such conditions are produced when a pressure wave traverses a combustion front, irrespective of the mode of interaction. Passage of a pressure wave temporarily enhances the heat release of the combustion front. This energy is released within the region of elevated pressure behind the pressure wave, which further increases its velocity and pressure. In Table 4.1 maximum RI values achieved as a result of the incident and the reflected interactions are tabulated for

different interaction modes and different incident shock Mach numbers. These results suggest that the “driving” capability of shock-flame interactions increases with the strength of the incident shock wave for the same mode of interaction. The RI intensity of the incident interaction for s/f and  $M_i = 1.55$  appears not to follow this trend. Such a low value results from the fact that in the corresponding experiments the incident interaction occurred at the very end of the measurement section. Thus, the flame was moved out of reach of the light guides by the wake of the incident shock before the heat release had enough time to evolve and reach its maximum value. A comparison of RI intensities of the two interaction modes s/f and f/s suggests that the f/s-interaction is a rather energetic process and provides higher rates of pressure wave amplification for the same  $M_i$ . These results are in good agreement with the findings reported by Kilchyk in [84] and [85].

	max. RI (incident interaction)	max. RI (reflected interaction)
s/f, $M_i = 1.26$	0.7	14
s/f, $M_i = 1.38$	4.5	185
s/f, $M_i = 1.55$	2.8	354
f/s, $M_i = 1.11$	3.7	70

**Table 4.1:** Maximum intensities of RI for different interaction modes and different incident shock Mach numbers

#### 4.4 Discussion and Conclusions

Analysis of the chemiluminescence profiles provides clear evidence of the effect of shock-flame interaction on the heat release of combustion. The heat released by the flame is amplified every time the chemical reaction zone is crossed by a pressure wave in both s/f and f/s modes of interaction. The increase in energy release is due to two effects: compression of the unburned gas and increase in flame surface area. The basic mechanism by which the surface area of the flame is augmented is the Richtmyer-Meshkov instability [81], [140]. Repeated interactions between pressure waves and the distorted flame further increase its surface area and enhance vorticity. Hence, the level of energy release is increase due to every successive interaction. The magnitude of increase in the flame heat release is dependent on the mode of interaction and the strength of the incident shock wave  $M_i$ . In Figure 4.19 the maximum values  $\Theta_{\max}$  of heat release measured by the different light guides after the incident interaction are normalised by the heat release intensity of the undisturbed flame  $\Theta_0$  and

plotted as a function of incident shock Mach number  $M_i$  for both interaction modes. The intensities of heat release rate after the reflected interaction are not shown here. The chemiluminescence intensities after the reflected interaction reached the saturation of the photomultipliers in some cases, see Figure A.2 L6-L9, and are therefore not representative.

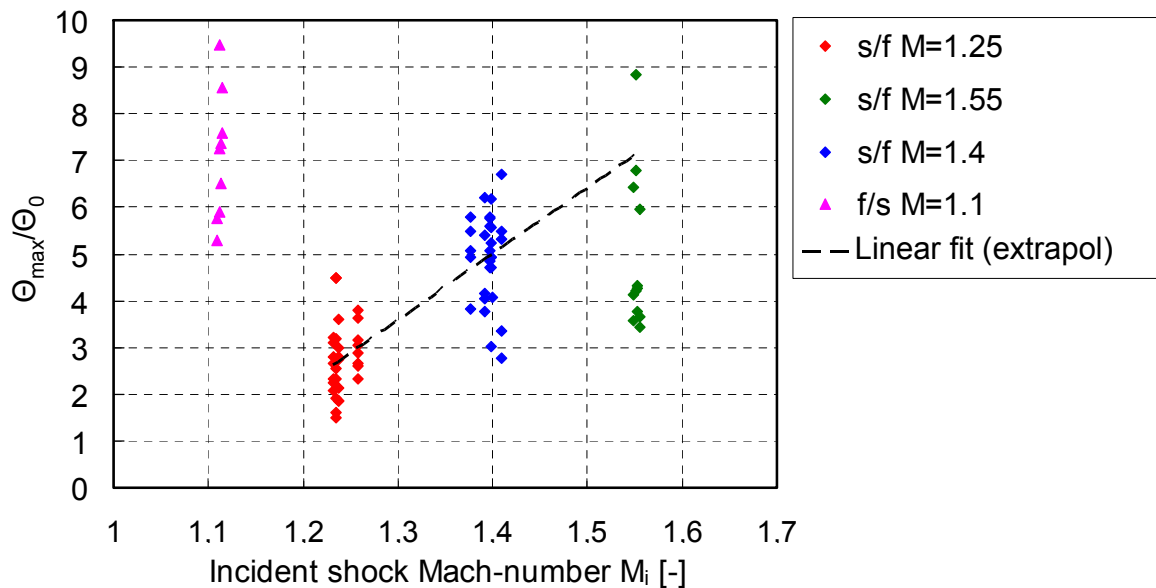


**Figure 4.19:** Max. chemiluminescence intensities  $\Theta_{\max}$  due to incident interaction normalised by the intensity of the undisturbed flame  $\Theta_0=0.065$ , for different interaction modes and  $M_i$

The increase in heat release rate due to the incident shock-flame interaction rises with  $M_i$  for s/f-interactions. Most of the heat release values for  $M_i = 1.55$  appear too low. As has been already mention in the previous chapter, this is because the flame was blown out of the instrumented area by the wake of the incident shock before the heat release could reach its maximum intensity. A straight line was selected to fit the values for  $M_i = 1.25$  and  $M_i = 1.4$ . This fit was extrapolated to  $M_i = 1.55$  in order to indicate the expected level of heat release increase for such incident shock Mach numbers. The level of heat release increase measured after incident f/s-interactions for  $M_i = 1.11$  is also shown in the diagram. These values correspond to those of  $M_i = 1.4$ - $1.6$  for s/f-interactions. Such behaviour confirms the results of Kilchyk [84], [85]. In his work he concludes that f/s-interactions produce up to four times higher rates of fuel consumption than s/f-interaction for the same incident shock Mach numbers. This is because of the higher rates of flame surface growth and stronger compression effects in this type of shock-flame interactions.

Computations of instantaneous Rayleigh index in the previous chapter demonstrate that the increase in heat release occurs immediately after the passage of the shock wave. Further, the rate of increase is high enough for the increased energy of combustion to be released

within the region of elevated pressure behind the shock wave. Thereby, amplification of the passing pressure waves is promoted. This effect is illustrated in Figure 4.20.

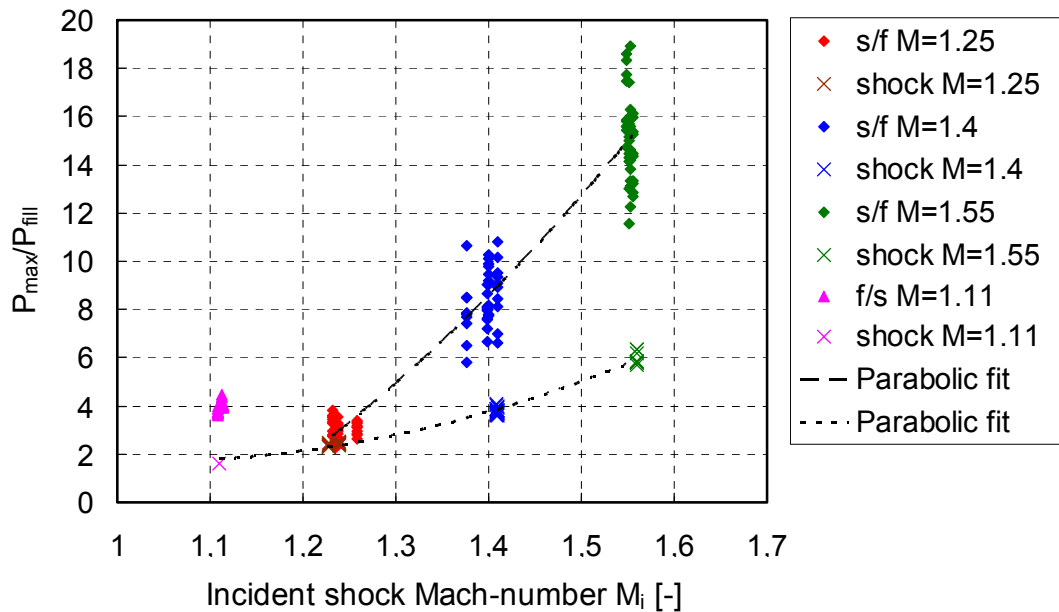


**Figure 4.20:** Maximum measured pressure values  $p_{max}$  normalised by the filling pressure  $p_{fill}=2.25$  bar, for different interaction modes and  $M_i$

In this figure the maximum pressure values, i.e. those behind the reflected shock wave, measured in various experiments are presented as a function of the incident shock Mach number  $M_i$ . All pressure values are normalised by the test rig filling pressure  $p_{fill} = 2.25$  bar. There are two sets of data points: those from interaction experiments, for both slow/fast and fast/slow interaction modes, and those from corresponding shock only experiments (no combustion) that were performed at the same  $M_i$ . It was not possible to conduct a shock only experiment in the burned gas without the presence of combustion fronts. For this reason, the pressure value for the shock experiment at  $M=1.11$ , shown in the diagram, was determined analytically. Data series for the s/f interactions as well as for the pure shock experiments were curve fitted. Best fit was achieved by using a second order polynomial in both cases. Comparison between these two data sets clearly indicates that pressure waves are amplified as a result of (multiple) shock-flame interactions. This amplification effect is a strong function of the incident shock Mach number. It grows non-linearly in magnitude with increasing  $M_i$ . Further, the normalised pressure values achieved in f/s  $M_i = 1.11$  are higher than those for s/f  $M_i = 1.25$ . Hence, the pressure amplification effect due to f/s-interaction appears to be stronger than for s/f-interactions. This is in line with the results reported for the interaction induced amplification in the heat release of combustion; see Figure 4.19. Fast/slow interactions induce stronger amplification of the flame heat release than the slow/fast interactions

for incident shocks of the same Mach number. This behaviour is responsible for higher pressure wave amplification rates.

Analysis of the experimental results demonstrates that shock-flame interaction temporally increases the heat released by combustion leading to a combustion induced amplification of traversing pressure waves. Both, the increase in heat release and in pressure are dependent on the strength of incident shock waves. They rise with increasing Mach numbers of the incident shock. Shock-flame interactions in the fast/slow mode seem to generate higher rates of heat release and pressure increase than slow/fast interactions. Hence, it is followed that f/s is the preferable type of shock-flame interactions with regard to PGC applications. In this context it is, however, mentioned that more energy is required to produce shock waves of the same strength in a hot gas than in a cold gas, if the pressure is the same in both fluids. A shock wave, or a sequence of shocks, is generated by suddenly bringing in contact two gases of different pressure, e.g. by opening and closing a valve between two volumes of different pressure [164]. For a high temperature driven gas (e.g. combustion products) a considerably higher pressure difference between the two volumes is necessary to generate a shock of a certain Mach number than for a low temperature driven gas [114].



## 5 Analytical Modelling of Shock Wave-Flame Interaction

The main objective of this work is to improve understanding of the process of shock wave and flame interaction and to assess its potential with regard to PGC applications. For this purpose a quasi-one-dimensional analytical model of the physical processes involved in the shock-flame interaction was developed. Experimental data reported in Chapter 4 were used for model verification. Results of the analytical calculation allow conclusion to be drawn regarding achievable pressure rise and reduction of combustion entropy rise due to a single shock-flame interaction event.

### 5.1 Description of the Analytical Model

The overall structure of the analytical model for the calculation of the shock-flame interaction phenomena is shown in Figure 5.1. The calculation procedure is broken down into four main thematic modules. These are:

- Module 1: Steady propagation of a shock wave in homogeneous media
- Module 2: Change of state across a combustion front (Deflagration)
- Module 3: Shock wave-flame interaction
- Module 4: Formation of a new, fully defined flow field after the interaction event

Module 3 is further subdivided into sub-modules, which will be described in detail later. The flow of information in the course of the calculation is indicated by arrows between the various modules in Figure 5.1. The thermodynamic and aerodynamic output parameters of the former modules are the input parameters for the subsequent modules. A set of external input parameters defining the initial gas state, the strength of the incident shock, the mode of interaction, as well as the initial geometry of the flame, i.e. at the moment of interaction, is required at the start of each calculation. Based on this set of input parameters the model produces a fully defined flow field at the end of a single shock-flame interaction event.

All pressure waves dealt with in the model are one-dimensional in nature. Consequently, the pressure and velocity fields produced at the end of the calculation are also 1-D. Such a situation would only be possible if the flame front was ideally plane and parallel to the shock wave at the instant of interaction. In reality, flame fronts usually have complex, three-dimensional geometries. Thus, transition of a plane, one-dimensional shock wave through such a convo-

luted flame front in a narrow channel will produce a complex system of transmitted and reflected pressure waves that propagate both longitudinally and transversally. However, these pressure waves coalesce and form a single one-dimensional wave already within a very short distance after the interaction event [82], [140], [155]. For this reason the one-dimensional approach in the modelling of pressure waves was deemed to be appropriate. Further, the fluid flow is adiabatic, i.e. no heat exchange with surroundings, with internal heat addition by combustion. Gravitation effects, as well as viscosity and thermal conductivity of gases are neglected.

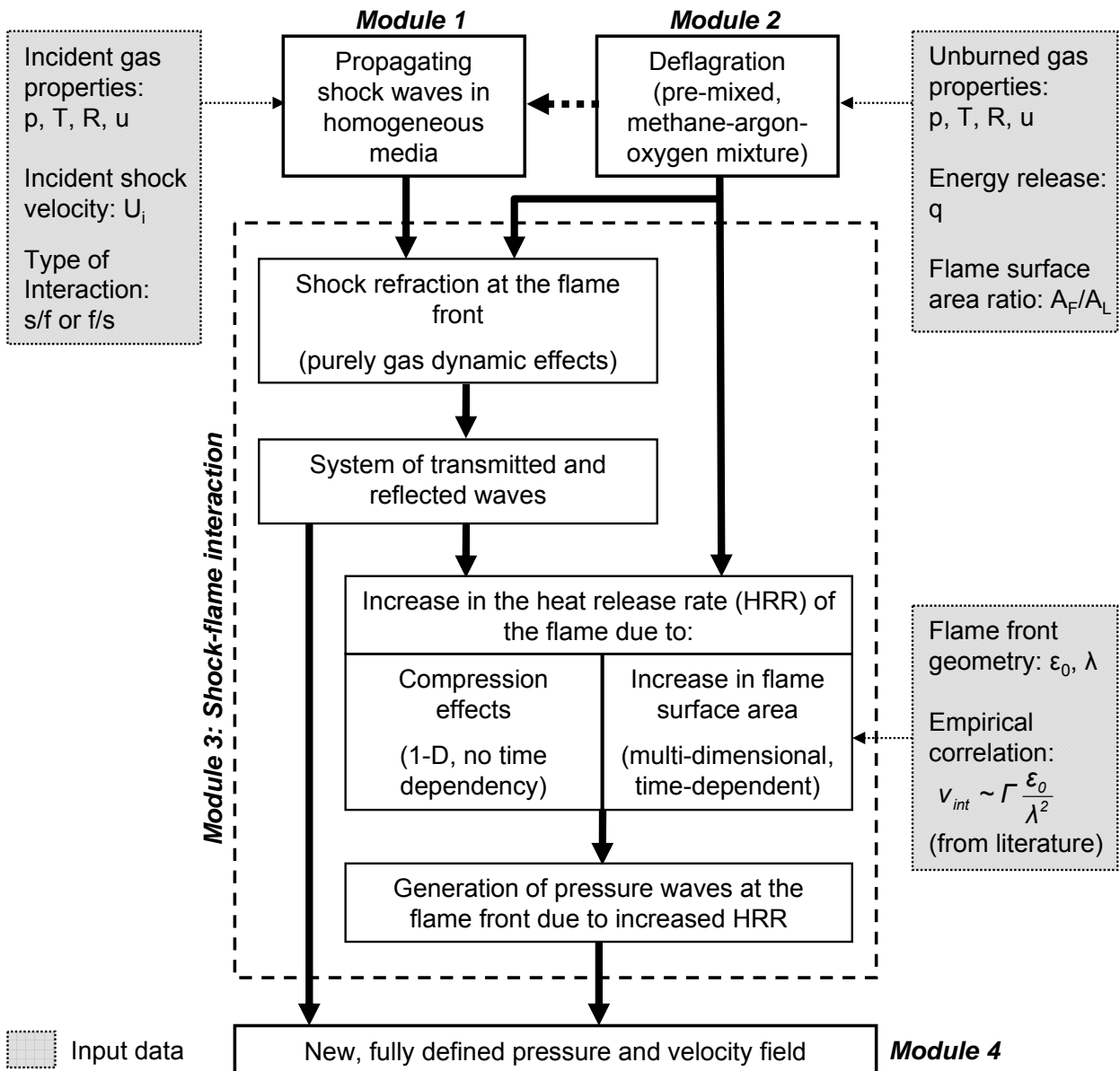


Figure 5.1: Structure of the analytical model

The two-dimensional CFD-predicted shape of the flame at the moment of incident shock arrival is shown in the upper picture of Figure 5.2. This image was extracted from numerical

combustion simulation discussed in Chapter 4.2.2. In the analytical model the geometrical shape of the flame is modelled by a simple sine-wave with the analytical equation:

$$x = \varepsilon_0 \sin\left(\frac{2\pi}{\lambda} y\right) \quad (5.1)$$

$$\text{with } 0 \leq y \leq D_T$$

Therein,  $D_T$  is the inner diameter of the shock tube,  $\varepsilon_0$  and  $\lambda = 2D_T$  are the initial amplitude and the wave length of the sine wave, respectively. Schematics of the geometrical sine-shape flame front model are presented in the lower part of Figure 5.2. The initial amplitude of the flame  $\varepsilon_0$  extends to the middle of the numerically predicted flame front thickness.

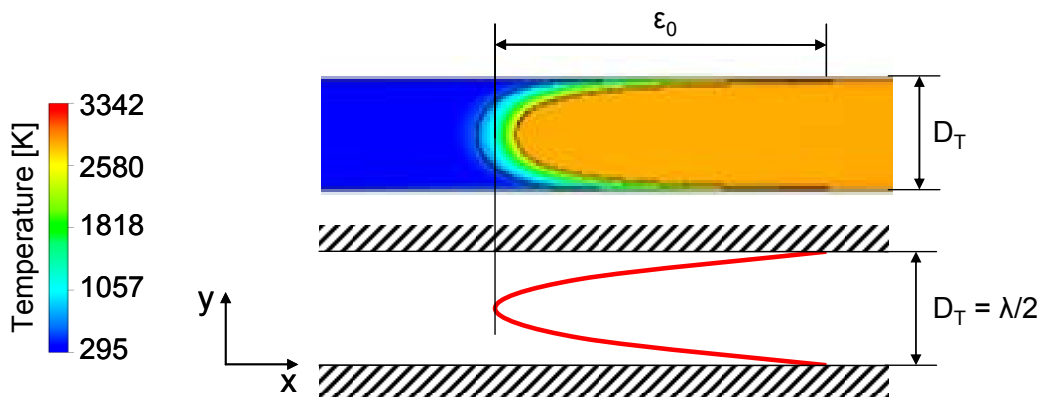


**Figure 5.2:** Flame geometry at the moment of interaction and corresponding two-dimensional model

### 5.1.1 Incident Shock Wave

An iterative calculation procedure implemented in Module 1 allows determining the flow conditions behind the incident shock wave. In order to perform this calculation the mode of interaction, i.e. s/f or f/s, the strength of the incident shock wave, and the flow conditions in the incident gas must be known. The strength of the incident shock is expressed as a combination of the incident shock propagation velocity in the absolute frame of reference  $U_i$  and the flow conditions in the incident gas into which the shock propagates. This translates into a single parameter – the incident shock Mach number  $M_i$  that is defined with respect to the gas state into which the shock propagates.

The type of interaction is an important input parameter to the model. If interaction is s/f, the incident shock propagates through unburned gas mixture, which defines the incident gas flow conditions. This situation is schematically shown in Figure 5.3 a). In the case of f/s-interaction the incident gas is the burned gas. Consequently, the flow conditions of the unburned gas mixture are fed into the combustion module (Module 2) to obtain the flow pa-

rameters in the burned gas. The resulting flow parameters in the combustion products are then used as the incident gas into which the incident shock propagates; see Figure 5.3 b).

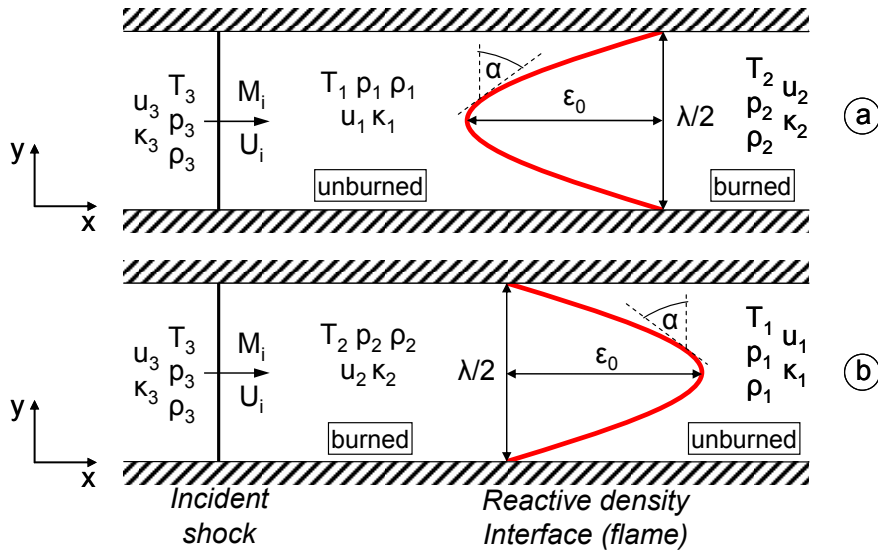
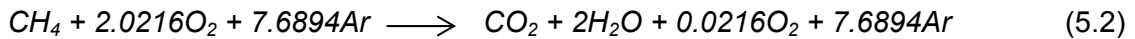


**Figure 5.3:** Initial configuration for calculation of a) s/f-interaction, b) f/s-interaction

Once the incident gas flow conditions and the strength of the incident shock are available a set of equations is applied to determine the flow parameters behind the incident shock. Equations used in this calculation are the commonly used one-dimensional flow equations that describe the change of state across a shock wave of certain strength (Rankine-Hugoniot relations). They can be found in [7], [47], [146] or [164]. The fluid model used in the calculation is described in Chapter 5.1.2.

### 5.1.2 Combustion Modelling

For the simulation of combustion within Module 2 an idealised reaction model of the combustible mixture is used:



Because of the slightly lean mixture ( $\Phi = 0.989$ ) the reaction (5.2) is not complete and some of the excess oxygen remains unconsumed. For this type of reaction the molar mass and hence, the specific gas constant can be assumed to remain constant for both the unburned and the burned gases. The respective values are  $\mathcal{M} = 0.03621$  kg/mol and  $R = \mathcal{R}/\mathcal{M} = 229.62$  J/kgK.

In order to correctly represent the varying fluid characteristics within the shock-flame interaction calculation a simplified fluid model was implemented. The fluid is modelled as ideal gas, where specific heat capacity  $C_p$  is assumed to be a function of the gas temperature only. An

empirical NASA polynomial is used to calculate the specific heat capacity  $C_{pi}$  of each species of the gas mixture [100], [124]:

$$C_{pi} = R_i \cdot (a_1 + a_2 T + a_3 T^2 + a_4 T^3 + a_5 T^4) \quad (5.3)$$

The coefficients  $a_1$ - $a_5$  for the equation (5.3), as well as the values of  $M_i$  required for calculation of the specific gas constant  $R_i$  are given in the Appendix A in Table A.1 for the unburned mixture, and in Table A.2 for the burned gas. The integral heat capacity of the gas mixture  $C_{pmix}$ , and this mixture's adiabatic index  $\kappa$  are then determined using equations (5.4) and (5.5) respectively [47], [162].

$$C_{pmix} = \sum_i Y_i C_{pi} \quad (5.4)$$

$$\kappa = \frac{1}{(1 - R / C_{pmix})} \quad (5.5)$$

In eq. (5.4)  $Y_i$  represents the mass fraction of each substance of a gas mixture. The values of  $Y_i$  for the reactants and products of the chemical reaction (5.2) are also tabulated in Table A.1 and Table A.2 respectively.

The combustion process is characterised by two parameters. These are the amount of heat added to the gas and the rate at which the fresh combustible mixture is consumed. The amount of heat released per unit mass of the combustible mixture is  $q = 2276000$  J/kg. This value was determined from the equation (5.6) [32], where  $T_1 = 298$  K and  $T_2 = 2886.2$  K, which is the adiabatic flame temperature for the reaction (5.2) at the constant reference pressure of 1 bar [13]. The value of  $q$  is taken as a constant property of the gas mixture.

$$q = C_{p2} T_2 - C_{p1} T_1 \quad (5.6)$$

The rate at which the unburned gas is consumed is expressed by the flame velocity relative to the fresh gas  $s_F$ . This effective flame velocity is related to the laminar burning velocity  $s_L$  by the following relation [123]:

$$s_F = s_L \frac{A_F}{A_L} \quad (5.7)$$

The surface area  $A_L$  of the reference ideal laminar flame corresponds to the cross-sectional area of the channel i.e. that of the shock tube with diameter  $D_T$ . The effective flame surface area  $A_F$  is determined from the equation (5.1) by the use of the Guldinus theorem [103]. The ratio of the flame surfaces  $A_F/A_L$  is an essential input parameter to the Module 2 of the analytical model.

An empirical correlation (5.8) valid for methane-oxygen-argon mixtures in the range of pressures  $p = 1$ -40 bar, unburned gas temperatures  $T_u = 298$ -650 K, and equivalence ratios  $\Phi = 0.8$ -1.2 is used for the laminar burning velocity  $s_L$  of the flame [128]:

$$s_L = s_{L0} [1 + a_1(\Phi - 1) + a_2(\Phi - 1)^2] \left( \frac{T_u}{T_{u0}} \right)^\alpha \left( \frac{p}{p_0} \right)^\beta \quad (5.8)$$

In eq. (5.8)  $s_{L0}$  is the reference laminar burning velocity at the reference pressure  $p_0 = 1$  bar, temperature  $T_{u0} = 298$  K, and fuel-oxidiser equivalence ratio  $\Phi_0 = 1$ . The values of  $s_{L0}$ , as well as of the empirical constants  $a_1$ ,  $a_2$ ,  $\alpha$ ,  $\beta$  are given in the Appendix A in Table A.3.

Besides the relations described above an iterative calculation procedure derived by Rudinger [132] from the mass, momentum, and energy conservation equations is implemented in Module 2. The full set of equations as well as their derivation can be found in [132]. The flow conditions in the burned gas as well as the absolute propagation velocity of the flame front are calculated using known gas properties and flow conditions in the unburned gas as well as the values of  $q$  and  $A_F/A_L$ .

### 5.1.3 Shock Refraction at the Flame Front

In Chapter 3.2 it was described that the process of shock wave and flame interaction is separable into two effects, which, to some degree, can be treated independently from each other. Such a two-step approach was taken in the analytical model being described here; see Module 3 in Figure 5.1. The first effect is the refraction of the incident shock at the reactive density interface, which occurs instantaneously and is locally one-dimensional. Modelling of this physical phenomenon is the subject of this sub-chapter. The second effect is related to multi-dimensional and time dependant flame-vortex interaction and thus resulting increase in flame surface area. It is treated in Chapter 5.1.4.

The refraction of the incident shock wave at the flame front is treated in purely one-dimensional manner. The actual geometry of the flame is disregarded in this step and the flame front is assumed to be planar and parallel to the incident shock wave. The systems of one-dimensional reflected and transmitted pressure waves that arise from such idealised “head on” refractions are illustrated in Figure 3.2 for slow-fast and fast-slow interactions.

An iterative calculation procedure proposed by Rudinger [132] is adopted to solve the refraction problem as per Figure 3.2. Thereby, the flow conditions in the unburned (state 1), burned (state 2) gas as well as behind the incident shock (state 3) are known from Modules 1 and 2. A variable, e.g. the static temperature, on the unburned side of the flame (state 4) is estimated determining all flow variables in this region. The combustion module is embedded at this point to calculate the burned gas conditions in region 5 accounting for the changes in pressure and temperature of the unburned gas. Continuity conditions (3.7) are applied across the contact surface to determine the pressure and flow velocity in region 6. One of these variables is then used to compute the strength of the remaining unknown wave, i.e.

transmitted shock if interaction is s/f, or reflected shock for an f/s-interaction. The other variable is calculated with the aid of this wave and compared with the former result. If the results are not compatible, the initial estimate is modified until agreement is reached. A successful iteration yields the flow conditions in all six regions as well as the absolute propagation velocities of all waves resulting from the refraction process.

All equations involved in the calculation procedure described above were adopted from [14] and [164]. They comprise well known and commonly used Rankine-Hugoniot shock relations, isentropic expansion wave equations, as well as the contact surface continuity conditions eq. (3.7).

#### 5.1.4 Deformation of the Flame Front due to Shock Wave Transition

In the analytical model the flame front is treated as a two-dimensional, reactive interface between the unburned and the burned methane-oxygen-argon gas mixtures; see Figure 5.3. Geometrical change of such interfaces following shock transition, which is related to the Richtmyer-Meshkov instability, is schematically illustrated in Figure 3.3. According to Kilchyk [84], see equation (3.9), the rate of interface length growth  $v_{int}$  is linearly dependant on the geometry of the interface, characterised by  $\varepsilon_0$  and  $\lambda$ , and the deposited circulation  $\Gamma$ . Vorticity generation is little affected by the presence of a chemical reaction at the interface, which allows dealing with this fluid dynamic effect separately from the combustion process [84].

As the incident shock traverses the interface, a misalignment of pressure and density gradients leads to a rapid vorticity deposition on the interface. The subsequent evolution of the interface is mainly driven by the deposited vorticity [139]. Samtaney, Zabusky et. al. developed approximate analytical expressions for shock deposited circulation  $\Gamma$  for both s/f and f/s types of interaction [138], [139]. For simple sinusoidal interfaces defined by eq. (5.1) the total first-order accurate circulation  $\Gamma$  is

$$\Gamma = \gamma \cdot \varepsilon_0, \quad (5.9)$$

where  $\gamma$  is the circulation per unit length of the undisturbed interface and  $\varepsilon_0$  is the interface amplitude or in other words the total extent of the interface in the x-direction. The value of  $\gamma$  is a function of incident shock Mach number  $M_i$ , the ratio of burned and unburned gas densities  $\rho_2/\rho_1$ , and the ratios of specific heats in the burned and unburned gas  $\kappa_1, \kappa_2$ . It is given as

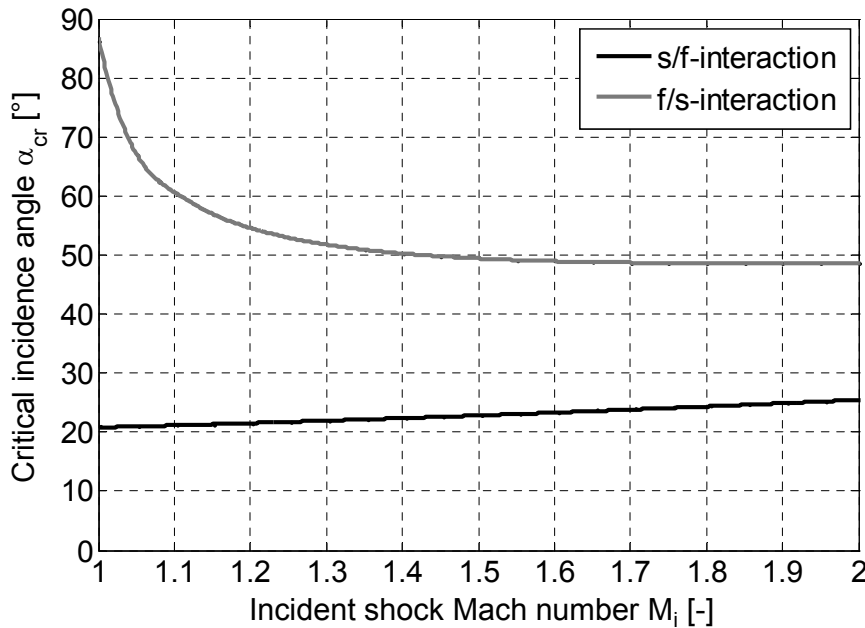
$$\gamma = \frac{a_1}{M_i} \left( \frac{\kappa_2}{\kappa_2 - 1} \frac{1 - \frac{\rho_3}{\rho_1} \frac{1 + \mu_2^2 \rho_3/\rho_1}{\mu_2^2 + \rho_3/\rho_1}}{\rho_2/\rho_1} - \frac{\kappa_1}{\kappa_1 - 1} \left( 1 - \left( \frac{\rho_4}{\rho_3} \right)^{\kappa_1 - 1/\kappa_1} \frac{\rho_3}{\rho_1} \frac{1 + \mu_1^2 \rho_3/\rho_1}{\mu_1^2 + \rho_3/\rho_1} \right) \right) \quad (5.10)$$

for the s/f type of interaction [139], and as

$$\gamma = \frac{a_2}{M_i} \left( \frac{\kappa_1}{\kappa_1 - 1} \frac{1 - \frac{\rho_5}{\rho_2} \frac{1 + \mu_1^2 \rho_5 / \rho_2}{\mu_1^2 + \rho_5 / \rho_2}}{\rho_1 / \rho_2} - \frac{\kappa_2}{\kappa_2 - 1} \left( 1 - \left( \frac{\rho_5}{\rho_3} \frac{1 + \mu_2^2 \rho_5 / \rho_3}{\mu_2^2 + \rho_5 / \rho_3} \right) \frac{\rho_3}{\rho_2} \frac{1 + \mu_2^2 \rho_3 / \rho_2}{\mu_2^2 + \rho_3 / \rho_2} \right) \right) \quad (5.11)$$

for the f/s-interaction [138]. The notation in eq. (5.10) and (5.11) corresponds to that of Figure 3.2 a) and b) respectively, and  $\mu_i^2 = (\kappa_i - 1)(\kappa_i + 1)$ . The flow variables in the different flow regions required for determination of  $\gamma$  are taken from the shock refraction calculation performed previously.

Generally, equations (5.10) and (5.11) produce a total value of  $\gamma$  irrespective of the fact whether the interaction along the interface is locally regular or irregular. Comparison of analytical first-order circulation values with corresponding numerical results (DNS) performed in [138], [139] have demonstrated that approximate solutions (5.10) and (5.11) tend to overestimate the total circulation  $\Gamma$ . The discrepancy increases with larger values of  $\varepsilon_0/\lambda$ , i.e. large values of  $\varepsilon_0$  assuming a constant interface wave length  $\lambda = 2D_T$ . This is because in such cases the interaction contains large areas of irregular refraction. The refraction becomes irregular if the characteristic angle  $\alpha$  between the incident shock and the interface locally exceeds a certain critical value  $\alpha_{cr}$ . In Figure 5.4  $\alpha_{cr}$  is given as a function of the incident shock Mach number for both interaction modes and the stratification  $\rho_2/\rho_1 = 0.114$  corresponding to the experimental methane-oxygen-argon flame. The values of  $\alpha_{cr}$  were calculated using the regular to irregular transition criterion  $M_t = 1$  (transmitted shock Mach number) [138], [139].



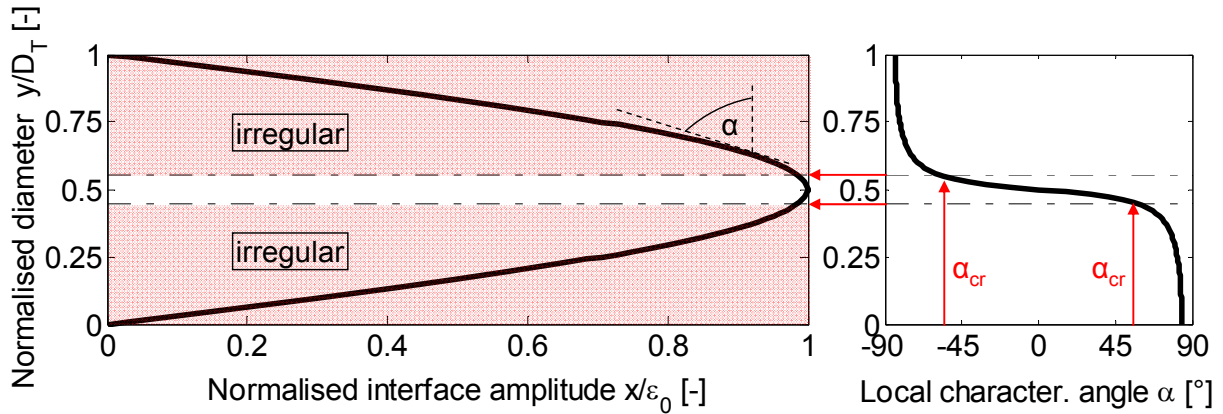
**Figure 5.4:** Critical angle  $\alpha_{cr}$  as a function of  $M_i$  for s/f and f/s interactions,  $\rho_2/\rho_1 = 0.114$



Figure 5.4 allows the calculation of the exact area of regular and irregular refraction for a given interface geometry, incident shock Mach number and interaction mode. An example is given in Figure 5.5 for an f/s-interaction with  $\varepsilon_0 = 1.48\lambda$ ,  $\lambda = 2D_T$ . For such large values of  $\varepsilon_0$  the main fraction of the refraction is irregular, hence leading to a major falsification of the circulation result. In order to overcome this difficulty a correction factor  $C_r$  for the deposited circulation  $\Gamma$  of the form

$$C_r = \frac{0.98}{1 + 0.277 \frac{L_{irr}}{L_0}} \quad (5.12)$$

was graphically derived from data reported in [138], [139] and implemented in the calculation procedure. This correction factor reduces the estimated circulation in terms of the proportion of irregular refraction. In eq. (5.12)  $L_{irr}$  is the length section of the interface where refraction is irregular, and  $L_0$  is the total initial length of the interface.



**Figure 5.5:** Areas of regular and irregular interaction for a f/s-interaction,  $\rho_2/\rho_1 = 0.114$ ,  
 $\varepsilon_0 = 1.48\lambda$ ,  $\lambda = 2D_T$

In his numerical studies with stoichiometric propane-air combustion Kilchyk [84] derived a linear approximation for the length growth rate  $v_{int}$  of a two-dimensional, sinusoidal interface in the form:

$$v_{int} = A \frac{\Gamma \varepsilon_0}{\lambda^2} + B \quad A, B = const. \quad (5.13)$$

This relation is valid for perturbation geometries with different initial aspect ratios  $\varepsilon_0/\lambda$ . Generally, the slope of the straight line, i.e. the constant  $A$  in eq. (5.13), is higher for fast/slow than for slow/fast interactions [84], [85]. The graphical data presented in [84] was digitised and the constant  $A$  was determined to be  $A_{s/f} = 1.31$  for the s/f-interactions, and  $A_{f/s} = 1.84$  for the f/s interactions. Because of the lack of according experimental data for the combustible gas mixture used in the experimental studies these constants  $A_{s/f}$  and  $A_{f/s}$ , derived for pro-

pane flames, were implemented in the relation (5.13) to give a first-order approximation of  $v_{int}$ . For the sake of simplicity the constant B was set to zero for both interaction modes. In order to determine the maximum increase in the length of the reactive interface  $\Delta L$  due to shock wave transition the maximum interface growth time  $t_{max}$  is necessary:

$$\Delta L = v_{int} t_{max} \quad (5.14)$$

$t_{max}$  is the time between the incidence of the shock wave and the instant when the interface length reaches its peak value. The flame length grows due shock induced deposition of vorticity at the flame front. At the same time, flame length is diminished by accelerated flame propagation. This “burning out” is related to the chemical kinetics of the flame, which is enhanced through the shock induced compression of the unburned gas mixture. The maximum flame length is reached when the rate of flame length destruction caused by flame propagation becomes equal to the rate of flame length increase. In Figure 5.6  $t_{max}$  is plotted as a function of  $M_i$  for s/f and f/s interaction modes. It is based on data reported by Kilchyk in [84] and [85] for stoichiometric propane-air combustion. In his work he demonstrates that  $t_{max}$  linearly depends on the fuel consumption rate per unit surface area of the flame  $\rho s_L$ , also called the burning rate. The burning rate of the methane-oxygen-argon mixture at standard conditions ( $p_{ref} = 1 \text{ bar}$ ,  $T_{ref} = 298 \text{ K}$ ) is  $(\rho s_L)_{Methane} = 1.045 \text{ kg/m}^2\text{s}$ . It is considerably higher than that of the propane-air gas mixture  $(\rho s_L)_{Propane} = 0.558 \text{ kg/m}^2\text{s}$ . Because of the higher rate of flame propagation, the maximum interface growth time is shorter in more reactive mixtures [84], [140]. Therefore, the growth times  $t_{max}$  reported by Kilchyk were multiplied by the correction factor  $C_t = (\rho s_L)_{Propane}/(\rho s_L)_{Methane}$ , in order to account for the higher burning rate of the combustible mixture used in the present study.

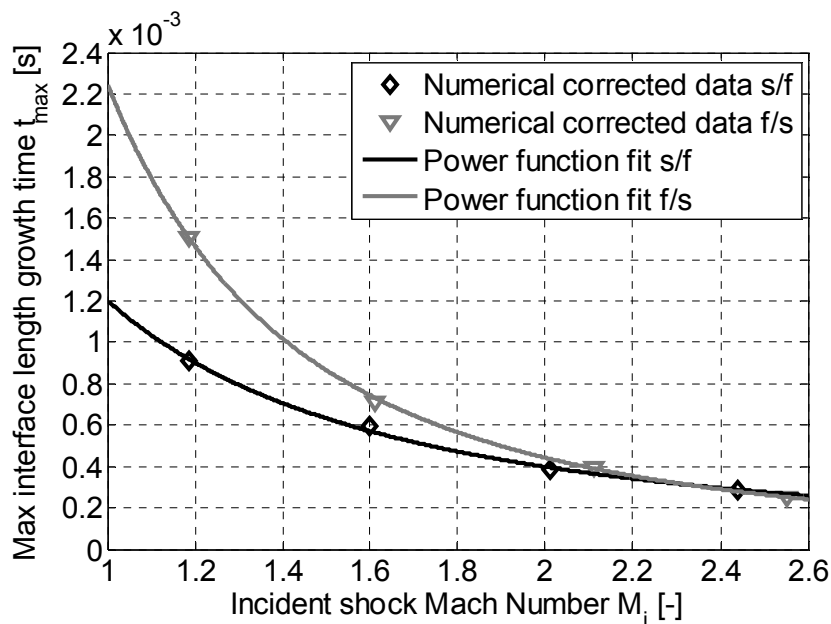


**Figure 5.6:** Maximum interface growth time as a function of incident shock Mach number

An increase in the strength of the incident shock wave has two effects: it produces higher interface growth rates  $v_{\text{int}}$  and enhances the chemical kinetics of combustion. The latter effect grows faster than  $v_{\text{int}}$  for stronger incident shocks. Such behaviour leads to a decrease of  $t_{\text{max}}$  with rising  $M_i$  in both interaction modes. This decrease is best described by a power function as shown in Figure 5.6. The former effect is stronger in f/s-interaction leading to higher values of  $t_{\text{max}}$  at low shock Mach numbers for this type of interaction. The compression effects and associated increases in the burning rate are stronger for f/s-interaction, which results in a higher decrease rate of  $t_{\text{max}}$  for strong incident shocks than in the s/f mode [84].

With the use of data presented in Figure 5.6 it is possible to calculate the maximum length increase of a two dimensional, sine-shape flame of a given initial geometry ( $\epsilon_0$ ,  $\lambda$ ) resulting from interaction with a shock wave of a given strength  $M_i$ . The corresponding total increase in the flame surface area of the deformed flame  $\Delta A_F$ , that is required for further treatment, is obtained by the Guldinus theorem. Thereby, the flame is assumed to have a symmetric shape as per Figure 3.3 d), and the centre of gravity of the curve halves is assumed to be at  $1/4D_T$  or  $3/4D_T$  respectively. Flame stretch effects have been shown to have a minor contribution to the overall change in the geometry of the flame [85] and are therefore neglected.

### 5.1.5 Generation of Pressure Waves at the Distorted Flame Front

The following relation is used to calculate the increase in the heat release rate of the flame  $\Delta\omega$  resulting from the known total increase in the flame surface area  $\Delta A_F$  [32]:

$$\Delta\omega = q \rho_u s_L \frac{\Delta A_F}{A_L} \quad (5.15)$$

In this equation  $q$  is the constant energy release per unit mass of the combustible mixture,  $A_L$  is the surface area of an ideal, planar laminar flame, and  $\rho_u$  is the density of the unburned gas. With regard to the notation of Figure 3.2 or Figure 5.7 the unburned gas corresponds to the gas in the state 4. The laminar flame velocity  $s_L$  is determined using equation (5.8).

The perturbation theory derived by Chu [30], [31], [32] (see Chapter 3.2.4) provides an analytical framework for calculating the finite pressure rise  $\Delta p$  that is generated in response to finite changes in the heat release rate of the flame  $\Delta\omega$ . For the idealised situation where the ratio of specific heat capacities is constant across the flame front, a simplified relation  $\Delta\omega = f(\Delta p)$  is given in eq. (3.15). For the case  $\kappa_u \neq \kappa_b$ , the pressure wave generated cannot be entirely attributed to changes in the flame HRR. The relationship between  $\Delta p$  and  $\Delta\omega$  is then more complex and involves a dependence on the changes in the burning velocity of the flame  $s_F$ , which is a function of mixture composition, and unburned gas temperature and pressure [51]. This relation is then given as follows [32]:

$$\Delta\omega = \frac{K_5}{K_5 - 1} \Delta p(u_5 - u_4) + \frac{K_5}{K_5 - 1} (p + \Delta p)(\Delta u_5 - \Delta u_4) + \left( \frac{K_5}{K_5 - 1} - \frac{K_4}{K_4 - 1} \right) (s_F \Delta p + p \Delta s_F + \Delta p \Delta s_F) \quad (5.16)$$

The notation in this equation is that of Figure 3.2 or of Figure 5.7 alternatively.  $\Delta u_5$  and  $\Delta u_4$  are the changes in the gas flow velocity in the burned and unburned gases, respectively. They result from the action of the generated pressure waves.

An iterative calculation procedure based on eq. (5.16) is implemented to determine the strength  $\Delta p$  of the generated pressure waves. In reality the process of shock wave generation is a continuous one, where every infinitesimal increase in flame surface area produces a weak pressure wave on both sides of the flame. Every successive pressure wave propagates at a higher velocity than the preceding one. These waves coalesce and form a finite amplitude pressure wave or even a shock wave, provided that the total increase in the HRR of the flame is high enough. In the present model the mechanism of pressure wave generation is implemented as a discontinuous process. Thereby, two weak shock waves of equal strength  $\Delta p$  are suddenly released at the flame front at the moment when the maximum interface growth time  $t_{max}$  is reached. This situation is schematically shown in Figure 5.7 for both interaction modes.

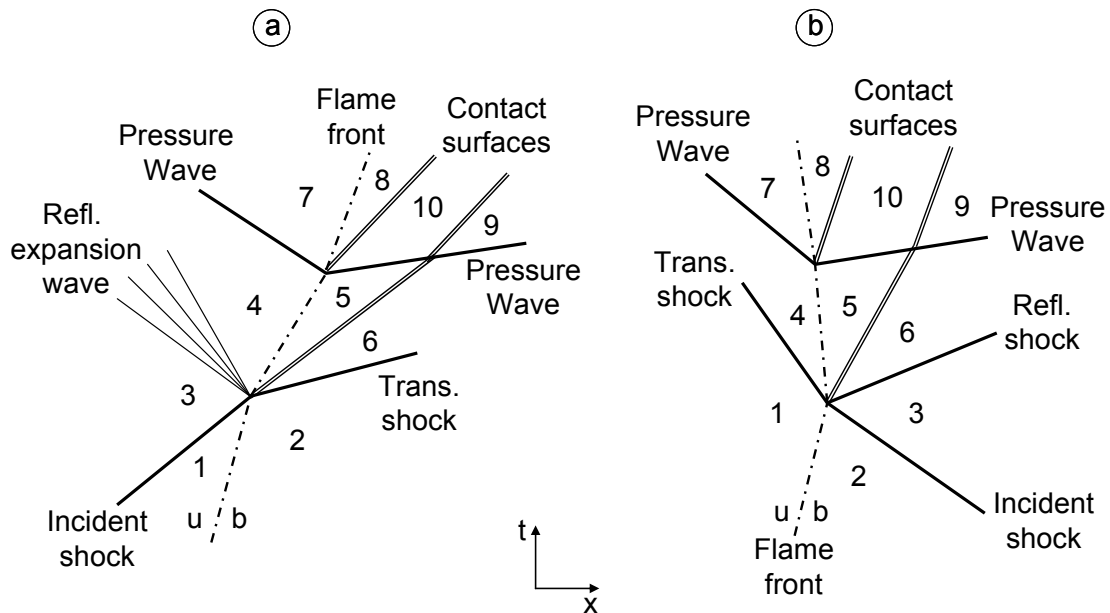


**Figure 5.7:** Wave diagrams of shock refractions and additional, combustion induced pressure waves generated at the flame front for a) s/f and b) f/s modes of interaction

The refraction part (regions 1-6) of the diagrams in Figure 5.7 is identical to the Figure 3.2. The growth of the flame front surface starts at the instant when the incident shock hits the

initial flame front. Both weak shock waves that are released at the flame at the moment of maximum flame surface area propagate at different absolute velocities in the burned and the unburned gas. An additional contact surface evolves when the pressure waves are released at the flame front. It separates two burned gas regions in which the gas undergoes a different entropy rise; see Chapter 3.2.4. Together with the generated pressure waves and the flame front it establishes four additional regions with different flow conditions (regions 7-10). Finally, a set of simple shock equations as well as the continuity conditions across the contact surface (eq. (3.7)) are applied in order to determine the unknown flow variables in these regions.

## 5.2 Model Verification on the Basis of Experimental Results

Experimental shock-flame interaction data reported in Chapter 4 was used for the verification of the analytical model. In Table 5.1 the sets of the model input parameters are presented for the four experimental cases.

	Case 1	Case 2	Case 3	Case 4
$p_{\text{fill}}$ [bar]		2.15		
$T_{\text{fill}}$ [K]		295.5		
$\lambda$ [m]		$2D_T = 0.092$		
$p_1$ [bar]	2.9	2.95	3.05	3.0
Interaction mode	s/f	s/f	s/f	f/s
$U_i$ [m/s]	354	400.5	461.2	1080
$u_1$ [m/s]	-73	-75	-75	30
$M_i$ [-]	1.24	1.39	1.56	1.12
$\varepsilon_0$ [m]	$0.7\lambda$	$1.222\lambda$	$1.574\lambda$	$1.48\lambda$
$A_F/A_L$ [-]	2.36	3.78	4.77	4.5

**Table 5.1:** Model input parameters for the four experimental cases

In Figure 5.8 a comparison between the experimentally acquired data and the analytical solution is presented in the form of wave diagrams for the four experimental Cases 1-4. Experimentally measured shock wave and flame front trajectories are given by blue circles and red crosses respectively. Solid lines represent the results of the analytical calculation. The analytical model predicts the physical phenomena after a single shock-flame interaction event. For this reason, the trajectories of all secondary reflected waves observed in the experiments, see Figure 4.16 and Figure 4.18 for reference, are omitted from these diagrams. The

times and lengths given on the axes of the diagrams do not correspond to the nominal experimental values. However, all time intervals and distances are reproduced correctly. Comparison is achieved by centering the predicted point of interaction (point I) at the light sensor at which the interaction occurred in the according experiment.

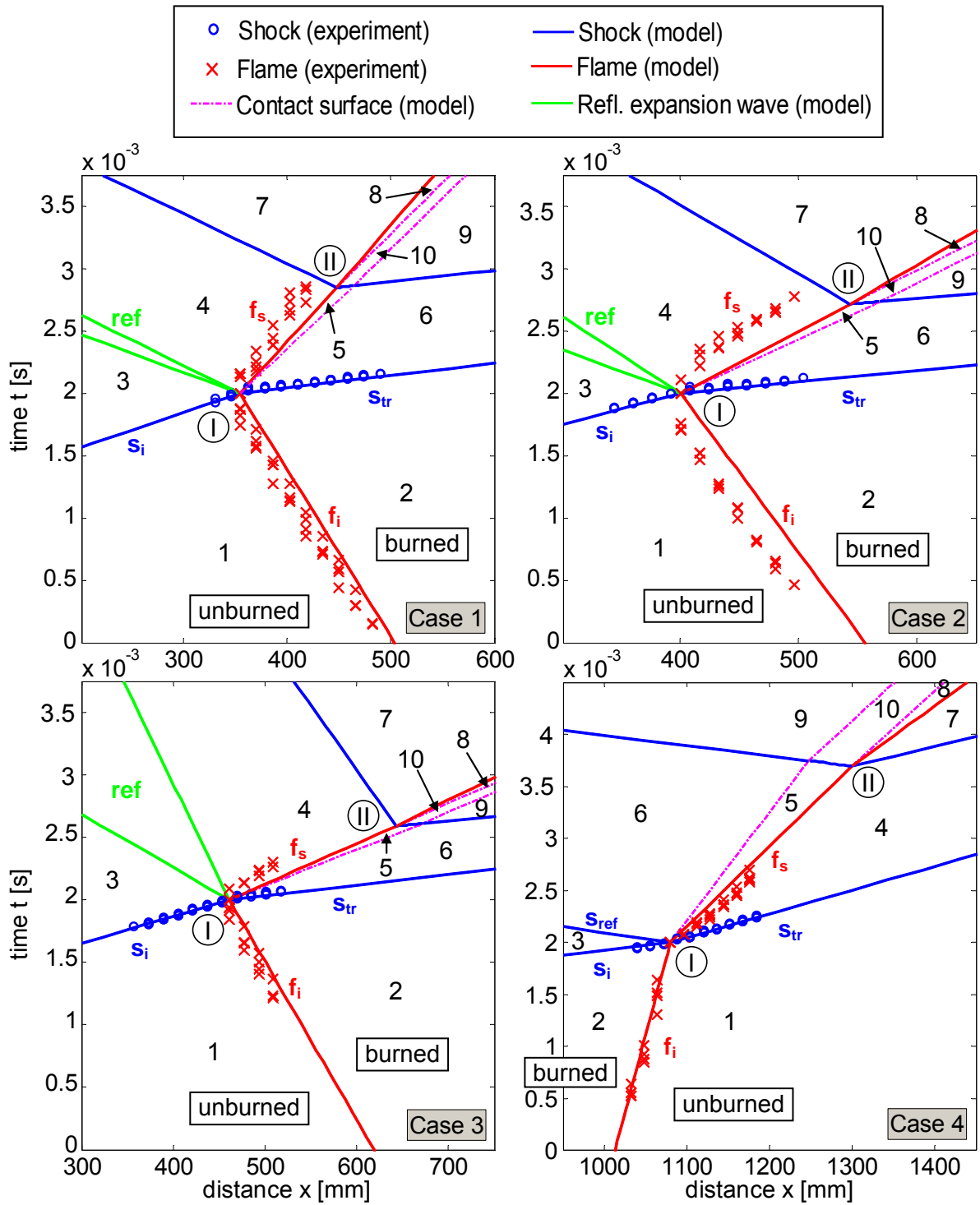


**Figure 5.8:** Wave diagrams of the shock-flame interaction event including experimental and analytically calculated data for the Cases 1-4

Point I in the diagrams marks the instant and location of interaction between the incident shock wave  $s_i$  and the undisturbed flame front  $f_i$ . In the Cases 1-3 the mode of interaction is slow-fast, which produces a transmitted shock  $s_{tr}$  and a reflected expansion wave  $ref.$  In the Case 4 both the reflected  $s_{rf}$  and the transmitted  $s_{tr}$  waves are shocks because of the  $f/s$  nature of interaction.

In the  $x-t$  diagrams the wave propagation velocity is represented by the slope of the wave trajectories. In all Cases, the experimentally measured absolute propagation velocities of the incident and the transmitted shocks as well as of the initial flame front are at very good agreement with the analytical calculation. The discrepancy between the location of the experimental and the analytically predicted initial flame front (e.g. Case 2) is due to the idealised modelling of the interaction event. In the analytical model the interaction is assumed to occur at a point in time and space, i.e. at an ideally plane flame front. Conversely, in the experiment, the interaction extends over an axial distance because of the elliptical geometry of the flame front. This difference renders an exact centring of the two events very difficult.

The analytical model seems to overestimate the propagation velocity of the distorted flame front  $f_s$  after the interaction in Cases 1-3. This may be due to the fact that the continued growth of the flame surface area is disregarded in the modelling of the propagation velocity of  $f_s$  between points I and II. As has been discussed previously, a flame is expected to continuously produce a series of weak pressure waves as its surface area grows. These pressure waves modify the flow conditions in the unburned gas, which as a consequence alters the absolute propagation velocity of the flame.

When the growing flame surface area reaches its maximum value two shock waves of equal strength are predicted to be released by the distorted flame front at the point II. These shock waves have the same strength  $\Delta p$ , but they propagate at different velocities in the burned and the unburned gases. Origination of pressure waves at points I and II leads to the formation of a gas contact surfaces at these points. The trajectories of the various pressure waves, flame fronts and the contact surfaces subdivide the fluid domain into ten regions containing different flow conditions.

An additional verification of the analytical model data is performed by the comparison of the analytically predicted static pressure levels in the different fluid regions with the experimental pressure data. In Figure 5.9 a representative pressure record is shown for each of the Cases 1-4 (pressure sensor P1 in all cases). These pressure records are best understood by drawing a vertical line through the first experimental shock point (first circle on the left hand side) in each of the diagrams of Figure 5.8. The presented pressure profiles correspond to the pressure records along this line. The different flow regions crossed by this line are marked through italic numbers in the diagrams of Figure 5.9. The measurement time is limited by the arrival of secondary reflections that appear on the right in each of the pressure diagrams.

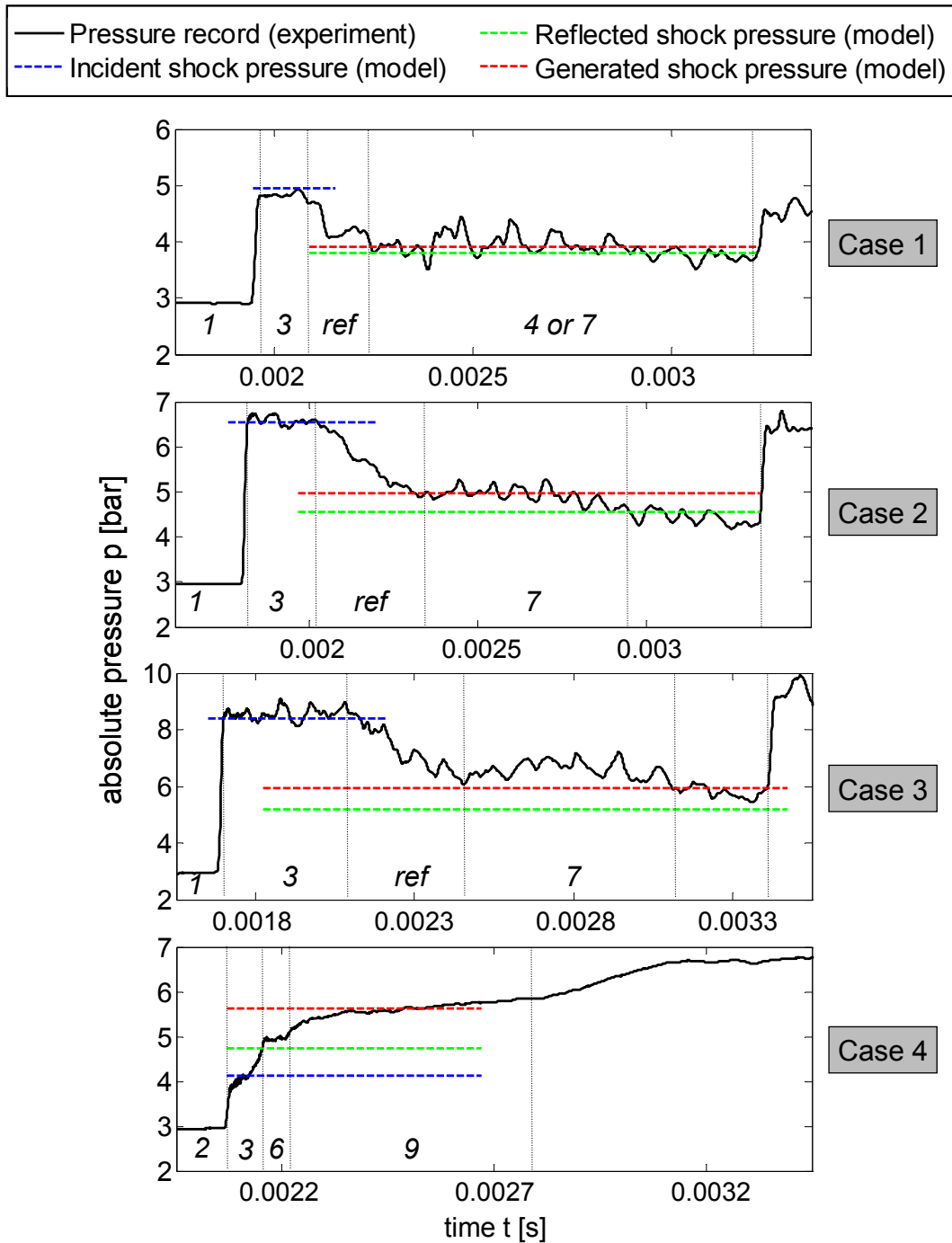


**Figure 5.9:** Comparison of experimentally measured and numerically predicted pressure levels for the experimental Cases 1-4

It is evident from the diagrams in Figure 5.9 that the pressure behind the incident shock wave (region 3) is correctly predicted by the analytical model (blue dashed line) for all experimental Cases 1-4. For the s/f-interactions, i.e. Cases 1-3, the pressure behind the incident shock is gradually reduced through the action of the reflected expansion wave ref. From the corresponding x-t-diagrams it is expected that the pressure behind the expansion wave would be that of region 4, which is represented by the green dashed line. However, the pressure in the



fluid behind the expansion wave temporally remains at an elevated level corresponding to that of the red dashed line. This line represents the pressure behind the additional shock wave (region 7) that is predicted to be generated at the end of the flame surface growth period. The difference between the dashed green and the red lines denotes the absolute strength  $\Delta p$  of the generated shock wave. Such behaviour agrees well with the more realistic assumption of the flame that produces pressure waves immediately when the process of flame surface growth is initiated. This means that the pressure waves emitted by the distorted flame arrive at the location of the pressure sensor before the expansion process is completed and the state of region 4 is attained. When the maximum flame growth time  $t_{\max}$  is reached the fine-scale structures of the deformed flame quickly burn out and the flame becomes wrinkled-laminar again [98], [140]. At the instant when the flame surface area ceases to grow, the amount of energy added to the fluid through elevated gas expansion rate is suddenly reduced. This causes the static pressure to drop from that of level 7 back to some level corresponding to the new flame shape. Since the flame does not regain the exact shape of the initial undisturbed laminar flame, this pressure is expected to lie above the pressure of region 4. It is noted that the unsteady, high-frequency pressure oscillations are disregarded in this analysis. The best agreement between the analytical results and the experimental data is achieved in the Case 2. For the Case 1 (weak incident shock) the strength of the flame-generated shock wave is very small and no clear conclusion can be drawn. For strong incident shocks (Case 3) the behaviour is analogous to that of Case 2. However, the strength of the flame-generated shock wave seems to be underestimated by the analytical model.

In the Case 4 the interaction mode is f/s. Thus, the incident shock wave (region 3) is followed by the reflected shock wave  $s_{\text{ref}}$ . The static pressure behind it (region 6) is slightly underestimated by the analytical model; see the green dashed line in Figure 5.9. A very short period of time later an additional increase in pressure is observed. This pressure rise is brought about by the passage of the flame-generated shock wave. The static pressure behind this wave corresponds to that of region 9 in Figure 5.8 Case 4. This pressure level is correctly predicted by the analytical model as shown by the dashed red line in the Case 4 of Figure 5.9.

It is concluded that the shock and flame propagation velocities following a refraction of an incident shock at a variable geometry flame front are predicted correctly for both interaction modes. The model also correctly reproduces the static pressure levels in the different flow regions of the shock refraction system. Further, the model yields a good prediction for the strength of the pressure waves that are generated due to a total increase in the surface area of the flame. The agreement is very good for low incident shock Mach numbers. For stronger incident shocks the strength of the generated pressure waves tends to be underestimated by the model. The discrepancy in static pressure behind the flame-generated pressure wave is around 15 % for  $M_i = 1.56$ . A rectification can be achieved by accordingly modifying the con-

starts used in the calculation of deposited circulation  $\Gamma$  and the interface growth rate  $v_{int}$ . This would require detailed numerical or experimental studies of shock induced deformation of methane-oxygen-argon flames. The Mach numbers of the shock waves generated at the flame at the point II are predicted to be  $M_{fs} = 1.012/1.036/1.058$  and  $1.076$  in the four experimental Cases 1-4 respectively.

### 5.3 Results and Discussion

One of the most practical questions in the area of shock-flame interactions is the dependence of the resulting effects on the strength of the incident shock wave. For this reason the results of the analytical model are presented as a function of two parameters: the incident shock Mach number  $M_i$  and the initial flame geometry characterised by the aspect ratio  $\varepsilon_0/\lambda$ . Additionally, the values belonging to the experimental Cases 1-4 (see Chapter 5.2) are shown for reference in the respective diagrams.

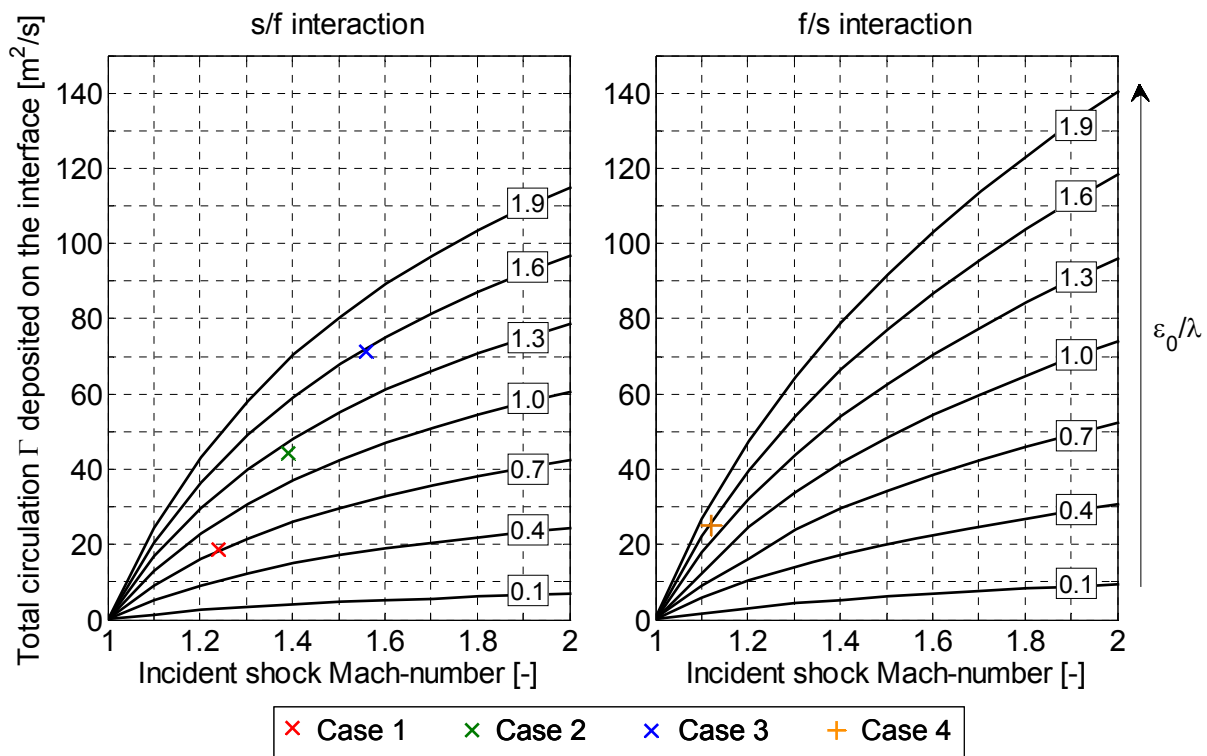


**Figure 5.10:** Total deposited circulation as a function of incident shock Mach number and initial flame geometry

In Figure 5.10 the total circulation  $\Gamma$  deposited on the flame front as a result of shock wave transition is presented for both interaction modes. The total amount of deposited circulation grows with the strength of the incident shock and with the curvature of the initial interface.

For the same values of  $M_i$  and  $\varepsilon_0/\lambda$  the circulation deposited in fast/slow interactions is higher than that of slow/fast interactions. These findings agree well with the results reported by Kilchuk in [84].

As per equation (5.13) the length growth rate  $v_{int}$  of the two-dimensional, sinusoidal flame front is a linear function of deposited circulation  $\Gamma$  and the geometrical parameters of the flame front  $\varepsilon_0$ ,  $\lambda$ . Consequently,  $v_{int}$  exhibits an analogous behaviour to that shown in Figure 5.10 when plotted as a function of  $M_i$  and  $\varepsilon_0/\lambda$ ; see Figure 5.11. The difference between the s/f and the f/s interaction modes is more pronounced in the interface growth velocities than it is for the deposited circulation. This is because of the higher proportionality constant  $A$  used for the fast/slow interaction mode in eq. (5.13). Such behaviour is based on the observations made by Kilchuk in [84] for stoichiometric propane-air flames. He reports significantly higher interface growth rates in fast/slow interactions for a given interface geometry and incident shock strength.

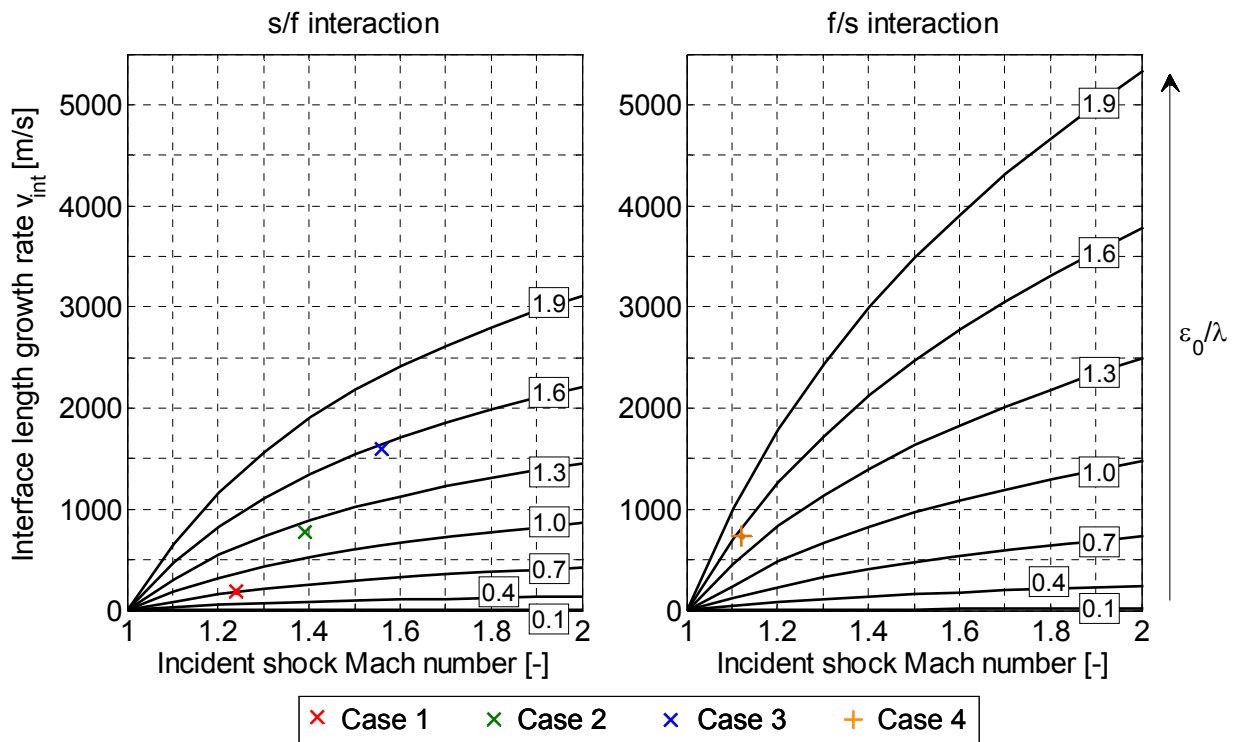


**Figure 5.11:** Length growth rate of the two-dimensional flame front as a function of incident shock Mach number and initial flame geometry

In Figure 5.12 the maximum change in the heat release rate (HRR) of the three-dimensional flame, normalised by the heat release rate of the initial undisturbed flame, is plotted as a function of  $M_i$  and the geometrical parameters of the flame front  $\varepsilon_0$ ,  $\lambda$ . The maximum value of flame heat release rate shown in Figure 5.12 is achieved at the point of maximum flame surface area. The total increase in the HRR of the flame rises with the curvature (aspect ratio

$\varepsilon_0/\lambda$ ) of the flame in both interaction modes. In terms of the incident shock Mach number a different trend is observed. For low values of  $M_i$  the flame HRR grows quickly with incident shock strength until a certain maximum value is reached. At this point the trend is reversed, and the maximum increase in the heat release rate diminishes with growing  $M_i$ . These effects are considerably stronger in the f/s type of interaction. Such behaviour is due to the linear dependence of the heat release rate on two opposing effects – gas compression and flame surface growth; see equation (5.15). For low shock Mach numbers the flame front distortion effects due to RMI are predominant, which leads to a strong increase in HRR in this region. The flame surface area grows at a significantly higher rate in f/s-interaction as can be seen from Figure 5.11. Subsequently, higher rates of gas compression caused by stronger incident shocks diminish the maximum interface growth time; see Figure 5.6. For growing incident shock strength the reduction of interface growth time is considerably faster than the increase in interface growth velocity. Hence, gas compression becomes dominant and the relative contribution of the flame deformation effect is reduced [84], [85]. As a consequence, the change in the heat release rate of the flame is reduced. This effect is significantly stronger in fast/slow interactions.

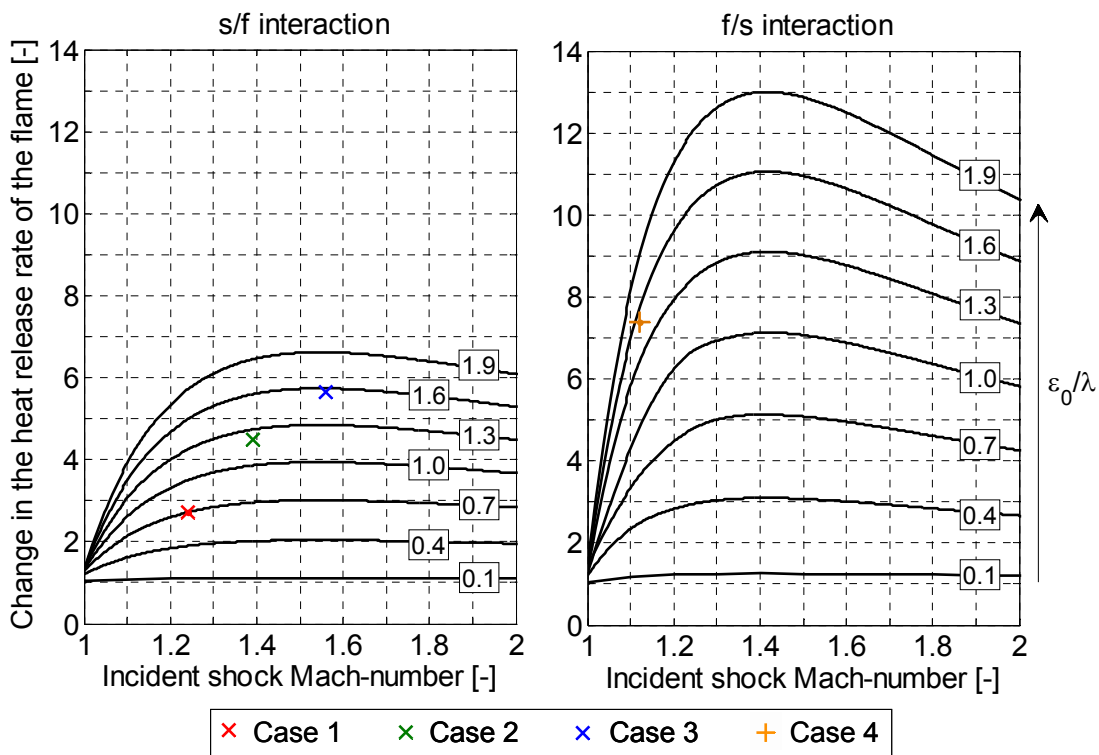


**Figure 5.12:** Maximum increase in the heat release rate of the flame relative to the undisturbed flame as a function of incident shock Mach number and initial flame geometry

The thermodynamic potential of a single shock-flame interaction is best assessed when compared to a reference isobaric combustion process with the same initial gas state. Be-92

cause of the very low Mach number ( $M_f \ll 1$ ) of the initial undisturbed flame front the pressure change across this flame is negligible [32], [47]. Hence, this burning process is a good approximation of an ideally isobaric combustion. In the wave diagrams of Figure 5.8 this process is represented by the change of state from region 1 to region 2.

The fluid regions 4-6 in Figure 5.8 describe the conditions in the burned and unburned gas after the shock refraction process. The final fluid conditions after the interaction process are represented by the regions 7-10. The shock-modified combustion process is described as follows. An imaginary gas particle of initial fresh gas is subject to the action of pressure waves along the path  $1 \rightarrow 3 \rightarrow 4 \rightarrow 7$  in s/f, or  $1 \rightarrow 4 \rightarrow 7$  in f/s interaction mode, respectively. Finally, the pre-compressed, unburned gas of region 7 is burned in a quasi-isobaric combustion process  $7 \rightarrow 8$  at the highest possible pressure in the domain. Consequently, the burned gas in region 8 is that with the lowest entropy rise relative to the initial gas in state 1.

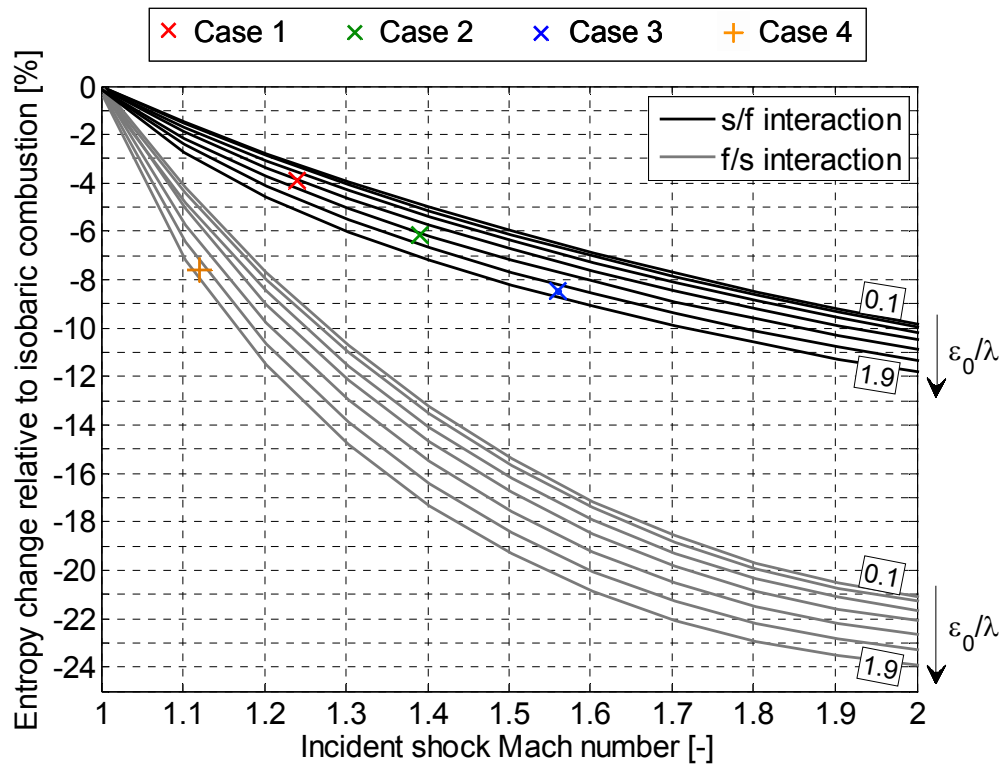


**Figure 5.13:** Change in entropy relative to isobaric combustion as a function of incident shock Mach number and initial flame geometry

In Figure 5.13 the change in entropy of the shock-augmented combustion process is given relative to the entropy gain across the reference isobaric combustion  $1 \rightarrow 2$ . The entropy for the shock-modified combustion is taken along the process path  $1 \rightarrow 3 \rightarrow 4 \rightarrow 7 \rightarrow 8$  for s/f, and  $1 \rightarrow 4 \rightarrow 7 \rightarrow 8$  for f/s-interaction, respectively. The change in entropy is plotted as a function of incident shock Mach number  $M_i$  and the flame front aspect ratio  $\epsilon_0/\lambda$  for both interaction modes. The combustion entropy is significantly reduced through a single shock-flame inter-

action compared to the reference isobaric combustion process. Interaction of strong incident shocks with highly curved flames produces higher rates of entropy reduction. The entropy reduction is more than twice as high in fast/slow than in slow/fast interactions. This is due to stronger gas compression effects as well as higher circulation deposition and interface growth rates in this type of interaction [84], [85]; see Figure 5.10 - Figure 5.12.

In Figure 5.14 the changes in static and total pressure at the end of the shock-flame interaction process (region 8 in Figure 5.8) are shown relative to the pressures at the end of the reference isobaric combustion. The achievable static pressure rise increases with growing incident shock strength and flame aspect ratio. The difference between the f/s and the s/f interaction modes is considerably larger than that in terms of the entropy in Figure 5.13. It grows with the incident shock Mach number  $M_i$ . This is a direct implication of the different nature of the refraction processes. The fact that in the f/s-refraction both resulting waves are shocks leads to a significantly higher gas compression than in the slow/fast case. These effects are analogous but even stronger in the total pressure comparison presented in the diagram on the right hand side of Figure 5.14.

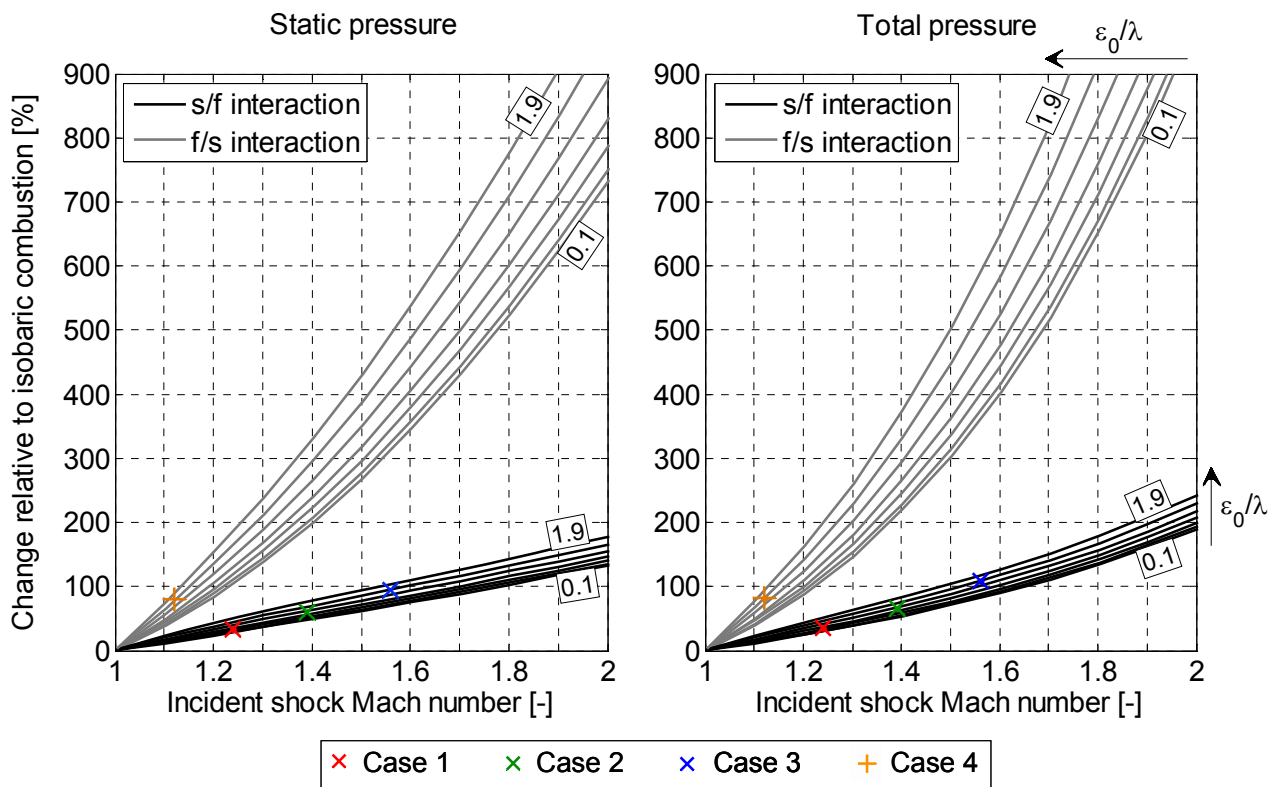


**Figure 5.14:** Change in static and total pressure relative to isobaric combustion as a function of incident shock Mach number and initial flame geometry

In Figure 5.15 the changes in static and total temperatures of the combustion products at the end of the shock-flame interaction process are given relative to the temperatures at the end

of the isobaric combustion. The static temperature at the end of the reference isobaric combustion process is 2913.4 K. Hence, one percent change in temperature in Figure 5.15 corresponds to a temperature difference of 29.13 K. The dependence on incident shock strength and flame geometry is analogous to that observed for the pressures in Figure 5.14. However, the total values of temperature increase are considerably smaller than those of the corresponding increase in pressure.

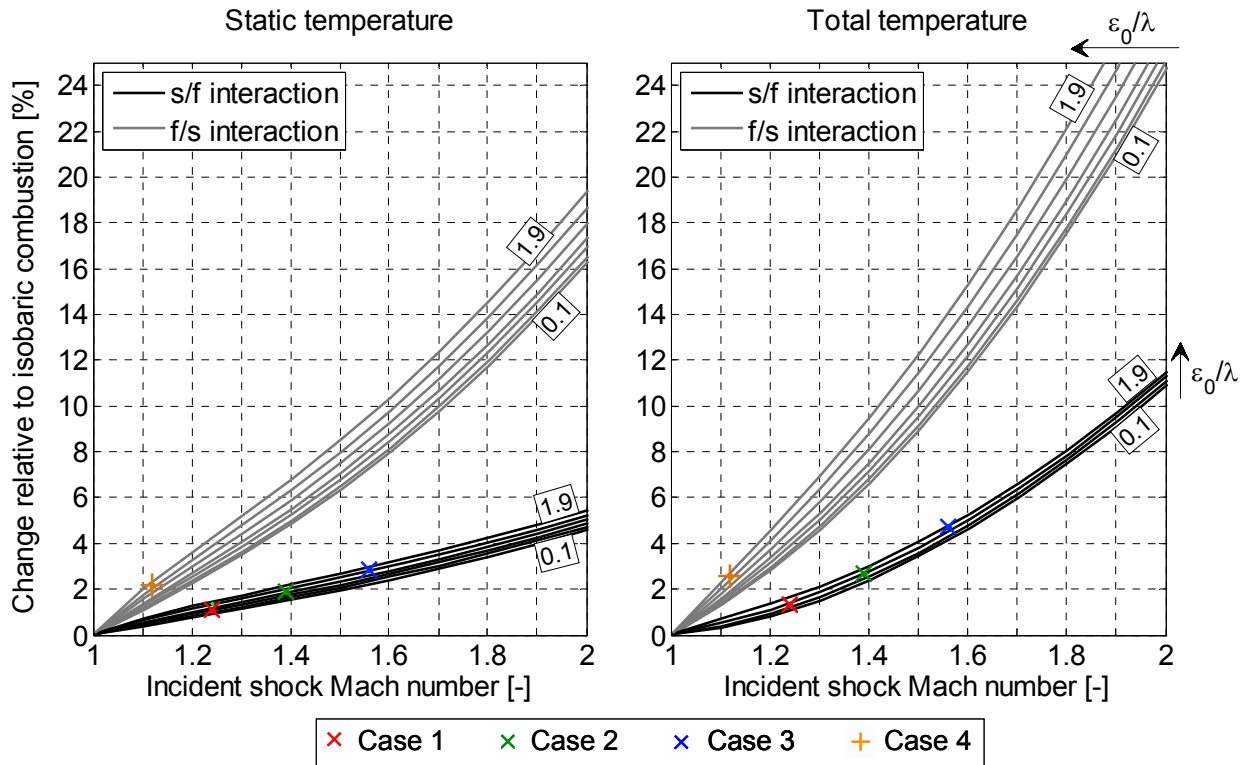


**Figure 5.15:** Change in static and total temperature relative to isobaric combustion as a function of incident shock Mach number and initial flame geometry

It is concluded that a single shock-flame interaction event temporally generates a significant increase in pressure, whereas the according increase in temperature remains at a relatively moderate level. Thus, weak incident shock waves with  $M_i < 1.3$  produce an increase in static pressure of up to 230 % or 60 % relative to the reference isobaric combustion for f/s or s/f interaction modes, respectively. The associated rise in static temperature is around 5.4 % (157.3 K) or 1.9 % (55.4 K), respectively. However, it is important to recognise that the reduction of entropy is not so temporary. Indeed if the subsequent expansion is isentropic, then it is long lived. It is noted that the comparison in total pressure and total temperature is made independently of the flow direction in the respective gas regions. In some cases the direction of the flow was reversed from state 2 to state 8 due to the action of propagating pressure waves.

In the case of a perfectly plane flame front only the effects brought about by shock refraction would be present. Such combustion process is represented by the combustion products in region 5 in the diagrams of Figure 5.8. Changes in entropy, pressure and temperature caused by this process relative to the reference isobaric combustion would be represented by the line with  $\varepsilon_0/\lambda = 0$ , when plotted into the Figures 5.13 – 5.15. This line virtually coincides with that for  $\varepsilon_0/\lambda = 0.1$  in each of the diagrams. The values of the two lines differ marginally by 0.02 – 0.05 percentage points. For the sake of clarity, the  $\varepsilon_0/\lambda = 0$  line is omitted from the diagrams. The  $\varepsilon_0/\lambda = 0.1$  line in each of the diagrams in Figures 5.13 – 5.15 can hence, be considered as a good approximation of the combustion effects resulting from the shock interaction with a perfectly plane flame front. This line in each of the respective diagrams therefore represents the effects brought about by shock refraction only, since no flame surface growth is possible in the case of a plane flame. The difference between the  $\varepsilon_0/\lambda = 0.1$  line and the lines depicting higher  $\varepsilon_0/\lambda$ -values represents the change in the thermodynamic state brought about by flame surface growth effects. From such comparison it is followed that for very weak incident shocks ( $M_i < 1.1$ ) changes in pressure, temperature and entropy rise are dominated by flame surface growth effects. For stronger incident shocks the proportions are reversed and the relative contribution of gas compression effects due to shock refraction becomes predominant.

The steady gas conditions given in region 8 of Figure 5.8 merely exist in a small gas volume for a very short period of time, as demonstrated by experimental data in Chapter 4.3. In order to achieve a resultant quasi-steady pressure rise the shock-flame interaction process must be repeated at a certain frequency. Volume and time averaging of the resulting unsteady fluid flow will reduce the achievable pressure-gain below that of a single shock-flame interaction process presented above in Figures 5.13 – 5.15. Conversely, repeated interaction between a shock wave and an already distorted flame will significantly enhance the thermodynamic pressure-rise potential of a single SFI event [81], [82]. These considerations highlight the importance and the need of further research into the topic of sequential shock-flame interaction and of an accurate flow averaging technique.



## 6 Engine Performance Studies

In this chapter the performance of a potential shock-wave-combustor enhanced gas turbine engine is assessed under steady-state operating conditions. A zero-dimensional [109], modular engine performance model is developed for two types of baseline engines: a small twin-spool industrial gas turbine and a twin-spool high-bypass turbofan engine. Subsequently, the conventional combustor of both baseline engines is replaced by a pressure-rising shock-wave-combustor including additional components for shock generation and turbine cooling. Steady-state performance of the shock-combustor modified engines is compared to their baseline engines' performance. The reported results highlight the improvement potential as well as the limitations of the shock-flame interaction based pressure-gain combustion concept.

### 6.1 Simplified Engine Performance Model

A Simplified Engine Performance Model was developed to calculate on-design engine performance. The simplifications particularly concern the modelling of engines' turbo components. Turbo-machinery maps are not used in the model. The different compressor and turbine modules are respectively characterised by single average polytropic efficiency values. Total pressure drops are implemented between the engine components to simulate the duct losses. The fuel applied in the model is kerosene with the heating value  $H_L = 43.124$  MJ/kg. The fluid is modelled as ideal gas, where specific heat capacity  $C_p$  is assumed to be a function of gas temperature and gas composition. Required gas properties are interpolated from tabulated thermo-chemical air-kerosene-mixture data with regard to local gas temperature and fuel-air-ratio (FAR). Given a set of design ambient conditions and a power setting, expressed through a given fuel mass flow rate  $\dot{m}_f$ , the model calculates necessary gas path values as well as global engine performance parameters.

#### 6.1.1 Baseline Gas Turbine Engine Models

Two baseline gas turbine engines were selected for engine performance studies. In Figure 6.1 the schematics of the baseline engines are presented for reference.

The first engine, denominated GT1, is a small twin-spool industrial gas turbine. In this gas turbine the useful power is extracted from the fluid by a power turbine that is also driving the low pressure compressor (LPC) of the engine. Exhaust gas is assumed to be expanded to ambient pressure, i.e. static pressure at station 8 is equal to the ambient pressure.

The second engine, called GT2, is a twin-spool high-bypass turbofan engine. This engine has a mixed exhaust flow and a convergent nozzle. At design conditions the nozzle is assumed to be choked, i.e.  $M_8 = 1$ .

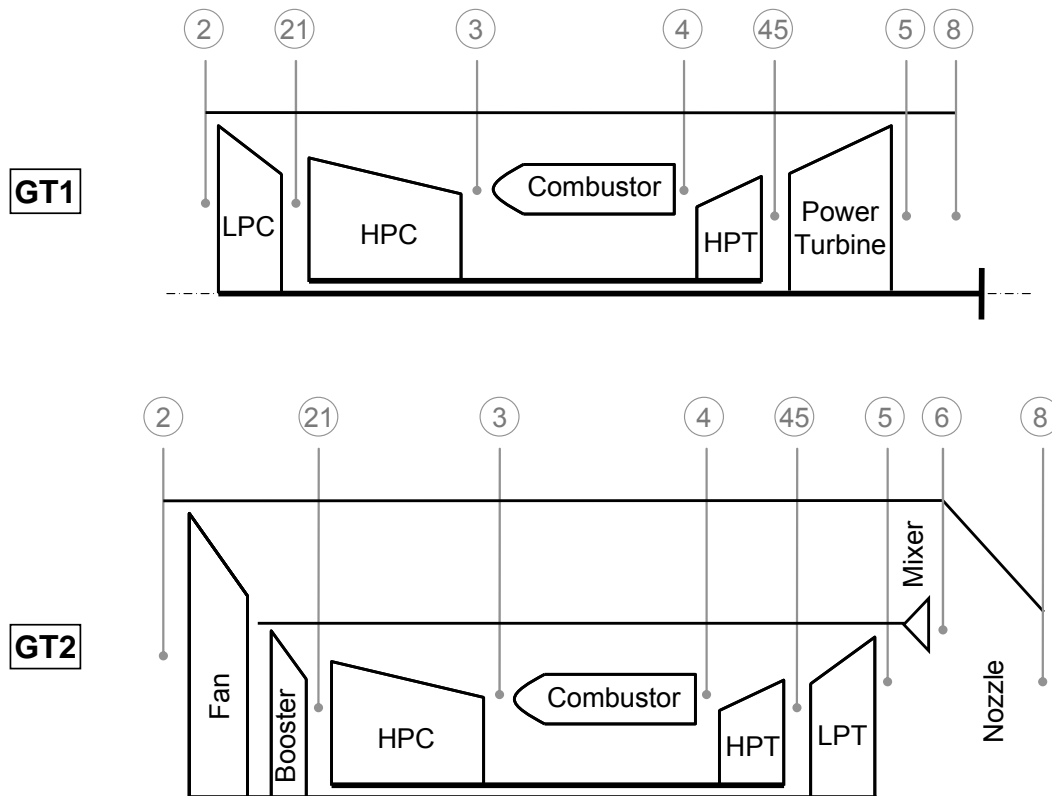


**Figure 6.1:** Configurations of the baseline engines, GT1: twin-spool industrial gas turbine, GT2: twin-spool high-bypass turbofan engine

Baseline engines GT1 and GT2 are realised using the Simplified Engine Performance Model described above. Design ambient conditions as well as selected performance characteristics of the two baseline engines are summarised in Table 6.1. Both engine models were successfully verified using the commercial gas turbine performance simulation software *GasTurb*<sup>TM</sup>.

	GT1	GT2
Altitude above sea level $h$ [m]	0	10668
Ambient pressure $p_{amb}$ [Pa]	101325	23848.05
Ambient temperature $T_{amb}$ [K]	288.15	218.8
Flight Mach number $M_{Fi}$ [-]	0	0.8
Total air mass flow $\dot{m}_2$ [kg/s]	4	143.6
Bypass ratio $\mu$ [-]	0	4.7
Overall pressure ratio OPR [-]	20	33
Combustor pressure ratio $\Pi$ [-]	0.97	0.97
Turbine entry temperature $T_{t4}$ [K]	1500	1425
HPT cooling mass flows to NGV / rotor $\dot{m}_{cool}$ [kg/s]	0.24 / 0.16	2.28 / 0.252
LPT cooling mass flows to NGV / rotor $\dot{m}_{cool}$ [kg/s]	0 / 0.08	2.771 / 0.63
Polytropic efficiency LPC / HPC $\eta_{pol}$ [-]	0.864 / 0.873	0.878 / 0.899
Polytropic efficiency HPT / LPT $\eta_{pol}$ [-]	0.860 / 0.855	0.881 / 0.904
Thermal efficiency $\eta_{th}$ [-]	0.332	0.432
Propulsive efficiency $\eta_{prop}$ [-]	-	0.755
Shaft power $P_s$ [kW]	1102.3	-
Power specific fuel consumption PSFC [kg/kWh]	0.2515	-
Net thrust $F_N$ [kN]	-	21.54
Thrust specific fuel consumption TSFC [kg/kNs]	-	0.0177

**Table 6.1:** Design ambient conditions and performance parameters of the baseline engines

## 6.2 Integration of a Shock Combustor into a Gas Turbine Engine

In order to assess changes in engine performance brought about by a shock-combustor topping a modification of the high-pressure cores of the baseline engines is required. In Figure 6.2 a shock-combustor engine integration variant proposed in this work is schematically presented. This scheme is analogously applied to the high-pressure cores of the two baseline engines.

First of all, a means of generating and controlling shock waves in the combustor is necessary. A shock wave, or a sequence of shocks, is generated by suddenly bringing in contact two gases of different pressure, e.g. by opening and closing a valve between two volumes of different pressure [114], [164]. If the pressure difference is high enough, the high-pressure

gas will expand into the low-pressure gas at a rate higher than the rate of acceleration of the low-pressure gas. This forms a propagating shock wave in the low-pressure medium. When the supply of high-pressure fluid is ceased, an expansion wave will evolve to expand the fluid behind the shock wave back to the initial pressure level. An idealised pressure profile of a propagating shock wave was shown and discussed in Figure 3.6. In the proposed integration scheme the high-pressure fluid for shock generation is provided by an additional shock compressor (SC). This compressor, which is driven by the high-pressure turbine (HPT), feeds a pressure vessel (PV). The pressure in the PV is assumed to be kept at a constant level that is sufficient to generate shock waves of certain strength in the combustor. The fraction  $\xi$  of the mass flow  $\dot{m}_3$  that is used for shock generation is extracted at the exit from the high pressure compressor (HPC). The air delivered by the HPC is also to be used for combustor cooling. Hence, the combustor is assumed to be appropriately cooled in the present model. For the mass flows it is assumed that at all times  $\dot{m}_4 = \dot{m}_3 + \dot{m}_f$ .

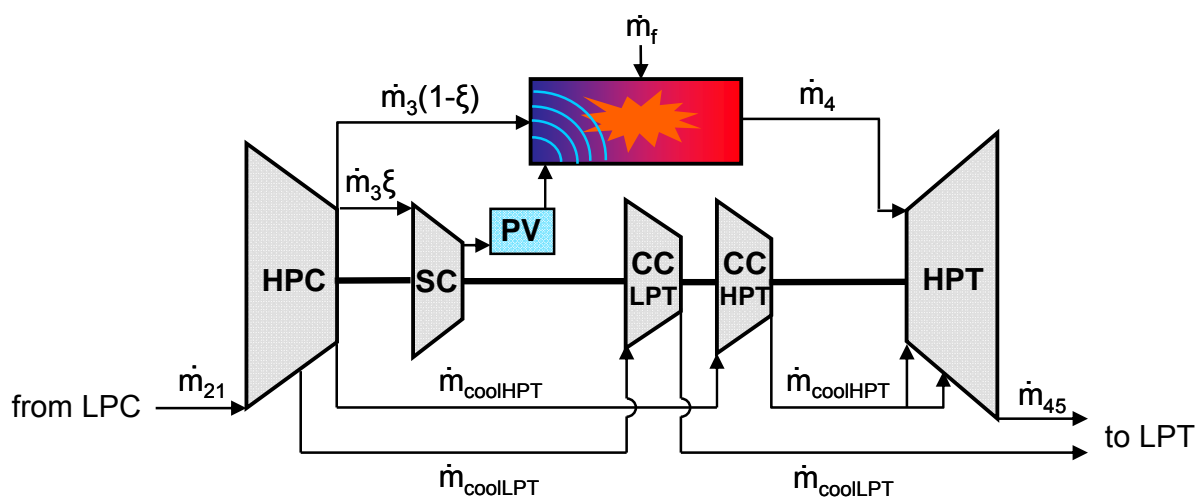


**Figure 6.2:** Schematics of the shock-combustor enhanced high-pressure engine core

The PV is connected to the combustion chamber through one or a series of fast-acting valves. Such configuration provides three independent variables for controlling or driving the shock-flame interaction process. These variables are the frequency of shock generation, the shock strength  $\Delta p$ , and the shock duration  $\Delta t$ ; see Chapter 3.3 for reference. The pressure amplitude of the shock waves  $\Delta p$  is defined by the pressure ratio between the PV and the combustor. The open phase time of the valve determines the high pressure duration  $\Delta t$  behind a propagating shock. At the moment of shock formation in the combustor a corresponding expansion wave is formed in the PV. This expansion wave propagates at the local velocity of sound. It reaches the opposite wall of PV, reflects from it, and finally returns to the valve [114]. The time interval between the opening of the valve and the arrival of the reflected ex-

pansion wave determines the maximum open phase of the valve. Consequently,  $\Delta t$  is limited by the length of the pressure vessel PV in the direction of rarefaction wave propagation. Finally, the shock frequency is directly governed by the operational frequency of the valve. The characteristic actuation time of the valve puts thereby a limitation upon the maximum achievable frequency. In practice, this restriction can be overcome by applying a series of valves that operate at a certain sequence.

The unsteady pressure-rise behaviour of such a shock-combustor as per Figure 6.2 would represent a major difficulty with regard to compressor air delivery. In practice, the operation of the compressor against a strong unsteady pressure gradient in the combustor may result in a temporal backflow of hot combustion gases into the compressor. In the present model it is assumed that the combustor is steadily fed by the upstream compressor. This issue will not be further addressed in the present work.

Another modification of the engine high-pressure core architecture is due to the need of turbine cooling. Because of the pressure rise in the combustor conventional methods of turbine cooling are not applicable. In the present study, this difficulty is overcome by compressing the turbine cooling air using two additional cooling compressors (CC). Both cooling compressors are modelled to be driven by the high pressure turbine. The location of cooling air extraction from the HPC is assumed to remain unchanged with regard to the baseline engines. Combustor modelling is modified in order to accommodate for the work-producing combustion process of a pressure-gain combustion chamber. Energy balance across a conventional steady-state gas turbine combustor is defined as follows using the notation of Figure 6.1 [109]:

$$\dot{m}_3 h_{t3} + \dot{m}_f H_L = \dot{m}_4 h_{t4} \quad (6.1)$$

Therein,  $\dot{m}_3$ ,  $h_{t3}$  and  $\dot{m}_4$ ,  $h_{t4}$  are the mass flow rates and the specific enthalpies at combustor inlet and exit respectively, and  $\dot{m}_4 = \dot{m}_3 + \dot{m}_f$ .  $\dot{m}_f$  is the fuel mass flow rate, and  $H_L$  represents the lower heating value of the fuel. The shock-combustor in Figure 6.2 is assumed to generate an average, steady-state total pressure rise resulting from sequential shock-flame interaction. This pressure rise is characterised by the combustor pressure ratio  $\Pi = p_{t4}/p_{t3}$ . Energy balance across the shock-combustor in Figure 6.2 yields the following equation:

$$\dot{m}_3 h_{tSC} \xi + \dot{m}_3 h_{t3} (1 - \xi) + \dot{m}_f H_L = \dot{m}_4 h_{t4} \quad (6.2)$$

The term  $h_{tSC}$  in eq. (6.2) represents the total enthalpy at the exit from the shock compressor. It is attained by using the compression ratio  $\pi_{SC}$  and the polytropic efficiency  $\eta_{SC}$  of the shock compressor; see Chapter 6.3. Consequently, a portion of the mass flow is added to the combustor at the enhanced enthalpy  $h_{tSC}$ . Given a pre-defined combustor entry temperature  $T_{t3}$  ( $h_{t3}$ ) a combustion process with pressure-rise (eq. (6.2)) yields a higher combustion end temperature  $T_{t4}$  ( $h_{t4}$ ) than the corresponding isobaric process (eq. (6.1)). Contrariwise, a pres-

sure-gain combustion process allows a reduction of the fuel mass flow rate that is necessary to reach a certain defined temperature  $T_{t4}$  at combustor outlet. Rearranging equation (6.2) one gets:

$$\dot{m}_f = \dot{m}_3 \frac{h_{t4} - h_{t3}(1 - \xi) - h_{tSC}\xi}{H_L - h_{t4}} \quad (6.3)$$

Equation (6.3) represents the corrected fuel mass flow rate for a given shock compressor characterised by  $h_{tSC}$  as a function of pre-defined enthalpies (temperatures) at combustor inlet and outlet.

### 6.3 Performance Results of Shock-Combustor Enhanced Engines

High-pressure cores of the two baseline engines are replaced by the shock-combustor topped configuration as per Figure 6.2.

The “redesigned” shock-combustor topped engines have the same airflow into the engine as well as the same cooling and bleed flows as their respective baseline engines at design ambient conditions (see Table 6.1). In addition, the compressor components of the baseline and the modified engines are identical.

The corrected mass flow rates  $\dot{m}\sqrt{RT_t}/p_t A$  to the HPT and LPT of the shock-combustor topped engines are reduced due to increased total pressure at combustor outlet. In the present calculations, the areas  $A$  of the turbines, i.e. their diameters, are assumed to be accordingly reduced to accommodate the lower corrected mass flow. Thereby, the polytropic efficiencies of the turbine components remain equal to those of the baseline engines, unless explicitly stated otherwise. In application, this change in corrected flow would require a complete redesign of the LPT and HPT to match the compression system and to accommodate the unsteady nature of the combustor flow. This issue is however not further addressed in the present work.

The effective compression ratio of the HPT and LPT cooling compressors is pre-determined by the ratio of the local pressure at the point of injection in the turbine to the local pressure at the point of extraction in the HPC. It is automatically set to the value 1 when the pressure at the extraction location is higher than the pressure at the injection location, which implies that no compression of the coolant is necessary.

The pressure in the shock pressure vessel PV is set to be 3.5 times higher than the combustor pressure  $p_{t4}$ . Under consideration of the local temperatures this pressure ratio is sufficient to generate shock waves with the strength  $M_s \approx 1.25$  in the combustion chamber [114]. Thus, the effective compression ratio of the shock compressor SC is  $\pi_{SC} = 3.5 \cdot \Pi$ .

The value  $\eta_{\text{polSC}} = 0.8$  is assumed for the polytropic efficiencies of the shock compressor in the shock-combustor enhanced engine models. The polytropic efficiencies of the two cooling compressors are set to  $\eta_{\text{polCC}} = 0.75$ , respectively.

At this stage there is no reliable data on the averaged, steady-state pressure-rise achievable by sequential shock-flame interaction. For this reason, the performance studies are carried out for a variable combustor pressure ratio that is altered in the range  $1 \leq \Pi \leq 2$ . Further, at this point it is not possible to exactly specify the mass flow fraction  $\xi$  required for shock generation. Hence,  $\xi$  is also varied within the range  $0.01 \leq \xi \leq 0.2$ . Consequently, the performance results of the shock-wave-combustor enhanced engines are presented as a function of the two variables  $\xi$  and  $\Pi$ .

### 6.3.1 Performance of a Shock-Combustor Topped Industrial Gas Turbine

#### Performance study GT1.1

In this study the performance of a shock-combustor topped industrial gas turbine is compared to the performance of the baseline engine GT1 at design ambient conditions. The turbine inlet temperature  $T_{t4}$  of the topped engine is equal to that of the baseline engine. The exhaust flow is expanded to ambient pressure so that  $p_8 = p_{\text{amb}}$ . Nozzle pressure ratio is kept at the constant value of the baseline engine  $p_{t8}/p_{\text{amb}} = 1.03$ . In order to enable such behaviour the cross sectional area of the exhaust duct  $A_8$  is allowed to change accordingly.

In Figure 6.3 selected performance variables of the shock-combustor topped industrial gas turbine are given as a function of the variables  $\xi$  and  $\Pi$ . These performance parameters are plotted in relation to the corresponding performance values of the baseline engine GT1. The value zero on the y-axis of the diagrams represents the benchmark performance level of the baseline engine. Such comparative presentation of the results highlights the potential of shock-combustor topping as well as its limitations with regard to existing technology.

A pressure-rise in the combustor increases the amount of useful power that is extractable from the fluid by the means of a power turbine. At the same time, the power required for the operation of the shock compressor and the cooling compressors grows with  $\Pi$ , which consequently reduces the extractable amount of useful power  $P_s$ . These contrary effects are highlighted in the shaft power results of the topped gas turbine; see Figure 6.3 a). The useful shaft power of the topped engine enhances with growing combustor pressure ratio. Thereby, the rate of increase is reduced for higher values of  $\Pi$ . The magnitude of  $\xi$  directly influences the power required for the driving of the shock combustor. In consequence, it is an essential parameter for the performance of the shock-combustor topped engine. For  $\xi < 0.04$  the predicted shaft power of the topped engine is higher than that of the baseline engine for the whole range of  $\Pi$  under consideration. For higher values of  $\xi$  the point, at which the perform-

ance of the topped engine becomes superior to the baseline engine, is moved towards higher values of  $\Pi$ . The resulting improvement in  $P_S$  is also significantly reduced with growing  $\xi$  for the same values of combustor pressure ratio. The shaft power of the topped engine is predicted to be inferior to the baseline case for all studied values of  $\Pi$  when  $\xi > 0.18$ .

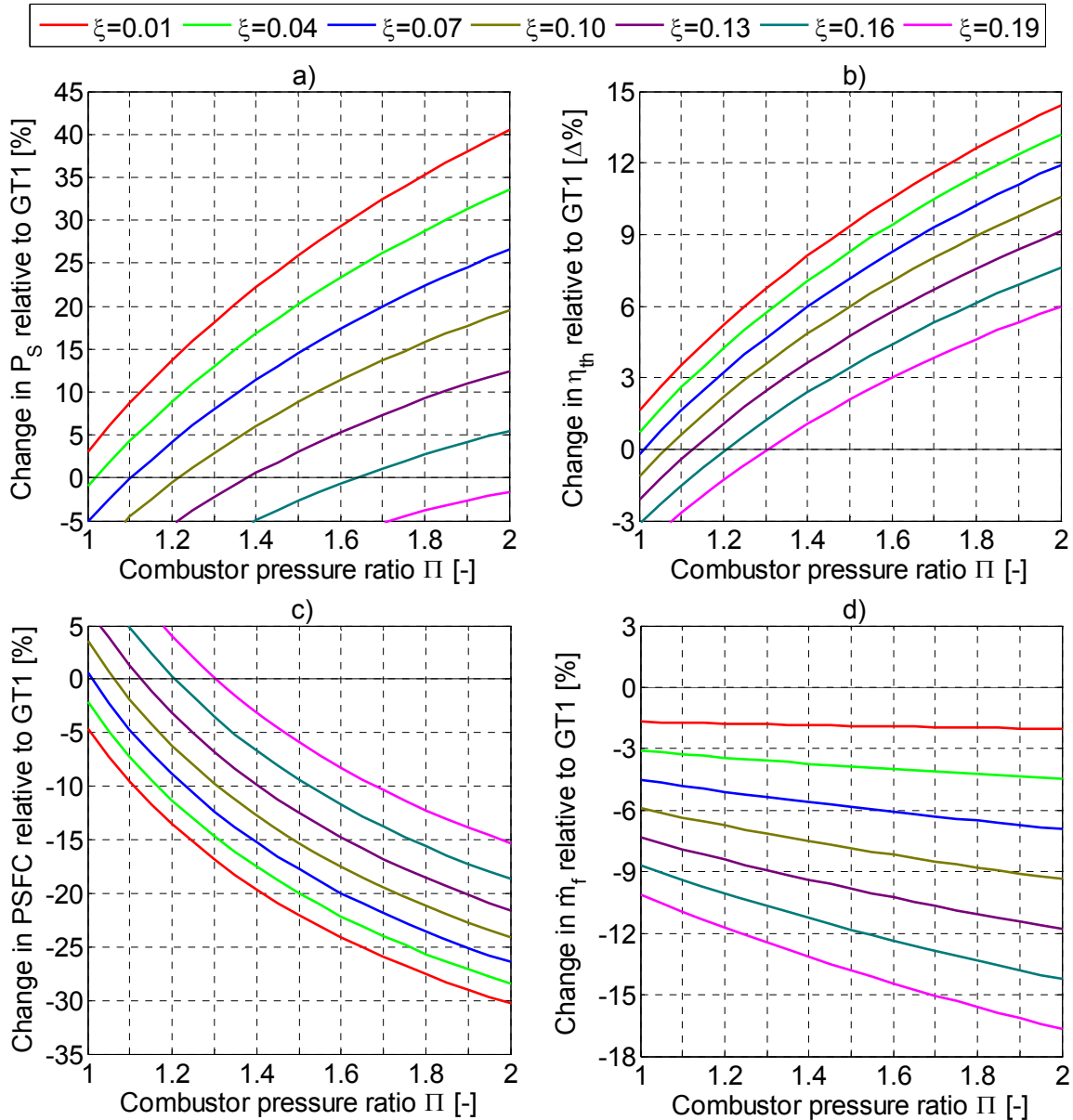


**Figure 6.3:** Performance parameters of the shock-combustor enhanced industrial gas turbine GT1.1 relative to the baseline engine GT1 for the fixed turbine inlet temperature  $T_{t4}$

In Figure 6.3 d) the forecast behaviour of the fuel mass flow rate  $\dot{m}_f$  of the topped engine is presented. As expected from eq. (6.3),  $\dot{m}_f$  decreases with growing  $\xi$ . It is also continuously reduced with increasing combustor pressure ratio.



The calculation results of thermal efficiency and specific fuel consumption are presented in Figure 6.3 b) and c) respectively. Both performance parameters improve with growing  $\Pi$ ; and deteriorate for larger values of  $\xi$ . Each of the two performance parameters  $\eta_{th}$  and PSCF is linearly governed by the variables  $P_s$  and  $\dot{m}_f$ . The behaviour of  $\eta_{th}$  and PSCF with  $\xi$  and  $\Pi$  represents a superposition of the two effects. Thus, an engine topping with  $\xi = 0.07$  and a moderate combustor pressure rise of  $\Pi = 1.2$  is predicted to improve the PSCF by approximately 8 %, and to increase the useful shaft power by 4 % relative to the baseline engine. The thermal efficiency is predicted to be augmented by around 3.2 percentage points. It is noted that the changes in thermal efficiency are presented in a different manner compared to other performance parameters. It is given as a simple difference ( $\Delta\%$ ) relative to the baseline engine's  $\eta_{th}$  value.

So far, the compression ratio of the shock combustor  $\pi_{SC}$  has been kept at the constant value  $3.5 \cdot \Pi$ . In order to assess the sensitivity of the model to changes in  $\pi_{SC}$  additional calculations at  $\pi_{SC} = 3.0 \cdot \Pi$  and  $4.0 \cdot \Pi$  were performed. These changes correspond to a variation in  $\pi_{SC}$  of  $\pm 14.3\%$  respectively. In Figure 6.4 the results of these calculations are presented on the basis of thermal efficiency. Therein the thermal efficiency results are exemplary plotted for  $\xi = 0.04$  and  $\xi = 0.16$ .

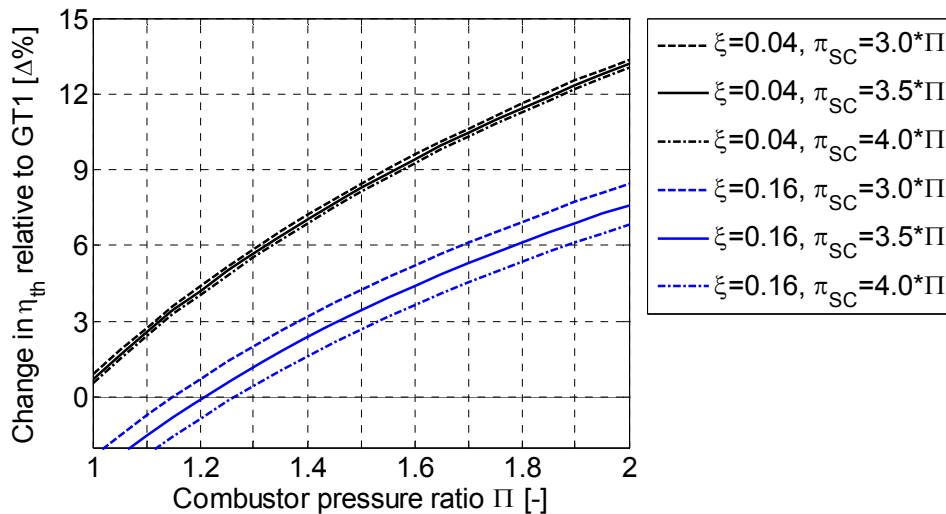


**Figure 6.4:** Influence of a variation in  $\pi_{SC}$  on the thermal efficiency of the shock-combustor enhanced industrial gas turbine

$\pi_{SC}$  directly influences the power consumed by the shock compressor. Hence, the influence of  $\pi_{SC}$  on the engine performance is expected to become stronger with growing  $\xi$ . This assumption is confirmed by the results presented in Figure 6.4. For low values of  $\xi$  the effect of the variations in  $\pi_{SC}$  is negligible. In contrast, for high  $\xi$  the same variation in  $\pi_{SC}$  exhibits a considerably stronger effect on the thermal engine efficiency. It constitutes up to  $\pm 0.8$  per-

centage points in  $\eta_{th}$  for  $\xi = 0.16$ , compared to  $\pm 0.2$  percentage points for  $\xi = 0.16$ . These effects also exhibit a slight dependence on the combustor pressure ratio. They become slightly stronger for higher  $\Pi$  values. The influence of  $\pi_{SC}$  on other engine performance parameters is analogous to that reported in Figure 6.4.

The magnitude of  $\pi_{SC}$ , in conjunction with the polytropic efficiency, defines the temperature  $T_{tSC}$  at the exit from the shock compressor. In Figure 6.5 this temperature is plotted as a function of  $\Pi$ . The temperature  $T_{t3}$  at the inlet to the shock compressor is also shown for reference.

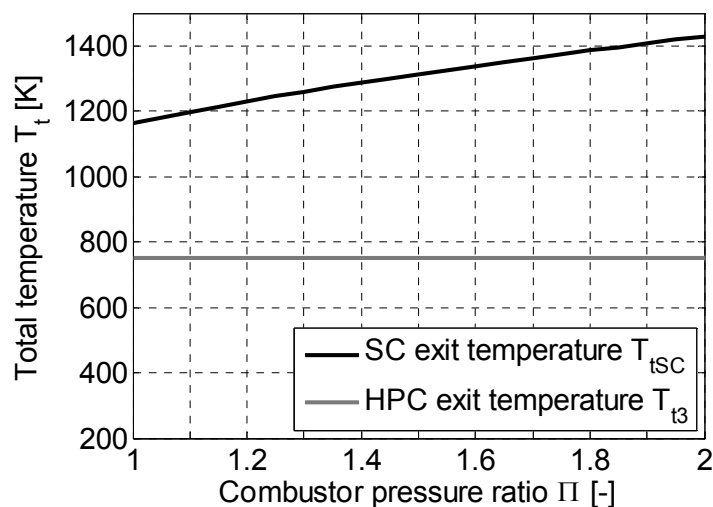


**Figure 6.5:** Total temperatures at the inlet and outlet of the shock compressor

Modern high-temperature blade materials are applicable at temperatures below about 1350 K [23], [104]. Hence, operation of the shock combustor at  $\Pi \geq 1.5$  would inevitably require inter-cooling of the shock compressor mass flow; see Figure 6.5. Inter-cooling positively affects the cycle performance and must be taken into consideration for a more detailed concept evaluation. It is not considered in the present study.

These results highlight the significance of the shock generation system with regard to the performance of shock-combustor topped engines, particularly for topping configurations with high values of  $\xi$  and  $\Pi$ .

The flow at the exit from the shock-flame interaction based combustor envisaged in this study is expected to be highly unsteady in time and spatially non-uniform to a much greater degree compared to a conventional combustor. This flow may also contain strong shock waves. A concern that arises in this context is: Can a conventional turbine, which is designed for steady flow conditions, operate efficiently with the unsteady inlet flow? Experimental and numerical studies have demonstrated the efficiency of conventional turbines to decrease when coupled to the unsteady outflow from a pulse detonation combustor or a reciprocating engine [119], [142], [161]. In this work, an additional study was carried out in order to assess

the effects of potentially reduced turbine efficiency on the performance of the shock-combustor topped industrial gas turbine. The polytropic efficiencies of both the HPT and the LPT were simultaneously reduced. The reduction increment was three percentage points respectively. The results of the study are presented in Figure 6.6 on the basis of thermal efficiency for  $\xi = 0.01$  and  $\xi = 0.16$ .

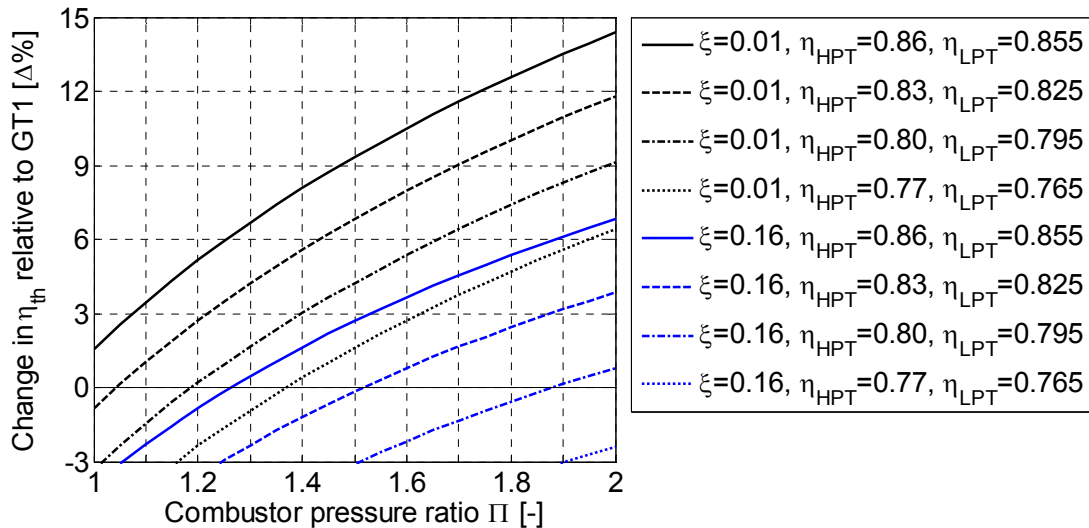


**Figure 6.6:** Influence of a reduced polytropic turbine efficiency on the thermal efficiency of the shock-combustor enhanced industrial gas turbine

For  $\xi = 0.01$  a moderate reduction in the efficiencies of the turbines causes a considerable degradation in the  $\eta_{th}$  of the topped engine. The deterioration in  $\eta_{th}$  amounts to around 2.5-3 percentage points per increment of reduction in turbine efficiency. This effect is marginally amplified with every successive turbine degradation increment. It is also slightly reinforced for growing values of  $\Pi$ . From the  $\xi = 0.16$  results it is evident that the detrimental effects caused by turbine impairment become more severe for higher values of  $\xi$ . Hence, the improvement potential of the shock-combustor topping concept discussed in this work essentially depends on the capability of the turbines to efficiently extract power from a non-uniform flow. Other engine performance parameters are analogously affected by the reduced turbine efficiency.

### Performance study GT1.2

Shock-combustor industrial gas turbine topping configuration is now modified relative to GT1.1. In this study the useful shaft power  $P_s$  is kept at the level of the baseline engine and the turbine inlet temperature  $T_{t4}$  of the topped engine is allowed to change accordingly. The exhaust flow is expanded to ambient pressure, i.e.  $p_8 = p_{amb}$ . Nozzle pressure ratio is kept at

the constant value of the baseline engine  $p_{t8}/p_{amb} = 1.03$ . In order to enable such behaviour the cross sectional area of the exhaust duct  $A_8$  is enabled to vary.

The presentation of the performance results of this study (see Figure 6.7) is analogous to that of Figure 6.3. Changes in performance parameters of the shock-combustor topped gas turbine relative to the corresponding performance values of the baseline engine GT1 are plotted as a function of the variables  $\xi$  and  $\Pi$ .

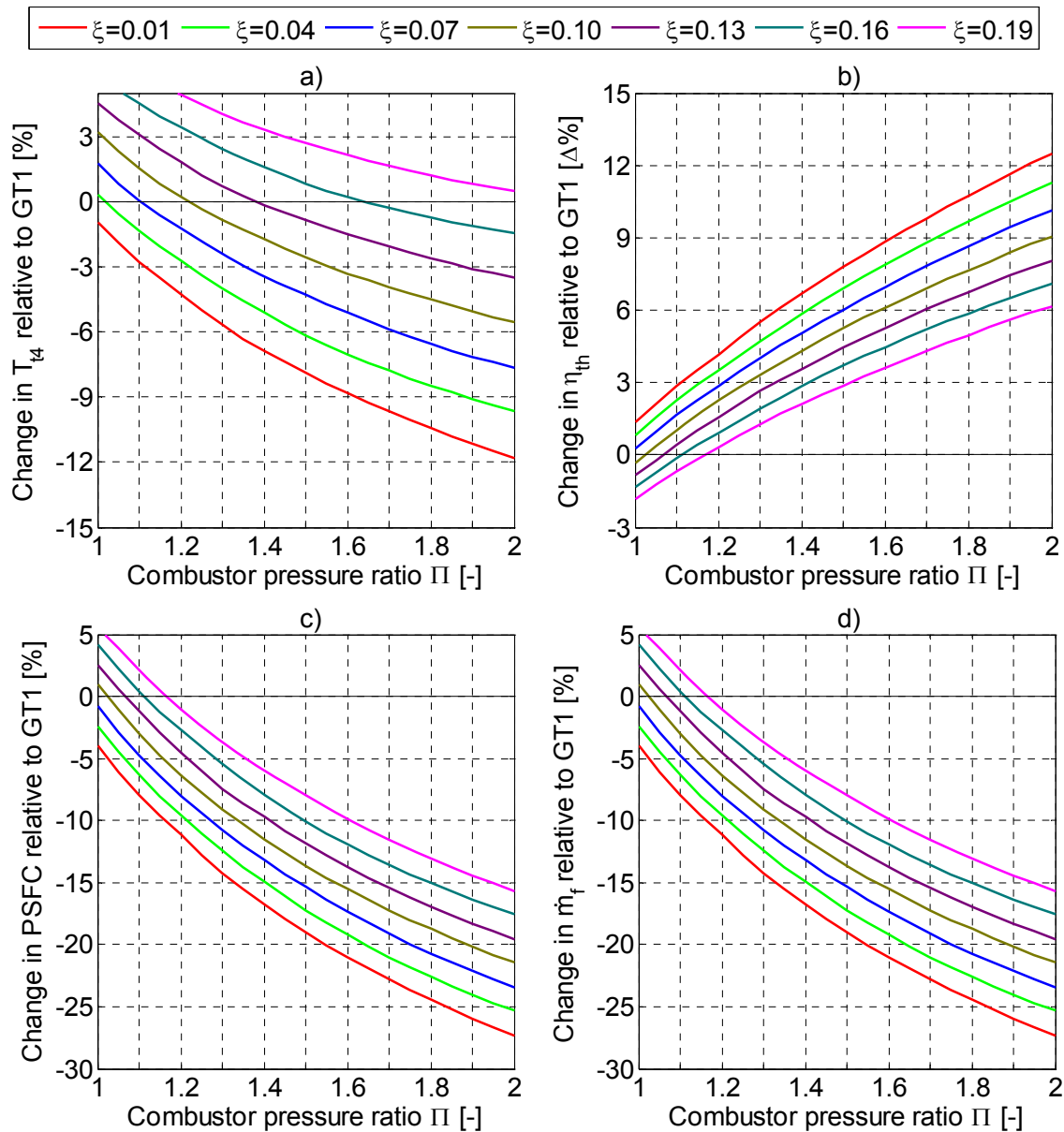


**Figure 6.7:** Performance parameters of the shock-combustor enhanced industrial gas turbine GT1.2 relative to the baseline engine GT1 for the fixed shaft power  $P_s$

The behaviour of the fuel mass flow rate  $\dot{m}_f$  with  $\xi$  and  $\Pi$  is shown in Figure 6.7 d). The maximum achievable reduction in  $\dot{m}_f$  is considerably higher compared to the study GT1.1.

This result is due to the variable turbine inlet temperature  $T_{t4}$  that is predicted to be reduced relative to the baseline engine for certain combinations of variables  $\xi$  and  $\Pi$ ; see Figure 6.7 a). In Figure 6.7 c) the change in the power specific fuel consumption PSFC of the topped engine is shown. Due to the fixed shaft power of the engine, the behaviour of the PSFC is identical to that of  $\dot{m}_f$ . The results of the thermal efficiency  $\eta_{th}$  calculation, presented in Figure 6.7 b), are similar to those reported for the study GT1.1 in Figure 6.3 b). The topping configuration GT1.2 is more advantageous in terms of  $\eta_{th}$  and PSFC for  $\xi > 0.1$  and  $\Pi < 1.4$  than the configuration GT1.1. A topped engine with  $\xi = 0.07$  and a relatively low combustor pressure rise of  $\Pi = 1.2$  is forecast to yield an improvement in the thermal efficiency of around 2.9 percentage points, in the PSFC of approximately 7 %, and a reduction in the  $T_{t4}$  of 1.4 % ( $\approx 21$  K) relative to the baseline engine GT1. Lower turbine inlet temperature has a positive effect on the life of the turbine. It also means that less cooling air is required, which is beneficial for cycle performance [104].

### Turbine cooling

The temperature of the blade metal has a fundamental influence on the life of a turbine aerofoil. Cooling effectiveness  $\phi$  is used as a measure of the blade metal temperature. The cooling effectiveness of a film cooled blade is defined as follows [104]:

$$\phi = \frac{T_g - T_{me}}{T_g - T_c} \quad (6.4)$$

In this equation  $T_g$  is the temperature of the working fluid,  $T_{me}$  is the external wall temperature of the blade, and  $T_c$  is the cooling air temperature. Cooling effectiveness is closely related to the amount of cooling flow that is required for a given aerofoil cooling scheme. In general, the cooling effectiveness increases with growing coolant flow rate [104].

In a gas turbine engine, the high-pressure turbine is often subject to gas temperatures that lie above the melting temperature of the blade material. For this reason, aerofoil cooling is vital for the operation and the integrity of the HPT. In the topping configuration GT1.1 the turbine inlet temperature  $T_{t4}$  was kept at the constant level of the baseline engine. In the configuration GT1.2 the  $T_{t4}$  was allowed to vary; see Figure 6.7 a). Thus, there exist operation conditions, depending on the combination of the two variables  $\xi$  and  $\Pi$ , under which  $T_{t4}$  is higher or lower than that of the baseline engine. Because of the need to compress the cooling air, the coolant temperature is also elevated. In Figure 6.8 the temperature of the HPT cooling air is normalised by the coolant temperature of the baseline engine ( $T_{cool} = 749.3$  K) and plotted as a function of  $\Pi$ . It is independent of  $\xi$  and identical for both topping studies GT1.1 and GT1.2. An increase in working gas temperature or in coolant temperature causes a reduction in the cooling effectiveness  $\phi$ . As a consequence, the blade wall temperature is increased, which

reduces the life of the turbine. There are two ways to countervail this problem. The first is to reduce the temperature of the coolant, which requires a complete redesign of the cooling system. The second is to accordingly increase the amount of cooling air. However, such an increase in the cooling air mass flow rate would adversely affect the overall engine performance.

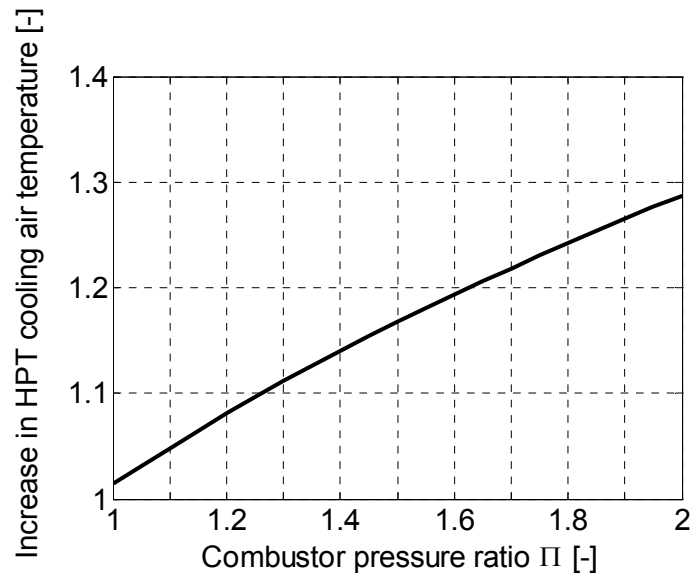


**Figure 6.8:** HPT cooling air temperature normalised by the coolant temperature of the baseline engine GT1

For the low pressure turbine the situation is less critical. Because of the need for the HPT to drive additional compressors for shock generation and cooling it extracts more work from the fluid. Consequently, the temperature  $T_{t45}$  at the inlet to the LPT is reduced compared to the baseline engine. The change in  $T_{t45}$  relative to the baseline engine is presented in Figure 6.9 for both topping configurations GT1.1 and GT1.2. Because of the fixed turbine inlet temperature in GT1.1 the LPT inlet temperature is reduced for all studied combinations of  $\xi$  and  $\Pi$ . In GT1.2, the  $T_{t45}$  is elevated relative to the baseline engine for certain combinations of  $\Pi$  and  $\xi$  ( $\Pi < 1.2$  and  $\xi > 0.07$ ). In general, for GT1.2 the rate of reduction in  $T_{t45}$  with  $\Pi$  is higher than for GT1.1. A reduction in the working gas temperature allows diminishing the required cooling air mass flow to the LPT. This would contribute to improve the overall performance of the topped engine.

In the engine performance studies presented above the cooling air mass flows are the same as in the baseline engine. The turbine cooling considerations have however demonstrated the need in changing the coolant mass flows in order to maintain the cooling effectiveness and the blade wall temperature at an appropriate level. Hence, a redesign of the turbine cooling system is necessary. Modification of the cooling air mass flows can considerably influ-

ence the overall performance of the topped engines presented in Figure 6.3 and Figure 6.7. Thus, further studies including cooling system adaptation are required to provide more realistic performance evaluation of shock-combustor enhanced engines.

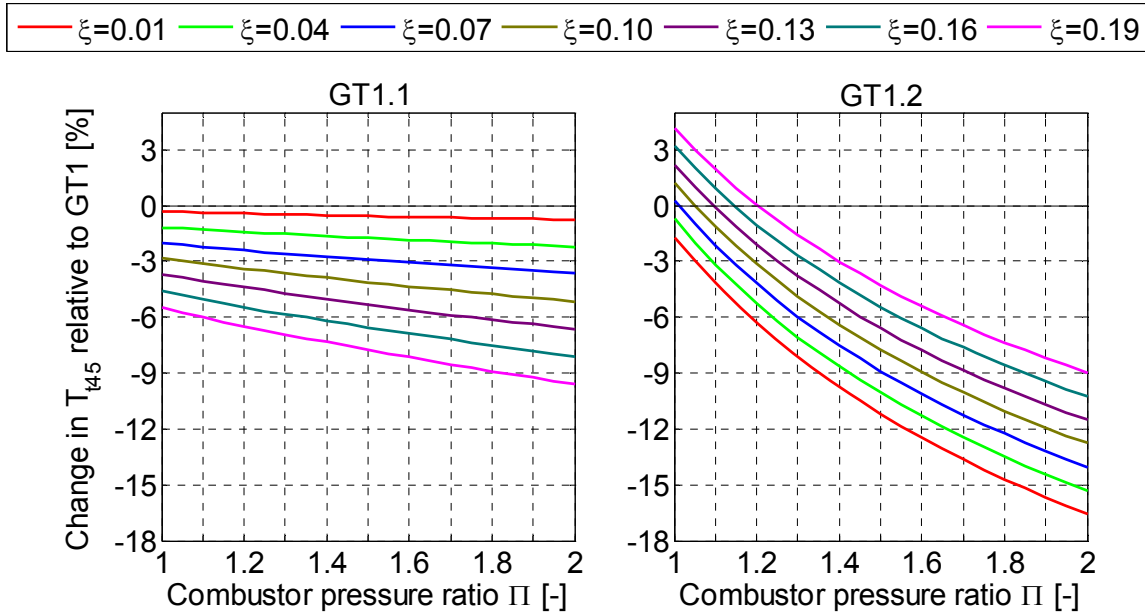


**Figure 6.9:** LPT inlet temperature for the two topping configurations GT1.1 and GT1.2 relative to the baseline engine GT1

### 6.3.2 Performance of a Shock-Combustor Topped Turbofan Engine

In this study the performance of a shock-combustor topped high-bypass turbofan engine is compared to the performance of the baseline engine GT2 at design ambient conditions. In the calculations the turbine inlet temperature  $T_{t4}$  of the topped engine is kept at the constant value of the baseline engine. This setting makes this study comparable to the performance study GT1.1 of the shock-combustor topped industrial gas turbine. The flow Mach number in the section 6 (see Figure 6.1), immediately behind the flow mixer, is kept equal to that of the baseline engine  $M_6 = 0.557$ . The bypass flow and the core flow are assumed to be perfectly mixed in this section. Further, the nozzle exhaust flow is assumed to be sonic, i.e. the flow Mach number at the nozzle exit is fixed at the constant value  $M_8 = 1$ . In order to enable such behaviour the cross sectional areas of the mixer  $A_6$  and of the exhaust nozzle  $A_8$  are allowed to vary accordingly in the model.

In Figure 6.10, selected performance variables of the shock-combustor topped turbofan engine are presented as a function of the variables  $\xi$  and  $\Pi$ . These performance parameters are plotted in relation to the corresponding performance values of the baseline engine GT2. The value zero on the y-axis of the diagrams represents the benchmark performance level of

the baseline engine. It is noted that both the changes in thermal efficiency  $\eta_{th}$  and propulsive efficiency  $\eta_{prop}$  are given as simple differences ( $\Delta\%$ ) relative to the baseline engine's values.

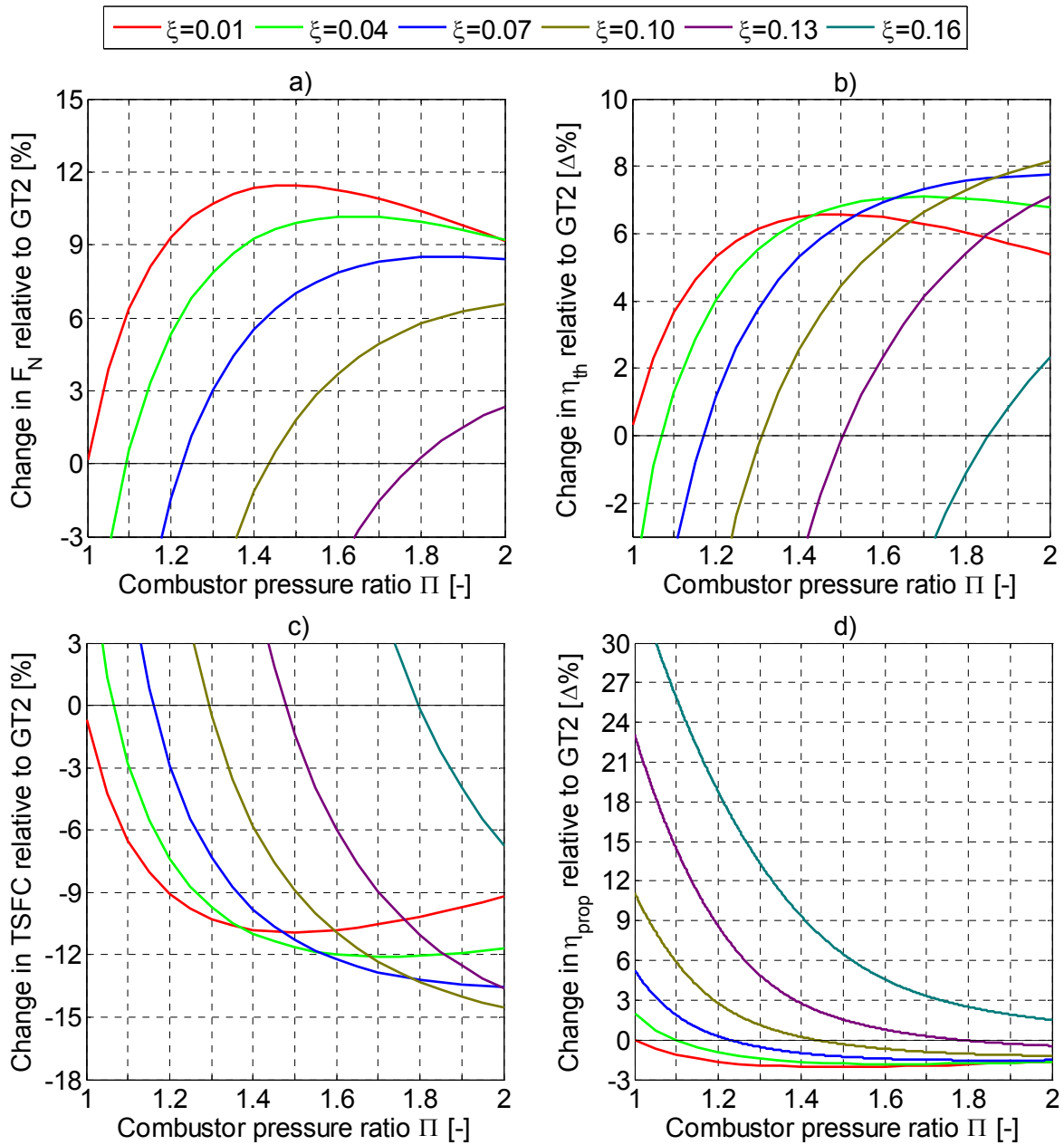


**Figure 6.10:** Performance parameters of the shock-combustor enhanced turbofan engine relative to the baseline engine GT2 for the fixed turbine inlet temperature  $T_{14}$

In Figure 6.10 a) predicted net thrust  $F_N$  of the topped turbofan engine is shown. Net thrust is a function of the nozzle flow velocity  $u_8$  and the nozzle pressure ratio  $p_{t8}/p_{amb}$  [109]. The variation of the nozzle pressure ratio with  $\xi$  and  $\Pi$  is shown in Figure 6.11. The pressure-gain in the combustor is counteracted by the increased power extraction at the HPT due to additional shock and cooling compressors. Thus, for each value of  $\xi$  there exists a range of  $\Pi$  values, for which the nozzle pressure ratio lies below that of the baseline engine. For higher



values of  $\Pi$  the combustor pressure-rise is partly maintained and the nozzle pressure ratio of the topped engine increases compared to the datum engine. The nozzle flow velocity  $u_8$  is predicted to be reduced relative to the baseline engine for all studied combinations of  $\Pi$  and  $\xi$ ; see Figure 6.12. Variation of the net thrust with  $\xi$  and  $\Pi$ , shown in Figure 6.10 a), combines the influences of the nozzle pressure ratio and the nozzle flow velocity.  $F_N$  increases with growing combustor pressure ratio until it reaches a maximum at a certain value of  $\Pi$ . Further increase in  $\Pi$  causes a reduction of net thrust. Growing  $\xi$  leads to a significant reduction of net thrust for the same values of  $\Pi$ . Further, the absolute achievable maximum value of  $F_N$  is reduced and shifted towards higher values of  $\Pi$ , when  $\xi$  is increased.

Predictions of propulsive efficiency of the shock-combustor topped engine are presented in Figure 6.10 d). The behaviour of  $\eta_{prop}$  with  $\Pi$  and  $\xi$  is also linked to the nozzle pressure ratio of the topped engine. Because of the fixed nozzle flow Mach number ( $M_8 = 1$ , convergent nozzle) an increase in the nozzle pressure ratio (Figure 6.11) results in higher losses in the kinetic energy of the jet. Thus, higher values of  $\xi$  increase the propulsive efficiency of the topped engine, whereas growing  $\Pi$  reduces it. The maximum reduction of  $\eta_{prop}$  compared to the baseline engine is predicted to be -2.2 percentage points at  $\xi = 0.1$  and  $\Pi = 1.5$ .

The calculation results of thermal efficiency  $\eta_{th}$  and thrust specific fuel consumption TSFC are presented in Figure 6.10 b) and c) respectively.  $\eta_{th}$  is defined as increase in kinetic energy of the gas stream across the engine divided by the amount of heat employed. TSFC is the ratio of fuel mass flow rate and net thrust [109]. Hence, both parameters are linearly dependent on the fuel mass flow rate  $\dot{m}_f$  of the engine. In Figure 6.13 the forecast behaviour of the fuel mass flow rate  $\dot{m}_f$  of the topped turbofan engine is presented. As expected from eq. (6.3)  $\dot{m}_f$  decreases with growing combustor pressure ratio and  $\xi$ . Both performance parameters  $\eta_{th}$  and TSFC behave analogously with  $\Pi$  and  $\xi$ . Increasing  $\Pi$  causes both parameters to improve until a certain maximum or minimum value is reached, respectively. This maximum/minimum is increased in magnitude and shifted towards higher values of  $\Pi$  with growing  $\xi$ .

An exemplary engine topping with  $\xi = 0.07$  and a moderate combustor pressure rise of  $\Pi = 1.2$  is predicted to improve the thermal efficiency by 1.7 percentage points and to reduce the TSFC by approximately 3 % relative to the baseline engine GT2. Propulsive efficiency is expected to improve by around 0.4 percentage points merely and the net thrust is deteriorated by approximately 1.6 %. Combustor pressure ratio must be increased beyond the value 1.23 in order to obtain an engine topping with an increased net thrust for the same  $\xi$ . In doing so, thermal efficiency and TSFC of the topped engine are further improved by approximately 1-1.5 percentage points, whereas  $\eta_{prop}$  is slightly reduced by around 0.5 percentage points.

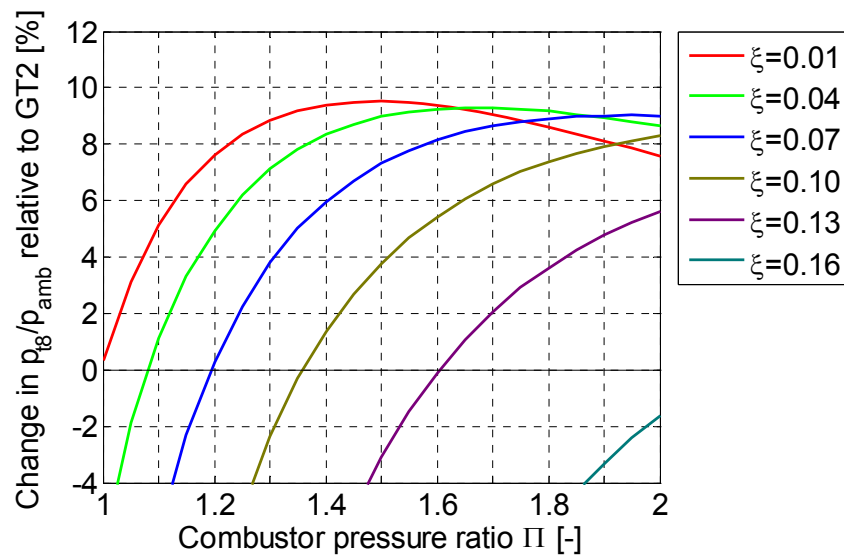


**Figure 6.11:** Nozzle pressure ratio of the shock-combustor enhanced turbofan engine relative to the baseline engine GT2 for the fixed turbine inlet temperature  $T_{t4}$

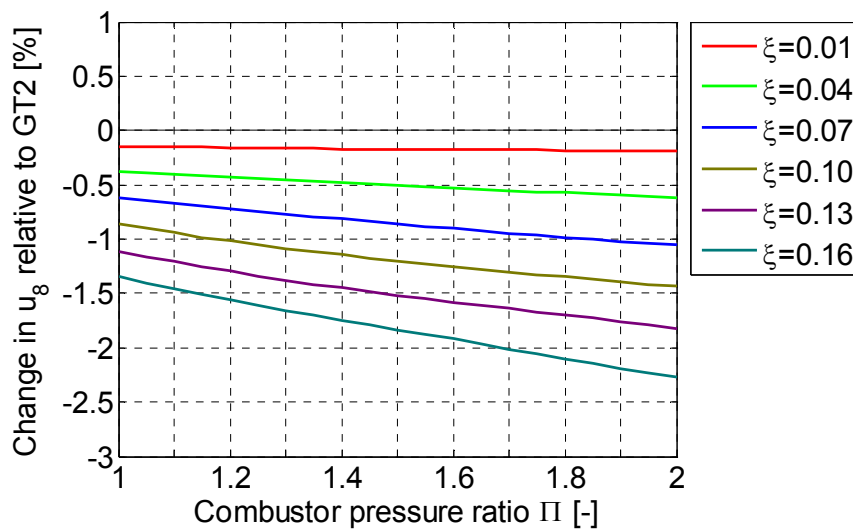


**Figure 6.12:** Nozzle exit flow velocity of the shock-combustor enhanced turbofan engine relative to the baseline engine GT2 for the fixed turbine inlet temperature  $T_{t4}$

Thermal efficiency and specific fuel consumption results of the shock-combustor topped turbofan engine (Figure 6.10) are now compared to the performance of the enhanced industrial gas turbine GT1.1 (Figure 6.3). Shock-combustor topping as per Figure 6.2 is more beneficial when applied to the industrial gas turbine GT1. Predicted improvements in  $\eta_{th}$  and SFC are significantly higher in the case of the topped industrial gas turbine for the same combinations of the parameters  $\Pi$  and  $\xi$ . This is particularly true for large values of  $\Pi$  and  $\xi$  within the range of this study. Degradation of achievable performance with growing  $\xi$  is much more

severe in the case of the topped turbofan engine. Furthermore, weight and safety constraints make the industrial gas turbines appear as a more adequate basis for pressure-gain combustor enhancement.

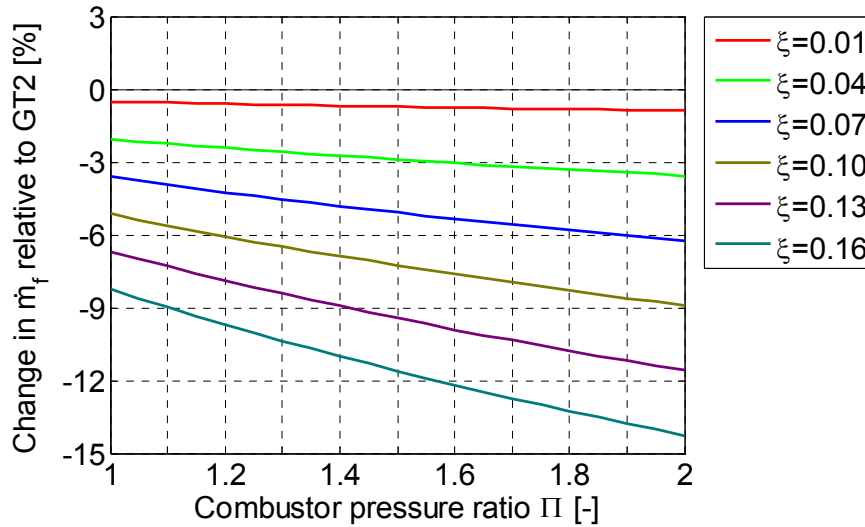


**Figure 6.13:** Fuel mass flow rate of the shock-combustor enhanced turbofan engine relative to the baseline engine GT2 for the fixed turbine inlet temperature  $T_{t4}$

Additional calculations at  $\pi_{SC} = 3.0 \cdot \Pi$  and  $4.0 \cdot \Pi$  were performed in order to assess the performance sensitivity of the topped turbofan engine to changes in  $\pi_{SC}$ . These changes correspond to a variation in  $\pi_{SC}$  of  $\pm 14.3\%$  respectively. In Figure 6.14 the results of these calculations are presented on the basis of thermal efficiency of the shock-combustor topped engine. Therein the thermal efficiency results are exemplary plotted for  $\xi = 0.04$  and  $\xi = 0.15$ .

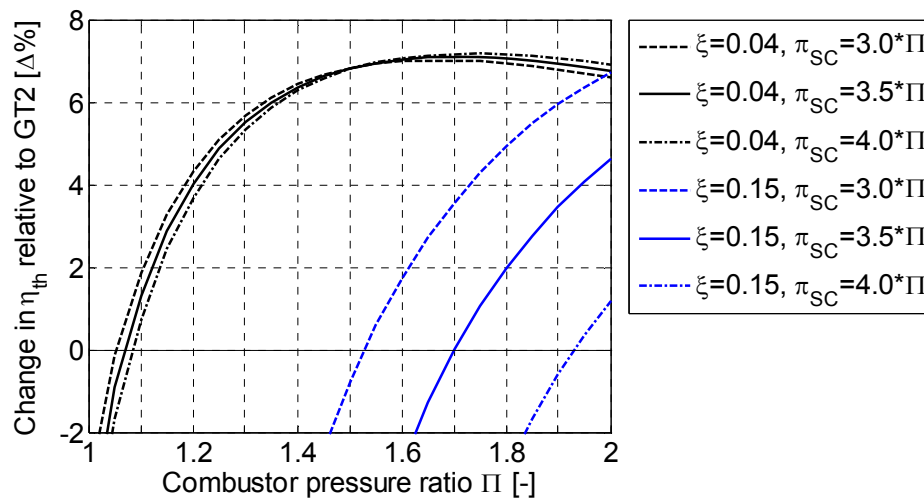


**Figure 6.14:** Influence of a variation in  $\pi_{SC}$  on the thermal efficiency of the shock-combustor enhanced turbofan engine

$\pi_{SC}$  has a direct effect on the power that is consumed by the shock compressor. Hence, the influence of  $\pi_{SC}$  on the engine performance is expected to become stronger with growing  $\xi$ . For low values of  $\xi$  and low  $\Pi$  the variations in  $\pi_{SC}$  cause  $\eta_{th}$  to change by approximately  $\pm 0.4$  percentage points; for larger  $\Pi$  this difference diminishes and becomes negligibly small for  $\Pi > 1.4$ . In contrast, for high  $\xi$  the same variation in  $\pi_{SC}$  exhibits a significantly stronger effect on the thermal engine efficiency. It is responsible for changes of up to  $\pm 2-3$  percentage points in  $\eta_{th}$  for  $\xi = 0.15$ . The influence of  $\pi_{SC}$  on other engine performance parameters is analogous to that reported in Figure 6.14.

An additional study was carried out in order to assess the effects of potentially reduced turbine efficiency on the performance of the shock-combustor topped turbofan engine. The polytropic efficiencies of both the HPT and the LPT were simultaneously reduced. The reduction increment was three percentage points respectively. The results of the study are presented in Figure 6.15 on the basis of thermal efficiency for  $\xi = 0.03$ . A moderate reduction in the efficiencies of the turbines causes a significant degradation in the  $\eta_{th}$  of the topped engine. The deterioration in thermal efficiency is the largest for low combustor pressure ratios. It reduces quickly with growing  $\Pi$ . The point of maximum  $\eta_{th}$  is shifted towards higher combustor pressure ratios with every turbine efficiency degradation step, whereas its magnitude remains unaltered. These effects are amplified with every successive turbine degradation increment. Other engine performance parameters are analogously affected by the reduced turbine efficiency.

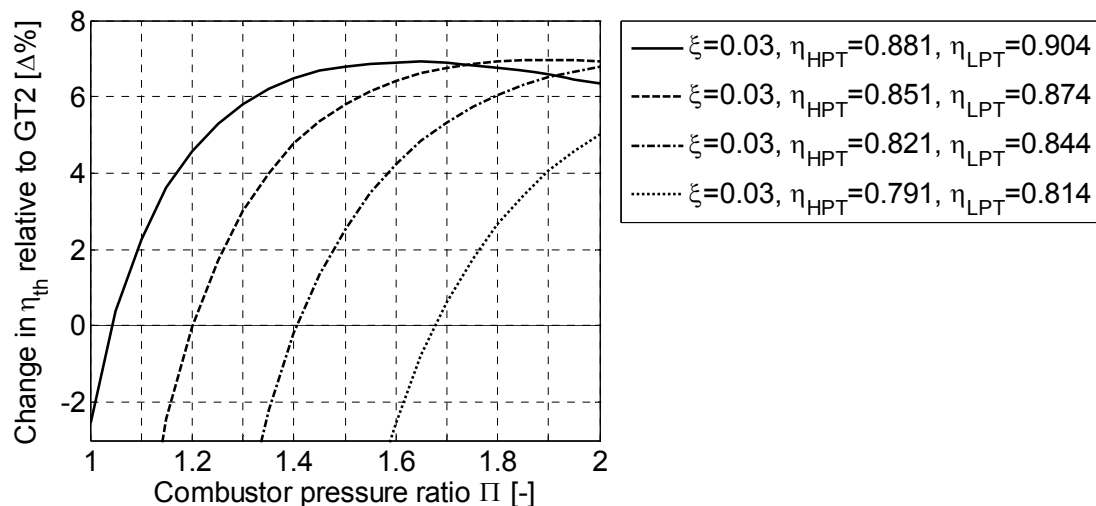


**Figure 6.15:** Influence of a reduced polytropic turbine efficiency on the thermal efficiency of the shock-combustor enhanced turbofan engine

Generally, it is concluded that the turbofan engine topping is more susceptible to variations in shock compressor pressure ratio and turbine efficiencies than the corresponding industrial gas turbine topping GT1.1. Changes in the performance caused by identical variations in  $\pi_{SC}$

and turbine efficiencies are predicted to be significantly higher in the case of the topped turbofan engine, particularly at high  $\xi$  and low  $\Pi$ .

## 7 Conclusions and Future Work

### 7.1 Summary and Conclusions

Today, both the transportation and the energy business sectors vitally rely on the power provided by gas turbines. These branches, which are essential for a consistent economic growth within an increasingly global business environment, are predicted to grow at an annual rate between 3 % and 5.5 % over the next 20 years. Hence, the demand in gas turbine power is expected to double over the next two decades. This market demand is opposed by ever growing fossil fuels prices and increasingly stringent combustion emission regulations. These challenges can only be managed by gas turbine manufacturers and operator through a further substantial improvement in the fuel efficiency of gas turbines.

One method of achieving this is to use a pressure-rising combustion process. The conventional quasi-isobaric, steady-flow gas turbine combustion is characterized by a highly irreversible conversion of chemical energy into heat. This represents a penalty to engine performance and limits the thermodynamic efficiency of the engine. In a combustion process that is accompanied by an increase in pressure a portion of heat release is reversibly converted into mechanical energy, which reduces the entropy rise and makes the process of heat addition more efficient. Hence, the central objective of pressure-gain combustion work is to modify the constant pressure mode of combustion in gas turbines so, that its performance moves closer to that of constant volume combustion. It is also concluded that such a pressure-rising combustion mode must inevitably be unsteady.

In this work it is proposed to use the interaction of shock waves with a pre-mixed flame to achieve a time-averaged, combustion-induced pressure rise. The passage of a shock wave through a pre-mixed flame is highly unsteady and non-uniform in time and space. It is known to cause a temporal increase in the heat release rate of the flame due to gas compression effects and increase in the flame surface area. Consequently, the rate of expansion of the burned gas is altered accordingly, which leads to formation of pressure waves at the disturbed flame. Under certain circumstances, these pressure waves coalesce and reinforce the initial pressure wave. The physical phenomena occurring in the course of shock-flame interaction are very complex and as yet not understood in detail.

An experimental investigation of shock-flame interaction phenomena was planned and conducted using a shock tube test rig. The use of the shock tube test facility allowed the generation of shock waves of different strength in a controlled and highly-repeatable manner. Premixed combustion of a nearly-stoichiometric methane-oxygen-argon mixture was used in the experiments. Spatially and temporally resolved measurement of static pressure and chemiluminescence, as a qualitative measure of flame heat release, were applied. Both modes (directions) of interaction, slow-fast and fast-slow, were tested. It was shown that the heat release rate of the flame is temporally amplified after each passage of a shock wave compared to the undisturbed flame. The maximum achieved pressure in the test rig has also been demonstrated to increase due to shock-flame interaction compared to shock experiments without combustion for the same incident shock strength. Both the increase in pressure and in heat release of the flame were shown to grow with the Mach number of the incident shock. The fast-slow mode of interaction produced considerably higher increases in pressure and heat release than the slow-fast mode for the same incident shock strength. This is due to higher rates of gas compression and flame surface growth in this type of interaction. The temporal relationship between pressure and heat release fluctuations was analysed using the Rayleigh Index. It was demonstrated that there exist regions of positive Rayleigh Index after each transition of a shock wave through a flame front. In these regions the increase in heat release is in phase with the increase in pressure, which satisfies the Rayleigh criterion and promotes the growth of pressure oscillations, i.e. the initial pressure wave is reinforced. The intensity of the Rayleigh Index was shown to increase by up to two orders of magnitude in the course of repeated shock-flame interactions.

Further, an analytical quasi-one-dimensional model of the shock wave and flame interaction was developed. Thereby, shock-flame interaction was broken down into three interrelated processes: shock refraction at a reactive density interface, deformation of the flame front, and generation of pressure waves at the deformed flame. Given a known initial flow field, initial two-dimensional flame geometry, and the Mach number of the incident shock wave the model allows the calculation of a fully defined one-dimensional flow field that is formed at the end of a single shock-flame interaction event. The geometry of the initial flame front was described by a simple single-mode half-sine wave. This shape is typical for laminar flames propagating in narrow channels. The analytical model was successfully verified using experimental data. Results of the analytical calculation allow one to relate the change of state across a shock-flame interaction event to that across an isobaric flame with the same initial conditions. It was found that a single shock-flame interaction event generates a significant increase in pressure, whereas the according increase in temperature remains at a relatively moderate level. Further, the combustion entropy is significantly reduced through a single shock-flame interaction event compared to the reference isobaric combustion process. The

resulting changes in pressure, temperature and entropy rise with increasing incident shock strength and growing curvature of the flame front. They are significantly stronger in the fast-slow mode of interaction. This is a consequence of higher rates of gas compression and flame surface growth in the fast-slow type of interaction. Thus, weak incident shock waves with  $M_i \leq 1.3$  produce an increase in static pressure of up to 230 %, 60 %, but merely a static temperature increase of around 5.4 %, 1.9 % relative to the reference isobaric combustion for fast-slow, slow-fast interaction mode, respectively. The corresponding reduction of generated entropy constitutes up to -15 %, -6 %, respectively. For very weak incident shocks ( $M_i < 1.2$ ) these changes are dominated by flame deformation effects. For stronger incident shocks the relative contribution of gas compression effects due to shock refraction is predominant.

These results substantiate the assumptions that shock-flame interaction represents a real route to achieve pressure-rise combustion. Additional insight is provided into the interaction mechanism of shock waves and pre-mixed flames. First estimate of increases in pressure and temperature as well as reduction in entropy achievable with a single interaction event is presented. Means of controlling and driving the shock-flame interaction are identified and highlighted.

In this work, it is envisaged to repeat the shock-flame interaction in a certain sequence in order to obtain a time- and volume-averaged total pressure rise in the burned gas compared to steady isobaric combustion. A simplified engine performance model was developed to assess the performance improvement potential as well as the limitations of this concept. A theoretical configuration of a shock-combustor enhanced high-pressure engine core was proposed and applied to two types of baseline engines: a twin-spool industrial gas turbine and a twin-spool high-bypass turbofan engine. The performance of the topped engines was evaluated using two variables: the combustor pressure ratio  $\Pi$  and the fraction of the core mass flow used to generate shock waves in the combustor  $\xi$ . Generally, the performance of the topped engines rises for growing  $\Pi$  and deteriorates with increasing  $\xi$ . It was found that already for relatively moderate combustor pressure ratios ( $\Pi \leq 1.4$ ) and relatively high  $\xi$  ( $\xi \leq 0.1$ ) the specific fuel consumption and the thermal efficiency of the topped engines are forecast to improve by up to 13 % and 5 percentage points compared to the baseline engines, respectively. In general, considerably higher improvements are predicted for the industrial gas turbine engine for the same combinations of variables  $\Pi$  and  $\xi$ . Further, the improvement potential of the topped engines was demonstrated to be strongly dependent on the turbine capability to efficiently extract power from the highly unsteady combustor exhaust flow. Their performance was shown to drop dramatically in response to relatively small changes in polytropic turbine efficiencies.



## 7.2 Future Work

The results of this study shed additional light on the physical phenomena involved in shock-flame interaction. They also allow the drawing of conclusions about the gas state that is induced at the end of a single interaction between a shock wave and a pre-mixed flame. However, these steady gas conditions merely exist in a small gas volume for a very short period of time. In order to achieve a resultant quasi-steady pressure rise, which is necessary for practical applications, the shock-flame interaction process must be repeated at a certain frequency. Volume and time averaging of the resulting unsteady fluid flow will reduce the achievable pressure-gain below that of a single shock-flame interaction process. Conversely, repeated interaction between a shock wave and an already distorted flame will significantly enhance the thermodynamic pressure-rise potential of a single interaction event. This highlights the importance and the need of further research into the topic of sequential shock-flame interaction and of an accurate flow averaging technique. Currently, there is very little understanding of sequential interaction, which is imperative for further concept development. Another important area of future work is the shock-flame interaction in two-phase combustion systems. In many gas turbines sprays of liquid fuels are burned in the combustion chamber. The interaction of propagating shock waves with dispersed reactive media differs significantly from the underlying interaction mechanism in pre-mixed combustion. Some historical work is available in this area that supports the idea of using shock-flame interactions in liquid fuels for pressure-gain combustion applications; see Chapter 3.2.5. Nevertheless, further research in this field is absolutely essential.

The integration of an unsteady pressure-gain combustor into a gas turbine engine will pose a plethora of technological challenges to engine designers and manufacturers. Among others following topics will arise: integration of a shock generation system (additional weight and complexity), prevention of backflow of hot combustion products to the compressor, combustor and turbine cooling, rematch of turbine and compressor modules, increased fatigue due to unsteady combustor operation. In fact, the introduction of a pressure-rising combustion chamber would require a complete redesign of the whole engine.

The exhaust flow from a shock wave enhanced pressure-gain combustor envisaged in this work is expected to be highly unsteady in time and spatially non-uniform. This flow may also contain strong shock waves. The efficiency of conventional turbines designed for steady flow conditions is significantly reduced under such flow conditions. Hence, a new turbine design must be found that is capable of efficiently extracting power from highly unsteady non-uniform flow including shock waves. This work has been tackled at the University of Stuttgart using a turbine row with a variable annulus height aiming at prevention of throat blockage and undue reflection of incident pressure waves [44].

## Appendix A

	$CH_4$	$O_2$	$Ar$
$Y_i [-]$	0.04139	0.16675	0.79186
$\mathcal{M}_i [kg/mol]$	0.01605	0.03199	0.03994
$a_1 [-]$	0.77874148	3.2129364	2.5
$a_2 [-]$	0.01747668	0.00112749	0
$a_3 [-]$	-2.7834E-05	-5.75615E-07	0
$a_4 [-]$	3.0497E-08	1.31388E-09	0
$a_5 [-]$	-1.2239E-11	-8.7686E-13	0

**Table A.1:** Mass fractions, molar masses, and coefficients for the unburned mixture, eq. (5.3),  $300\text{ K} < T < 1000\text{ K}$ , from [100], [124]

	$CO_2$	$H_2O$	$O_2$	$Ar$
$Y_i [-]$	0.11347	0.09289	0.00178	0.79186
$\mathcal{M}_i [kg/mol]$	0.04401	0.01801	0.03199	0.03994
$a_1 [-]$	4.4536228	2.6721456	3.6975782	2.5
$a_2 [-]$	0.00314017	0.00305629	0.00061352	0
$a_3 [-]$	-1.27841E-06	-8.73026E-07	-1.25884E-07	0
$a_4 [-]$	2.394E-10	1.201E-10	-1.77528E-11	0
$a_5 [-]$	-1.669E-14	-6.3916E-15	-1.1364E-13	0

**Table A.2:** Mass fractions, molar masses, and coefficients for the combustion products, eq. (5.3),  $1000\text{ K} < T < 5000\text{ K}$ , from [100], [124]

$s_{LO} [m/s]$	$a_1 [-]$	$a_2 [-]$	$\alpha [-]$	$\beta [-]$
0.7077	0.237	-3.411	1.39	-0.016

**Table A.3:** Empirical constants for the calculation of laminar burning velocity, eq. (5.8)

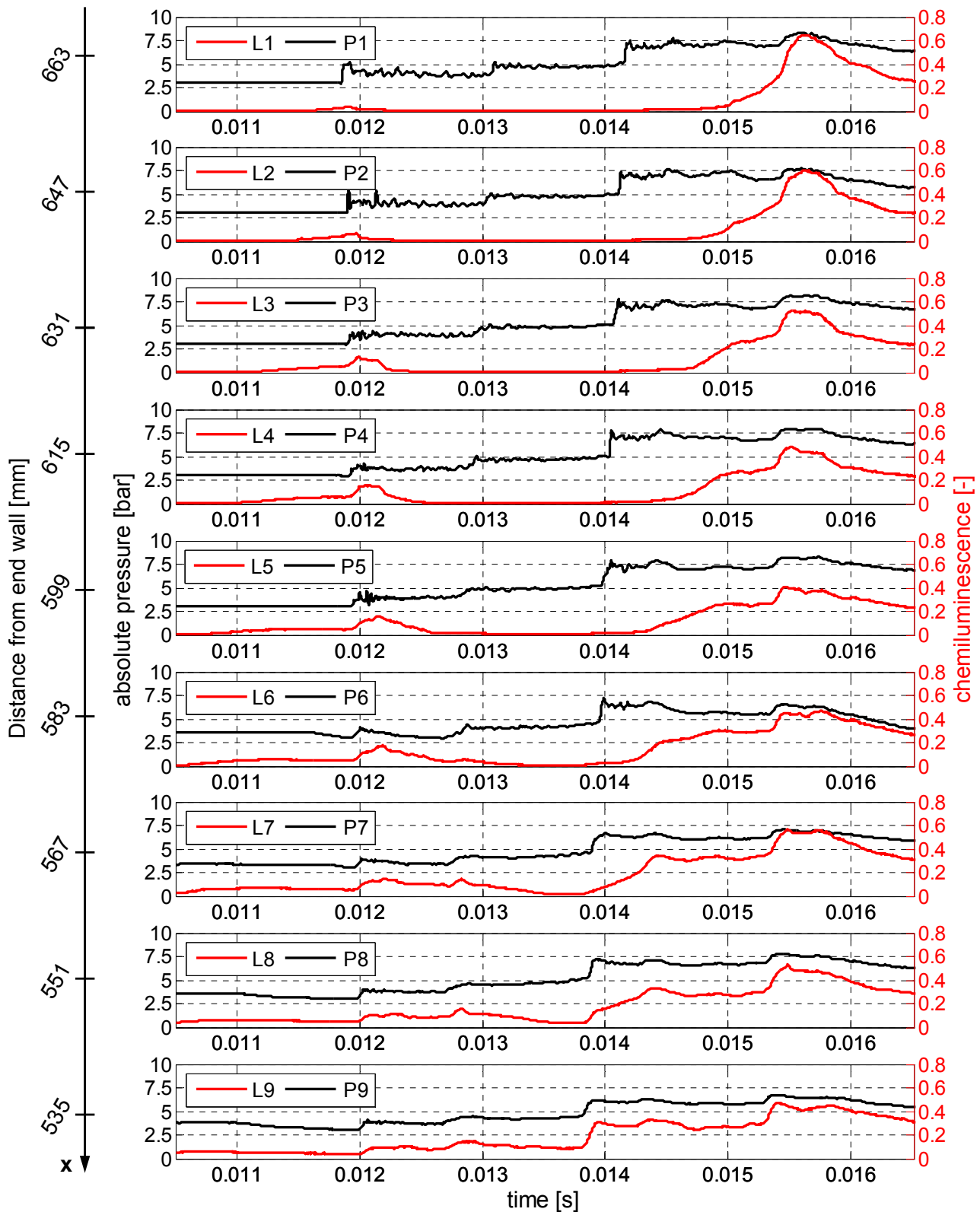


**Figure A.1:** Pressure and chemiluminescence profiles of the incident and the reflected shock waves, s/f,  $M_i = 1.26$

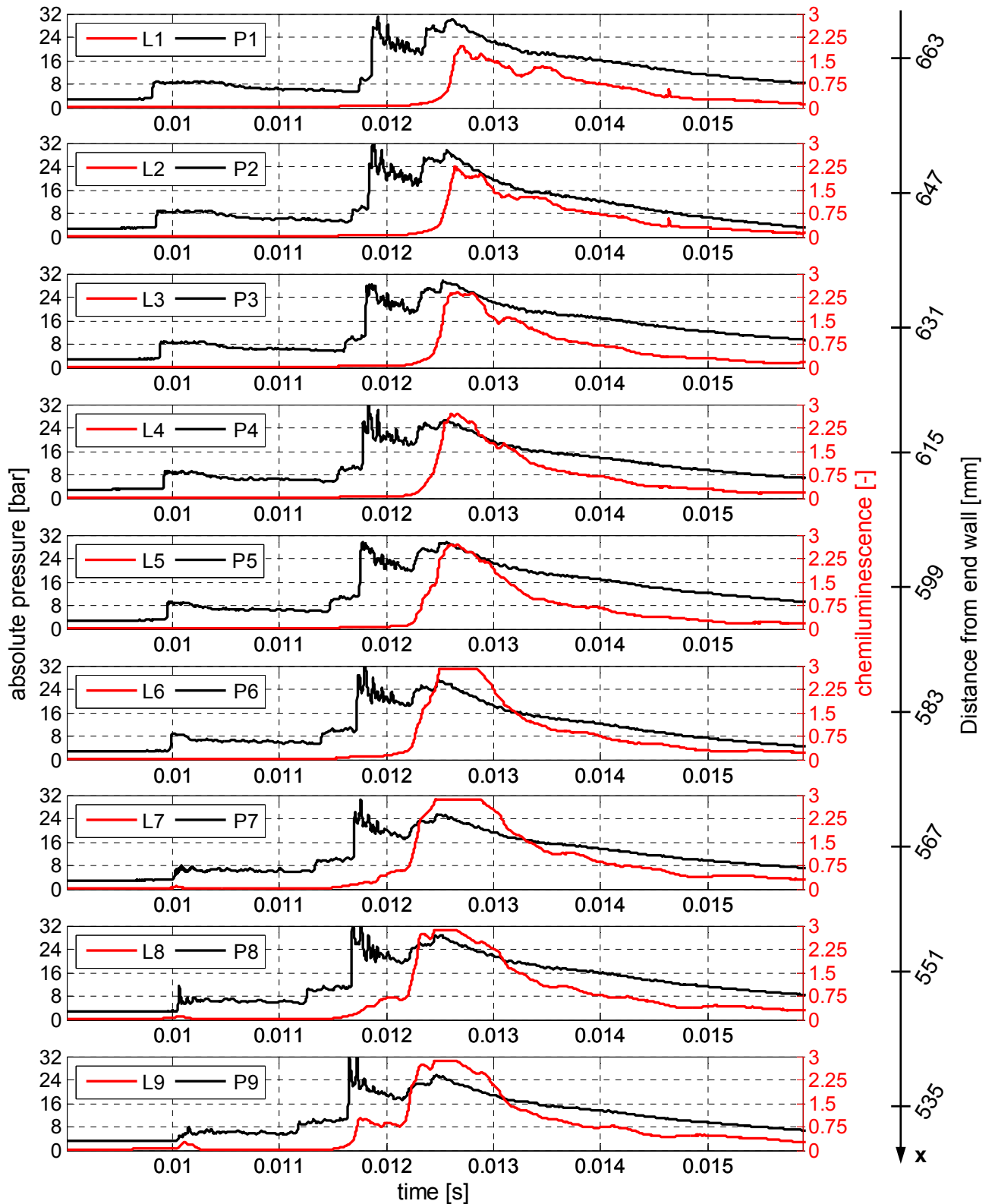


**Figure A.2:** Pressure and chemiluminescence profiles of the incident and the reflected shock waves, s/f,  $M_i = 1.55$

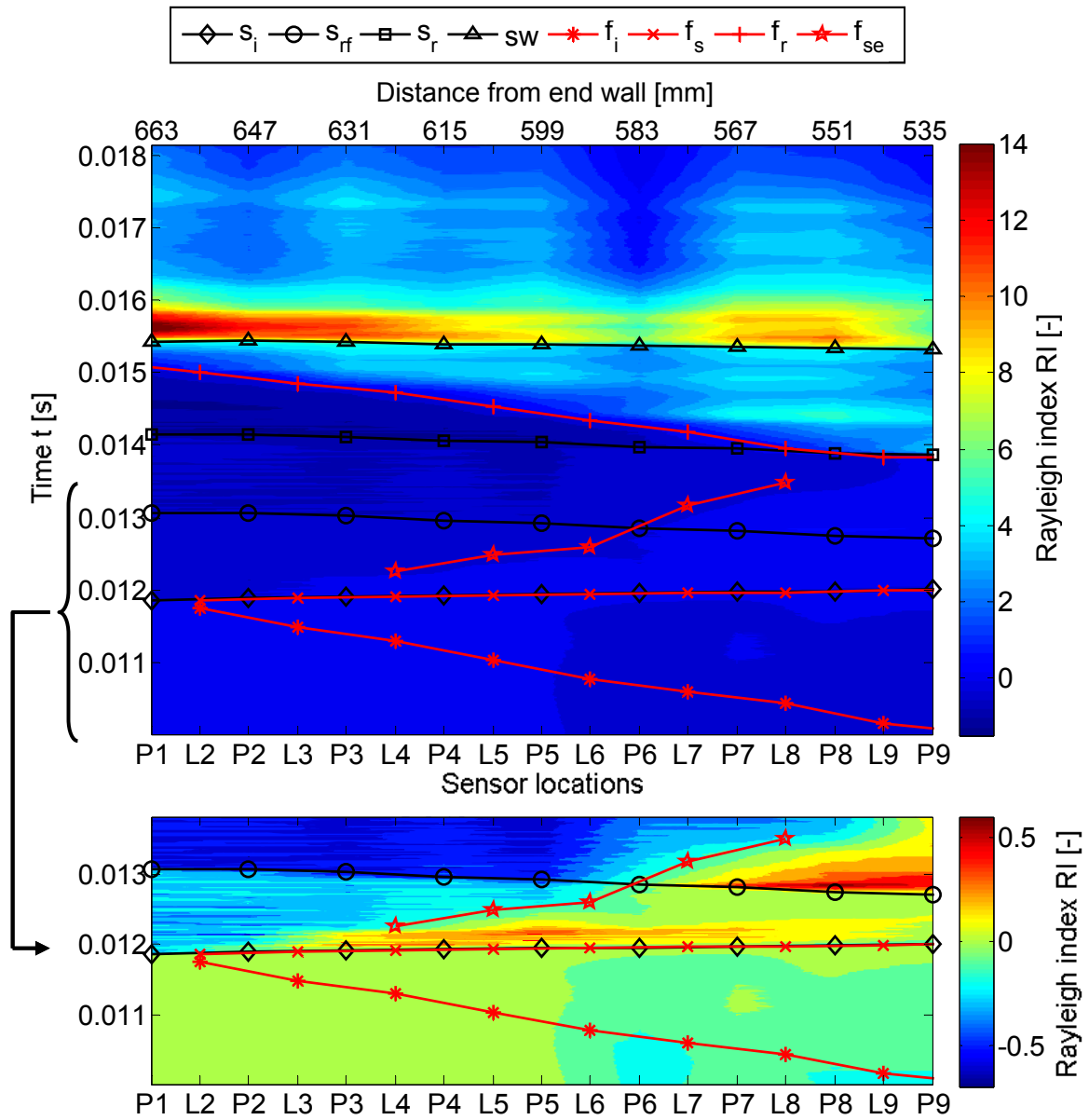
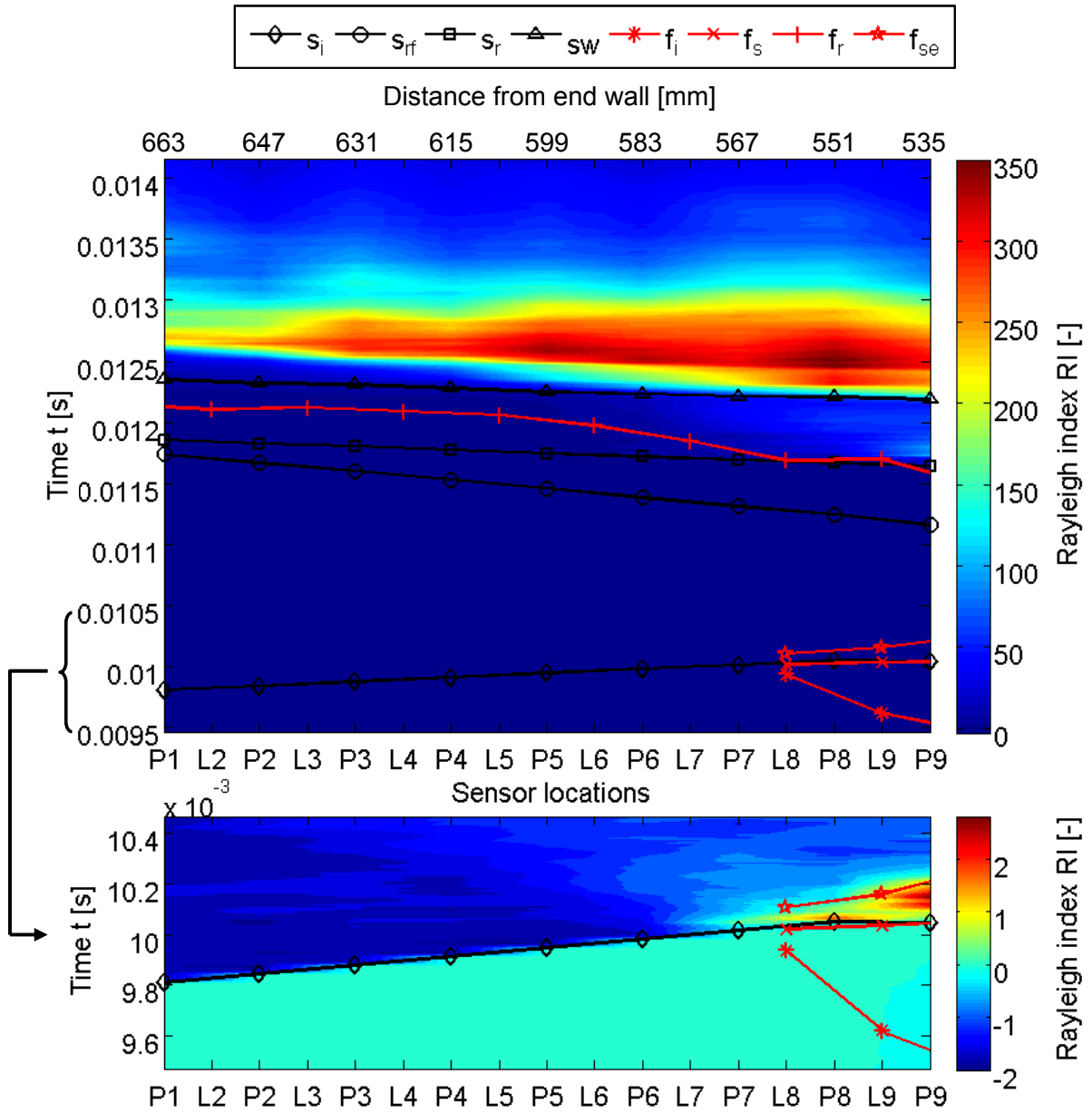


Figure A.3: Instantaneous Rayleigh index RI,  $s/f$ ,  $M_i = 1.26$



**Figure A.4:** Instantaneous Rayleigh index RI, s/f,  $M_i = 1.55$

## Bibliography

- [1] **Abd-El-Fattah, A. M. ; Henderson, L. F.:** *Shock Waves at a Slow-Fast Gas Interface*, Journal of Fluid Mechanics, Vol. 89, pp. 79-94, **1978**
  
- [2] **Adams, G. K. ; Pack, D. C.:** *Some Observations on the Problem of Transition Between Deflagration and Detonation*, 7th Symposium (International) on Combustion, Butterworths, London, UK, **1959**
  
- [3] **Advisory\_Council\_for\_Aeronautics\_Research\_in\_Europe:** *Strategic Research Agenda*, <http://www.acare4europe.com/docs/ASD-volume1-2nd-final-ss%20illus-171104-out-asd.pdf>, **01.07.2011**
  
- [4] **Airbus\_S.A.S.:** *Airbus Global Market Forecast 2010-2029*, <http://www.airbus.com/company/market/gmf2010/>, **01.07.2011**
  
- [5] **Akbari, P. ; Müller, N.:** *Performance Investigation of Small Gas Turbine Engines Topped with Wave Rotors*, 39th AIAA/ASME/SAE/ASEE Joint Propulsion Conference and Exhibit, AIAA 2003-4414, Huntsville, Alabama, US, **2003**
  
- [6] **Akbari, P. ; Nalim, M. R.:** *Review of Recent Developments in Wave Rotor Combustion Technology*, AIAA Journal of Propulsion and Power, Vol. 25 (4), pp. 833-844, **2009**
  
- [7] **Anderson, J. D.:** *Fundamentals of Aerodynamics*, 2. Edition, McGraw Hill, **1991**
  
- [8] **Andriani, R. ; Ghezzi, U. ; Infante, E.:** *Thermal Analysis of Constant Volume Combustion Gas Turbine*, 43rd AIAA Aerospace Science Meeting and Exhibit, AIAA 2005-1010, Reno, Nevada, US, **2005**

- [9] **Andriani, R. ; Ghezzi, U. ; Infante, E.:** *Characteristics and Performances of Constant Volume Combustion Turbine Engine*, 41st AIAA/ASME/SAE/ASEE Joint Propulsion Conference & Exhibit, AIAA 2005-2415, Tucson, Arizona, US, **2005**
- [10] **Azoury, P. H.:** *Engineering Applications of Unsteady Fluid Flow*, John Wiley&Sons, **1992**
- [11] **Baehr, H. D. ; Kabelac, S.:** *Thermodynamik, Grundlagen und technische Anwendungen*, 13. Edition, Springer Verlag, **2006**
- [12] **Bauer, S. G.:** *Improved Gas Generator and Method for Generating Combustion Gas Under Pressure*, Patent, 858,601, **1958**
- [13] **Bauknecht, A.:** *Numerische Simulation von Verdichtungsstoß-Flammen-Interaktionen*, Studienarbeit, Institut of Aircraft Propulsion Systems, Stuttgart University, Stuttgart, **2010**
- [14] **Ben-Dor, G. ; Igra, O. ; Elperin, T.:** *Handbook of Shock Waves. Theoretical, Experimental and Numerical Techniques*, Academic Press, **2001**
- [15] **Birch, N. T.:** *2020 Vision: The Prospects for Large Civil Aircraft Propulsion*, ICAS 2000 Congress, 22nd International Congress of Aeronautical Sciences, Harrogate, UK, **2000**
- [16] **Bloxside, G. J. ; Dowling, A. P. ; Hooper, N.; et al.:** *Active Control of Reheat Buzz*, 25th AIAA Aerospace Science Meeting, Reno, NV, US, **1987**
- [17] **Bobula, G. A. ; Wintucky, W. T. ; Castor, J. G.:** *Compound Cycle Engine Program*, NASA Technical Memorandum 88879, **1986**
- [18] **Boeing\_Corporation:** *Current Market Outlook 2011-2030*, [http://www.boeing.com/commercial/cmo/pdf/Boeing\\_Current\\_Market\\_Outlook\\_2011\\_to\\_2030.pdf](http://www.boeing.com/commercial/cmo/pdf/Boeing_Current_Market_Outlook_2011_to_2030.pdf), **01.07.2011**
- [19] **Borisov, A. A. ; Gelfand, B. E. ; Gubin, S. A.; et al.:** *Mechanism of Formation of a Compression Wave Behind the Front of a Weak Shock Wave Propagated Through a Combustible Mixture*, Doklady Akademii Nauk SSSR. Chemical Physics., Vol. 190 (3), pp. 621-624, **1970**



- [20] **Borisov, A. A. ; Gelfand, B. E. ; Gubin, S. A.; et al.:** *Amplification of Weak Shocks in a Burning Two-Phase Liquid-Gas System*, Zhurnal Prikladnoi Mekhaniki i Tekhnicheskoi Fiziki, Vol. 11 (1), pp. 168-174, **1970**
- [21] **Borisov, A. A. ; Gelfand, B. E. ; Gubin, S. A.; et al.:** *The Onset of Detonation in Two-Phase (Liquid-Gas) Mixtures*, 13th Symposium (International) on Combustion, **1971**
- [22] **Borisov, A. A. ; Gelfand, B. E. ; Gubin, S. A.; et al.:** *Attenuation of Shock Waves in Two-Phase Gas-Liquid Medium*, Fluid Dynamics, Vol. 6 (5), pp. 892-897, **1971**
- [23] **Bräunling, W. J. G.:** *Flugzeugtriebwerke*, Springer Verlag Berlin Heidelberg, **2001**
- [24] **British\_Petroleum:** *BP Energy Outlook 2030*, [http://www.bp.com/liveassets/bp\\_internet/globalbp/globalbp\\_uk\\_english/reports\\_and\\_publications/statistical\\_energy\\_review\\_2011/STAGING/local\\_assets/pdf/2030\\_energy\\_outlook\\_booklet.pdf](http://www.bp.com/liveassets/bp_internet/globalbp/globalbp_uk_english/reports_and_publications/statistical_energy_review_2011/STAGING/local_assets/pdf/2030_energy_outlook_booklet.pdf), **04.07.2011**
- [25] **British\_Petroleum:** *BP Statistical Review of World Energy*, [http://www.bp.com/assets/bp\\_internet/globalbp/globalbp\\_uk\\_english/reports\\_and\\_publications/statistical\\_energy\\_review\\_2011/STAGING/local\\_assets/pdf/statistical\\_review\\_of\\_world\\_energy\\_full\\_report\\_2011.pdf](http://www.bp.com/assets/bp_internet/globalbp/globalbp_uk_english/reports_and_publications/statistical_energy_review_2011/STAGING/local_assets/pdf/statistical_review_of_world_energy_full_report_2011.pdf), **04.07.2011**
- [26] **Brouillette, M.:** *The Richtmyer-Meshkov Instability*, Annual Review of Fluid Mechanics, Vol. 34, pp. 445-467, **2002**
- [27] **Caldwell, N. ; Glaser, A. ; Dimicco, R.; et al.:** *Acoustic Measurements of an Integrated Pulse Detonation Engine with Gas Turbine System*, 43th AIAA Aerospace Sciences Meeting and Exhibit, AIAA 2005-413, Reno, Nevada, US, **2005**
- [28] **Castor, J. G.:** *Compound Cycle Turbofan Engine*, AIAA/SAE/ASME 19th Joint Propulsion Conference, AIAA-83-1338, Seattle, Washington, US, **1983**
- [29] **Chang, E. J. ; Kailasanath, K.:** *Shock Wave Interactions with Particles and Liquid Fuel Droplets*, Shock Waves, Vol. 12 (4), pp. 333-341, **2003**

- [30] **Chu, B.-T.:** *On the Generation of Pressure Waves at a Plane Flame Front*, 4th Symposium (International) on Combustion, Baltimore, US, **1953**
- [31] **Chu, B.-T.:** *Pressure Waves Generated by Addition of Heat in a Gaseous Medium*, National Advisory Committee for Aeronautics, NACA Technical Note 3411, **1955**
- [32] **Chu, B.-T.:** *Mechanism of Generation of Pressure Waves at Flame Fronts*, National Advisory Committee for Aeronautics, Technical Note No. 3683, **1956**
- [33] **Chu, B.-T.:** *Stability of Systems Containing a Heat Source - The Rayleigh Criterion*, National Advisory Committee for Aeronautics, NACA Technical Report RM 56D27, **1956**
- [34] **Chu, B.-T.:** *On the Energy Transfer to Small Disturbances in Fluid Flow*, Acta Mechanica, Vol. 1 (3), pp. 215-234, **1965**
- [35] **Ciccarelli, G. ; Dorofeev, S.:** *Flame Acceleration and Transition to Detonation in Ducts*, Progress in Energy and Combustion Science, Vol. 34, pp. 499-550, **2008**
- [36] **Culick, F. E. C.:** *A Note on Rayleigh's Criterion*, Combustion Science and Technology, Vol. 56, pp. 159-166, **1987**
- [37] **DARPA:** *Vulcan Phase II. Turbine/Constant Volume Combustion Engine Demonstration Programme*, DARPA/Tactical Technology Office, US Department of Defense, Broad Agency Announcement, **2010**
- [38] **Dowling, A. P. ; Morgans, A. S.:** *Feedback Control of Combustion Oscillations*, Annual Review of Fluid Mechanics, Vol. 37, **2005**
- [39] **Dunlap, R. ; Brehm, R. L. ; Nicholls, J. A.:** *A Preliminary Study of the Application of Steady-State Detonative Combustion to a Reaction Engine*, Jet Propulsion, Vol. 28 (7), **1958**
- [40] **Dunn-Rankin, D. ; Sawyer, R. F.:** *Tulip Flames: Changes in Shape of Premixed Flames Propagating in Closed Tubes*, Experiments in Fluids, Vol. 24, pp. 130-140, **1998**

- 
- [41] **Dyer, R. S. ; Kaemming, T. A.:** *The Thermodynamic Basis of Pulsed Detonation Engine Thrust Production*, 38th AIAA/ASME/SAE/ASEE Joint Propulsion Conference & Exhibit, AIAA 2002-4072, Indiana, Indianapolis, US, **2002**
- [42] **Eidelman, S. ; Yang, X.:** *Analysis of the Pulse Detonation Engine Efficiency*, AIAA 98-3877, **1998**
- [43] **Fickett, W. ; Davis, W. C.:** *Detonation Theory and Experiment*, Dover Publications Inc., **2001**
- [44] **Figureu, C.:** *The Interaction of a Strong Propagating Shock Wave With an Axial Turbine Stage*, Diploma Thesis, Institute of Aircraft Propulsion Systems, University of Stuttgart, **2012**
- [45] **Foa, J. V.:** *Single Fow Jet Engines - a Generalized Treatment*, Journal of the American Rocket Society, Vol. 21, **1951**
- [46] **Foa, J. V.:** *Elements of Flight Propulsion*, John Wiley & Sons, Inc., **1960**
- [47] **Frohn, A.:** *Einführung in die Technische Thermodynamik*, 3., Verlag Konrad Wittwer Stuttgart, **1998**
- [48] **Gel'fand, B. E. ; Gubin, S. A. ; Kogarko, S. M.:** *Amplification of Triangular Shock Waves in a Flammable Two-Phase Medium*, Zhurnal Prikladnoi Mekhaniki i Technicheskoi Fiziki, Vol. 1, **1971**
- [49] **Giuliani, F.:** *Gas Turbine Combustion. Technology, Dimensioning, Diagnostics*, Vorlesungsskript, Institute for Thermal Turbomachinery Machine Dynamics, Combustion Division, TU Graz, **2007**
- [50] **Glassman, A. J. ; Snyder, C. A. ; Knip Jr., G.:** *Advanced Core Technology: Key to Subsonic Propulsion Benefits*, National Aeronautics and Space Administration, NASA Technical Memorandum 101420, **1989**
- [51] **Glassman, I. ; Yetter, R. A.:** *Combustion*, 4. Edition, Elsevier, **2008**

- [52] **Haber, L. C. ; Vandsburger, U. ; Saunders, W. R.; et al.:** *An Examination of the Relationship Between Chemiluminascent Light Emissions and Heat Release Rate Under Non-Adiabatic Conditions*, ASME International Gas Turbine Institute, 2000-GT-0121, Munich, Germany, **2000**
- [53] **Hawthorne, W. R.:** *Reflections on the United Kingdom. Aircraft Gas Turbine History*, Journal of Engineering for Gas Turbines and Power, Vol. 116, pp. 495-510, **1994**
- [54] **Heffer, J. H. ; Miller, R.:** *Performance of Choked Unsteady Ejector-Nozzles for use in Pressure-Gain Combustors*, 47th AIAA Aerospace Sciences Meeting Including The New Horizons Forum and Aerospace Exposition, Orlando, Florida, US, **2009**
- [55] **Heiser, W. H. ; Pratt, D. T.:** *Thermodynamic Cycle Analysis of Pulse Detonation Engines*, AIAA Journal of Propulsion and Power, Vol. 18 (1), **2002**
- [56] **Henderson, L. F.:** *On the Refraction of Shock Waves*, Journal of Fluid Mechanics, Vol. 198, pp. 365-385, **1989**
- [57] **Hilfer, M.:** *Numerische Simulation von Verdichtungsstoß-Flammen-Interaktionen*, Studienarbeit, Institute of Aircraft Propulsion Systems, Stuttgart University, Stuttgart, **2011**
- [58] **Horlock, J.:** *Thermodynamic Availability and Propulsion*, 14th International Symposium on Air Breathing Engines, Florence, Italy, **1999**
- [59] **Horlock, J. H.:** *Advanced Gas Turbine Cycles*, Elsevier Science Ltd., **2003**
- [60] **Hutchins, T. E. ; Metghalchi, M.:** *Energy and Exergy Analyses of the Pulse Detonation Engine*, ASME Journal of Engineering for Gas Turbines and Power, Vol. 125, **2003**
- [61] **Intergovernmental\_Panel\_on\_Climate\_Change:** *IPCC Special Report: Aviation and the Global Atmosphere*, <http://www.ipcc.ch/ipccreports/sres/aviation/index.php?idp=3>, **04.07.2011**

- [62] **Janus, M. C. ; Richards, G. A. ; Gemmen, R. S.; et al.:** *An Analytical Approach to Understanding the Pressure-Gain Combustor*, Journal of Energy Resources Technology, Vol. 119, **1997**
- [63] **Joos, F.:** *Technische Verbrennung, Verbrennungstechnik, Verbrennungsmodellierung, Emissionen*, Springer Verlag, **2006**
- [64] **Ju, Y. ; Shimano, A. ; Inoue, O.:** *Vorticity Generation and Flame Distortion Induced by Shock Flame Interaction*, 27th Symposium (International) on Combustion/The Combustion Institute, **1998**
- [65] **Kailasanath, K.:** *Recent Developments in the Research an Pulse Detonation Engines*, 40th AIAA Aerospace Sciences Meeting and Exhibit, AIAA 2002-0470, Reno, Nevada, US, **2002**
- [66] **Karpov, V. P. ; Sokolik, A. S.:** *Reinforcement of Shock Waves Interacting with a Cellular Flame*, Combustion, Explosion and Shock Waves, Vol. 5 (2), pp. 136-141, **1969**
- [67] **Karpov, V. P.:** *Determination of the Acceleration of combustion associated with shock-flame interaction*, Fizika Goreniya i Vzryva, Vol. 4, **1970**
- [68] **Keller, J. O. ; Westbrook, C. K.:** *Response of a Pulse Combustor to Changes in Fuel Composition*, 21st symposium (International) on Combustion, **1986**
- [69] **Keller, J. O. ; Bramlette, T. T. ; Dec, J. E.; et al.:** *Pulse Combustion: The Importance of Characteristic Times*, Combustion and Flame, Vol. 75, **1989**
- [70] **Keller, J. O.:** *Pulse Combustion: The Mechanisms of NO<sub>x</sub> Production*, Combustion and Flame, Vol. 80, pp. 219-257, **1990**
- [71] **Keller, J. O. ; Bramlette, T. T. ; Barr, P. K.; et al.:** *NO<sub>x</sub> and CO Emissions From a Pulse Combustor Operating in a Lean Premixed Mode*, Combustion and Flame, Vol. 99, pp. 460-466, **1994**

- [72] **Kentfield, J. A. C. ; Rehman, M. ; Marzouk, E. S.:** *A Simple Pressure-Gain Combustor for Gas Turbines*, Journal of Engineering for Power, Vol. 99, pp. 153-158, **1977**
- [73] **Kentfield, J. A. C. ; Rehman, A. ; Cronje, J.:** *Performance of Pressure-Gain Combustor Without Moving Parts*, AIAA Journal of Energy, Vol. 4, pp. 56-64, **1980**
- [74] **Kentfield, J. A. C. ; O'Blenes, M.:** *Methods for Achieving a Combustion-Driven Pressure-Gain in Gas Turbines*, ASME Gas Turbine Conference and Exhibition, Anaheim, US, **1987**
- [75] **Kentfield, J. A. C. ; Yerneni, P.:** *Pulsating Combustion Applied to a Small Gas Turbine*, International Journal of Turbo and Jet-Engines, Vol. 4, pp. 45-53, **1987**
- [76] **Kentfield, J. A. C. ; Fernandes, L. C. V.:** *Improvements to the Performance of a Prototype Pulse, Pressure-Gain, Gas Turbine Combustor*, ASME Journal of Engineering for Gas Turbines and Power, Vol. 112, pp. 67-52, **1990**
- [77] **Kentfield, J. A. C. ; O'Blenes, M. J.:** *Small Gas Turbine Using a Second-Generation Pulse Combustor*, AIAA Journal of Propulsion and Power, Vol. 6 (2), pp. 214-220, **1990**
- [78] **Kentfield, J. A. C. ; Kumar, J. C.:** *Liquid Fuel Systems for Gas Turbine, Pulse, Pressure-Gain Combustor*, 33rd AIAA/ASME/SAE/ASEE Joint Propulsion Conference & Exhibit, Seattle, Washington, US, **1997**
- [79] **Kentfield, J. A. C.:** *Thermodynamics of Pulse-Detonation Engines*, AIAA Journal of Propulsion and Power, Vol. 18 (6), **2002**
- [80] **Kentfield, J. A. C.:** *Fundamentals of Idealized Airbreathing Pulse-Detonation Engines*, AIAA Journal of Propulsion and Power, Vol. 18 (1), **2002**
- [81] **Khokhlov, A. M. ; Oran, E. S. ; Chtchelkanova, A. Y.; et al.:** *Interaction of a Shock With a Sinusoidally Perturbed Flame*, Combustion and Flame, Vol. 117, pp. 99-116, **1999**

- 
- [82] **Khokhlov, A. M. ; Oran, E. S. ; Thomas, G. O.:** *Numerical Simulation of Deflagration-to-Detonation Transition: The Role of Shock-Flame Interactions in Turbulent Flames*, Combustion and Flame, Vol. 117, pp. 323-339, **1999**
- [83] **Kiehl, J. T. ; Kevin, E. T.:** *Earth's Annual Global Mean Energy Budget*, National Center for Atmospheric Research, Bulletin of the American Meteorological Society, Vol. 78, **1997**
- [84] **Kilchyk, V.:** *Pressure-Wave Amplification of Flame Area in Wave Rotor Channels*, Dissertation, Purdue University, West Lafayette, Indiana, **2009**
- [85] **Kilchyk, V. ; Nalim, R. ; Merkle, C.:** *Laminar Flame Fuel Consumption Rate Modulation by Shocks and Expansion Waves*, Combustion and Flame, **2010**
- [86] **Kim, J.-R. ; Akamatsu, F. ; Choi, G.-M.; et al.:** *Observation of Local Heat Release Rate With Changing Combustor Pressure in the CH<sub>4</sub>/Air Flame (wrinkled laminar regime)*, Thermocimica Acta, Vol. 491, pp. 109-116, **2009**
- [87] **Koff, B. L.:** *Spanning the Globe With Jet Propulsion*, AIAA Annual Meeting and Exhibit, AIAA-1991-2987 Arlington, VA, US, **1991**
- [88] **Koff, B. L.:** *Gas Turbine Technology Evolution: A Designer's Perspective*, Journal of Propulsion and Power, Vol. 20 (4), pp. 577-595, **2004**
- [89] **Krugger-Emden, H. ; Scherer, V. ; Wirtz, S.:** *Thermodynamische Prozessanalyse von Mikrogasturbinenprozessen*, Report, Institut für Energie-, System-, Material- und Umwelttechnik e.V., Ruhr-Universität Bochum, **2004**
- [90] **Kuo, K. K.:** *Principles of Combustion*, 2. Edition, John Wiley & Sons, Inc, **2005**
- [91] **Lampinen, M. J. ; Turunen, R.:** *Thermodynamic Analysis of a Pulse Combustion System and its Application to a Gas Turbine*, International Journal of Energy Research, Vol. 16, pp. 259-276, **1992**
- [92] **Lauer, M. ; Sattelmayer, T.:** *On the Adequacy of Chemiluminescence as a Measure for Heat Release in Turbulent Flames With Mixture Gradients*, ASME Journal of Engineering for Gas Turbines and Power, Vol. 132, **2010**

- [93] **Lechner, C. ; Seume, J.:** *Stationäre Gasturbinen*, Springer Verlag, **2003**
- [94] **Lee, J. G. ; Santavicca, D. A.:** *Experimental Diagnostics for the Study of Combustion Instabilities in Lean Premixed Flames*, AIAA Journal of Propulsion and Power, Vol. 15, pp. 735-750, **2003**
- [95] **Lefebvre, A. H.:** *Gas Turbine Combustion*, 2. Edition, Taylor&Francis, **1998**
- [96] **Li, H. ; Akbari, P. ; Nalim, M. R.:** *Air-Standard Thermodynamic Analysis of Gas Turbine Engines Using Wave Rotor Combustion*, 43rd AIAA/ASME/SAE/ASEE Joint Propulsion Conference & Exhibit, AIAA 2007-5050, Cincinnati, Ohio, US, **2007**
- [97] **Lieuwen, T. ; Neumeier, Y.:** *Nonlinear Pressure-Heat Release Transfer Function Measurements in a Premixed Combustor*, Proceedings of the Combustion Institute, Vol. 29, pp. 99-107, **2002**
- [98] **Markstein, G. H.:** *A Shock-Tube Study of Flame Front-Pressure Wave Interaction*, 6. Symposium (International) on Combustion, New Haven, Connecticut, US, **1956**
- [99] **Mawid, M. A. ; Park, T. W. ; Sekar, B.; et al.:** *Application of Pulse Detonation Combustion to Turbofan Engines*, ASME Turbo Expo, 2001-GT-0448, New Orleans, Louisiana, USA, **2001**
- [100] **McBride, B. J. ; Gordon, S. ; Reno, M. A.:** *Coefficients for Calculating Thermodynamic and Transport Properties of Individual Species*, National Aeronautics and Space Administration, NASA Technical Memorandum 4513, **1993**
- [101] **McManus, K. R. ; Poinso, T. ; Candel, S. M.:** *A Review of Active Control of Combustion Instabilities*, Progress in Energy and Combustion Science, Vol. 19, **1993**
- [102] **Meece, C. E.:** *Gas Turbine Technologies of the Future*, 12th International Symposium on Air Breathing Engines (ISABE), ISABE 95-7006, Melbourne, Australia, **1995**
- [103] **Merziger, G. ; Wirth, T.:** *Repetitorium der Höheren Mathematik*, 4. Edition, Binomi Verlag, **1999**



- [104] **Moustapha, H. ; Zelesky, M. F. ; Baines, N. C.; et al.:** *Axial and Radial Turbines*, Concepts ETI Inc., **2003**
- [105] **Murrow, K. R. ; Franer, M. T. ; Giffin, R. G.:** *Rotary Pressure Rise Combustor for a Gas Turbine Engine*, United States Patent, US 2009/0196733 A1, General Electric Company, US, **2009**
- [106] **Nalim, M. R. ; Pekkan, K.:** *A Review of Rotary Pressure-Gain Combustion Systems for Gas Turbine Applications*, ASME Turbo Expo 2003, GT-2003-38349, Atlanta, Georgia, US, **2003**
- [107] **Nalim, R. ; Pekkan, K.:** *Internal Combustion Wave Rotors for Gas Turbine Engine Enhancement*, International Gas Turbine Congress, Tokyo, Japan, **2003**
- [108] **Narayanaswami, L. ; Richards, G. A.:** *Pressure-Gain Combustion: Part I - Model Development*, ASME Journal of Engineering for Gas Turbines and Power, Vol. 118, pp. 461-468, **1996**
- [109] **NATO:** *Performance Prediction and Simulation of Gas Turbine Engine Operation for Aircraft, Marine, Vehicular, and Power Generation*, The Research and Technology Organisation (RTO) of NATO, TR-AVT-036, **2007**
- [110] **Nicoud, F. ; Poinso, T.:** *Thermoacoustic instabilities: Should the Rayleigh criterion be extended to include entropy changes?*, Combustion and Flame, Vol. 142, pp. 153-159, **2005**
- [111] **Nori, V. ; Seitzman, J.:** *Evaluation of Chemiluminescence as a Combustion Diagnostic Under Varying Operating Conditions*, 46th AIAA Aerospace Sciences Meeting and Exhibit, AIAA 2008-953, Reno, Nevada, US, **2008**
- [112] **Norris, G.:** *Pulse Power: PDE-powered Flight Demonstration Marks Milestones in Mojave*, Aviation Week&Space Technology, Vol. 168, **2008**
- [113] **Norris, J. W. ; Twelves Jr., W. V.:** *Pulsed Combustion Engine*, United States Patent, US 6,886,325 B2, United Technologies Corporation, USA, **2005**
- [114] **Oertel, H.:** *Stossrohre*, Springer Verlag, **1966**

- [115] **Offord, T. ; Miller, R. J. ; Dawson, J. R.; et al.:** *Improving the Performance of a Valveless Pulse Combustor Using Unsteady Fuel Injection*, 46th AIAA Aerospace Sciences Meeting and Exhibit, Reno, Nevada, US, **2008**
- [116] **Oppenheim, A. K.:** *Gasdynamic Analysis of the Development of gaseous Detonation and its Hydraulic Analogy*, Proceedings of the Combustion Institute, Vol. 4, **1953**
- [117] **Oran, E. S. ; Gardener, J. H.:** *Chemical-Acoustic Interactions in Combustion Systems*, Progress in Energy and Combustion Science, Vol. 11, **1985**
- [118] **Oran, E. S. ; Gamezo, V. N.:** *Origins of Deflagration-to-Detonation Transition in Gas-Phase Combustion*, Combustion and Flame, Vol. 148, pp. 4-47, **2007**
- [119] **Palfreyman, D. ; Martinez-Botas, R. F.:** *The Pulsating Flow Field in a Mixed Flow Turbocharger Turbine: An Experimental and Computational Study*, Transactions of the ASME, Vol. 127, **2005**
- [120] **Paxson, D.:** *Pressure-Gain Combustion for Gas Turbine*, Presentation, Pennsylvania State University Turbine System Research Workshop, **2010**
- [121] **Paxson, D. E.:** *A Performance Map for Ideal Air Breathing Pulse Detonation Engines*, National Aeronautics and Space Administration, NASA/TM-2001-211085, **2001**
- [122] **Penner, S. S.:** *Chemistry Problems in Jet Propulsion*, Pergamon Press, **1957**
- [123] **Peters, N.:** *Turbulent Combustion*, Cambridge University Press, **2000**
- [124] **Peters, N.:** *Technische Verbrennung*, Vorlesungsskript, Institut für Technische Mechanik, RWTH Aachen, **2006**
- [125] **Picone, J. M. ; Oran, E. S. ; Boris, J. P.; et al.:** *Theory of Vorticity Generation by Shock Wave and Flame Interactions*, NRL Memorandum Report 5366, Naval Research Laboratory, Washington D.C., **1984**
- [126] **Probst, M.:** *Development of a Pressure-Gain Combustor for Use in a Gas Turbine Cycle*, Diplomarbeit, ETH Zurich, Zürich, **2002**

- 
- [127] **Pun, W. ; Palm, S. L. ; Culick, F. E. C.:** *Combustion Dynamics of an Acoustically Forced Flame*, Combustion Science and Technology, Vol. 175, pp. 499-520, **2003**
- [128] **Rahim, F. ; Elia, M. ; Ulinski, M.; et al.:** *Burning Velocity Measurements of Methane-Oxygen-Argon Mixtures and an Application to Extend Methane-Air Burning Velocity Measurements*, Journal of Engine Research, Vol. 3 (2), pp. 81-93, **2002**
- [129] **Rayleigh, J. W. S.:** *The Theory of Sound*, Dover Publications, **1945**
- [130] **Reynolds, W.:** *The Element Potential Method for Chemical Equilibrium Analysis: Implementation in the Interactive Program Stanjan.*, Technical Report, Mechanical Engineering Department, Stanford University, **1986**
- [131] **Roy, G. D. ; Frolov, S. M. ; Borisov, A. A.; et al.:** *Pulse Detonation Propulsion: Challenges, Current Status, and Future Perspective*, Progress in Energy and Combustion Science, Vol. 30, pp. 545-672, **2004**
- [132] **Rudinger, G.:** *Shock Wave and Flame Interactions*, Combustion and Propulsion. Third AGARD Colloquium, Palermo, Italy, **1958**
- [133] **Rupert, V.:** *Shock-Interface Interaction: Current Research on the Richtmyer-Meshkov Problem*, 18th International Symposium on Shock Waves, Sendai, Japan, **1991**
- [134] **Sabatiuk, A.:** *Gas Turbine Engines Employing Fixed Volume Combustion*, United States Patent, 4,693,075, USA, **1987**
- [135] **Sadot, O. ; Erez, L. ; Alon, U.; et al.:** *Study of Nonlinear Evolution of Single-Mode and Two-Bubble Interaction under Richtmyer-Meshkov Instability*, Physical Review Letters, Vol. 80 (8), pp. 1654-1657, **1998**
- [136] **Salamandra, G. D. ; Sevastyanova, I. K.:** *Formation of Weak Shock Waves Ahead of a Flame Front and Their Intensification During Passage Through the Flame*, Combustion and Flame, Vol. 7, pp. 169-174, **1963**

- [137] **Sammann, B. C. ; Twelves Jr., W. V. ; Jones, G. D.:** *Pulsed Combustion Turbine Engine*, United States Patent, US 6,901,738 B2, United Technologies Corporation, USA, **2005**
- [138] **Samtaney, R. ; Zabusky, N. J.:** *Circulation Deposition on Shock-Accelerated Planar and Curved Density-Stratified Interfaces: Models and Scaling Laws*, Journal of Fluid Mechanics, Vol. 269, pp. 45-78, **1994**
- [139] **Samtaney, R. ; Ray, J. ; Zabusky, N. J.:** *Baroclinic Circulation Generation on Shock Accelerated slow/fast Gas Interfaces*, Physics of Fluids, Vol. 10 (5), pp. 1217-1230, **1998**
- [140] **Scarinci, T. ; Lee, J. H. ; Thomas, G. O.; et al.:** *Amplification of a Pressure Wave by Its Passage Through a Flame Front*, 13th International Colloquium on the Dynamics of Explosions and Reactive Systems, Nagoya, Japan, **1991**
- [141] **Schauer, F. ; Stutrud, J. ; Bradley, R. P.:** *Detonation Initiation Studies and Performance Results for Pulse Detonation Engine Applications*, 9th AIAA Aerospace Sciences Meeting and Exhibit, AIAA 2001-129, Reno, Nevada, US, **2001**
- [142] **Schauer, F. ; Bradley, R. P. ; Hoke, J.:** *Interaction of a Pulsed Detonation Engine with a Turbine*, 41st AIAA Aerospace Sciences Meeting and Exhibit, Reno, Nevada, US, **2003**
- [143] **Schmidt, F. A. F. ; Heitland, H.:** *Möglichkeiten zur Steigerung der Energieumsetzung durch pulsierende Verbrennung*, Forschung im Ingenieurwesen, Vol. 31 (5), **1965**
- [144] **Schneider, E.:** *Modellbasierte Regelung von Gasturbinenbrennkammern zur Optimierung von Stickoxidemissionen und Verbrennungsinstabilitäten*, Dissertation, Institute of Aircraft Propulsion Systems, University of Stuttgart, Stuttgart, **2009**
- [145] **Sehra, A. K. ; Whitlow Jr., W.:** *Propulsion and Power for the 21st Century Aviation*, Progress in Aerospace Science, Vol. 40, pp. 199-235, **2004**
- [146] **Shapiro, A. H.:** *The Dynamics and Thermodynamics of Compressible Fluid Flow*, The Ronald Press Company, NY, **1953**

- 
- [147] **Shchelkin, K. I.:** *Intensification of Weak Shock Wave by a Cellular Flame*, Combustion, Explosion and Shock Waves, Vol. 2 (2), pp. 20-21, **1966**
- [148] **Siemens\_AG:** *Siemens setzt drei Weltrekorde mit zukunftsweisender Kraftwerkstechnik*, [http://www.siemens.com/press/pool/de/pressemitteilungen/2011/fossil\\_power\\_generation/EFP201105064d-wp.pdf](http://www.siemens.com/press/pool/de/pressemitteilungen/2011/fossil_power_generation/EFP201105064d-wp.pdf), **01.07.2011**
- [149] **Staudacher, S.:** *Lufffahrtantriebe*, Vorlesungsskript, Institut für Lufffahrtantriebe, Universität Stuttgart, **2004**
- [150] **Sterling, J. D. ; Zukoski, E. E.:** *Nonlinear Dynamics of Laboratory Combustor Pressure Oscillations*, Combustion Science and Technology, Vol. 77, pp. 225-238, **1991**
- [151] **Stotz, I. ; Lamanna, G. ; Weigand, B.; et al.:** *A Double-Diaphragm Shock Tube for Hydrocarbon Desintergration Studies*, AIAA /AHI Space Planes and Hypersonic Systems and Technologies Conference, AIAA 2006-8109, **2006**
- [152] **Suresh, A. ; Hofer, D. C. ; Tangirala, V. E.:** *Turbine Efficiency for Unsteady, Periodic Flows*, 47th AIAA Aerospace Sciences Meeting, AIAA 2009-504, Orlando, Florida, US, **2009**
- [153] **Terao, K. ; Inagaki, T.:** *Interaction Between Combustion and Shock Waves*, Japanese Journal of Applied Physics, Vol. 28 (7), pp. 1226-1234, **1989**
- [154] **Thomas, G. ; Bambrey, R.:** *Schlieren Observation of Flame Acceleration as Precursors of Transition to Detonation*, 24th International Congress on High Speed Photography and Photonics, Sendai, Japan, **2000**
- [155] **Thomas, G. ; Bambrey, R. ; Brown, C.:** *Experimental Observations of Flame Acceleration and Transition to Detonation Following Shock-Flame Interaction*, Combustion Theory and Modelling, Vol. 5, pp. 573-594, **2001**
- [156] **Thring, W. M.:** *Pulsating Combustion. The Collected Works of F. H. Reynst*, Pergamon, **1961**
- [157] **Tichý, J. ; Gautschi, G.:** *Piezoelektrische Messtechnik*, Springer Verlag, **1980**

- [158] **Ton, V. T. ; Karagozian, A. R. ; Marble, F. E.; et al.:** *Numerical Simulations of High-Speed Chemically Reacting Flow*, Theoretical and Computational Fluid Dynamics, Vol. 6, **1994**
- [159] **Troshin, Y. K.:** *The Generalized Hugoniot Adiabatic Curve*, Proceedings of the Combustion Institute, pp. 789-798, **1959**
- [160] **TU\_Clausthal\_Institut\_für\_Energieforschung\_und\_Physikalische\_Technologien:** *Prinzip der Holzwarth-Gasturbine*, [http://www2.pe.tu-clausthal.de/agbalck/vorlesung/energ2001/en-vor07/img\\_6536.htm](http://www2.pe.tu-clausthal.de/agbalck/vorlesung/energ2001/en-vor07/img_6536.htm), **31.10.2011**
- [161] **Van Zante, D. ; Envia, E. ; Turner, M. G.:** *The Attenuation of a Detonation Wave by an Aircraft Engine Axial Turbine Stage*, 18th ISABE Conference, ISABE-2007-1260, Beijing, China, **2007**
- [162] **Verein\_Deutscher\_Ingenieure:** *VDI-Wärmeatlas*, 10. Edition, Springer Verlag, **2006**
- [163] **Walther, R.:** *Verbrennungsprobleme der Luft- und Raumfahrt*, Vorlesungsskript, MTU AeroEngines/Universität Stuttgart, **2003**
- [164] **Weber, H. E.:** *Shock Wave Engine Design*, John Wiley & Sons, Inc., **1995**
- [165] **Weinberg, F. J.:** *Advanced Combustion Methods*, Academic Press Inc. Ltd, **1986**
- [166] **Welch, G. E. ; Jones, S. M. ; Paxson, D. E.:** *Wave-Rotor-Enhanced Gas Turbine Engines*, ASME Journal of Engineering for Gas Turbines and Power, Vol. 119, pp. 469-477, **1997**
- [167] **Whurr, J.:** *Aircraft Compound Cycle Propulsion Engine*, United States Patent, 5,692,372, Rolls-Royce plc, **1997**
- [168] **Williams, A.:** *Combustion of Droplets of Liquid Fuels: A Review*, Combustion and Flame, Vol. 21, pp. 1-29, **1973**
- [169] **Williams, F. A.:** *Combustion Theory*, 2. Edition, The Benjamin/Cummings Publishing Company, Inc., **1988**

- 
- [170] **Willis, E. A. ; Wintucky, W. T.:** *An Overview of NASA Intermittent Combustion Engine Research*, Lewis Research Center, Cleveland, Ohio, US, NASA Technical Memorandum 83668, AIAA-84-1393, **1984**
- [171] **Wilson, J. ; Paxson, D. E.:** *Jet Engine Performance Enhancement Through Use of a Wave Rotor Topping Cycle*, National Aeronautics and Space Administration, NASA-TM-4486, **1993**
- [172] **Wilson, J. ; Paxson, D. E.:** *Wave Rotor Optimization for Gas Turbine Engine Topping Cycles*, AIAA Journal of Propulsion and Power, Vol. 12 (4), pp. 778-785, **1996**
- [173] **Wintenberger, E. ; Shepherd, J. E.:** *The Performance of Steady Detonation Engines*, 41st Aerospace Science Meeting & Exhibit, AIAA 2004-1033, Reno, Nevada, US, **2003**
- [174] **Wintenberger, E.:** *Application of Steady and Unsteady Detonation Waves to Propulsion*, Dissertation, California Institute of Technology, Pasadena, California, **2004**
- [175] **Wintenberger, E. ; Shepherd, J. E.:** *Thermodynamic Analysis of Combustion Processes for Propulsion Systems*, 42nd AIAA Aerospace Sciences Meeting and Exhibit, 4004-1033, Reno, NV, US, **2004**
- [176] **Wintenberger, E. ; Shepherd, J. E.:** *Thermodynamic Cycle Analysis for Propagating Detonations*, AIAA Journal of Propulsion and Power, Technical Note, Vol. 22 (3), **2006**
- [177] **Wintenberger, E. ; Shepherd, J. E.:** *Model for the Performance of Airbreathing Pulse-Detonation Engines*, AIAA Journal of Propulsion and Power, Vol. 22 (3), **2006**
- [178] **Wu, Y. ; Ma, F. ; Yang, V.:** *System Performance and Thermodynamic Cycle Analysis of Airbreathing Pulse Detonation Engines*, AIAA Journal of Propulsion and Power, Vol. 19 (4), **2003**
- [179] **Zeldovich, Y. B.:** *To the Question of Energy Use of Detonation Combustion*, Zhurnal Tekhnicheskoi Fiziki (Journal of Technical Physics), Vol. 10 (17), pp. 1453-1461, **1940**

- [180] **Zeller, P. W.:** *Effizienzsteigerung von Turboluftstrahltriebwerken durch Optimierung des sekundären Luftsystems*, Dissertation, Institute of Aircraft Propulsion Systems, University of Stuttgart, Stuttgart, **2007**
- [181] **Zeller, P. W. ; Staudacher, S.:** *Exergy Analysis for the Performance Evaluation of Different Setups of the Secondary Air System of Aircraft Gas Turbines*, ASME Turbo Expo 2007: Power for Land, Sea and Air, GT2007-27278, Montreal, Canada, **2007**



## Curriculum Vitae

### Personal Data

Name: Eugen Lutoschkin  
Date and place of birth: 21<sup>st</sup> of May 1981, Rudnyj (Kazakhstan)  
Nationality: German, Russian  
Marital Status: Married, 1 child

### Professional Experience

07/2006 – 06/2007 Industrial placement and Diploma Thesis in the field of quality assurance in the manufacturing of high pressure compressor blades, Rolls-Royce plc, Glasgow, UK

09/2007 – 05/2012 Research Assistant at the Institute of Aircraft Propulsion Systems, University of Stuttgart

06/2012 – 08/2012 R&D Engineer  
Advanced Development of Automotive Turbo-Chargers  
Bosch Mahle TurboSystems GmbH & Co KG, Stuttgart

Since 10/2012 Patent Examiner  
Joint Cluster: Civil Engineering and Thermodynamics  
European Patent Office, Munich

### Education

1988 – 1994 Comprehensive School in Russia and Kazakhstan

1994 – 1998 Secondary School, Schramberg-Sulgen, Germany

1998 – 2001 Technisches Gymnasium, Rottweil, Germany

10/2001 – 07/2007 University of Stuttgart, Germany  
Studies of Aerospace Engineering (Diploma Programme)  
Specialisations: 1. Statics und Dynamics,  
2. Aircraft Propulsion Systems & Turbo-Machinery